Universidad de Navarra

Facultad de Ciencias

Polymeric and Soft Nanocomposites Based on Cyclodextrin-Modified Barium Titanate Nanoparticles

Rafael Serra Gómez

Universidad de Navarra

School of Science

Polymeric and Soft Nanocomposites Based on Cyclodextrin-Modified Barium Titanate Nanoparticles

Submitted by **Rafael Serra Gómez** in partial fulfillment of the requirements for the Doctoral Degree of the University of Navarra

Rafa S.

This dissertation has been written under our supervision in the Doctoral Program in Natural and Applied Sciences, and we approve its submission to the Defense Committee.

Signed on October 13, 2016

Dr. Gustavo González Gaitano

Dr. Francisco Javier González Benito

Declaración:

Por la presente yo, **D. Rafael Serra Gómez**, declaro que esta tesis es fruto de mi propio trabajo y que en mi conocimiento, no contiene ni material previamente publicado o escrito por otra persona, ni material que sustancialmente haya formado parte de los requerimientos para obtener cualquier otro título en cualquier centro de educación superior, excepto en los lugares del texto en los que se ha hecho referencia explícita a la fuente de la información.

(I hereby declare that this submission is my own work and that, to the best of my knowledge and belief, it contains no material previously published or written by another person nor material which to a substantial extent has been accepted for the award of any other degree of the university or other institute of higher learning, except where due acknowledgment has been made in the text.)

De igual manera, autorizo a la Facultad de Ciencias de la Universidad de Navarra, la distribución de esta tesis y, si procede, de la "fe de erratas" correspondiente por cualquier medio, sin perjuicio de los derechos de propiedad intelectual que me corresponden.

Signed on October 13, 2016

Rafael Serra Gómez

© Rafael Serra Gómez

Derechos de edición, divulgación y publicación:
© Facultad de Ciencias, Universidad de Navarra

A la memoria de mis padres

AGRADECIMIENTOS / ACKNOWLEDGEMENTS

No sé si me será posible condensar en unos pocos párrafos todos los agradecimientos que se derivan de la realización de esta tesis doctoral, y que en mi caso van más allá, concretamente desde que llegué a la Universidad para cursar la Licenciatura en Química, hace casi más de 10 años, lo que hace que haya pasado casi un tercio de mi vida ligado, de una manera y otra, a esta querida institución. Para no olvidarme de nadie, voy a seguir un orden recorriendo los despachos.

En primer lugar, quiero agradecer a la Universidad de Navarra haberme concedido la posibilidad de realizar esta tesis doctoral en el departamento de Química de la Facultad de Ciencias, con la ayuda inestimable de la Asociación de Amigos de la Universidad de Navarra a través de una de sus becas.

A mis directores, el Dr. Gustavo González Gaitano y al Dr. Francisco Javier González Benito, por escogerme como alumno de doctorado y por confiar en mí durante todos estos años. A Gustavo, no debo agradecerle sólo la formación científica o la tutoría que empezó mucho antes de la tesis, sino también la infinitud de ayudas, consejos, ánimos, empujones, y también la libertad de dejar que me equivoque para así aprender de los errores (también por invitarme a tiro con arco). A Javier, aunque en los últimos años nos hemos visto poco por la distancia, ha mantenido una dedicación constante, y sin su ayuda en el máster y en los inicios de la tesis no me hubiera introducido en el mundo de los materiales. La estancia en la Universidad Carlos III, aunque breve, ha sido un período de gran aprendizaje.

Al personal de la facultad y a los profesores del departamento, desde los más veteranos a los más recientes. Tuve la inmensa suerte de ser una de las últimas promociones que recibió las magistrales clases del Prof. D. Miguel Sánchez González y de la Prof. Carmen Martín Bachiller, con la que pude compartir luego trabajo en el departamento durante mi tesis doctoral. A la Dra. Cristina Martínez Ohárriz y a la Dra. Arantza Zornoza, por su ayuda en los temas científicos, pero también por su disponibilidad completa para ayudar en cualquier momento y en cualquier materia, personal o profesional. Al Dr. José Ramón Isasi y la Dra. Itziar Vélaz, por su ayuda con sus conocimientos, por la gestión del departamento, por el conocimiento adquirido durante las horas de prácticas compartidas y por la posibilidad de implicarme en iniciativas de promoción de la Facultad que atraigan a nuevos estudiantes al mundo de la Química.

A la Dra. Cristina Sola, ya desde mis prácticas en la carrera todos sabíamos que eras la persona a la que acudir cuando algo iba mal o la fastidiábamos, y tus comentarios, aunque a veces “punzantes”, nos ayudaban siempre a pensar y aprender. Luego he tenido la suerte de compartir departamento, horas de laboratorio y hasta de sustituirte en tu baja maternal, viendo lo duro e importante que es tu trabajo, a veces invisible, y lo bien que lo haces día a día, sacando tiempo para innovar y sacar iniciativas tan buenas como los experimentos caseros y la promoción. Espero que los alumnos puedan disfrutar de tus conocimientos muchos años.

Al resto de profesores del departamento, la Dra. Carolina Santamaría y el Dr. Iñigo Navarro, con los que he pasado muchas horas de laboratorio, así como al resto de integrantes de los grupos MIMED, del LICA, y de Ingeniería, que, aunque no hemos tenido una colaboración tan estrecha, las puertas siempre están abiertas para cualquier tipo de ayuda y consulta. Al resto de personal del departamento, empezando por Marisa, por estar siempre pendiente y de la que un “ahora no puedo” nunca ha salido de su boca; a los técnicos, Blanca, Cristina, Josemi, Marta, Guillermo, Gorka y Mikel, imprescindibles para que los laboratorios del departamento funcionen.

A todos los compañeros que he tenido en el departamento, que son muchos: Raquel, Eneko, Rubén, Bárbara, Sheila, Marcos, David, María Pérez, Beatriz, María López, Yasser, Maitane, Nerea, Nekane y Pablo, con todos hemos pasado muchas horas y momentos muy divertidos. He aprendido mucho de todos vosotros, y tengo la suerte de teneros como amigos. A mis compañeros de la Carlos III, Edwin, Eva, Kesman, Carol, Amaia, Sonia, Sandra y Javier.

También me gustaría agradecer al Prof. Guillermo Martínez de Tejada, a Sergio Bárcena y a todo el departamento de Microbiología por su ayuda en el desarrollo de los ensayos de citotoxicidad. Al Prof. Jean Bragard por su ayuda para los cálculos de SANS.

I would like to thank Prof. Khademhosseini and the staff in the laboratory at the Brigham and Women’s Hospital in Boston for the opportunity and great learning experience of doing a research stay at his laboratories and under his mentoring. It was a great learning experience and came back with valuable ideas, friends and contacts. I would also like to thank the Max Planck Society for the Prince of Asturias Mobility grant to visit the Max Planck Institute of Colloids and Interfaces, where the Prof. Fratzl, the Dr. John Dunlop and the student Sebastien Ehrig welcomed me and helped me learn so much about biomaterials. I would like to thank Prof. Cécile Dreiss for welcoming me at the King’s College in London, for her smart input in the last part of this PhD project, and for allowing me to have the experience of performing SANS experiments.

Con esto acabo la parte académica de los agradecimientos, pero quiero seguir con las personas que son muy importantes en mi vida, y sin las cuales no hubiera podido llegar hasta aquí.

A mis amigos del IQS, Estel·la, Joan María y Majo, y a vuestras familias, hemos compartido tantos momentos juntos, de clase, estudio, diversión, conversaciones…en primero de carrera soñábamos con hacer una tesis y ser investigadores, y aquí estamos. Aunque estemos en la distancia os agradezco vuestra amistad. A mis amigos de la carrera, Blanca, Almu, Marta, Mercedes, Iñigo, Rosario y tantos otros, muchas gracias por acogerme cuando aparecí por vuestra clase o por la biblioteca. A mis compañeros de piso, Txustin, Diego y Zozi, por ser tan buenos amigos, aunque temían que fuera un ogro cuando entré al piso, en el fondo sabéis lo que pienso de vosotros. A mi pseudohermana Mercedes y a toda la familia Blasi-Puig, por acogerme siempre y por ayudarme a tomar la decisión de venir a Pamplona, ellos son los que enlazan la amistad con la familia, ya que realmente están más cerca de lo segundo.

A mi familia, podría escribir otras 200 páginas y en mucho menos tiempo, agradeciéndoos todo lo que habéis hecho y hacéis por mí. A mis padres, aunque yo no pude pasar mucho tiempo con ellos, educaron a mi hermana y a mis hermanos de forma excelente, y eso es lo que mi hermana y mis hermanos me han transmitido a mí, estoy seguro que, en cada uno de ellos, en su diferencia, se puede reconocer a mis padres. Los primeros recuerdos que tengo es estar cerca de mi padre mientras él leía el periódico con un vaso de whiskey y me vigilaba de reojo, noto esa protección día a día en mi vida. Mi madre era química, y recuerdo estar en casa jugando mientras ella daba clases a estudiantes, sin duda influyó desde lo alto en mi decisión de estudiar esta carrera y en el día a día hasta hoy que presento esta memoria.

A mi hermana y madrina María, por ser nuestra hermana mayor y educarme con el ejemplo desde que tengo memoria en todo y por seguir haciéndolo ahora conmigo y el resto de hermanos. Por hacerme parte de su propia familia, junto con Carlos y sus 10 hijos.

A José (y a su mujer Sara), por ser nuestro hermano mayor y enseñarme el valor de la lucha diaria contra las adversidades de todo tipo con una sonrisa en la cara, buen humor y un comentario alegre.

A Joaquín, mi hermano y padrino, que siempre ha estado y está allí para ayudarme cuando lo necesito, siempre con una sonrisa y recientemente compañero de viajes y aventuras, que espero se sigan repitiendo.

A Javier, que, aunque probablemente no sepa que estoy acabando una tesis doctoral o donde estoy en este momento, es un ejemplo de innovación, trabajo, y ayuda sin pedir nada a cambio.

A Juanito (y a su mujer Mickey), eres un ejemplo de responsabilidad, esfuerzo y cultura de trabajo constante y bien hecho, a quién nadie le ha regalado nada y afrontas cada día con una sonrisa.

A Jorge, aunque seamos muy diferentes te admiro, eres un ejemplo de lucha y superación diaria frente a las adversidades y de darte a los demás. Te debo las gracias por enseñarme a jugar a futbol y tantas otras cosas que me has enseñado tanto siendo yo un niño como ahora en la distancia.

En general gracias a todos, por ser tan diferentes y a la vez estar tan unidos, por ser tan alegres y por cuidar los unos de los otros siempre, pase lo que pase. Sin vosotros no podría haber estudiado una carrera, aprendido idiomas, mucho menos realizar un doctorado…pero tampoco hubiera podido viajar, trabajar de camarero, repartiendo pan, repartir folletos, programar, o hacer cada una de las cosas que me han llevado hasta donde estoy ahora y que me han educado. Muchas gracias.

And last, but not least, thank you MelJean. And thank you to your family for taking me in and showing me the great values of a Filipino family through your example, *salamat po*. I do not know how to put in words what you mean to me. Thank you for keeping up with me in that archery class where I was not able to shoot a single arrow, and for accepting that ginger cookie in return. The rest is an awesome story that we are building together. Thank you for helping me in my Ph.D., translating, correcting, taking care of me, calming me, listening to me talk about nano things and teaching me new things every day while you keep up with my stubbornness. Thank you for always smiling and having my back when my Ph.D. brought me to the US, to Germany and to the UK, for the long hours of staying up late and facetime. You are an example to me of hard work, of education and respect, of ambition, and of always following your dreams and going beyond your comfort zone with a positive attitude. I feel like at your side I can do everything, thank you. And thank you Nounours, for always being at my side protecting me and protecting MelJean when we are apart.

Por todo esto y mucho más, *thank you, salamat, gracias*.

TABLE OF CONTENTS

Table of Contents

INTRODUCTION

Foreword

Previous to the start of this introduction the author would like to explain in a few lines the outline of this project, so the reader does not feel surprised by what might look like an unrelated combination of topics developed in the following pages.

There are two guiding threads, Barium Titanate (BT) nanoparticles and Cyclodextrins (CDs), which had never been combined before this project was started. Barium Titanate is commonly known for its dielectric and piezoelectric properties, and CDs as stabilizing and solubilizing agents. Our idea is to prepare different kinds of polymeric nanocomposites, hence the first section that introduces them. These different kind of nanocomposites have in common the presence of BT as a filler. However, it would be interesting to prepare nanocomposites from soluble polymeric precursors. For that purpose, CDs are proposed as a way to stabilize the dispersion of the nanoparticles in the polymer solution. The culmination of the mix is the preparation of a hydrogel nanocomposite that can combine the characteristic properties of BT and the host-guest complexation ability of the CDs.

The author is aware that this project covers a wide range of topics, and each of them, nanocomposites, barium titanate piezoelectric nanoparticles, cyclodextrins, inclusion complexes and hydrogels, are really extensive if taken into consideration individually. For this reason, and to prevent an excessively long introduction, this section seeks to compile the main characteristics, properties and state of the art of each of them, but always without losing the focus on the purpose in which they are used in this thesis. To make up for that, the author will provide with the latest and most complete reviews on the topics for further reference.

1. COMPOSITE AND NANOCOMPOSITE MATERIALS

1.1 Definition

In order to expand and understand better what a nanocomposite is, it seems appropriate to start with the definition of composite materials, also commonly known as composites. Composites are materials constituted of more than one constituent which the differ in composition (physically or chemically), form or microstructure, leading to an heterogeneous mixture system. In general, one of the phases is a discontinuous phase, which is also called the *filler* or *strengthening*, and it is embedded in the continuous phase, the matrix.

Each component keeps their individual properties when forming the composite, without merging into one another. Due to the fact that they retain their identities they can

be physically identified easily. Besides, the interfaces or the boundary regions where two or more components interact, are well defined (Defense 2002), and what is more important, the combination of the different components usually yields a material with properties that exceed those of the individual components, creating a synergetic effect.

On the other hand, nanocomposite materials are defined as composite or multiphase materials that have at least one of its constituents in the nano scale, that is to say, with one of their dimensions below 100 nm (Ajayan et al. 2003). By having at least one of the components in the nanoscale, and considering that the surface area-to-volume ratio of the nanoparticles is known to be high, the interface between the nanosized phase and the other components of the composite is large enough to be considered as another phase (interface) capable of producing its own effects (Novak 1993).

This fact is of great interest, as the ability to control the nanophase provides an unprecedented variety of building blocks that can be combined to form composites, yielding properties that cannot be achieved in a traditional material. In a sense, thank to our ability to perceive and work on the nanoscale, science is starting to have access to the same type of building blocks that nature uses, with the possibilities are enormous and promising, as on top of different materials we can control dispersions, disposition, interactions and the hierarchy and order level of the new materials.

1.2 Historical background

Composite materials are ubiquitously present in nature, and have been around human civilization since the beginning of its era. Wood might be considered a composite made out of cellulose fiber and lignin; a different disposition of the same two elements, with a hollow interior gives way to bamboo, a light and, at the same time, stiff structure. Another example of a natural composite material is bone, consisting of a ceramic matrix, formed by inorganics salts of calcium and phosphate mostly, and magnesium, carbonate and sodium in a minor amount, being calcium hydroxyapatite the major one, that wraps around the organic part, composed mostly of short and soft collagen fibers. Overall it conforms a lightweight load-bearing material (Hall & Guyton 2011; Weiner & Wagner 1998).

Composites have been long used over the course of human history whenever there were needs that could not be fulfilled with the common materials available at the time. Wattle and daub is a long lasting man-made construction composite that has existed since the Neolithic (Shaffer 1993), in which woven strips of wood form a lattice, the wattle, that is later filled with the daub, a mixture of mud, sand, animal feces and straw to achieve long

lasting buildings. Other examples of composites in construction can be found throughout history, as the first forms of cement, a mixture of sand, water and minerals, as well as the introduction of iron bars into masonry (Blezard 2003). Mongolian bows, dated from the 1200 AD, made from bamboo, horns and animal glue provided the Genghis Khan empire with the most powerful and precise weapon until gunpowder was invented (Halpin 1992). A more recent application is the addition of carbon black to rubber to produce tires, at the end of the 19th century (Mark et al. 2005).

However, it was not until the 20th century that the composite production experienced a boost. Phenolic resins were introduced into the industry; fiberglass came into action on the production of boats (Marsh 2006), reinforced plastics were introduced in the electrical components and in the aviation industry during the WWII (Rosato et al. 2004), and during the following years of cold war and technological progress in aerospace. DuPont developed aramidic fibers in the early 70's (Kwoleck 1974)that further developed into materials as Kevlar and other high-modulus fiber composites in the 80's (Clement et al. 2012). In the recent years the composite industry has exponentially grown in the automotive, aerospace (Cabrera & Miranda 2015), construction (Bartos et al. 2009), environmental and biomedical industries (Aguilar 2013) among others, and it would be difficult to mention an industry where they do not play a key role (Sanchez et al. 2011).

1.3 Types of composite materials and most common applications

Composites can be classified depending on the disposition of their components, the way the filler is embedded in the matrix being a paramount factor towards the properties of the new material. Based on the disposition of the phases composites can be classified into three main groups (Brigante 2014) (Table i.1):

1. ***Fiber-reinforced:*** The filler are continuous or discontinuous fibers, either randomly oriented or aligned in the matrix in an ordered fashion. The properties are derived from the length of the fibers, the dispersion and order scale inside the matrix. They represent the majority of the high performance composites.
2. ***Particle-reinforced:***. The matrix provides most of the performance while the particles restrain the displacement of the matrix. They are the most widely used composites and also the cheapest. They can be divided into:
    a. ***Large particle composites:*** Their properties are a combination of the individual ones and can be predicted by the rule of mixtures. Some useful examples are concrete (cement and gravel and sand),

cermets (ceramic matrix and metal particles), and reinforced rubber in tires.

b. ***Dispersion-strengthened composites:*** They contain particles in the nanometer scale, as, for example, Al_2O_3 in sintered aluminum powder, ThO_2 in nickel alloys or WC in cutting tools. The controlled dispersion and homogeneity of the particles determines the properties of the material.

3. Structural composites: The properties depend mainly on the geometry of the elements forming the composite. There are two main types:

a. ***Laminated composites:*** Formed by stacked sheets that can exhibit orthotropic properties (layers with main properties in orthogonal directions) or anisotropic (isotropic properties in the transverse plane) (Gürdal et al. 1999).

b. ***Sandwiched composites:*** Composed of two sheets with a lightweight foam or honeycomb structure in between them bound by and adhesive.

Table i.1: Types of composites by filler

Filler	Types	Properties
Fiber	Short Fibers Disoriented Long Fibers Oriented Long Fibers	High Strength High Stiffness Low Density Good Shear properties
Particle	Large Particles Dispersion-Strengthened	Modulus Increase Ductility Improvement Permeability decrease
Structural	Laminated Sandwiched	In-plane stiffness Lightweight, large bend stiffness

Another common way of classification is based on the type of material that constitutes the matrix of the composite. According to this, three main types of composites can be stablished:

1. Ceramic-Matrix Composites (CMC): They consist of fibers (ceramic or carbon based mostly) embedded in a ceramic matrix, commonly alumina or silicon

oxide and their derivatives to improve the crack resistance, response against thermal shock and elongation. They are the most capable composites in terms of temperature resistance and mechanical features. The main drawback is the difficulty to ensure a proper dispersion of the filler to obtain a homogeneous material. Amongst their applications are heat shields in the aerospace industry, components in combustion chambers and jet engines, flame holders or brake disks.

2. ***Metal-matrix composites (MMC):*** Materials where the matrix is a metal, which is combined with another metal, ceramic or organic compound as a filler, usually with the purpose of obtaining low density materials with high strength, yielding what is commonly known as light metals (Kainer 2006). Some examples are cast iron with graphite reinforcement or steel with a high content of carbide. The usual applications are structural components of rockets, jets and car components, high performance cutting tools or power electronics.

3. ***Polymeric-Matrix Composites (PMC):*** In this case the filler are fibers bound together by an organic polymer matrix, with the aim of providing the matrix with stiffness and high strength. They can be divided into reinforced plastics and advanced plastic composites. The first type usually consists in polyester resins reinforced with glass fibers, being relatively cheap. The second type Their main advantage is the light weight and increased mechanical properties, but their main drawback is the temperature of operation, as they are limited to the temperature of decomposition of the matrix material, usually below 300°C. PMCs can be found mainly in the aerospace industry, sporting goods and automobile sector (Eyring 1988).

The diversity of composite materials is growing at such a rate, in number and importance, that they already constitute a branch of materials science in itself. The number of applications of composites is also vast, as we are surrounded of many of them in our everyday life as it has been described above. Added to that, the nanocomposite industry is also blooming in the last decades, and according to ISI Web of Science there have been over 90.000 publications over the last 20 years.

Their use in aerospace allows for high performance materials with light weight that lowers fuel consumption as the recent Boeing 787, containing 35% of its structure of carbon-fiber-reinforced polymer substituting the aluminum used before (Cabrera & Miranda 2015). In the automotive industry they are found in disk brakes, racing cars, light weigh structures in motorbikes and bicycles, cover and in the car interior panels (Y.-H. Lee et al. 2013; Garcés et al. 2000). The construction industry could be considered the first area where composite materials were used and therefore composite materials for construction have evolved and grown providing materials with better corrosion resistance, weight performance, design flexibility and durability among others, not to mention the crucial role they play in the renewable energy with the materials for windmills and wind turbines (Lee et al. 2010).

In the biomedical field, composite materials provide better prosthetic materials, of light weigh, increased mechanical properties and biocompatibility, or in dentistry allowing for lightweight braces or filling materials. Sporting goods are full of applications of composite materials in skis, sailing skulls, bicycles, shoes or balls that we use every day when exercising (Dattaguru & Gopalakrishnan 2013).

Overall, in our time, nanocomposites are of crucial importance in almost all fields of science, and the multiple possibilities of different combinations and innovative structures offer a vast amount of new properties that translate into new applications. In our case, this project focusses around the preparation of new nanocomposites based on polymeric matrices and ceramic nanoparticles of barium titanate ($BaTiO_3$, BT) as a filler. The general information about structure, properties and applications of this ceramic are introduced in the following lines.

2. BARIUM TITANATE

Barium titanate is a ceramic of the perovskites family, with the general formula ABO_3. It presents and array of properties that has made $BaTiO_3$ a ceramic of interest since its discovery until the present days. It is ferroelectric, possesses high dielectric constant and low dielectric loss, and most of their crystalline structures present piezoelectricity.

2.1 History

$BaTiO_3$ was discovered in 1941, during the Second World War, as the supply of mica, a material used in capacitors, was threatened by the war situation (Randall et al. 2004). As a consequence of that, the research on ceramics with enhanced dielectric properties gained importance, and military research studies tried to dope TiO_2 with BaO, which lead to the first

patent (H. Thurnaurer and J. Deaderick 1947). The material thus produced presented high permittivity and dielectric constants about 10 times greater than TiO_2, which led to a growing number of studies to understand that difference, and in consequence to the demonstration of the ferroelectric switching in ceramics (Von Hippel et al. 1946).

Further studies followed on the discovery of the different crystalline structures and phase transitions of $BaTiO_3$ (Megaw et al. 1945; Miyake & Ueda 1946; Kay et al. 1949), the growth of the crystals and its dielectric anisotropy (J.P. Remeika 1954; Merz 1949; Blattner et al. n.d.; Miller & Savage 1959). However, despite being fundamentally a research funded by the government for military purpose, the interest in the use of Barium Titanate for non-military applications grew, as a component in electronic devices, such as circuits in televisions and radios, ultrasonic generators, phonographs, accelerometers and many other applications that have kept growing exponentially ever since and translated into the development of new materials and technology (Dranetz et al. 1948; Haertling 1999).

2.2 Structure and Properties

2.2.1 Structure

As briefly introduced before, Barium Titanate is a perovskite-like ceramic, with the general formula ABO_3. The structure of the perovskite ($CaTiO_3$) is cubic with the larger cation at the corners (A), the smaller cation (B) in the center of the cube and the oxygen atoms placed in the center of the faces, as can be seen in Fig i.1 (F. Jona 1993).

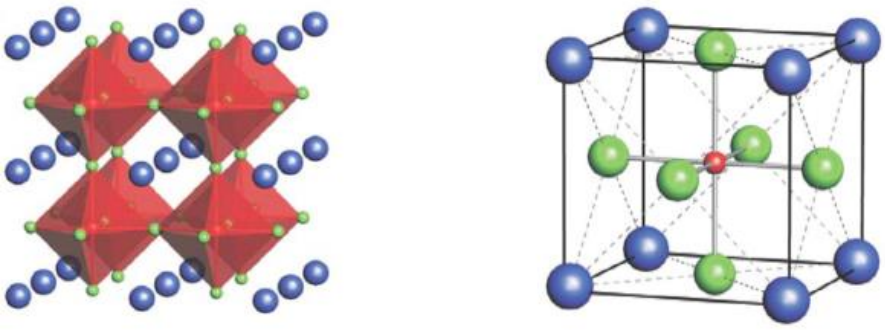

Fig. i.1: Common structure of the perovskite-like ceramics.

The cubic crystalline structure of $BaTiO_3$, with a spatial group Pm-3m, is the most common one for the ceramic. However, other structures can be found that derive from the distortion in the lattice parameters of the cubic cell vacants of some of the atoms that conform it. Therefore, rhombohedral, orthorhombic, tetragonal, cubic and hexagonal Barium Titanate can be formed, and each and every one of these phases presents different properties in terms of pyroelectricity, ferroelectricity and piezoelectricity. The distortions in

the lattice can be originated by the temperature; once a transition temperature is reached the unit cell becomes unstable and transforms to a more stable one. Table i.1 shows the different structures (Momma & Izumi 2011) as a function of the temperature and the corresponding properties:

Table i.2: $BaTiO_3$ crystalline structures as a function of temperature.

Temperature	Structure	Unit Cell	Properties
T< -90 °C	Rhombohedral	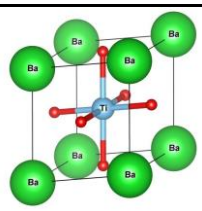	Ferroelectric Piezoelectric
-90 °C < T < 5 °C	Orthorhombic	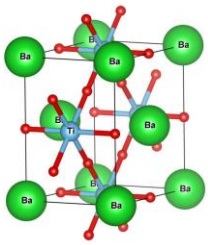	Ferroelectric Piezoelectric
5 °C < T < 120 °C	Tetragonal	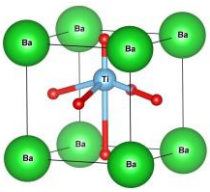	Ferroelectric Piezoelectric
120 °C < T < 1460 °C	Cubic	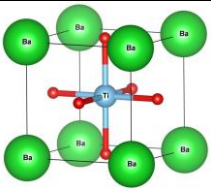	Paraelectric
T> 1460 °C	Hexagonal	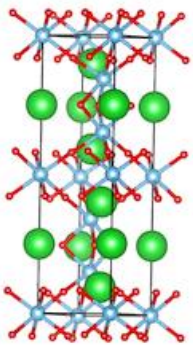	Paraelectric

Out of these structures the most important ones are the tetragonal and the cubic. The temperature at which the transition from the Tetragonal phase to the cubic phase takes place is known as the *Curie Temperature* (T_c) (Pascoe 1973). Below the Curie point, a displacement of the electric charges would yield a polarization, whereas above the Curie point the structure becomes cubic and symmetric, therefore the material becomes dielectric. For Barium Titanate, this temperature is around 120 °C (Begg et al. 1996). In order to explore and understand the main properties of Barium Titanate it is important to briefly revise the terms of dielectricity, ferroelectricity and piezoelectricity.

2.2.2 Properties

Dielectric materials are electrical insulator that can be polarized by an applied electric field. In the dielectric materials the electronic charge is localized, in a similar way to ions and, when under the influence of an electric field, the charges experience a small shift in their equilibrium position resulting in dielectric polarization, opposite to the free flowing of charge occurring in a conductor. The dielectric polarization creates an inner electric field inside the material, as the positive charges move away from the negative ones (Hippel 1954). The measure of how polarized a dielectric gets by the action of and electric field is the *Electronic Susceptibility* (χ_e):

$$P = \varepsilon_0 x_e E \qquad \text{[Eq i.1]}$$

Where P is the polarization density, E the intensity of the electric field and ε_0 the electric permittivity of vacuum. Dielectric properties are only observed in the non-centrosymmetric crystallographic point groups, as those are the only ones capable of achieving a net polarization and create dipoles. Of the 32 existent point groups, only 20 meet the previous condition and will present dielectric properties as ferroelectricity and piezoelectrity (Tilley 2006).

For Barium Titanate and other ceramics with similar characteristics, the dielectric constant is highly dependent on the synthesis route followed, and consequently on internal factors as the grain size, purity and density. It also depends on external factors, as the temperature or the frequency at which it is measured. The table i.3, summarizes the dielectric constants of barium titanate obtained by different synthesis methods (Vijatovic et al. 2008).

Table i.3: Dielectric Constants of BT obtained from different synthesis routes. * Data not published. From (Vijatovic et al. 2008)

Synthesis Method	Synthesis T (°C)	Dielectric Constant at room temperature	Dielectric Constant at T_C	Frequency	Reference
Sol-Gel	1200 /1300 20min	500-650/700-900	*	1 MHz	(Arya et al. 2003)
Hydrothermal	1250 / 2h	2000	7000	1 kHz	(Boulos et al. 2005)
Hydrothermal	900/ 2h	6900	11000	*	(Xu et al. 2003)
Pechini	1300 / 3h	1700	2840	1 kHz	(Vinothini et al. 2006)
Pechini	1260 / 1-5h	>5000	10000	1 kHz	(Duran et al. 2002)
Mechanochemical	1330 / 2h	2500	7500	100 kHz	(Stojanovic et al. 2005)
Precipitation	1310 /*	665	880	10 kHz	(Buscaglia et al. 2004)
Oxalate coprecipitation	1350/ 4h	2200	8000	1,10,100 kHz	(Simon-Seveyrat et al. 2007)

In dielectrics, the dielectric polarization is usually small and linear. However, some materials with non-centrosymmetric structure suffer spontaneous high polarization states below the Curie temperature. The spontaneous electric polarization is called ferroelectricity, and was discovered in the Rochelle salt in 1921 (Valasek 1971). Ferroelectric materials differ from dielectrics in various ways. Primary, the polarization is not linear and, more important, when the applied electric field value is zero they present some residual polarization. The polarization can also be reversed by an applied field in the opposite direction, creating a hysteresis loop as shown in Figure i.2.

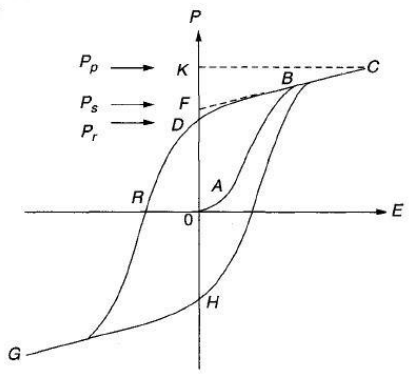

Fig. i 2: Schematic hysteresis loop of a ferroelectric material.

The abscise axis represents the electric field applied *(E)* and the ordinate represents the polarization *(P)*. The first segment is the OA, where the electric field is small and the polarization increases linearly, as the field is not capable of inducing a preferential orientation in the crystalline domains. As the field increases the polarization increases non-linearly (AB), as all the domains are already oriented towards the field. The polarization keeps increasing (BC) until it reaches a saturation point due to the orientation of all the domains. When the applied field is reduced (CBF) the polarization diminishes, however when the field reaches a value of zero, a net polarization value is seen (D). The value of the field necessary for the polarization to be zero again (R) is called the *coercivity field*. When that point is reached and the electric field is brought back to zero, the polarization reverts (H) as the result of the formation of the domains. The area enclosed by the hysteresis loop is a measure of the energy dissipated during the process.

The hysteresis loop in ferroelectric materials occurs below the Curie point. Once the T_c is surpassed, the structure evolves into a centrosymmetric structure that does not have the ability to form the dipoles (Jonscher 1983; Kao 2004).

Piezoelectricity is also a property of some dielectric materials, associated to the low symmetry of the point groups, and establishes a direct relation between an electric field and a mechanical stress. When the material is experiencing a mechanical tension there is a displacement of the atoms forming its unit cell, and that deformation turns into a polarization along the polar axis (Fig i.3). Piezoelectricity is a reversible process, and the application of an electric field, either permanent or oscillating, would induce a mechanical tension of contraction or expansion in the material. BT presents also pyroelectricity, closely related to piezoelectricity, consisting in the generation of a temporary voltage when they experience a temperature variation (Webster 1999).

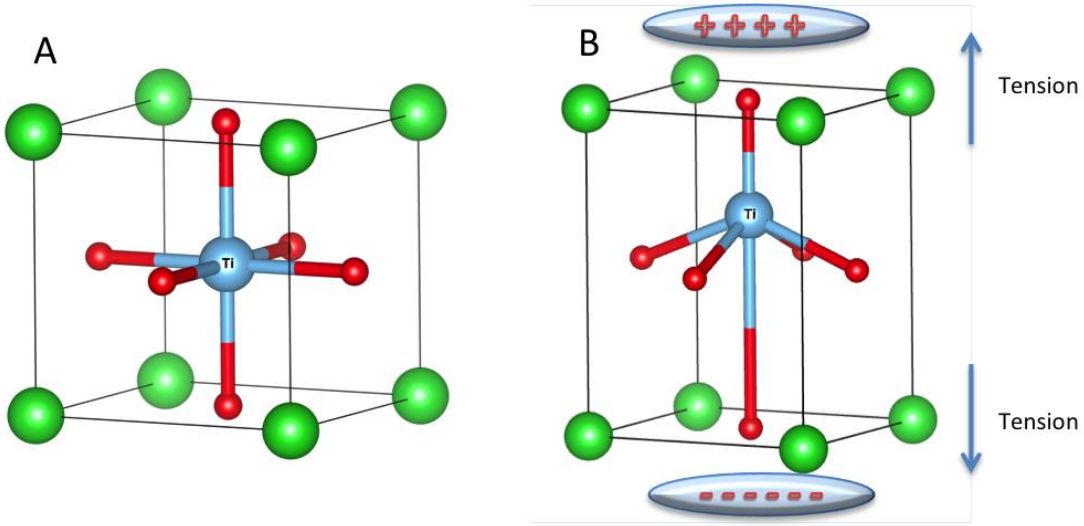

Fig. i.3: Example of piezoelectric polarization in a $BaTiO_3$ unit cell. a) Shows a non-polarized cubic cell and b) shows a tetragonal cell polarized by mechanical deformation.

There are two main mechanisms to explain the piezoelectric effect. The first one is the concept of linear piezoelectricity, which states that the dipolar moments will compensate themselves when there is no pressure over the material. The variation of the electrical field and the pressure is linear and the piezoelectricity will always require a non-centrosymmetric cell. In the second case the individual dipolar moments do not cancel, but they distribute themselves along one axis of the unit cell, allowing the spontaneous polarization. This effect is called ferroelectric piezoelectricity, as the variation of the polarization with the electric field follows the hysteresis loop. The materials that show this kind of behavior present a high dielectric constant and high piezoelectric coefficients.

Depending on how we relate the electric field and the mechanical tension applied two piezoelectric coefficients can be defined by their respective Maxwell relations (Duerloo & Reed 2013; Duerloo et al. 2012; Kochervinskii 2003):

$$\boldsymbol{e_{i\alpha}} = \left(\frac{\partial \boldsymbol{P_i}}{\partial \boldsymbol{\varepsilon_\alpha}}\right)_{E,T} = -\left(\frac{\partial \boldsymbol{\sigma_\alpha}}{\partial \boldsymbol{E_i}}\right)_{\varepsilon,T} \qquad \text{[Eq. i.2]}$$

$$\boldsymbol{d_{i\alpha}} = \left(\frac{\partial \boldsymbol{P_i}}{\partial \boldsymbol{\varepsilon_\alpha}}\right)_{E,T} = \left(\frac{\partial \boldsymbol{\varepsilon_\alpha}}{\partial \boldsymbol{E_i}}\right)_{\alpha,T} \qquad \text{[Eq. i.3]}$$

Where P_i is the polarization, E_i the electric field, σ_α is the mechanical stress and ε_α the deformation or strain. Generally, the coefficients of more interest are the in-plane ones, commonly known as the d_{33} and ε_{33}. Table i.4 contains these coefficients for $BaTiO_3$ in comparison to other ceramics (ZnO) and nanoscale materials as boron nitride nanotubes (h-BN) extracted from the literature at 300K (J. Zhang et al. 2014).

Table i.4: Bulk Piezoelectric coefficients for $BaTiO_3$, ZnO and h-BN at Room Temperature (J. Zhang et al. 2014).

Material	ε_{33} (C m^{-2})	d_{33} (pm V^{-1})
$BaTiO_3$	6.71	92
ZnO	1.22	9.93
h-BN	0.20	0.60

From the practical point of view, to obtain piezoelectricity from BT bulk powders it is necessary to align the domains, as after the sintering (synthesis route of a ceramic from its powder precursors) and cooling processes the crystalline domains will be arranged in random directions with no net polarization. The process to align the domains is called *Poling* (Fig. i.4). During the poling process the material is heated up to a temperature below the T_c and a high electric field is applied to orientate the domains to a single direction, maintained during the cooling process to room temperature. When the electric field is removed, although some domains will change their orientation, the majority will remain in the poled position and consequently the bulk material will retain the net polarization (Baxter et al. 2010).

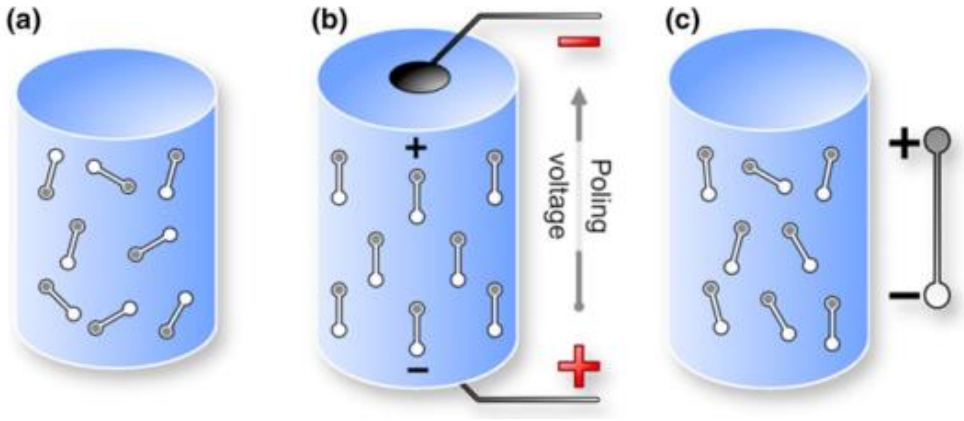

Fig. i.4: Poling process of ferroelectric ceramics. (a) shows the ceramic state after sintering, (b) the application of the electric field that causes the domains to align, and (c) the state of the ceramic once the poling process has ended. Extracted from *Baxter et al. 2010*.

2.2.3 Main applications

These interesting properties of BT have led to a number of applications since its discovery, mostly in the electronics field as transducers and other engineering areas in the

form of crystals, bulk ceramics, multilayer and thin films. The most important are the following:

1. *Multilayer Ceramic Capacitors (MLC's).* $BaTiO_3$ is the first ceramic used for high-dielectric-constant capacitors (1950), being present in practically every electronic device in our everyday life. It consists of a pair of parallel metal plates with an insulator material in-between. When a voltage is applied to the plates in absence of the insulator the charge on the plates is proportional to the voltage, however, when the insulator is placed, the charge of the plates is proportionally increased by the dielectric constant of the ceramic. Nowadays the miniaturization required for electronic components has produced capacitors with more than 500 thin dielectric layers of around 2µm (Kuo et al. 2006), and BT has been substituted by lead containing interceramics as PMN's (Lead magnesium neobites) and PZT's (Lead zirconium titanates) (Takenaka et al. 1989). The typical applications are as MLC's, Voltage-variable capacitors and energy-storage capacitors (Buchanan 2004).
2. *Positive Temperature Coefficient (PCT) Thermistors*. Another application of Barium Titanate widely used in the engineering field is as PCT's. Even though Barium Titanate is an insulator, when doped with trivalent (La, Sb, Y) or pentavalent donors (Nb, Ta) it becomes a semiconductor used as a switching device, constant-temperature heaters and as thermostats to temperature variations (Stojanović et al. 1999; Syrtsov et al. 2002).
3. *Waveguide Modulators.* Due to its low dielectric constant and large electro-optic coefficients, thin films of $BaTiO_3$ and MgO are used as waveguide modulators. These kinds of modulators are crucial for high speed and wide broadband communication systems. (Zgonik et al. 1994; Tang et al. 2004)
4. *IR Detectors.* The ferroelectric and pyroelectric properties of Barium Strontium Titanates are used in thermal IR detectors, as they present a high pyroelectric coefficient, high dielectric constant, and dielectric loss factor (Whatmore et al. 1987; Dubey et al. 2011; Watton 1989) .

2.3 Barium Titanate in nanocomposites

On top of the applications described above, with the uprising of the nanoscience and nanocomposite technology, barium titanate has played an important role in piezoelectric nanocomposites. Amongst the different compositions of nanocomposites described in section 1.3, Barium titanate presents a higher number of applications in polymer-matrix nanocomposites, most of them in the same fields as before, as dielectric capacitors, MLC's

and PCT's (Bai et al. 2000; Zhang et al. 2002; Lu & Wong 2008). As a ceramic material, Barium titanate requires high processing temperatures for sintering, molding or shaping procedures. On the other hand, polymers usually present low processing temperatures, mechanical flexibility and relatively low prices. Therefore it is clear that preparing nanocomposites that can combine the mechanical, electrical and thermal properties of Barium Titanate as a filler with a polymeric matrix, is a good solution and opens a wide range of applications and strategies to prepare BT nanoparticles and nanocomposites at relatively low temperature, such as hydrothermal methods (Slamovich & Aksay 1996; Boulos et al. 2005; Shi et al. 2005), sol-gel processes (Frey & Payne 1995; Shimooka & Kuwabara 1996) and precursor decomposition methods (Cho 1998; Hsiang & Yen 1996).

In order for the nanocomposite to present adequate properties it is very important a proper homogeneous dispersion of the filler in the matrix, preventing agglomeration and high aggregation of the nanoparticles. The elevated energy surface of barium titanate usually leads to phenomena of aggregation and phase separation, which result in poor processability and a high density of defects in the nanocomposite structure that yields a nanocomposite with poor properties (Kim et al. 2009).

Different approaches have been described to ensure the homogeneity of the new nanomaterial. On one side there is the chemical modification of the nanoparticles (Ash et al. 2004; Yang & Dan 2005), which can be carried out by attaching a monomer on the surface of the filler to react with a co-monomer in the polymeric matrix (Bikiaris et al. 2005) by in-situ polymerization (Reynaud et al. 2001), sol-gel methods (He et al. 2006) or other dispersing techniques during the preparation of the nanocomposite, as is the addition of surfactants and dispersants (Tseng & Lin 2003; Kamiya et al. 2003). On the other side physical approaches have also been considered, providing good results when the load of nanoparticles is high, generally above 5% in weight. Amongst them, *High-energy ball milling* (HEBM) has proven to be a good method for the preparation of nanocomposites in the solid state (Pantaleón & González-Benito 2010; Olmos et al. 2011; Olmos et al. 2009; Serra-Gómez et al. 2012). The physical methods have obvious advantages in terms of no need of using organic solvents or other chemical reagents

Once the homogeneity problem is addressed, nanocomposites based on barium titanate appear in many applications showing its distinctive properties. Phosphonic-acid modified barium titanate nanoparticles in poly(vinylidenefluoride-*co*-hexafluoropropylene) present high permittivity and unusual dielectric strength (Kim et al. 2007), the piezoelectric properties of the BT are usually combined with PVDF (Sánchez et al. 2015; Olmos et al. 2013),

a piezoelectric polymer to obtain large dielectric constants and high thermal conductivity (Li et al. 2011; L. Lee et al. 2013). Nanogenerators and thin films to form bendable capacitors allow for high performance flexible devices (Park, Lee, et al. 2010; Park, Xu, et al. 2010). Nanocomposites consisting on polyanilines and BT are also used for high permittivity and dielectric purposes (Saini et al. 2013) and also as flame retardants when combined with epoxy (Zhang et al. 2013) and as capacitors (Polizos et al. 2010; Park, Lee, et al. 2010; Xu et al. 2003). Diblock copolymers have been uses as shielding layers for high energy density nanocomposites (Jung et al. 2010) and polyurethane nanocomposites with BT and iron oxide present interesting microwave properties as enlarged coercitivity and increased dielectric constant and thermal stability (Guo et al. 2009).

In recent years Barium Titanate has been replaced in the majority of these applications by Lead Zirconate Titanate, also known as PZT's. PZT's are inorganic compounds with the formula $Pb[Zr_xTi_{1-x}]O_3$ ($0 \leq x \leq 1$) who also present good piezoelectric properties (Furukawa et al. 1979). The main advantage of PZT's when compared to Barium Titanate is the possibility of tailoring the composition of the three components of the nanofiller depending on the use they are intended for, and therefore many applications that used to contain BT now use PZT's in its different forms (Hilczer et al. 2002; Tang et al. 2011; Chaisan et al. 2009; Tajima et al. 1999).

2.4 Barium Titanate in Biomaterials

If in the field of nanocomposites for electrical applications, the traditional ground for barium titanate, PZT's are taking the lead, a very important area were BT uses are growing fast, is the biomaterials field. Biomaterials are required to interact and be compatible with biological systems, and for that purpose the materials involved in biomedical science and biomedical engineering have to be cytocompatible and non-harmful for the living tissue, in addition to be biodegradable, inert, or being able to be processed by the kidney and be disposed by the body when their function is over

The use of Barium Titanate and other bioactive ceramics as biomaterials has been approached during the last two decades and it is gaining importance. Once again the piezoelectricity of Barium Titanate makes it appealing for these kind of materials, and because of the need to be biocompatible, the absence of lead is in this case and advantage of BT over PZT's (Jeong et al. 2013; Sakai et al. 2006; Tsuchiya et al. 2011). Being able to control or enhance piezoelectricity in electrically excitable cells, as muscle cells, nervous

cells or the inner bone, is of high interest and promising for the future (Gianni Ciofani, Danti, et al. 2010; Gianni Ciofani, Leonardo Ricotti, et al. 2010).

So far, the applications in biotechnology for Barium Titanate nanoparticles have been focused on three aspects: Ceramic fillers for bone regeneration, tissue engineering, intracellular nanovectors and biocompatible nanocrystals for imaging probes.

a) **Tissue Engineering:** The good results that BT exhibit in biocompatibility encourages to test BT in other uses in regenerative medicine, more specifically as scaffolds. Scaffolds provide the structure where the tissue has to grow, and the trend is to load them with components to promote the tissue regeneration processes. Some of these scaffolds present, aligned hydroxyapatite and BT composites prepared by freeze casting (Y. Zhang et al. 2014), BT-loaded polymeric nanocomposites (Bagchi et al. 2014; Nacer et al. 2015). Other uses besides the scaffolds comprise nanoparticles composed of Poly(lactic-co-glycolic) acid (PLGA) and poly(L-lactic acid) (PLGA) for enhanced cellular proliferation (Ciofani et al. 2011) or the effect of the raw BT nanoparticles in differentiation of stem cells (Ciofani et al. 2013).

b) **Ceramic Fillers for Bone Regeneration:** Bone is a composite material and the second largest organ in the body only after skin. It is made of a mix of minerals, macromolecules as collagen, cells and other components forming a highly orientated network that overall presents singular mechanical properties and stress generated potential, which plays a very important role in regulating the bone metabolism (Ravaglioli & Krajewski 1992; Park et al. 1980). Thanks to the existing stress generated potential, the addition of piezoelectric bioactive ceramics can promote osteogenesis, the formation of bone, as it contributes to the stimulation of the electrical current in situ. The first studies, dating from 1997, show how the mix of Barium titanate and Hydroxyapatite (HA) in jawbones of dogs presented better results than HA alone, confirming the promotion of osteogenesis (Feng et al. 1997). This approach has been further investigated over the last 20 years, with cytocompatibility studies of the HA-BT with different kind of cells (Baxter et al. 2009; Baxter et al. 2010; Teixeira et al. 2010; Marino et al. 2015) and later on with the use of BT in polymeric nanocomposites based on PVDF (Teixeira et al. 2010; Gimenes et al. 2004), poly(ε-caprolactone) (Bagchi et al. 2014) and oxidized polypyrrole (Barrère et al. 2008), the addition of piezoelectric BT resulting in a beneficial enhancement for the osteogenesis process.

c) **Intracellular Nanovectors:** Barium Titanate nanoparticles can also be used for smart delivery of genes and drugs in the organism, as they can be interiorized by cells. In order to achieve this goal the modification of the nanoparticles to obtain a homogeneous colloidal dispersion is of extreme importance. Different modification approaches have been studied in the recent years, coating the nanoparticles with glycol-chitosan and Doxorubicin for cancer therapy (G Ciofani, Danti, D'Alessandro, et al. 2010), and Poly-l-lysine (PLL) coupled with fluorescence labeled bovine serum albumin for protein delivery(G Ciofani, Danti, Moscato, et al. 2010)., just to mention some.

d) **Imaging Probes:** Barium titanate nanoparticles can also be used as non-linear optical nanoprobes, offering better outcome than fluorescence probes and quantum dots at that scale, what makes them really useful for in vitro and in vivo imaging (Pantazis et al. 2010; Joulaud et al. 2013). In particular, BT is being used for second harmonic generation (SHG), a process that involves two photons of a specific frequency ω that combine into one with a frequency of 2ω and the wavelength reduced by half by interaction with a non-centrosymmetric crystal (Genchi et al. 2016). SHG is a process highly dependent in particle size, and the different sizes of the BT used will determine its applications in biological matrices as BT can be found in a wide range of sizes from 22nm up to 300nm in its different crystalline structures (Kim et al. 2013). As aforementioned, coating or surface modification of the nanoparticles in order to obtain a good dispersion is crucial, as the studies of Hsieh et al. showed, they functionalized the nanoparticles with amines for further 3-D holographic imaging of HeLa cells (Hsieh et al. 2009) and for bioconjugation of immunoglobulin G antibody (Hsieh et al. 2010). Imaging guided photodynamic therapy has been performed using nanoparticles coated with polyelectrolytes (Wang et al. 2016); coating the nanoparticles with polyethylenimine showed improvements in their cellular uptake, and allows their use for coupled imaging as well as gene delivery, fulfilling both of the applications mentioned above (Dempsey et al. 2013). Lastly, in-vivo zebra fish imaging has been achieved thanks to the utilization of PEG-coated BT nanoparticles (Čulić-Viskota et al. 2012).

3. CYCLODEXTRINS

One of the common efforts when using BT nanoparticles for the applications described above in biomaterials is the necessity to obtain a stable dispersion of the nanoparticles in

solution. The best way to achieve that objective is the surface modification of the nanoparticles to prevent the high aggregation that they undertake. Different approaches have been proposed in the literature, and in our case we want to explore the use of cyclodextrins in the surface of the nanoparticles to achieve two goals: preventing the aggregation and to achieve extra functionality through host-guest interactions with the cyclodextrins cavity.

Cyclodextrins (CDs) are a family of cyclic oligosaccharides composed of α-1,4-linked glucopyranose units that originate from the enzymatic degradation of starch. These macrocycles form a peculiar "doughnut" or toroid shape with an apolar cavity and a hydrophilic exterior that boosts the utility of these macromolecules in a wide range of applications in many industries as the pharmaceutical, food and beverage or textile. In the following lines we will take a closer look at these chemical compounds.

There is a recent review by Prof. Crini on the history of the CDs (Crini 2014) that covers, with great extent, the most important milestones of their discovery, the evolution, early applications and the main contributors of the CDs study and development. In the following lines, it is our goal to provide the reader with a summary of the main events and achievements related to CDs, in order to help with the understanding of their chemistry and properties. We encourage the reader to the consult the review in case more depth is required.

The first evidence of CD was reported by Villiers in 1891 when he obtained a crystalline substance out of the enzymatic degradation of starch (Villiers 1891), which he named "cellulosine" or "dextrins". Later on, in 1903, Schardinger identified the cyclodextrin glucosiltranferase (CGTase) as the enzyme responsible for the transformation, and named the resulting two molecules as "dextrines A and B", or how they were most known "Schardinger dextrines", and described the preparation, separation and purification of them, as well as their chemistry in the presence of alcohols, ethers and iodine solutions. (Szejtli 1988; Crini 2014). In 1911 he described the *Bacillus Macerans* as a producer of large amounts of crystalline dextrins, which he named as "crystalline dextrin α" with 6 units and "crystalline dextrin β" with 7 units. The structure of CDs was first elucidated and published in 1938 by Freudenberg, who suggested that CDs were cyclic oligosaccharides formed by composed of α-1,4-linked glucopyranose units, introducing the idea of the hydrophobicity of the inner surface and their ability to accept inclusions of other molecules (Freudenberg 1939; Freudenberg & Meyer-Delius 1938). Later on, in 1942 the structures of α-cyclodextrin

(αCD) and β-cyclodextrin (βCD) were determined by X-ray crystallography (Buschmann & Schollmeyer 2002).

At that point the research on cyclodextrins grew exponentially and researchers started working on the synthesis, purification and physico-chemical characterization of the CDs (French 1957; Cramer 1952). The first patent associated to CDs was published in 1953 describing the formation of inclusion complexes as the main applications of CDs (Freudenberg, K.; Cramer, F.; Plieninger 1953). However, the costs of production of CDs during those decades were extremely high (around 2500USD per kg of βCD) and there was a lack of knowledge in relation to the toxicity of the molecules. In the 60's decade some studies showed that CDs lack toxicity, and the impurities form the synthetics methods that are trapped in the cavity are responsible for the toxic effects (Cohen & Lach 1963; Lach & Cohen 1963). It was not until the 70's when new synthetic routes were found and the production cost dropped(currently 5USD per kg of βCD), that the applications of CDs started to grow at a steady pace, backed by the acceptance of the lack of toxicity and companies worldwide that produced and marketed them(Del Valle 2004; Loftsson & Brewster 1996). From that moment onwards the research on CDs has been very extensive, and the work of Saenger and Szejtli stand out due to the importance of their work and publications. Saenger described to a greater extent the mechanisms of inclusion complexes and the structures of CDs by X-ray crystallography among many others (Saenger 1980; Saenger et al. 1998). Prof. Szejtli was the founder of the Cyclodextrin Research and Development Laboratory Cyclolab Ltd. , which focusses on transferring CDs technology from research to the industry, and he is the author of the first set of reviews of CDs and its derivatives on industrial applications (Szente & Szejtli 1999; Szejtli 1997; Szejtli 1992; Szejtli 1988).

3.1 Structure and Properties

CDs are cyclic oligosaccharides formed by α-D-glucopyranose rings. The most common CDs are the ones that have 6, 7 and 8 rings respectively, also known as αCD, βCD and γCD (Figure i.5). The characteristic hollow truncated cone structure of the CDs (Figure i.6) comes from the combination of the chair conformation of the glucose monomers and the α-(1,4) glycosidic bonds. Larger CDs have been described, up until the one formed by 12 glucose rings named ηCD, but the yields are considerably lower, as well as their complex formation properties (Larsen et al. 1998).

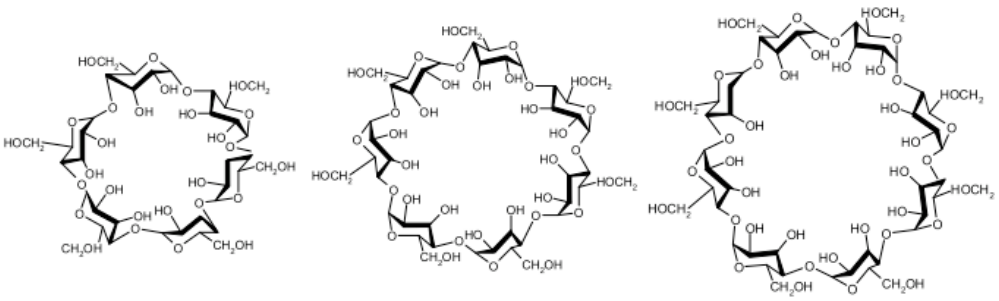

Fig. i.5: Structure of α-, β- and γ-CDs.

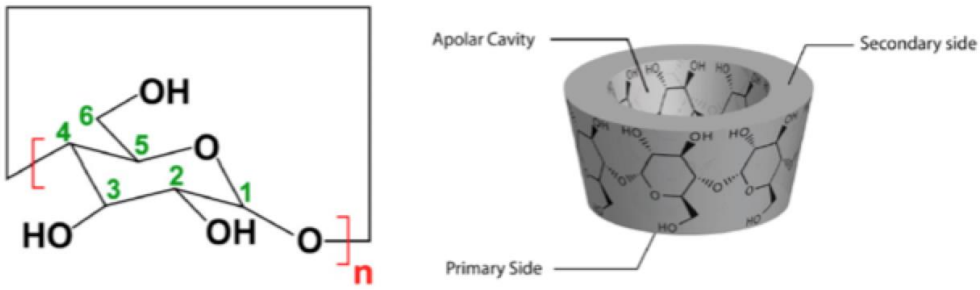

Fig. i.6: Chair conformation of the glucose monomer (left) and truncated cone structure of the CDs (right).

The structure becomes stabilized by an intramolecular hydrogen bonding network between the secondary hydroxyl groups of the C_2 and C_3 of adjacent residues, providing the macrocycle with rigidity. The steric impediment does not allow the glucose units to rotate along the α-(1,4) bond, which locates the H_3 and H_5 in the interior of the cone whereas the H_1, H_2 and H_4 are on the exterior rim. In the interior area is where the glycosidic oxygen atoms are located with its lone pairs orientated towards the cavity with a certain Lewis Base character. These characteristics, added to the disposition of the hydroxyl groups at the cavity rims, provide the outer part with a hydrophilic character, which is the main reason contributing to the solubility of the CDs in water. Due to this particular structure, the cavity is able to host chemical groups of hydrophobic nature forming reversible inclusion complexes that are soluble in water due to the exterior properties of the CDs (Dodziuk 2006).

Table i.5 contains the physico-chemical properties of the three main CDs. It is worth noting that all the properties but the solubility in water presents a correlation with the number of glucose units. In the case of the solubility in water, differences between the three CDs does not correlate with the size as γCD is the most soluble followed by αCD and lastly βCD. The reason for this effect is the difference in intramolecular hydrogen bonds in between the C_2 and C_3 of each CD (Gelb et al. 1982). In the case of βCD the hydrogen bonding is more favoured due to the cavity size, and hence the low solubility. CDs are stable

in a wide range of pH (3.5<pH<14) but in acid medium they suffer a hydrolysis yielding linear oligosaccharides (Li & Purdy 1992).

Table i.5: Physical properties and molecular dimensions of α, β and γ-CDs.(Szejtli 1988)

Property	αCD	βCD	γCD
Nº glucose units	6	7	8
Molecular Weight (g/mol)	972	1135	1297
Water solubility at 25 °C (g/100 ml)	14.5	1.85	23.2
Internal diameter (Å)	4.7-5.3	6.0-6.5	7.5-8.3
External diameter (Å)	14.6±0.4	15.4±0.4	17.5±0-4
Height (Å)	7.9±0.1	7.9±0.1	7.9±0.1
Molecular volume of the cavity ($Å^3$)	100	160	250
pK_a at 25 °C in water (potentiometry)*	12.33	12.20	12.08

*(Gelb et al. 1980; Gelb et al. 1982)

With the aim of improving the solubility and the toxicity of CDs, research then focussed on the alteration of the CDs to develop derivatives, consisting mainly on the modification of the hydroxyl groups with different chemical groups (methyl, hydroxyalkyls, various anionic and cationic groups), as well as CDs polymers (Harada et al. 2006; Wenz 1994). The modified CDs have been in the market for some decades and offer a key improvement on the solubility and toxicity, contributing to an exponential growth on the applications of CDs (Eastburn & Tao 1994). The toxicity of the derivatives was then also explored, concluding that CDs are mainly innocuous, undertaking little hydrolysis in the small intestine and almost no absorption and enzymatic degradation once in the colon (Duchěne & Wouessidjewe 1990; Irie & Uekama 1997). However, if administered intravenously, some haemolytic activity has been reported as a result of the complexes that CDs are able to form with some components of the cell membranes as cholesterol, phospholipids or proteins (Szejtli et al. 1986). Due to the wide arrange of applications in which they are used nowadays, and given the general understanding of the non-toxicity of the main CDs, the toxicity of the new derivatives, CD polymers supramolecular assemblies is explored every time a new use is proposed, and the most updated reviews on the topics always include the most relevant toxicity studies (Gidwani & Vyas 2015; Gould & Scott 2005; Zhang & Ma 2013; van de Manakker et al. 2009).

3.2 Inclusion complexes

The combination of the structures and properties described above is the key to the main application of CDs, which is the formation of supramolecular host-guest interactions, also known as inclusion complexes, where there is no covalent bonding between the molecules involved. These complexes can take place with hydrophobic molecules or relatively hydrophobic parts of molecules with a certain polar character, and they can present various stoichiometries, depending on steric factors, as is the size of the cavity and the guest, and the thermodynamic conditions. Small molecules will usually yield 1:1 complexes, but bigger molecules can be hosted by 2 or 3 CDs, and in the case of linear polymers they can thread various CDs forming structures known as polyrotaxanes (Harada 1998; Wenz et al. 2006).

Cyclodextrins were first used as separation agents for enantiomers in chromatography columns due to their excellent specificity (Duchêne 1987), but because of the capability to form inclusion complexes, the uses quickly multiplied and nowadays CDs show a wide range of applications as they can alter the physical, biological and chemical properties of the guest molecule. The majority of uses are found in the pharmaceutical field as excipients to help stabilize and solubilize the drugs, as well as enhancing its bioavailability (Loftsson & Brewster 1996; Uekama et al. 2006). Smart delivery of drugs is also a very important improvement in the pharmaceutical field where CDs, in the form of nanospheres, nanosponges (Trotta et al. 2012; Tejashri et al. 2013) and microspheres, polymeric films or pellets (Li & Loh 2008; van de Manakker et al. 2009; Gidwani & Vyas 2015), and other nanostructures (Mazzaglia et al. 2012), play a crucial role in various routes of administration. By controlling the release of the drug through the host-guest interaction properties and releasing it only when it is needed, or when it has reached the target, the dosage can be reduced as there is no wasted product and consequently, the possibility of secondary effects is also lessened (Challa et al. 2005; Loftsson et al. 2005).

CDs also present an important role in the food and beverage industry, where α-, β- and γCD are labelled as “Generally Recognized As Safe” by the Food and Drug Administration (FDA 2000; FDA 2001; FDA 2004). The increasing applications of CDs in the food industry has been reviewed recently by Fenyvesi et al. (Fenyvesi et al. 2016a). Their use is becoming common as stabilizing agents of additives as flavors, essential oils, sweeteners, colorants, vitamins and preservatives among others. The benefit of including those compounds as inclusion complexes is that they are more protected against degradation processes, as they are usually very sensitive to oxidation and UV degradation (Marques 2010). Overall, the

protection and the smart delivery over time prevents the waste of those compounds and it allows for a reduction of the net amount introduced in the food or drink (Szente & Szejtli 2004). Another prevalent use in food processing is to remove cholesterol from animal products, such as fatty acids, eggs or milk, removing up to 80% of its original content (Hedges & Hedges 1998). CDs are also gaining importance in the field of nutraceuticals, where CDs help solubilize and protect antioxidants, vitamins, carotenoids and flavonoids among others, reducing at the same time the presence of unwanted substances as trans-fats, allergens and bitter compounds.

In the cosmetic and personal industry the inclusion complexes improve the solubility of fragrances, mainly organic molecules, and their controlled release upon contact with the human body, as well as reducing body odors (Buschmann & Schollmeyer 2002; Holland et al. 2000; Trinh et al. 1997).

In environmental chemistry polymers of CDs are being extensively studied as adsorbents and encapsulating agents of pollutants to treat industrial residues, water processing and to remove heavy metals from soils (Morin-Crini & Crini 2013), as most of the contaminants are polar substances (dyes, drugs, phenolic pollutants, fungicides) that can be effectively trapped by CDs in their cavities for further recycling or reuse of the molecules of interest (Crini 2003; Romo et al. 2008; Szejtli 1997; Lezcano et al. 2002).

3.3 Cyclodextrins in materials and biomaterials.

Despite the increasing use of CDs for pharmaceutical, food and environmental applications, their applications in materials science, derived from their ability to form inclusion complexes, are much less developed although increasing at a fast pace.

For example, in the textile industry the use of CDs confers novel and added properties to the fabrics. Scientists at Wacker have successfully attached covalently reactive βCD modified with monochlorotriazinyl (MCT)-treated fibers, providing an excellent finish to cottons and woolens (Bereck 2010). The introduction of CDs in the fibers enables them to trap and mask odors, either from the body or from external agents as tobacco smoke (Sricharussin et al. 2009; Buschmann et al. 1998). On the other hand, they can also form inclusion complexes with perfumes or fragrances and release them when in contact with moisture (Trinh et al. 1989). In addition to that, their ability to encapsulate dyes increases the uptake of dyes by the fibers contributes to a reduction in the overall amount of dye used, and the dye lost in the water when washed (Savarino et al. 1999). An evolution of these textile applications is the incorporation into textiles, to make them capable of taking a sweat probe from the patient for further analysis, obtaining an original method of medical

diagnostic of organic compounds. In addition to that, drugs can be loaded into the fabrics modified with CDs and the release directly to the skin can be controlled, simplifying the treatment of many extensive skin diseases (Schollmeyer & Buschmann 1999; Kuwabara 2006).

Smart packaging is an application of materials to the food and beverage industry that has experienced significant growth over the last decade. The use of nanocomposites confers the package with properties different than mere protection, enhancing the shelf life of the product and at the same time providing information of the product to the consumer. Some examples of active packaging are oxygen scavengers, moisture absorbers, antimicrobial packing or ethylene scavenger, and in the area of intelligent packing systems indicators of freshness, integrity, and time-temperature are commercially available (Biji et al. 2015). CDs have been widely used in these applications, as the combinations of the CDs complexes with fragrances and flavors in polymeric films of LLDPE or tissue paper (Koontz & Marcy 2007; Wintersgill 2004), antioxidants in PE films (Siró et al. 2006), dyes (Kuwabara 2005), antibacterial and antimicrobial agents (Hirose & Yamamoto 2001; Raouche et al. 2011), UV filters, ripening agents (Hotchkiss et al. 2007), ripening inhibitors (Wood et al. 2010) among others. The combination with thermoplastic polymers as PVC or PLA allows for the production of nanocomposite films, trays or laminates with tailored properties becoming active barriers, that interact with food and contribute to its preservation, at the same time reducing the amount of plastifiers needed (Fenyvesi et al. 2007). It is also possible to simply attach empty CDs to the packaging material with the purpose to remove certain molecules from the content. Examples of these applications are the removal of volatiles by entrapping aromas and odor adsorption (Wood & Beaverson NJ 2005; Wood 2001), acting as a barrier agent and increasing the permselectivity of CO_2/O_2 (López-de-Dicastillo et al. 2010), reducing the cholesterol levels of milk by encapsulating the fatty acids in their cavities (López-de-Dicastillo, Jordá, et al. 2011; López-de-Dicastillo, Catalá, et al. 2011) or trapping contamination secreted by the food, as the mycotoxins from green coffee beans (Verrone et al. 2007). Finally, another interesting property derived from the introduction of empty CDs in polymeric films is the reduction of the release of plasticizers onto the food (Fenyvesi et al. 2007; Yu et al. 2008).

CDs are also present in the field of biomaterials, mainly forming part of hydrogels. The combinations of the CDs, its inclusion complexes and the polymers and biopolymers used to for the hydrogels open up multiple possibilities of application. Some of them directly use the CDs to form the hydrogel whereas the rest uses the complexation ability to deliver

molecules of interest. Some examples are photoresponsive hydrogels containing αCD used for molecular recognition (Itsuro et al. 2005), oral delivery systems for insulin using hydrogel microparticles (Sajeesh et al. 2010) or hydrogels loaded with bone marrow cells for cardiac tissue repairs (Wang et al. 2009). Supramolecular hydrogels deserve a special mention, as they are three-dimensional networks with non-covalent bonds, synthetized from usually hydrophilic molecules and show stimuli response and self-healing properties (Harada 2013). αCD is one of the most used CDs in this area as it is able to complex PEO blocks and other block copolymers forming micelles that could lead to gels (González-Gaitano, Müller, et al. 2015; Dreiss et al. 2009). Some examples are injectable hydrogels of PEO-PHB-PEO and αCD used for drug delivery (Li et al. 2006; Li et al. 2003), PEG-based hydrogels (Zhao et al. 2006; Ren et al. 2009), and other block copolymers forming polyrotaxanes for drug and gene delivery (Ni et al. 2009; Liu et al. 2011; Li et al. 2001). Recently, there are some studies where these supramolecular hydrogels incorporate a third component, as nanoparticles of TiO_2, SiO_2 or $BaTiO_3$, carbon nanotubes (CNTs), to improve the mechanical properties of the hydrogel and confer them with the extra properties of the added nanocomponent (Guo et al. 2008; Hui et al. 2010; Serra-Gómez et al. 2016).

With the purpose of summarizing the large number of applications described in the previous paragraphs, we have ordered the most relevant reviews of this century in a table format (Table i.6) that can serve for further reference:

Table i.6: Most relevant reviews of Cyclodextrins applications from year 2000 onwards.

Application Field	Title	Reference
Drug Delivery	Supramolecular Nanostructures Based On Cyclodextrin And Poly(Ethylene Oxide): Syntheses, Structural Characterizations And Applications For Drug Delivery.	(Zheng & Wyman 2016)
	Cyclodextrin Nanoassemblies: A Promising Tool For Drug Delivery.	(Bonnet et al. 2015)
	A Comprehensive Review On Cyclodextrin-Based Carriers For Delivery Of Chemotherapeutic Cytotoxic Anticancer Drugs.	(Gidwani & Vyas 2015)
	Cyclodextrin-Based Host–Guest Supramolecular Nanoparticles For Delivery: From Design To Applications.	(Hu et al. 2014)
	Chemically Cross-Linked And Grafted Cyclodextrin Hydrogels: From Nanostructures To Drug-Eluting Medical Devices.	(Concheiro & Alvarez-Lorenzo 2013)
	Cyclodextrin based nanosponges for pharmaceutical use: A review.	(Tejashri et al. 2013)
	Cyclodextrin-Based Supramolecular Systems For Drug Delivery: Recent Progress And Future Perspective.	(Zhang & Ma 2013)
	Cyclodextrin-Based Nanosponges As Drug Carriers.	(Trotta et al. 2012)
	Cyclodextrin-based gene delivery systems.	(Mellet et al. 2011)
	Cyclodextrin Functionalized Polymers As Drug Delivery Systems	(Zhou & Ritter 2010)
	Cyclodextrin based novel drug delivery systems.	(Vyas et al. 2008)
	Cyclodextrin-based supramolecular architectures: Syntheses, structures, and applications for drug and gene delivery.	(Li & Loh 2008)
	Cyclodextrins As Pharmaceutical Solubilizers.	(Brewster & Loftsson 2007)
	Cyclodextrins In Drug Delivery.	(Loftsson et al. 2005)
	Design And Evaluation Of Cyclodextrin-Based Drug. Formulation.	(Uekama 2004)
	Self-Assembling Nucleic Acid Delivery Vehicles Via Linear, Water-Soluble, Cyclodextrin-Containing Polymers.	(Davis et al. 2004)
	Cyclodextrin-Based Pharmaceutics: Past, Present And Future.	(Davis & Brewster 2004)

Application Field	Title	Reference
Textile	Applications Of Cyclodextrins In Medical Textiles - Review.	(Radu et al. 2016)
	Application Of Cyclodextrins In Textile Processes.	(Andreaus et al. 2010)
Food and Beverage	Cyclodextrins In Food Technology And Human Nutrition: Benefits And Limitations.	(Fenyvesi et al. 2016b)
	Smart Packaging Systems For Food Applications: A Review.	(Biji et al. 2015)
	Alpha-Cyclodextrin: Enzymatic Production And Food Applications.	(Li et al. 2014)
	A Review On Cyclodextrin Encapsulation Of Essential Oils And Volatiles.	(Marques 2010)
	A Review On The Use Of Cyclodextrins In Foods.	(Astray et al. 2009)
	Cyclodextrins As Food Ingredients.	(Szente & Szejtli 2004)
Cosmetic	Applications Of Cyclodextrins In Cosmetic Products: A Review.	(Buschmann & Schollmeyer 2002)
Environmental	Progress in the Immobilization of β-Cyclodextrin and Their Application in Adsorption of Environmental Pollutants.	(Han et al. 2016)
	Environmental Applications Of Water-Insoluble β -Cyclodextrin–Epichlorohydrin Polymers.	(Morin-Crini & Crini 2013)
Biomedical	Cyclodextrin-based hydrogels toward improved wound dressings.	(Pinho et al. 2014)
	Cyclodextrin based rotaxanes, polyrotaxanes and polypseudorotaxanes and their biomedical applications.	(García-Río et al. 2014)
	Cyclodextrin-Based Nanogels For Pharmaceutical And Biomedical Applications.	(Moya-Ortega et al. 2012)
	Cyclodextrin-Based Polymeric Materials: Synthesis, Properties, And Pharmaceutical/Biomedical Applications.	(van de Manakker et al. 2009)
	Biomedical Applications Of Cyclodextrin Based Polyrotaxanes.	(Loethen et al. 2007)
	Host–Guest Interactions Mediated Nano-Assemblies Using Cyclodextrin-Containing Hydrophilic Polymers And Their Biomedical Applications.	(Zhang & Ma 2010)
Other	*Supramolecular Polymeric Materials Via Cyclodextrin-Guest Interactions.*	(Harada et al. 2014)
	Cyclodextrin-Based Inclusion Complexation Bridging Supramolecular Chemistry And Macromolecular Self-Assembly.	(Chen & Jiang 2011)

Application Field	Title	Reference
Other	Self-Assembled Cyclodextrin Aggregates And Nanoparticles.	(Messner et al. 2010)
	Cyclodextrin-Based Supramolecular Polymers.	(Harada, Takashima, et al. 2009)
	Cyclodextrin Inclusion Polymers Forming Hydrogels.	(Li 2009)
	Cyclodextrin Rotaxanes And Polyrotaxanes.	(Wenz et al. 2006)
	Cyclodextrin-Based Molecular Mechanics.	(Harada 2001)

4. HYDROGELS AND SOFT NANOCOMPOSITES

Hydrogel uses in the biomaterials field are constantly increasing in the recent years. Hydrogels are highly hydrated polymeric cross-linked networks with the ability to form three dimensional structures that can be easily casted into a wide range of desired shapes and sizes (Wichterle & Lím 1960). Because of its structure, their degree of flexibility is very similar to natural tissue, and therefore hydrogels were the first biomaterials designed for use in human applications (Kopecek 2007). However, the main drawbacks of traditional hydrogels are the poor mechanical resistance and the slow response times to external stimuli (Kopeček & Yang 2007).

There are many different ways of classifying hydrogels, based on the source (natural or synthetic), the polymeric composition (homopolymeric, copolymeric or multipolymer interprenetating networks), physical structure and chemical composition (Amorphous, semicrystalline or crystalline), electrical charge (Nonionic, ionic, amphoteric electrolytes and zwitterionics). Another classification that is important for the hydrogels described in this thesis is the one based on the type of cross-linking, where we can find chemically cross-linked hydrogels, which present permanent junctions created by the action of a cross-linker, and physically cross-linked hydrogels, that consist of networks with junctions that arise from polymeric chain entanglements, ionic interactions, hydrogen bonding or hydrophobic interactions, and they do not require the action of an external cross-linker agent (Ahmed 2015). Figure i.7 shows a schematic of the most common methods of formation of physically cross-linked hydrogels.

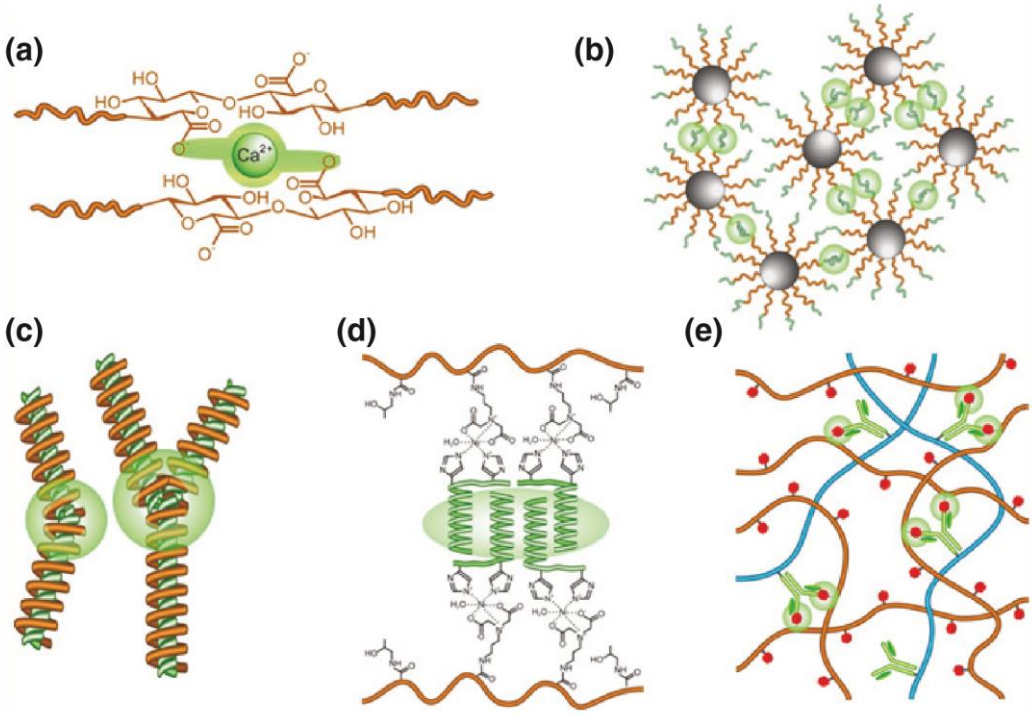

Fig. i.7: Formation methods of physically cross-linked hydrogels. a) Ionic interactions, b) Hydrophobic interactions, c) Self-assembly of stereocomplex structures, d) coiled-coil interactions and e) specific molecular recognition. Image extracted from (Aoyagi et al. 2014).

4.1 Soft Nanocomposites

In the section 3.3, the applications of CDs as components of supramolecular hydrogels have been discussed, but these supramolecular materials play a crucial role nowadays in the biomaterials field and deserve a more detailed explanation. *Soft nanocomposites* come from the combination of hydrogels and nanoparticles, answering to the demand of new materials with specific characteristics for new applications in a wide variety of fields. Two recent reviews by Gaharwar et al. (Gaharwar et al. 2014) and Schexnailder et al. (Schexnailder & Schmidt 2008) offer an outstanding state of the art of the preparation, characterization and uses of soft nanocomposites for biomedical purposes. Another recent review by Prof. Dreiss covers with great detail the latest applications of hydrogels in combination with nanoparticles to obtain soft nanocomposites and tune the gel properties, we recommend them for further information (da Silva & Dreiss 2016) and we present here a brief summary to introduce them.

Originally, the main objective to introduce nanoparticles into a hydrogel has been to improve its mechanical properties with an inorganic nanosized component, to prevent one of the main drawbacks of hydrogels, the lack of mechanical strength. Examples are clays (Haraguchi et al. 2003; Haraguchi et al. 2005), graphene oxide (Liu et al. 2012; Shin et al. 2013), silica (Wang et al. 2012; Rose et al. 2013), titania and barium titanate (Xu et al. 2013; Serra-Gómez et al. 2016) and cellulose nanocrystals (Yang et al. 2014). However, applications other than the mechanical reinforcement have risen due to the extensive research on the topic and the variety of nanofillers available, for instance to improve the biological properties of the matrix which would allow them to be used in medicine (Peppas et al. 2006), incorporating antimicrobial properties through silver and graphene oxide nanofillers (Fan et al. 2014; García-Astrain et al. 2015), improving bone regeneration in tissue engineering with hydroxyapatite, calcium phosphate and silica nanoplatelets (Nejadnik et al. 2014; Paul et al. 2016; Gaharwar et al. 2013) and controlled and sustained drug delivery over time with graphene oxide and iron oxide nanoparticles (Fusco et al. 2015; Zeng & Lu 2014).

Being able to modify the optical properties of the hydrogels is also a remarkable feature of soft nanocomposites, providing color changes used in copper colorimetric sensors based on gelatin and silver nanoparticles (Jeevika & Ravi Shankaran 2014) or confer new optical properties to the hydrogel, as birefringence (Vaia & Maguire 2007) and optical anisotropy (Murata et al. 2007).

Smart materials are also play an important role in the soft nanocomposites area. The investigations are focusing on materials that are able to alter their properties as the result of the response triggered by an external stimulus, which is of crucial importance for drug delivery (Koetting et al. 2015). In this sense, one of the most studied hydrogels are those based in Poly(N-isopropylacrylamide) (PNIPAAm), which when embedded with clay present the possibility of thermally adjusting its volume (Schild 1992; Haraguchi et al. 2012), and when combining different crosslinking grades of the matrix and silica nanoparticles it allows to control their swelling and deswelling (Fei et al. 2012). The nanoparticles that form the nanocomposite can also convert an external stimulus into one to which the matrix can respond, for example gels with magnetic iron oxide that vibrates and produce heat under a magnetic field, and in turn the matrix changes volume and delivers the molecule of interest (Satarkar & Hilt 2008). Another good example are light-activated actuators with carbon nanotubes responsive to IR that trigger a modification in the morphology of the matrix (Zhang et al. 2011) and many others under development.

4.2 Supramolecular Hydrogels: Poloxamers and poloxamines.

Although PNIPAAm has been the subject of investigation for smart soft nanocomposites, other supramolecular block copolymers, as poloxamers and poloxamines, are also being used and show great potential because of their versatile structure and tailorable properties.

Poloxamers and poloxamines are block copolymers formed by Polyethylene oxide (PEO) and Polypropylene oxide (PPO) that are able to form supramolecular hydrogels. They were first introduced in the 50's as new nonionic detergents (Vaughn et al. 1951), and the further studies on their aggregation in aqueous solution revealed their characteristic properties (Schmolka & Bacon 1967; Schmolka 1977). They are also known by their commercial name, as they have been long available since being patented by BASF in 1973 (Schmolka 1973) as Synperonics®, Pluronics® or Kolliphor® for the poloxamers and Tetronics® for the poloxamines.

4.2.1 Structure and Properties

Poloxamers present a linear structure of PPO and PEO alternating units as PEO-PPO-PEO (Fig.i.8 a), whereas poloxamines present a structure of four arms that stretch out of an ethilendiamine central block. Each of those arms is formed by a block of PEO and PEO (Fig i.8b). Two other variations exist, which involve the inversion of the position of the blocks, and are known as reverse poloxamers and reverse poloxamines.

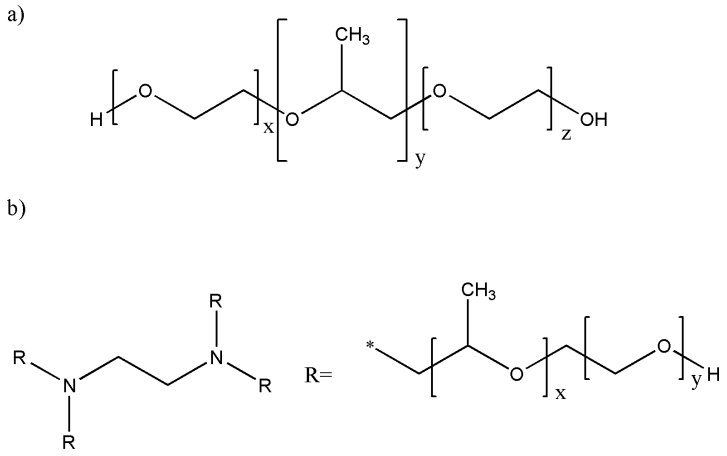

Fig i.8: a) Poloxamer and b) Poloxamine chemical structures.

Because of the singular disposition of the blocks, poloxamers present two differentiated zones: the central PPO block is mainly hydrophobic, whereas the external PEO groups are hydrophilic, providing the whole molecule with an amphiphilic character responsible for the formation of micelles in water as a function of temperature and concentration (Alexandridis & Hatton 1995). Both block copolymers are synthetized in a similar way, with the sequential addition of methyl oxirane in a first instance and following with the addition of oxirane to a polyethylenglycol molecule. If the synthesis starts with the ethylendiamine initiator the same procedure yields the poloxamines, and when the addition order is reversed, the reverse poloxamers and poloxamines are obtained (Schmolka 1977).

As expected with block copolymers and as a result of the structure described above, there is a huge range of poloxamers and poloxamines available based on the number of units of each block commercialized by BASF and summarized in the Table i.7. The naming code of the poloxamers and poloxamines is related to the chemical state and composition: the letter designates the state of the matter as liquid (L), paste (P) or flakes (F) for solids, and the first number (or the first two) multiplied by 300 indicate the molecular weight of the PPO blocks. Finally the last number multiplied by 10 indicates the weight percentage of the PEO block (Alexandridis & Hatton 1995). In the case of reverse pluronics, tetronics and reversed tetronics the nomenclature changes as the letter designating the state is lost, and the numbers before the R (reverse) multiplied by 100 relate to the molecular weight of the PPO blocks and the last number multiplied by 10 indicates the PEO block weight percentage.

Table i. 7: Main physicochemical characteristics of the block copolymers manufactured by BASF.

Pluronic	State	# EO	# PO	Mw	Cloud Point (°C)	Viscosity (cps)
L31	Liquid	1 (x2)	17	1100	37	175
L61	Liquid	2 (x2)	31	2000	24	325
L81	Liquid	3 (x2)	43	2750	20	475
L101	Liquid	4 (x2)	59	3800	15	800
L121	Liquid	5 (x2)	68	4400	14	1200
L42	Liquid	4 (x2)	22	1630	37	280
L62	Liquid	6 (x2)	34	2500	32	450
L72	Liquid	6 (x2)	38	2750	510	25
L92	Liquid	8 (x2)	50	3650	26	700
L122	Liquid	11 (x2)	69	5000	19	1750
L43	Liquid	6 (x2)	22	1850	42	310
L63	Liquid	9 (x2)	32	2650	34	490
P103	Paste	17 (x2)	60	4950	86	285
P123	Paste	20 (x2)	69	5750	90	350
L44	Liquid	10 (x2)	23	2200	65	440
L64	Liquid	13 (x2)	30	2900	58	850
P84	Paste	19 (2x)	43	4200	280	74
P104	Paste	27 (x2)	61	5900	81	390
L35	Liquid	11 (x2)	16	1900	73	375
P65	Paste	19 (x2)	29	3400	82	180
P75	Paste	24 (x2)	36	4150	82	250
P85	Paste	26 (x2)	40	4600	85	310
P105	Paste	37 (x2)	56	6500	91	750
F77	Solid	53 (x2)	34	6600	>100	480
F87	Solid	61 (x2)	40	7700	>100	700
F127	Solid	100 (x2)	65	12600	>100	3100
F38	Solid	43 (x2)	16	4700	>100	260
F68	Solid	76 (x2)	29	8400	>100	1000
F88	Solid	104 (x2)	39	11400	>100	2300
F98	Solid	118 (x2)	45	13000	>100	2700
F108	Solid	133 (x2)	50	14600	>100	2800
Pluronic R	**State**	**# EO**	**# PO**	**Mw**	**Cloud Point (°C)**	**Viscosity (cps)**
10R5	Liquid	22	8 (x2)	1950	69	440
17R2	Liquid	10	15 (x2)	2150	35	450

17R4	Liquid	24	14 (x2)	2650	46	600
25R2	Liquid	14	21 (x2)	3100	29	680
25R4	Liquid	33	19 (x2)	3600	40	1110
31R1	Liquid	7	25 (x2)	3250	25	660
Tetronic	**State**	**# EO**	**# PO**	**Mw**	**Cloud Point (°C)**	**Viscosity (cps)**
701	Liquid	2 (x4)	14 (x4)	3600	18	600
901	Liquid	3 (x4)	18 (x4)	4700	20	700
1301	Liquid	4 (x4)	26 (x4)	6800	16	1000
304	Liquid	4 (x4)	4 (x4)	1650	75	450
904	Paste	15 (x4)	17 (x4)	6700	74	320
1107	Solid	60 (x4)	20 (x4)	15000	>100	1100
1307	Solid	72 (x4)	23 (x4)	17000	>100	2700
908	Solid	114 (x4)	22 (x4)	25000	>100	8200
Tetronic R	**State**	**# EO**	**# PO**	**Mw**	**Cloud Point (°C)**	**Viscosity (cps)**
150R1	Liquid	5 (x4)	31 (x4)	8000	20	1840
90R4	Liquid	16 (x4)	18 (x4)	6900	43	3870

*Cloud point for aqueous solutions is measured at 1% wt. and the viscosity is measured at 25°C for liquids, 60°C for pastes and 77° for solids. (Larrañeta 2012)

The abovementioned variety of formulations and compositions results in a wide range of physical and chemical properties. However, the most interesting property of these block copolymers is the aggregation behavior in water forming spherical micelles above the critical micelle concentration (CMC) for a specific temperature (CMT), which are determined by the molecular weight, the composition of the blocks and their position within the molecule (Pillai & Shah 1996). The longitude of the PPO blocks, mainly hydrophobic, is the main factor to consider in the process of micelle formation. CMC exponentially decreases with the increase of the length of the PPO blocks, whereas CMT decreases linearly (Wanka et al. 1990; Alexandridis et al. 1994). Because of this effect, poloxamers and poloxamines of higher molecular weight are able to form more complex structures derived from the close packing of the micelles that due to the temperature rise, see their hydrophilic ends entangle because of dehydration, yielding gels (Schmolka 1991; Brown et al. 1992).

When poloxamers and poloxamines interact with cyclodextrins the PEO-PPO chains can form inclusion complexes. Because of the singular structure of the chains, the PEO-PPO blocks can thread one or multiple CDs forming what is known as rotaxanes or polyrotaxanes (Fig i.9). When only one molecule is threading the polymer chain they called rotaxanes, and if there are more than one, they become polyrotaxanes. The prefix *pseudo* is used when

there is no capping at the end of the chain that prevents the threaded molecules to go out of the chain (Harada 1998; Harada, Hashidzume, et al. 2009).

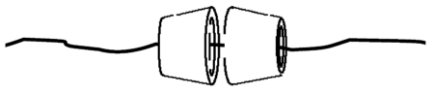

Fig i.9: Scheme of a polyrotaxane complex formed by two CD molecules and a block copolymer chain.

The threading process is somehow selective, as depending on the size of the cavity of the CD it will enter further on the block copolymer chain. B-CD and γ-CD preferentially form polyrotaxanes with the PPO, whereas α-CD forms it with the PEO, as the cavity is not big enough to host the PPO chains (Fig i.10) (Harada et al. 1995; Li et al. 2001).

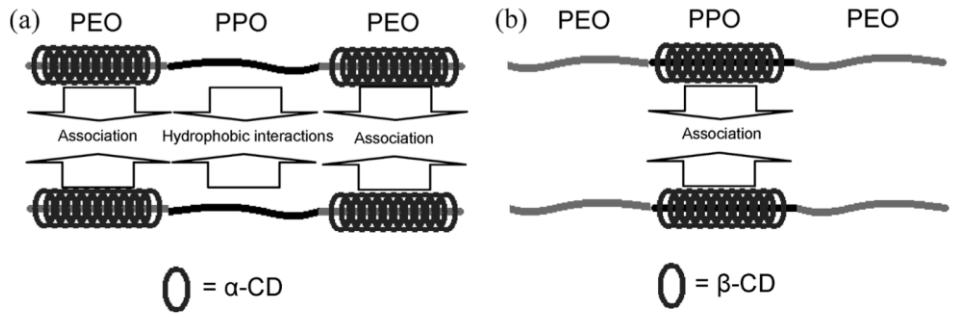

Fig i.10: Example of polypseudorotaxanes: a) αCD and pluronic chain b) βCD and Pluronic chain.

An important feature of the formation of pseudopolyrotaxanes by poloxamers, poloxamines and CDs is that they can alter their micellation and gelation profile, allowing for a fine tuning of the conditions when modifying the concentration, temperature and pH. Some examples of the tailoring of the properties are the studies of Larrañeta, Isasi, González-Gaitano and Dreiss on the subject (González-Gaitano, da Silva, et al. 2015; González-Gaitano, Müller, et al. 2015; Larrañeta & Isasi 2013; Larrañeta & Isasi 2012).

4.3 Applications in biomaterials

As presumed, because of the interesting properties of hydrogels and soft nanocomposites the applications of hydrogels and soft nanocomposites in biomaterials are extensive and constantly growing, and a simple bibliographic research yields more than 350 reviews in the last 15 years that cover all kinds of hydrogels used for biomedical applications, tissue engineering and drug delivery among others. In the following table (Table i. 8) we want to reunite the more up to date and relevant reviews on the topic before entering on

the description of the applications that have poloxamers and poloxamines as their matrix, as those are the ones used in this thesis.

As for the Poloxamers and Poloxamines, they can be found in a wide range of industries, as surfactants, emulsifiers and dispersing agents (Hamley 2004), but they present multiple benefits which make them interesting for their use in biomaterials. Since they do not require chemical crosslinking, they lack the toxicity of the common chemical crosslinkers (Williams et al. 2005), they can be formed in-situ, even at physiological pH and temperature, allowing for injectable preparations that form the gel once inside the organism (Van Tomme et al. 2008). Their degradation products are non-toxic and easily removed by the body (Li et al. 2006), which makes them perfect candidates for pharmaceutical, biomedical and gene (Kabanov et al. 2002)and drug delivery applications (Moreno et al. 2014; Alvarez-Lorenzo et al. 2007; Dreiss et al. 2009).

Pluronic-based biomaterials have been proposed for injectable hydrogels for vitreous substitutes and lens materials (Annaka et al. 2011; Portolés et al. 1994; Han 2003; Kwon et al. 2005). Poloxamer-based nanocomposites with laponite, mesenchymal stem cells and growth factors have been tested for bone regeneration in bone defects both in vitro and in vivo (Nie et al. 2011; Wu et al. 2011; Lippens et al. 2010). The capacity of this hydrogels to react to a thermal stimuli is of great value, and thermoresponsive hydrogels based on poloxamers have been developed for cartilage regeneration (Park et al. 2009; Chen et al. 2013), tissue engineering of lung tissue (Cortiella et al. 2006) or photopatternable hydrogels for MEMS applications (Guan et al. 2012).

On the other hand, Tetronic hydrogels have been less used and are currently being investigated in the biomaterials field. Some recent examples are as soft tissue adhesives in surgical glues (Sanders et al. 2015; Balakrishnan 2013; Cho et al. 2012), multifunctional scaffolds for tissue regeneration (Go et al. 2008; Nguyen et al. 2013; Sivaraman et al. 2015), in-situ delivery of growth factors (Rey-Rico et al. 2011) or enhanced cell adhesion (Sosnik & Sefton 2006). Poloxamine hydrogels and preparations show multifunctional inhibitory activity of ATP-binding cassettes transporters in cancer cell lines and are helpful to overcome drug resistance of cancer cell lines (Sosnik & Sefton 2005; Cuestas et al. 2011; Alvarez-Lorenzo et al. 2011).

Nanocomposite hydrogels based on tetronics with CDs and nanofillers as graphene oxide or barium titanate show promising applications and improved mechanical, electric or piezoelectric properties (Shen et al. 2015; Serra-Gómez et al. 2016).

Table i.8: Most relevant reviews of hydrogels and nanocomposite hydrogels applications from year 2000 onwards.

Application Field	Title	Reference
General	Carbon Nanotubes (CNTs) Nanocomposite Hydrogels Developed for Various Applications: A Critical Review	(Adewunmi et al. 2016)
	Soft nanocomposites: nanoparticles to tune gel properties	(da Silva & Dreiss 2016)
	Hydrogel: Preparation, characterization, and applications: A review	(Ahmed 2015)
	Recent advances in clay mineral-containing nanocomposite hydrogels	(Zhao et al. 2015)
	Smart biomaterials	(Aoyagi et al. 2014)
	Magnetic hydrogel nanocomposites and composite nanoparticles--a review of recent patented works.	(Daniel-da-Silva et al. 2013)
	Gel-nanocomposites: materials with promising applications.	(Das et al. 2012)
	Synthesis and properties of soft nanocomposite materials with novel organic/inorganic network structures.	(Haraguchi 2011)
	Nanocomposite polymer hydrogels	(Schexnailder & Schmidt 2008)
	Hydrogels as smart biomaterials	(Kopeček & Yang 2007)
	Hydrogel biomaterials: A smart future?	(Kopecek 2007)
	Nanocomposite hydrogels	(Haraguchi 2007)
	Review on Polymer, Hydrogel and Microgel Metal Nanocomposites: A Facile Nanotechnological Approach	(Thomas et al. 2007)
	Hydrogels in biology and medicine: From molecular principles to bionanotechnology	(Peppas et al. 2006)
	In situ-forming hydrogels—review of temperature-sensitive systems	(Ruel-Gariépy & Leroux 2004)
	Thermosensitive sol – gel reversible hydrogels	(Jeong et al. 2002)
Pharmaceutical: Drug Delivery	Nanocomposite Hydrogels: 3D Polymer–Nanoparticle Synergies for On-Demand Drug Delivery	(Merino et al. 2015)
	Nanocomposite hydrogels and their applications in drug delivery and tissue engineering	(Song et al. 2015)
	Environment-sensitive hydrogels for drug delivery	(Qiu & Park 2012)
	Nanocomposites for neurodegenerative diseases: Hydrogel-nanoparticle combinations for a challenging drug delivery	(Giordano et al. 2011)

Application Field	Title	Reference
Pharmaceutical: Drug Delivery	Hydrogels in drug delivery: Progress and challenges	(Hoare & Kohane 2008)
	Hydrogels in pharmaceutical formulations	(Peppas, Bures, et al. 2000)
	Hydrogels: from controlled release to pH-responsive drug delivery	(Gupta et al. 2002)
Biomaterials	Recent Advances in the Synthesis and Biomedical Applications of Nanocomposite Hydrogels	(Spizzirri et al. 2015)
	Thermoresponsive hydrogels in biomedical applications A seven-year update	(Klouda 2015)
	Nanocomposite hydrogels for biomedical applications.	(Gaharwar et al. 2014)
	Hydrogel-based nanocomposites and mesenchymal stem cells: A promising synergistic strategy for neurodegenerative disorders therapy	(Albani et al. 2013)
	Hydrogels in Regenerative Medicine	(Slaughter et al. 2009)
	Thermoresponsive hydrogels in biomedical applications - a review	(Klouda & Mikos 2008)
	Injectable hydrogels as unique biomedical materials	(Yu & Ding 2008)
	Hydrogels for biomedical applications	(Hoffman 2002)
	Physicochemical Foundations and Structural Design of Hydrogels in Medicine and Biology	(Peppas, Huang, et al. 2000)
Tissue Engineering	Self-assembled monolayers and nanocomposite hydrogels of functional nanomaterials for tissue engineering applications	(Kehr et al. 2015)
	Vascularized Bone Tissue Engineering: Approaches for Potential Improvement	(Nguyen et al. 2012)
	Superabsorbent hydrogel composites and nanocomposites: A review.	(Kabiri et al. 2011)
	Microengineered hydrogels for tissue engineering	(Khademhosseini & Langer 2007)
	Hydrogels for tissue engineering: Scaffold design variables and applications	(Drury & Mooney 2003)
	Hydrogels for tissue engineering	(Lee & Mooney 2001)

Afterword

To wrap up the introduction, the author would like to use this space to present the general aims of this thesis, expanded in the next section, and which have led to an introduction with such broad topics. Two main characters were proposed from start, barium titanate, a piezoelectric ceramic and cyclodextrins, with the objective of preparing different kind of polymeric nanocomposites, based on thermoplastic an thermostable polymers. Cyclodextrins have been used as modifiers of the surface of the barium titanate to improve their stability in water-based systems, opening the possibility to prepare polymeric nanocomposites based on solution precursors. This, in turn, offered another extra functionality as the cyclodextrins are able to lodge molecules in their cavity, not only using them as stabilizers but also as platforms able to carry and deliver molecules of interest. With all that in mind, our final idea was to put into testing with the preparation of a soft nanocomposite, based on a poloxamine hydrogel and the CD-modified barium titanate nanoparticles, with prospect applications in the biomaterials field.

The detailed objectives are explained in the next section, and the four chapters that follow show the work and the results obtained throughout the research. A discussion of the results will follow to put in common the chapters and analyse the results, and finally the conclusions of the thesis will be described.

5. REFERENCES

Adewunmi, A.A., Ismail, S. & Sultan, A.S., 2016. Carbon Nanotubes (CNTs) Nanocomposite Hydrogels Developed for Various Applications: A Critical Review. *Journal of Inorganic and Organometallic Polymers and Materials*, 26(4), pp.717–737.

Aguilar, Z.P., 2013. *Biocompatibility and Functionalization* Z. P. Aguilar, ed., Elsevier Ltd.

Ahmed, E.M., 2015. Hydrogel: Preparation, characterization, and applications: A review. *Journal of Advanced Research*, 6(2), pp.105–121.

Ajayan, P.M., Schadler, L.S. & Braun, P. V, 2003. *Nanocomposite Science and Technology*, Wiley-VCH.

Albani, D. et al., 2013. Hydrogel-based nanocomposites and mesenchymal stem cells: A promising synergistic strategy for neurodegenerative disorders therapy. *The Scientific World Journal*, 2013, pp.1–9.

Alexandridis, P. & Hatton, A., 1995. Poly(ethylene oxide)-poly(propylene oxide)-poly(ethylene oxide) block copolymer surfactants in aqueous solutions and at interfaces: thermodynamics, structure, dynamics, and modeling. *Colloids and Surfaces A: Physicochemical and Engineering Aspects*, 96(1–2), pp.1–46.

Alexandridis, P., Holzwarth, J.F. & Hatton, T.A., 1994. Micellization of Poly(ethylene oxide)-Poly(propylene oxide)-Poly(ethylene oxide) Triblock Copolymers in Aqueous Solutions: Thermodynamics of Copolymer Association. *Macromolecules*, 27(9), pp.2414–2425.

Alvarez-Lorenzo, C. et al., 2007. Tetronic micellization, gelation and drug solubilization: Influence of pH and ionic strength. *European journal of pharmaceutics and biopharmaceutics : official journal of Arbeitsgemeinschaft für Pharmazeutische Verfahrenstechnik e.V*, 66(2), pp.244–52.

Alvarez-Lorenzo, C., Sosnik, A. & Concheiro, A., 2011. PEO-PPO Block Copolymers for Passive Micellar Targeting and Overcoming Multidrug Resistance in Cancer Therapy. *Current Drug Targets*, 12(8), pp.1112–1130.

Andreaus, J. et al., 2010. Aplicação de ciclodextrinas em processos têxteis. *Química Nova*, 33(4), pp.929–937.

Annaka, M. et al., 2011. Design of an injectable in situ gelation biomaterials for vitreous substitute. *Biomacromolecules*, 12(11), pp.4011–21.

Aoyagi, M.E. et al., 2014. Smart biomaterials. *Membrane Technology*, 1992(22), p.4.

Arya, P.R. et al., 2003. Polymeric citrate precursor route to the synthesis of nano-sized barium lead titanates. *Materials Research Bulletin*, 38(4), pp.617–628.

Ash, B.J., Siegel, R.W. & Schadler, L.S., 2004. Mechanical behavior of alumina/poly(methyl methacrylate) nanocomposites. *Macromolecules*, 37, pp.1358–1369.

Astray, G. et al., 2009. A review on the use of cyclodextrins in foods. *Food Hydrocolloids*, 23(7), pp.1631–1640.

Bagchi, A. et al., 2014. Perovskite ceramic nanoparticles in polymer composites for augmenting bone tissue regeneration. *Nanotechnology*, 25(48), p.485101.

Bai, Y. et al., 2000. High-dielectric-constant ceramic-powder polymer composites. *Applied Physics Letters*, 76, pp.3804–3806.

Balakrishnan, N., 2013. *Evaluating Mechanical Performance of Hydrogel-Based Adhesives for Soft Tissue*.

Barrère, F. et al., 2008. Advanced biomaterials for skeletal tissue regeneration: Instructive and smart functions. *Materials Science and Engineering: R: Reports*, 59(1–6), pp.38–71.

Bartos, P.J.M. et al., 2009. *Nanotechnology in construction* Z. Bittnar et al., eds., Berlin, Heidelberg: Springer Berlin Heidelberg.

Baxter, F.R. et al., 2009. An in vitro study of electrically active hydroxyapatite-barium titanate ceramics using Saos-2 cells. *Journal of materials science. Materials in medicine*, 20(8), pp.1697–708.

Baxter, F.R. et al., 2010. Electrically active bioceramics: a review of interfacial responses. *Annals of biomedical engineering*, 38(6), pp.2079–92.

Begg, B.D., Vance, E.R. & Finnie, K.S., 1996. Raman Study of the Relationship between Room-Temperature Tetragonality and the Curie Point of Barium Titanate. *Journal of the American Ceramic Society*, 79(10), pp.2666–2672.

Bereck, A., 2010. Cyclodextrins in Textile Finishing: Fixation and Analysis. *Advanced Materials Research*, 93–94, pp.1–4.

Biji, K.B. et al., 2015. Smart packaging systems for food applications: a review. *Journal of food science and technology*, 52(10), pp.6125–35.

Bikiaris, D.N. et al., 2005. Compatibilisation effect of PP-g-MA copolymer on iPP/SiO2 nanocomposites prepared by melt mixing. *European Polymer Journal*, 41, pp.1965–1978.

Blattner, H., Kanzig, W. & Merz, W., Herstellung und untersuchung von Batio3 einkristallen. *Helvetica physica acta*, 22(1), pp.35–65.

Blezard, R.G., 2003. The History of Calcareous Cements. In *Lea's Chemistry of Cement and Concrete*. pp. 1–23.

Bonnet, V. et al., 2015. Cyclodextrin nanoassemblies: a promising tool for drug delivery. *Drug Discovery Today*, 20(9), pp.1120–1126.

Boulos, M. et al., 2005. Hydrothermal synthesis of nanosized BaTiO powders and dielectric properties of corresponding ceramics. *Solid State Ionics*, 176(13–14), pp.1301–1309.

Brewster, M.E. & Loftsson, T., 2007. Cyclodextrins as pharmaceutical solubilizers. *Advanced Drug Delivery Reviews*, 59(7), pp.645–666.

Brigante, D., 2014. *New Composite Materials* D. Brigante, ed., Switzerland: Springer International Publishing.

Brown, W., Schillen, K. & Hvidt, S., 1992. Triblock copolymers in aqueous solution studied by static and dynamic light scattering and oscillatory shear measurements: influence of relative block sizes. *The Journal of Physical Chemistry*, 96(14), pp.6038–6044.

Buchanan, R.C., 2004. *Ceramic Materials for Electronics, Third Edition*, Taylor & Francis.

Buscaglia, V. et al., 2004. Nanostructured barium titanate ceramics. *Powder Technology*, 148(1), pp.24–27.

Buschmann, H.-J. et al., 1998. The Use of Cyclodextrins in Textile Processes — An Overview. *Journal of the Textile Institute*, 89(3), pp.554–561.

Buschmann, H.-J. & Schollmeyer, E., 2002. Applications of cyclodextrins in cosmetic products: A review. *Journal of cosmetic science*, 53(3), pp.185–91.

Cabrera, C.R. & Miranda, F.A., 2015. *Advanced nanomaterials for aerospace applications*, Pan Stanford Publishing.

Chaisan, W., Yimnirun, R. & Ananta, S., 2009. Preparation and characterization of ceramic nanocomposites in the PZT–BT system. *Ceramics International*, 35(1), pp.121–124.

Challa, R. et al., 2005. Cyclodextrins in drug delivery: An updated review. *AAPS PharmSciTech*, 6(2), pp.E329–E357.

Chen, G. & Jiang, M., 2011. Cyclodextrin-based inclusion complexation bridging supramolecular chemistry and macromolecular self-assembly. *Chemical Society Reviews*, 40(5), p.2254.

Chen, J. et al., 2013. Mechanical, Rheological and Release Behaviors of a Poloxamer 407/ Poloxamer 188/Carbopol 940 Thermosensitive Composite Hydrogel. *Molecules*, 18(10), pp.12415–12425.

Cho, E., Lee, J.S. & Webb, K., 2012. Formulation and characterization of poloxamine-based hydrogels as tissue sealants. *Acta Biomaterialia*, 8(6), pp.2223–2232.

Cho, W.-S., 1998. Structural evolution and characterization of BaTiO3 nanoparticles synthesized from polymeric precursor. *Journal of Physics and Chemistry of Solids*, 59(5), pp.659–666.

Ciofani, G., Danti, S., D'Alessandro, D., et al., 2010. Barium Titanate Nanoparticles: Highly Cytocompatible Dispersions in Glycol-chitosan and Doxorubicin Complexes for Cancer Therapy. *Nanoscale research letters*, 5(7), pp.1093–101.

Ciofani, G. et al., 2013. Effects of barium titanate nanoparticles on proliferation and differentiation of rat mesenchymal stem cells. *Colloids and surfaces. B, Biointerfaces*, 102, pp.312–20.

Ciofani, G., Danti, S., et al., 2010. Enhancement of Neurite Outgrowth in Neuronal-Like Cells following Boron Nitride Nanotube-Mediated Stimulation. *ACS Nano*, 4(10), pp.6267–6277.

Ciofani, G., Leonardo Ricotti, L., et al., 2010. Investigation of interactions between poly-L-lysine-coated boron nitride nanotubes and C2C12 cells: up-take, cytocompatibility, and differentiation. *International Journal of Nanomedicine*, Volume 5, p.285.

Ciofani, G., Danti, S., Moscato, S., et al., 2010. Preparation of stable dispersion of barium titanate nanoparticles: Potential applications in biomedicine. *Colloids and surfaces. B, Biointerfaces*, 76(2), pp.535–43.

Ciofani, G., Ricotti, L. & Mattoli, V., 2011. Preparation, characterization and in vitro testing of poly(lactic-co-glycolic) acid/barium titanate nanoparticle composites for enhanced cellular proliferation. *Biomedical microdevices*, 13(2), pp.255–66.

Clement, K. et al., 2012. Nanostructured Materials: Industrial Applications. In *Handbook of Industrial*

Chemistry and Biotechnology. Boston, MA: Springer US, pp. 265–306.
Cohen, J. & Lach, J.L., 1963. Interaction of Pharmaceuticals with Schardinger Dextrins I. *Journal of Pharmaceutical Sciences*, 52(2), pp.132–136.
Concheiro, A. & Alvarez-Lorenzo, C., 2013. Chemically cross-linked and grafted cyclodextrin hydrogels: From nanostructures to drug-eluting medical devices. *Advanced Drug Delivery Reviews*, 65(9), pp.1188–1203.
Cortiella, J. et al., 2006. Tissue-Engineered Lung: An *In Vivo* and *In Vitro* Comparison of Polyglycolic Acid and Pluronic F-127 Hydrogel/Somatic Lung Progenitor Cell Constructs to Support Tissue Growth. *Tissue Engineering*, 12(5), pp.1213–1225.
Cramer, F., 1952. Einschlußverbindungen der Cyclodextrine. *Angewandte Chemie*, 64(5), pp.136–136.
Crini, G., 2014. Review: A history of cyclodextrins. *Chemical Reviews*, 114(21), pp.10940–10975.
Crini, G., 2003. Studies on adsorption of dyes on beta-cyclodextrin polymer. *Bioresource Technology*, 90(2), pp.193–198.
Cuestas, M.L., Sosnik, A. & Mathet, V.L., 2011. Poloxamines display a multiple inhibitory activity of ATP-binding cassette (ABC) transporters in cancer cell lines. *Molecular pharmaceutics*, 8(4), pp.1152–64.
Čulić-Viskota, J. et al., 2012. Surface functionalization of barium titanate SHG nanoprobes for in vivo imaging in zebrafish. *Nature protocols*, 7(9), pp.1618–33.
Daniel-da-Silva, A.L., Carvalho, R.S. & Trindade, T., 2013. Magnetic hydrogel nanocomposites and composite nanoparticles--a review of recent patented works. *Recent patents on nanotechnology*, 7(2), pp.153–66.
Das, D., Kar, T. & Das, P.K., 2012. Gel-nanocomposites: materials with promising applications. *Soft Matter*, 8(8), p.2348.
Dattaguru, B. & Gopalakrishnan, S., 2013. Foreword to Composites for the 21st Century: Current & Future Trends. *http://dx.doi.org/10.1080/15376494.2014.865473*.
Davis, M. et al., 2004. Self-Assembling Nucleic Acid Delivery Vehicles via Linear, Water-Soluble, Cyclodextrin-Containing Polymers. *Current Medicinal Chemistry*, 11(2), pp.179–197.
Davis, M.E. & Brewster, M.E., 2004. Cyclodextrin-based pharmaceutics: past, present and future. *Nature Reviews Drug Discovery*, 3(12), pp.1023–1035.
Defense, D. of, 2002. *Composite materials handbook* Department of Defense United States of America, ed., Department of Defense. United States of America.
Dempsey, C. et al., 2013. Coating barium titanate nanoparticles with polyethylenimine improves cellular uptake and allows for coupled imaging and gene delivery. *Colloids and surfaces. B, Biointerfaces*, 112, pp.108–12.
Dodziuk, H., 2006. *Cyclodextrins and Their Complexes* H. Dodziuk, ed., Weinheim, FRG: Wiley-VCH Verlag GmbH & Co. KGaA.
Dranetz, A.E., Howatt, G.. & Crownover, J.W., 1948. Barium Titanate as Circuit Elements. *Tele-Tech*, 8(4), pp.29–31.
Dreiss, C.A. et al., 2009. Assembling and de-assembling micelles : competitive interactions of cyclodextrins and drugs with Pluronics. *Soft Matter*, 5, pp.1888–1896.
Drury, J.L. & Mooney, D.J., 2003. Hydrogels for tissue engineering: Scaffold design variables and applications. *Biomaterials*, 24(24), pp.4337–4351.
Dubey, A.K. et al., 2011. Dielectric and Pyroelectric Properties of HAp-BaTiO3 Composites. *Ferroelectrics*, 423(1), pp.63–76.
Duchêne, D., 1987. *Cyclodextrins and Their Industrial Uses*, Paris: Editions de Santé.
Duchêne, D. & Wouessidjewe, D., 1990. Pharmaceutical Uses of Cyclodextrins and Derivatives. *Drug Development and Industrial Pharmacy*, 16(17), pp.2487–2499.
Duerloo, K.-A.N., Ong, M.T. & Reed, E.J., 2012. Intrinsic Piezoelectricity in Two-Dimensional Materials. *The Journal of Physical Chemistry Letters*, 3(19), pp.2871–2876.
Duerloo, K.-A.N. & Reed, E.J., 2013. Flexural electromechanical coupling: a nanoscale emergent property of boron nitride bilayers. *Nano letters*, 13(4), pp.1681–6.
Duran, P. et al., 2002. Densification behaviour, microstructure development and dielectric properties of pure BaTiO3 prepared by thermal decomposition of (Ba,Ti)-citrate polyester resins. *Ceramics International*, 28(3), pp.283–292.
Eastburn, S.D. & Tao, B.Y., 1994. Applications of modified cyclodextrins. *Biotechnology Advances*, 12(2), pp.325–339.
Eyring, G., 1988. *Advanced Materials by Design* U.S. Congress, ed., Washington, DC: U.S. Government

Printing Office,.
F. Jona, G.S., 1993. *Ferroelectric crystals,* New York: Dover Publications, INC.
Fan, Z. et al., 2014. A Novel Wound Dressing Based on Ag/Graphene Polymer Hydrogel: Effectively Kill Bacteria and Accelerate Wound Healing. *Advanced Functional Materials*, 24(25), pp.3933–3943.
FDA, 2000. *FDA GRAS Notice Inventory (N^o 000046): gamma-cyclodextrin.*,
FDA, 2001. *FDA GRAS Notice Inventory (N^o 000074): beta-cyclodextrin.*,
FDA, 2004. *FDA GRAS Notice Inventory (N^o 000155): alpha-cyclodextrin.*,
Fei, R. et al., 2012. Thermoresponsive nanocomposite double network hydrogels. *Soft Matter*, 8(2), pp.481–487.
Feng, J., Yuan, H. & Zhang, X., 1997. Promotion of osteogenesis by a piezoelectric biological ceramic. *Biomaterials*, 18(23), pp.1531–4.
Fenyvesi, É. et al., 2007. Permeability and release properties of cyclodextrin-containing poly(vinyl chloride) and polyethylene films. *Journal of Inclusion Phenomena and Macrocyclic Chemistry*, 57(1–4), pp.371–374.
Fenyvesi, É., Vikmon, M. & Szente, L., 2016a. Cyclodextrins in Food Technology and Human Nutrition: Benefits and Limitations. *Critical reviews in food science and nutrition*, 56(12), pp.1981–2004.
Fenyvesi, É., Vikmon, M. & Szente, L., 2016b. Cyclodextrins in Food Technology and Human Nutrition: Benefits and Limitations. *Critical reviews in food science and nutrition*, 56(12), pp.1981–2004.
French, D., 1957. The Schardinger Dextrins. *Advances in carbohydrate Chemistry*, 12, pp.189–280.
Freudenberg, K.; Cramer, F.; Plieninger, H., 1953. Process for the preparation of inclusion compounds of physiologically active organic compounds.
Freudenberg, K., 1939. Polysaccharides and Lignin. *Annual Review of Biochemistry*, 8(1), pp.81–112.
Freudenberg, K. & Meyer-Delius, M., 1938. Über die Schardinger - Dextrine aus Stärke. *Berichte der deutschen chemischen Gesellschaft (A and B Series)*, 71(8), pp.1596–1600.
Frey, M.H. & Payne, D.A., 1995. Synthesis and processing of barium titanate ceramics from alkoxide solutions and monolithic gels. *Chemistry of Materials*, 7(1), pp.123–129.
Furukawa, T., Ishida, K. & Fukada, E., 1979. Piezoelectric properties in the composite systems of polymers and PZT ceramics. *Journal of Applied Physics*, 50(7), p.4904.
Fusco, S. et al., 2015. Shape-switching microrobots for medical applications : the influence of shape in drug delivery and locomotion . *ACS Appl. Mater. Interfaces*, 7(12), pp.6803–6811.
Gaharwar, A.K. et al., 2013. Bioactive silicate nanoplatelets for osteogenic differentiation of human mesenchymal stem cells. *Advanced materials*, 25(24), pp.3329–36.
Gaharwar, A.K., Peppas, N.A. & Khademhosseini, A., 2014. Nanocomposite hydrogels for biomedical applications. *Biotechnology and bioengineering*, 111(3), pp.441–53.
Garcés, J.M. et al., 2000. Polymeric Nanocomposites for Automotive Applications. *Advanced Materials*, 12(23), pp.1835–1839.
García-Astrain, C. et al., 2015. Biocompatible hydrogel nanocomposite with covalently embedded silver nanoparticles. *Biomacromolecules*, 16(4), pp.1301–10.
García-Río, L. et al., 2014. Cyclodextrin based rotaxanes, polyrotaxanes and polypseudorotaxanes and their biomedical applications. *Current Topics in Medicinal Chemistry*, 14(4), pp.478–493.
Gelb, R.I. et al., 1980. Acid dissociation of cyclohexaamylose and cycloheptaamylose. *Bioorganic Chemistry*, 9(3), pp.299–304.
Gelb, R.I., Schwartz, L.M. & Laufer, D.A., 1982. Acid dissociation of cyclooctaamylose. *Bioorganic Chemistry*, 11(3), pp.274–280.
Genchi, G.G. et al., 2016. Barium titanate nanoparticles: promising multitasking vectors in nanomedicine. *Nanotechnology*, 27(23), p.232001.
Gidwani, B. & Vyas, A., 2015. A Comprehensive Review on Cyclodextrin-Based Carriers for Delivery of Chemotherapeutic Cytotoxic Anticancer Drugs. *BioMed research international*, 2015, p.198268.
Gimenes, R. et al., 2004. Composites PVDF-TrFE/BT used as bioactive membranes for enhancing bone regeneration. , pp.539–547.
Giordano, C. et al., 2011. Nanocomposites for neurodegenerative diseases: Hydrogel-nanoparticle combinations for a challenging drug delivery. *International Journal of Artificial Organs*, 34(12), pp.1115–1127.
Go, D.H. et al., 2008. Tetronic-oligolactide-heparin hydrogel as a multi-functional scaffold for tissue regeneration. *Macromolecular bioscience*, 8(12), pp.1152–60.
González-Gaitano, G., Müller, C., et al., 2015. Modulating the self-assembly of amphiphilic x-shaped block copolymers with cyclodextrins: structure and mechanisms. *Langmuir : the ACS journal of*

surfaces and colloids, 31(14), pp.4096–105.
González-Gaitano, G., da Silva, M. a., et al., 2015. Selective Tuning of the Self-Assembly and Gelation of a Hydrophilic Poloxamine by Cyclodextrins. *Langmuir*, 31(20), pp.5645–5655.
Gould, S. & Scott, R.C., 2005. 2-Hydroxypropyl-β-cyclodextrin (HP-β-CD): A toxicology review. *Food and Chemical Toxicology*, 43(10), pp.1451–1459.
Guan, T. et al., 2012. Development and fabrication of a novel photopatternable electric responsive Pluronic hydrogel for MEMS applications. *Sensors and Actuators A: Physical*, 186, pp.184–190.
Guo, M. et al., 2008. Supramolecular Hydrogels Made of End-Functionalized Low-Molecular-Weight PEG and α-Cyclodextrin and Their Hybridization with SiO2 Nanoparticles through Host−Guest Interaction. *Macromolecules*, 41(24), pp.9744–9749.
Guo, Z. et al., 2009. Fabrication, characterization and microwave properties of polyurethane nanocomposites reinforced with iron oxide and barium titanate nanoparticles. *Acta Materialia*, 57(1), pp.267–277.
Gupta, P., Vermani, K. & Garg, S., 2002. Hydrogels: from controlled release to pH-responsive drug delivery. *Drug Discovery Today*, 7(10), pp.569–579.
Gürdal, Z., Haftka, R.T. & Hajela, P., 1999. *Design and Optimization of Laminated Composite Materials*, Wiley.
H. Thurnaurer and J. Deaderick, 1947. U.S. Patent No. 2,429,588.
Haertling, G.H., 1999. Ferroelectric Ceramics: History and Technology. *Journal of the American Ceramic Society*, 82, p.797.
Hall, J.E. & Guyton, A.C., 2011. *Guyton and Hall Textbook of Medical Physiology* 13th ed. J. E. Hall, ed., Elsevier Academic Press.
Halpin, J.., 1992. *Primer on composite materials analysis* 2nd ed. J. Halpin, ed., CRC Press.
Hamley, I.W., 2004. *Developments in block copolymer science and technology*, J. Wiley.
Han, Y. et al., 2016. Progress in the Immobilization of β -Cyclodextrin and Their Application in Adsorption of Environmental Pollutants. *Chinese Journal of Organic Chemistry*, 36(2), p.248.
Han, Y.K., 2003. In vitro and in vivo study of lens refilling with poloxamer hydrogel. *British Journal of Ophthalmology*, 87(11), pp.1399–1402.
Harada, A., 2001. Cyclodextrin-Based Molecular Mechanics. *Accounts of Chemical Research*, 34(6), pp.456–464.
Harada, A., Hashidzume, A., et al., 2009. Polymeric Rotaxanes. *Chemical Reviews*, 109(11), pp.5974–6023.
Harada, A., 1998. Polyrotaxanes. *Acta Polymerica*, 49(1), pp.3–17.
Harada, A. et al., 1995. Preparation and Characterization of Inclusion Complexes of Poly(propylene glycol) with Cyclodextrins. *Macromolecules*, 28(24), pp.8406–8411.
Harada, A., 2013. Supramolecular Hydrogels. In *Encyclopedia of Polymeric Nanomaterials*. Berlin, Heidelberg: Springer Berlin Heidelberg, pp. 1–7.
Harada, A., Hashidzume, A. & Miyauchi, M., 2006. Polymers Involving Cyclodextrin Moieties. In *Cyclodextrins and Their Complexes*. Weinheim, FRG: Wiley-VCH Verlag GmbH & Co. KGaA, pp. 65–92.
Harada, A., Takashima, Y. & Nakahata, M., 2014. Supramolecular polymeric materials via cyclodextrin-guest interactions. *Accounts of Chemical Research*, 47(7), pp.2128–2140.
Harada, A., Takashima, Y. & Yamaguchi, H., 2009. Cyclodextrin-based supramolecular polymers. *Chemical Society Reviews*, 38(4), p.875.
Haraguchi, K. et al., 2003. Compositional Effects on Mechanical Properties of Nanocomposite Hydrogels Composed of Poly(N , N -dimethylacrylamide) and Clay. *Macromolecules*, 36(15), pp.5732–5741.
Haraguchi, K. et al., 2005. Mechanism of Forming Organic / Inorganic Network Structures during In-situ Free-Radical Polymerization in PNIPA - Clay Nanocomposite Hydrogels. *Macromolecules*, 38, pp.3482–3490.
Haraguchi, K., 2007. Nanocomposite hydrogels. *Current Opinion in Solid State and Materials Science*, 11(3–4), pp.47–54.
Haraguchi, K., 2011. Synthesis and properties of soft nanocomposite materials with novel organic/inorganic network structures. *Polymer Journal*, 43(3), pp.223–241.
Haraguchi, K., Murata, K. & Takehisa, T., 2012. Stimuli-responsive nanocomposite gels and soft nanocomposites consisting of inorganic clays and copolymers with different chemical affinities. *Macromolecules*, 45(1), pp.385–391.

He, J.P. et al., 2006. In situ preparation of poly(ethylene terephthalate)-SiO2 nanocomposites. *European Polymer Journal*, 42, pp.1128–1134.

Hedges & Hedges, A.R., 1998. *Industrial Applications of Cyclodextrins*, [Easton, Pa., etc.]: American Chemical Society.

Hilczer, B. et al., 2002. Dielectric relaxation in ferroelectric PZT–PVDF nanocomposites. *Journal of Non-Crystalline Solids*, 305(1–3), pp.167–173.

Von Hippel, A. et al., 1946. High dielectric constant ceramics. *Industrial & Engineering Chemistry*, 38(11), pp.1097–1109.

Hippel, V., 1954. *Dielectric materials and applications*, John Wiley & Sons.

Hirose, T. & Yamamoto, Y., 2001. Cyclic olefin-based resin composition and its molded product.

Hoare, T.R. & Kohane, D.S., 2008. Hydrogels in drug delivery: Progress and challenges. *Polymer*, 49(8), pp.1993–2007.

Hoffman, A.S., 2002. Hydrogels for biomedical applications. *Advanced Drug Delivery Reviews*, 54(1), pp.3–12.

Holland, L., Rizzi, G. & Malton, P., 2000. Cosmetic compositions containing cyclic oligosaccharides for long-lasting fragrances. *PCT Int. Appl.*, p.20 pp.

Hotchkiss, J.H., Watkins, C.B. & Sanchez, D.G., 2007. Release of 1-Methylcyclopropene from Heat-Pressed Polymer Films. *Journal of Food Science*, 72(5), pp.E330–E334.

Hsiang, H.-I. & Yen, F.-S., 1996. Effect of Crystallite Size on the Ferroelectric Domain Growth of Ultrafine BaTiO3 Powders. *Journal of the American Ceramic Society*, 79(4), pp.1053–1060.

Hsieh, C.-L. et al., 2010. Bioconjugation of barium titanate nanocrystals with immunoglobulin G antibody for second harmonic radiation imaging probes. *Biomaterials*, 31(8), pp.2272–7.

Hsieh, C.-L. et al., 2009. Three-dimensional harmonic holographic microcopy using nanoparticles as probes for cell imaging. *Optics express*, 17(4), pp.2880–91.

Hu, Q.-D., Tang, G.-P. & Chu, P.K., 2014. Cyclodextrin-Based Host–Guest Supramolecular Nanoparticles for Delivery: From Design to Applications. *Accounts of Chemical Research*, 47(7), pp.2017–2025.

Hui, Z. et al., 2010. Carbon nanotube-hybridized supramolecular hydrogel based on PEO-b-PPO-b-PEO/alpha-cyclodextrin as a potential biomaterial. *Journal of Applied Polymer Science*, 116(4), pp.1894–1901.

Irie, T. & Uekama, K., 1997. Pharmaceutical Applications of Cyclodextrins. III. Toxicological Issues and Safety Evaluation. *Journal of Pharmaceutical Sciences*, 86(2), pp.147–162.

Itsuro, T., Akihito, H. & Harada, A., 2005. Photoresponsive Hydrogel System Using Molecular Recognition of α-Cyclodextrin. *Macromolecules*, 38(12), pp.5223–5227.

J.P. Remeika, 1954. A method for growing barium titanate single crystals. *J. Am. Ceram. Soc.*, 76(3), pp.940–941.

Jeevika, A. & Ravi Shankaran, D., 2014. Visual colorimetric sensing of copper ions based on reproducible gelatin functionalized silver nanoparticles and gelatin hydrogels. *Colloids and Surfaces A: Physicochemical and Engineering Aspects*, 461, pp.240–247.

Jeong, B., Wan, S. & Han, Y., 2002. Thermosensitive sol – gel reversible hydrogels. *Advanced drug delivery reviews*, 54(1), pp.37–51.

Jeong, C.K. et al., 2013. Virus-Directed Design of a Flexible BaTiO3 Nanogenerator. *ACS Nano*, 7(12), pp.11016–11025.

Jonscher, A.K., 1983. *Dielectric Relaxation in Solids*, London: Chelsea Dielectric Press.

Joulaud, C. et al., 2013. Characterization of the nonlinear optical properties of nanocrystals by Hyper Rayleigh Scattering. *Journal of nanobiotechnology*, 11 Suppl 1(Suppl 1), p.S8.

Jung, H.M. et al., 2010. Barium Titanate Nanoparticles with Diblock Copolymer Shielding Layers for High-Energy Density Nanocomposites. *Chemistry of Materials*, 22(2), pp.450–456.

Kabanov, A. V., Batrakova, E. V. & Alakhov, V.Y., 2002. Pluronic® block copolymers as novel polymer therapeutics for drug and gene delivery. *Journal of Controlled Release*, 82(2–3), pp.189–212.

Kabiri, K. et al., 2011. Superabsorbent hydrogel composites and nanocomposites: A review. *Polymer Composites*, 32(2), pp.277–289.

Kainer, K.U., 2006. *Metal Matrix Composites. Custom-made Materials for Automotive and Aerospace Engineering.* K. U. Kainer, ed., WILEY-VCH Verlag GmbH & Co.

Kamiya, H. et al., 2003. Preparation of Highly Dispersed Ultrafine Barium Titanate Powder by Using Microbial-Derived Surfactant. *Journal of the American Ceramic Society*, 86(12), pp.2011–2018.

Kao, K.C., 2004. *Dielectric Phenomena in Solids*, Elsevier Academic Press.

Kay, H.F., Wellard, H.J. & Vousden, P., 1949. Atomic Positions and Optical Properties of Barium Titanate. *Nature*, 163(4147), pp.636–637.

Kehr, N.S., Atay, S. & Ergün, B., 2015. Self-assembled monolayers and nanocomposite hydrogels of functional nanomaterials for tissue engineering applications. *Macromolecular Bioscience*, 15(4), pp.445–463.

Khademhosseini, A. & Langer, R., 2007. Microengineered hydrogels for tissue engineering. *Biomaterials*, 28(34), pp.5087–5092.

Kim, E. et al., 2013. Second-Harmonic Generation of Single BaTiO3 Nanoparticles down to 22 nm Diameter. *ACS Nano*, 7(6), pp.5343–5349.

Kim, P. et al., 2009. High energy density nanocomposites based on surface-modified BaTiO3 and a ferroelectric polymer. *Acs Nano*, 3(9), pp.2581–2592.

Kim, P. et al., 2007. Phosphonic Acid-Modified Barium Titanate Polymer Nanocomposites with High Permittivity and Dielectric Strength. *Advanced Materials*, 19(7), pp.1001–1005.

Klouda, L., 2015. Thermoresponsive hydrogels in biomedical applications A seven-year update. *European Journal of Pharmaceutics and Biopharmaceutics*, 97, pp.338–349.

Klouda, L. & Mikos, A.G., 2008. Thermoresponsive hydrogels in biomedical applications. *European journal of pharmaceutics and biopharmaceutics : official journal of Arbeitsgemeinschaft für Pharmazeutische Verfahrenstechnik e.V*, 68(1), pp.34–45.

Kochervinskii, V. V., 2003. Piezoelectricity in crystallizing ferroelectric polymers: Poly(vinylidene fluoride) and its copolymers (A review). *Crystallography Reports*, 48(4), pp.649–675.

Koetting, M.C. et al., 2015. Stimulus-responsive hydrogels: Theory, modern advances, and applications. *Materials Science and Engineering R: Reports*, 93, pp.1–49.

Koontz, J.L. & Marcy, J.E., 2007. Controlled release of active ingredients from polymer food packaging by molecular encapsulation with cyclodextrins. *Abstracts Of Papers Of The American Chemical Society*, 234.

Kopecek, J., 2007. Hydrogel biomaterials: a smart future? *Biomaterials*, 28(34), pp.5185–92.

Kopeček, J. & Yang, J., 2007. Hydrogels as smart biomaterials. *Polymer International*, 56(9), pp.1078–1098.

Kuo, D.-H., Wang, C.-H. & Tsai, W.-P., 2006. Donor- and acceptor-cosubstituted BaTiO3 for nonreducible multilayer ceramic capacitors. *Ceramics International*, 32(1), pp.1–5.

Kuwabara, T., 2005. Film, or fiber, of modified cyclodextrin, and process for producing the same.

Kuwabara, T., 2006. Modified cyclodextrin film or fiber used for medicinal wafers, comprises modified cyclodextrin molecules having high-order linkage to each other.

Kwoleck, S., 1974. Wholly aromatic carbocyclic polycarbonamide fiber having orientation angle of less than about 45{20.

Kwon, J.W. et al., 2005. Biocompatibility of poloxamer hydrogel as an injectable intraocular lens. *Journal of Cataract & Refractive Surgery*, 31(3), pp.607–613.

Lach, J.L. & Cohen, J., 1963. Interaction of Pharmaceuticals with Schardinger Dextrins II. *Journal of Pharmaceutical Sciences*, 52(2), pp.137–142.

Larrañeta, E., 2012. *Geles autoensamblados de poloxaminas y poloxámeros con ciclodextrinas.* Universidad de Navarra.

Larrañeta, E. & Isasi, J., 2012. Self-assembled supramolecular gels of reverse poloxamers and cyclodextrins. *Langmuir*, (28), pp.12457–12462.

Larrañeta, E. & Isasi, J.R., 2013. Phase behavior of reverse poloxamers and poloxamines in water. *Langmuir*.

Larsen, K.L. et al., 1998. Inclusion Complex Formation Constants of Alpha-, Beta-, Gamma-, Delta-, Epsilon-, Zeta-, Eta- and Theta-cyclodextrins Determined with Capillary Zone Electrophoresis. *Carbohydrate Research*, No. 309, pp.153–159.

Lee, J., Mahendra, S. & Alvarez, P.J.J., 2010. Nanomaterials in the Construction Industry: A Review of Their Applications and Environmental Health and Safety Considerations. *ACS Nano*, 4(7), pp.3580–3590.

Lee, K.Y. & Mooney, D.J., 2001. Hydrogels for tissue engineering. *Chemical Reviews*, 101(7), pp.1869–1879.

Lee, L., Park, S.-J. & Kim, S., 2013. Effect of nano-sized barium titanate addition on PEO/PVDF blend-based composite polymer electrolytes. *Solid State Ionics*, 234, pp.19–24.

Lee, Y.-H., Kim, H.-J. & Park, J.-H., 2013. Synthesis and characterization of polyester-based nanocomposites coatings for automotive pre-coated metal. *Progress in Organic Coatings*,

76(10), pp.1329–1336.
Lezcano, M. et al., 2002. Complexation of Several Benzimidazole-Type Fungicides with α- and β-Cyclodextrins. *Journal of Agricultural and Food Chemistry*, 50(1), pp.108–112.
Li, J., 2009. Cyclodextrin Inclusion Polymers Forming Hydrogels. *Advances in Polymer Science*, 222(1), pp.79–113.
Li, J. et al., 2001. Formation of Supramolecular Hydrogels Induced by Inclusion Complexation between Pluronics and α-Cyclodextrin. *Macromolecules*, 34(21), pp.7236–7237.
Li, J. et al., 2006. Self-assembled supramolecular hydrogels formed by biodegradable PEO–PHB–PEO triblock copolymers and α-cyclodextrin for controlled drug delivery. *Biomaterials*, 27(22), pp.4132–4140.
Li, J. & Loh, X.J., 2008. Cyclodextrin-based supramolecular architectures: Syntheses, structures, and applications for drug and gene delivery. *Advanced Drug Delivery Reviews*, 60(9), pp.1000–1017.
Li, J., Ni, X. & Leong, K.W., 2003. Injectable drug-delivery systems based on supramolecular hydrogels formed by poly(ethylene oxide)s and α-cyclodextrin. *Journal of Biomedical Materials Research*, 65A(2), pp.196–202.
Li, S. & Purdy, W.C., 1992. Cyclodextrins and their applications in analytical chemistry. *Chemical Reviews*, 92(6), pp.1457–1470.
Li, Y. et al., 2011. Large Dielectric Constant and High Thermal Conductivity in Poly(vinylidene fluoride)/Barium Titanate/Silicon Carbide Three-Phase Nanocomposites. *ACS Applied Materials & Interfaces*, 3(11), pp.4396–4403.
Li, Z. et al., 2014. Alpha-cyclodextrin: Enzymatic production and food applications. *Trends in Food Science & Technology*, 35(2), pp.151–160.
Lippens, E. et al., 2010. Evaluation of Bone Regeneration with an Injectable, *In Situ* Polymerizable Pluronic ® F127 Hydrogel Derivative Combined with Autologous Mesenchymal Stem Cells in a Goat Tibia Defect Model. *Tissue Engineering Part A*, 16(2), pp.617–27.
Liu, J. et al., 2012. Synthesis of Graphene Peroxide and Its Application in Fabricating Super Extensible and Highly Resilient Nanocomposite Hydrogels. *ACS*, 6(9), pp.8194–8202.
Liu, K.L., Zhang, Z. & Li, J., 2011. Supramolecular hydrogels based on cyclodextrin–polymer polypseudorotaxanes: materials design and hydrogel properties. *Soft Matter*, 7(24), p.11290.
Loethen, S., Kim, J. & Thompson, D.H., 2007. Biomedical Applications of Cyclodextrin Based Polyrotaxanes. *Journal of Macromolecular Science, Part C: Polymer Reviews*.
Loftsson, T. et al., 2005. Cyclodextrins in drug delivery. *Expert Opinion on Drug Delivery*, 2(2), pp.335–351.
Loftsson, T. & Brewster, M.E., 1996. Pharmaceutical applications of cyclodextrins. 1. Drug solubilization and stabilization. *Journal of pharmaceutical sciences*, 85(10), pp.1017–25.
López-de-Dicastillo, C., Jordá, M., et al., 2011. Development of Active Polyvinyl Alcohol/β-Cyclodextrin Composites To Scavenge Undesirable Food Components. *J Agric Food Chem*, 59(20), pp.11026–33.
López-de-Dicastillo, C., Catalá, R., et al., 2011. Food applications of active packaging EVOH films containing cyclodextrins for the preferential scavenging of undesirable compounds. *Journal of Food Engineering*, 104(3), pp.380–386.
López-de-Dicastillo, C. et al., 2010. Immobilization of β-cyclodextrin in ethylene-vinyl alcohol copolymer for active food packaging applications. *Journal of Membrane Science*, 353(1), pp.184–191.
Lu, J.X. & Wong, C.P., 2008. Recent Advances in High-k Nanocomposite Materials for Embedded Capacitor Applications. *Ieee Transactions on Dielectrics and Electrical Insulation*, 15, pp.1322–1328.
van de Manakker, F. et al., 2009. Cyclodextrin-Based Polymeric Materials: Synthesis, Properties, and Pharmaceutical/Biomedical Applications. *Biomacromolecules*, 10(12), pp.3157–3175.
Marino, A. et al., 2015. Barium titanate nanoparticles and hypergravity stimulation improve differentiation of mesenchymal stem cells into osteoblasts. , pp.433–445.
Mark, J.E., Erman, B. & Eirich, F.R., 2005. *Science and technology of rubber*, Elsevier Academic Press.
Marques, H.M.C., 2010. A review on cyclodextrin encapsulation of essential oils and volatiles. *Flavour and Fragrance Journal*, 25(5), pp.313–326.
Marsh, G., 2006. 50 years of reinforced plastic boats. *Reinforced Plastics*, 50(9), pp.16–19.
Mazzaglia, A. et al., 2012. Cyclodextrin-based nanoconstructs for photoactivated therapies. *Journal of Drug Delivery Science and Technology*, 22(3), pp.235–242.

Megaw, H.D., Hinde, W.F. & Forrester M., R., 1945. Crystal Structure of Barium Titanate. *Nature*, 155(3938), pp.484–485.

Mellet, C.O., Fernández, J.M.G. & Benito, J.M., 2011. Cyclodextrin-based gene delivery systems. *Chem. Soc. Rev.*, 40(3), pp.1586–1608.

Merino, S. et al., 2015. Nanocomposite Hydrogels: 3D Polymer–Nanoparticle Synergies for On-Demand Drug Delivery. *ACS Nano*, 9(5), pp.4686–4697.

Merz, W.J., 1949. The Dielectric Behavior of BaTiO3 Single-Domain Crystals. *Physical Review*, 75(4), pp.687–687.

Messner, M. et al., 2010. Self-assembled cyclodextrin aggregates and nanoparticles. *International Journal of Pharmaceutics*, 387(1), pp.199–208.

Miller, R.C. & Savage, A., 1959. Asymmetric Hysteresis Loops and the Pyroelectric Effect in Barium Titanate. *Journal of Applied Physics*, 30(6), p.808.

Miyake, S. & Ueda, R., 1946. On polymorphic change of BaTiO3. *Journal of the physical society of Japan*, 1(JUL), pp.32–33.

Momma, K. & Izumi, F., 2011. VESTA 3 for three-dimensional visualization of crystal, volumetric and morphology data. *Journal of Applied Crystallography*, 44(6), pp.1272–1276.

Moreno, E. et al., 2014. Thermosensitive hydrogels of poly(methyl vinyl ether-co-maleic anhydride) - Pluronic(®) F127 copolymers for controlled protein release. *International journal of pharmaceutics*, 459(1–2), pp.1–9.

Morin-Crini, N. & Crini, G., 2013. Environmental applications of water-insoluble β-cyclodextrin–epichlorohydrin polymers. *Progress in Polymer Science*, 38(2), pp.344–368.

Moya-Ortega, M.D. et al., 2012. Cyclodextrin-based nanogels for pharmaceutical and biomedical applications. *International Journal of Pharmaceutics*, 428(1), pp.152–163.

Murata, K. et al., 2007. Optical anisotropy in polymer–clay nanocomposite hydrogel and its change on uniaxial deformation. *Journal of Materials Chemistry*, 17(32), p.3385.

Nacer, R.S. et al., 2015. Biocompatibility and osteogenesis of the castor bean polymer doped with silica (SiO2) or barium titanate (BaTiO3) nanoparticles. *Acta Cirurgica Brasileira*, 30(4), pp.255–263.

Nejadnik, M.R. et al., 2014. Self-healing hybrid nanocomposites consisting of bisphosphonated hyaluronan and calcium phosphate nanoparticles. *Biomaterials*, 35(25), pp.6918–6929.

Nguyen, D.H., Tran, N.Q. & Nguyen, C.K., 2013. Tetronic-grafted chitosan hydrogel as an injectable and biocompatible scaffold for biomedical applications. *Journal of Biomaterials Science, Polymer Edition*, 24(14), pp.1636–1648.

Nguyen, L.H. et al., 2012. Vascularized Bone Tissue Engineering: Approaches for Potential Improvement. *Tissue Engineering Part B: Reviews*, 18(5), pp.363–382.

Ni, X., Cheng, A. & Li, J., 2009. Supramolecular hydrogels based on self-assembly between PEO-PPO-PEO triblock copolymers and α-cyclodextrin. *Journal of Biomedical Materials Research Part A*, 88A(4), pp.1031–1036.

Nie, S. et al., 2011. Thermoreversible Pluronic F127-based hydrogel containing liposomes for the controlled delivery of paclitaxel: in vitro drug release, cell cytotoxicity, and uptake studies. *International journal of nanomedicine*, 6, pp.151–66.

Novak, B.M., 1993. Hybrid Nanocomposite Materials -between inorganic glasses and organic polymers. *Advanced Materials*, 5(6), pp.422–433.

Olmos, D. et al., 2009. Crystallization and final morphology of HDPE: Effect of the high energy ball milling and the presence of TiO2 nanoparticles. *Polymer*, 50, pp.1732–1742.

Olmos, D. et al., 2011. Effect of the presence of silica nanoparticles in the coefficient of thermal expansion of LDPE. *European Polymer Journal*, 47(8), pp.1495–1502.

Olmos, D. et al., 2013. Structure and morphology of composites based on polyvinylidene fluoride filled with BaTiO3 submicrometer particles: Effect of processing and filler content. *Polymer Composites*, 34(12), pp.2094–2104.

Pantaleón, R. & González-Benito, J., 2010. Structure and thermostability of PMMA in PMMA/silica nanocomposites: Effect of high-energy ball milling and the amount of the nanofiller. *Polymer Composites*, 31(9), pp.1585–1592.

Pantazis, P. et al., 2010. Second harmonic generating (SHG) nanoprobes for in vivo imaging. *Proceedings of the National Academy of Sciences*, 107(33), pp.14535–14540.

Park, J.B. et al., 1980. Piezoelectric ceramic implants: a feasibility study. *Journal of biomedical materials research*, 14(3), pp.269–77.

Park, K.-I., Lee, S.Y., et al., 2010. Bendable and Transparent Barium Titanate Capacitors on Plastic Substrates for High Performance Flexible Ferroelectric Devices. *Electrochemical and Solid-State Letters*, 13(7), p.G57.

Park, K.-I., Xu, S., et al., 2010. Piezoelectric BaTiO3 Thin Film Nanogenerator on Plastic Substrates. *Nano letters*, 10(12), pp.4939–43.

Park, K.M. et al., 2009. Thermosensitive chitosan–Pluronic hydrogel as an injectable cell delivery carrier for cartilage regeneration. *Acta Biomaterialia*, 5(6), pp.1956–1965.

Pascoe, K., 1973. *Chemical and Physical Properties of Materials for Electrical Engineers.*, John Wiley & Sons Ltd.

Paul, A. et al., 2016. Nanoengineered biomimetic hydrogels for guiding human stem cell osteogenesis in three dimensional microenvironments. *J. Mater. Chem. B*, 4, pp.3544–3554.

Peppas, N.A. et al., 2006. Hydrogels in Biology and Medicine: From Molecular Principles to Bionanotechnology. *Advanced Materials*, 18(11), pp.1345–1360.

Peppas, N.A., Bures, P., et al., 2000. Hydrogels in pharmaceutical formulations. *European Journal of Pharmaceutics and Biopharmaceutics*, 50(1), pp.27–46.

Peppas, N.A., Huang, Y., et al., 2000. Physicochemical Foundations and Structural Design of Hydrogels in Medicine and Biology. *Annual Review of Biomedical Engineering*, 2(1), pp.9–29.

Pillai, V. & Shah, D., 1996. *Dynamic Properties of Interfaces and Association Structures*, Champaign IL: AOCS Press.

Pinho, E. et al., 2014. Cyclodextrin-based hydrogels toward improved wound dressings. *Critical Reviews in Biotechnology*, 34(4), pp.328–337.

Polizos, G. et al., 2010. Epoxy-based nanocomposites for electrical energy storage. II: Nanocomposites with nanofillers of reactive montmorillonite covalently-bonded with barium titanate. *Journal of Applied Physics*, 108(7), p.74117.

Portolés, M., Refojo, M.F. & Leong, F.-L., 1994. Poloxamer 407 as a bacterial abhesive for hydrogel contact lenses. *Journal of Biomedical Materials Research*, 28(3), pp.303–309.

Qiu, Y. & Park, K., 2012. Environment-sensitive hydrogels for drug delivery. *Advanced Drug Delivery Reviews*, 64(3), pp.49–60.

Radu, C.-D., Parteni, O. & Ochiuz, L., 2016. Applications of cyclodextrins in medical textiles - review. *Journal of controlled release : official journal of the Controlled Release Society*, 224, pp.146–157.

Randall, C.A., Newnham, R.E. & Cross, L.E., 2004. *History of the First Ferroelectric Oxide, BaTiO3*,

Raouche, S. et al., 2011. Combined effect of high pressure treatment and anti-microbial bio-sourced materials on microorganisms' growth in model food during storage. *Innovative Food Science & Emerging Technologies*, 12(4), pp.426–434.

Ravaglioli, A. & Krajewski, A., 1992. *Bioceramics*, Dordrecht: Springer Netherlands.

Ren, L. et al., 2009. Dual-Responsive Supramolecular Hydrogels from Water-Soluble PEG-Grafted Copolymers and Cyclodextrin. *Macromolecular Bioscience*, 9(9), pp.902–910.

Rey-Rico, A. et al., 2011. Osteogenic efficiency of in situ gelling poloxamine systems with and without bone morphogenetic protein-2. *European Cells and Materials*, 21(14876), pp.317–340.

Reynaud, E. et al., 2001. Nanofillers in polymeric matrix: a study on silica reinforced PA6. *Polymer*, 42, pp.8759–8768.

Romo, A. et al., 2008. Extraction of phenols from aqueous solutions by β-cyclodextrin polymers. Comparison of sorptive capacities with other sorbents. *Reactive and Functional Polymers*, 68(1), pp.406–413.

Rosato, D. V., Rosato, D. V. & Murphy, J., 2004. *Reinforced plastics handbook.*, Elsevier Advanced Technology.

Rose, S. et al., 2013. Time Dependence of Dissipative and Recovery Processes in Nanohybrid Hydrogels. *Macromolecules*, 46(10), pp.4095–4104.

Ruel-Gariépy, E. & Leroux, J.-C., 2004. In situ-forming hydrogels—review of temperature-sensitive systems. *European Journal of Pharmaceutics and Biopharmaceutics*, 58(2), pp.409–426.

Saenger, W., 1980. Cyclodextrin Inclusion Compounds in Research and Industry. *Angewandte Chemie International Edition in English*, 19(5), pp.344–362.

Saenger, W. et al., 1998. Structures of the Common Cyclodextrins and Their Larger Analogues-Beyond the Doughnut. *Chemical reviews*, 98(5), pp.1787–1802.

Saini, P. et al., 2013. High permittivity polyaniline–barium titanate nanocomposites with excellent electromagnetic interference shielding response. *Nanoscale*, 5(10), p.4330.

Sajeesh, S. et al., 2010. Cyclodextrin complexed insulin encapsulated hydrogel microparticles: An oral

delivery system for insulin. *Journal of Controlled Release*, 147(3), pp.377–384.
Sakai, T., Hoshiai, S. & Nakamachi, E., 2006. Biochemical compatibility of PZT piezoelectric ceramics covered with titanium thin film. *Journal of Optoelectronics and Advanced Materials*, 8(4), pp.1435–1437.
Sanchez, C. et al., 2011. Applications of advanced hybrid organic–inorganic nanomaterials: from laboratory to market. *Chemical Society Reviews*, 40(2), p.696.
Sánchez, F.A., Redondo, M. & González-Benito, J., 2015. Influence of BaTiO3 submicrometric particles on the structure, morphology, and crystallization behavior of poly(vinylidene fluoride). *Journal of Applied Polymer Science*, 132(8), pp.41497–41506.
Sanders, L. et al., 2015. Mechanical characterization of a bifunctional Tetronic hydrogel adhesive for soft tissues. *Journal of Biomedical Materials Research Part A*, 103, pp.861–868.
Satarkar, N.S. & Hilt, J.Z., 2008. Magnetic hydrogel nanocomposites for remote controlled pulsatile drug release. *Journal of controlled release : official journal of the Controlled Release Society*, 130(3), pp.246–51.
Savarino, P. et al., 1999. Reactivity and effects of cyclodextrins in textile dyeing. *Dyes and Pigments*, 42, pp.143–147.
Schexnailder, P. & Schmidt, G., 2008. Nanocomposite polymer hydrogels. *Colloid and Polymer Science*, 287(1), pp.1–11.
Schild, H.G., 1992. Poly(N-isopropylacrylamide): experiment, theory and application. *Progress in Polymer Science*, 17(2), pp.163–249.
Schmolka, I., 1973. Polyoxyethylene-polyoxypropylene aqueous gels.
Schmolka, I.R., 1991. A comparison of block copolymer surfactant gels. *Journal of the American Oil Chemists' Society*, 68(3), pp.206–209.
Schmolka, I.R., 1977. A review of block polymer surfactants. *Journal of the American Oil Chemists' Society*, 54(3), pp.110–116.
Schmolka, I.R. & Bacon, L.R., 1967. Viscosity characteristics of aqueous solutions of block copolymers of propylene and ethylene oxides. *Journal of the American Oil Chemists' Society*, 44(10), pp.559–562.
Schollmeyer, E. & Buschmann, H.-J., 1999. Textile material useful for transdermal delivery of a drug which is incorporated into cyclodextrin fixed to the material.
Serra-Gómez, R. et al., 2016. Structure and Rheology of Poloxamine T1107 and its Nanocomposite Hydrogels with Cyclodextrin-Modified Barium Titanate Nanoparticles. *Langmuir*, 32(25), pp.6398–6408.
Serra-Gómez, R., Gonzalez-Gaitano, G. & González-Benito, J., 2012. Composites based on EVA and barium titanate submicrometric particles: Preparation by high-energy ball milling and characterization. *Polymer Composites*, 33(9), pp.1549–1556.
Shaffer, G.D., 1993. An Archaeomagnetic Study of a Wattle and Daub Building Collapse. *Journal of Field Archaeology*, 20, pp.59–75.
Shen, J. et al., 2015. Supramolecular hydrogels of α-cyclodextrin/reverse poloxamines/carbon-based nanomaterials and its multi-functional application. *RSC Adv.*, 5(50), pp.40173–40182.
Shi, E.-W. et al., 2005. Crystallographic Properties of Hydrothermal Barium Titanate Crystallites. *Journal of the American Ceramic Society*, 80(6), pp.1567–1572.
Shimooka, H. & Kuwabara, M., 1996. Crystallinity and Stoichiometry of Nano-Structured Sol-Gel-Derived BaTiO3 Monolithic Gels. *Journal of the American Ceramic Society*, 79(11), pp.2983–2985.
Shin, S.R. et al., 2013. Cell-laden microengineered and mechanically tunable hybrid hydrogels of gelatin and graphene oxide. *Advanced Materials*, 25(44), pp.6385–6391.
da Silva, M.A. & Dreiss, C.A., 2016. Soft nanocomposites: nanoparticles to tune gel properties. *Polymer International*, 65(3), pp.268–279.
Simon-Seveyrat, L. et al., 2007. Re-investigation of synthesis of BaTiO3 by conventional solid-state reaction and oxalate coprecipitation route for piezoelectric applications. *Ceramics International*, 33(1), pp.35–40.
Siró, I. et al., 2006. Release of alpha-tocopherol from antioxidative low-density polyethylene film into fatty food simulant: Influence of complexation in beta-cyclodextrin. *Food Additives and Contaminants*, 23(8), pp.845–853.
Sivaraman, S. et al., 2015. Tetronic ® -based composite hydrogel scaffolds seeded with rat bladder smooth muscle cells for urinary bladder tissue engineering applications. *Journal of Biomaterials Science, Polymer Edition*, 26(3), pp.196–210.

Slamovich, E.B. & Aksay, I.A., 1996. Structure Evolution in Hydrothermally Processed (<100°C) BaTiO3 Films. *Journal of the American Ceramic Society*, 79(1), pp.239–247.
Slaughter, B.B. V et al., 2009. Hydrogels in Regenerative Medicine. *Advanced Materials*, 21(32–33), pp.3307–3329.
Song, F. et al., 2015. Nanocomposite hydrogels and their applications in drug delivery and tissue engineering. *Journal of Biomedical Nanotechnology*, 11(1), pp.40–52.
Sosnik, A. & Sefton, M. V, 2006. Methylation of poloxamine for enhanced cell adhesion. *Biomacromolecules*, 7(1), pp.331–8.
Sosnik, A. & Sefton, M. V, 2005. Poloxamine hydrogels with a quaternary ammonium modification to improve cell attachment. *Journal of biomedical materials research. Part A*, 75(2), pp.295–307.
Spizzirri, U. et al., 2015. Recent Advances in the Synthesis and Biomedical Applications of Nanocomposite Hydrogels. *Pharmaceutics*, 7(4), pp.413–437.
Sricharussin, W. et al., 2009. Modification of cotton fabrics with β-cyclodextrin derivative for aroma finishing. *The Journal of The Textile Institute*, 100(8), pp.682–687.
Stojanovic, B.D. et al., 2005. Mechanochemical synthesis of barium titanate. *Journal of the European Ceramic Society*, 25(12), pp.1985–1989.
Stojanović, B.D., Skorokhod, V. V. & Nikolić, M.V. eds., 1999. *Advanced Science and Technology of Sintering*, Boston, MA: Springer US.
Syrtsov, S.R. et al., 2002. Positive temperature coefficient of resistivity in thin films of barium titanate. *Materials Science in Semiconductor Processing*, 5(2–3), pp.223–225.
Szejtli, J., 1988. *Cyclodextrin Technology*, Dordrecht: Springer Netherlands.
Szejtli, J., 1992. The properties and potential uses of cyclodextrin derivatives. *Journal of Inclusion Phenomena and Molecular Recognition in Chemistry*, 14(1), pp.25–36.
Szejtli, J., 1997. Utilization of cyclodextrins in industrial products and processes. *Journal of Materials Chemistry*, 7(4), pp.575–587.
Szejtli, J., Cserháti, T. & Szögyi, M., 1986. Interactions between cyclodextrins and cell-membrane phospholipids. *Carbohydrate Polymers*, 6(1), pp.35–49.
Szente, L. & Szejtli, J., 2004. Cyclodextrins as food ingredients. *Trends in Food Science & Technology*, 15(3–4), pp.137–142.
Szente, L. & Szejtli, J., 1999. Highly soluble cyclodextrin derivatives: chemistry, properties, and trends in development. *Advanced Drug Delivery Reviews*, 36(1), pp.17–28.
Tajima, K. et al., 1999. PZT nanocomposites reinforced by small amount of oxides. *Journal of the European Ceramic Society*, 19(6–7), pp.1179–1182.
Takenaka, T. et al., 1989. Dielectric, Piezoelectric, and Pyroelectric Properties of Lead Zirconate-Lead Zinc Niobate Ceramics. *Journal of the American Ceramic Society*, 72(6), pp.1016–1023.
Tang, H. et al., 2011. Nanocomposites with increased energy density through high aspect ratio PZT nanowires. *Nanotechnology*, 22(1), p.15702.
Tang, P. et al., 2004. Electrooptic modulation up to 40 GHz in a barium titanate thin film waveguide modulator. *Optics Express*, 12(24), p.5962.
Teixeira, L.N. et al., 2010. In vitro biocompatibility of poly(vinylidene fluoride-trifluoroethylene)/barium titanate composite using cultures of human periodontal ligament fibroblasts and keratinocytes. *Acta biomaterialia*, 6(3), pp.979–89.
Tejashri, G., Amrita, B. & Darshana, J., 2013. Cyclodextrin based nanosponges for pharmaceutical use: a review. *Acta pharmaceutica*, 63(3), pp.335–58.
Thomas, V. et al., 2007. Review on Polymer, Hydrogel and Microgel Metal Nanocomposites: A Facile Nanotechnological Approach. *Journal of Macromolecular Science, Part A*, 45(1), pp.107–119.
Tilley, R.J.D., 2006. *Crystals and Crystal Structures*, John Wiley & Sons.
Van Tomme, S.R., Storm, G. & Hennink, W.E., 2008. In situ gelling hydrogels for pharmaceutical and biomedical applications. *International Journal of Pharmaceutics*, 355(1), pp.1–18.
Trinh, T. et al., 1997. Compositions for reducing body odor.
Trinh, T. et al., 1989. Treatment of fabric with perfume/cyclodextrin complexes.
Trotta, F., Zanetti, M. & Cavalli, R., 2012. Cyclodextrin-based nanosponges as drug carriers. *Beilstein Journal of Organic Chemistry*, 8, pp.2091–2099.
Tseng, W.J. & Lin, C.-L., 2003. Effect of dispersants on rheological behavior of BaTiO3 powders in ethanol–isopropanol mixtures. *Materials Chemistry and Physics*, 80(1), pp.232–238.
Tsuchiya, K. et al., 2011. Design of biocompatible high-piezoelectric BaTiO3 with additives. In S. Juodkazis & M. Gu, eds. *Smart Nano-Micro Materials and Devices*. International Society for

Optics and Photonics, p. 82042A.
Uekama, K., 2004. Design and Evaluation of Cyclodextrin-Based Drug Formulation. *Chemical & Pharmaceutical Bulletin*, 52(8), pp.900–915.
Uekama, K., Hirayama, F. & Arima, H., 2006. Pharmaceutical Applications of Cyclodextrins and Their Derivatives. In *Cyclodextrins and Their Complexes*. Weinheim, FRG: Wiley-VCH Verlag GmbH & Co. KGaA, pp. 381–422.
Vaia, R. & Maguire, J., 2007. Polymer Nanocomposites with Prescribed Morphology: Going beyond Nanoparticle-Filled Polymers. *Chemistry of Materials*, 19, pp.2736–2751.
Valasek, J., 1971. Early History of Ferroelectricity. *Ferroelectrics*, 2(4), p.239.
Del Valle, E.M.M., 2004. Cyclodextrins and their uses: a review. *Process Biochemistry*, 39(9), pp.1033–1046.
Vaughn, T.H. et al., 1951. Properties of some newly developed nonionic detergents. *Journal of the American Oil Chemists' Society*, 28(7), pp.294–299.
Verrone, R. et al., 2007. Effect of β-cyclodextrin on spectroscopic properties of ochratoxin A in aqueous solution. *Journal of Inclusion Phenomena and Macrocyclic Chemistry*, 57(1–4), pp.475–479.
Vijatovic, M.M.M., Bobic, J.D.D. & Stojanovic, B.D.D., 2008. History and challenges of barium titanate: Part II. *Science of Sintering*, 40(3), pp.235–244.
Villiers, A., 1891. Sur la transformation de la fécule en dextrine par le ferment butyrique. *Compt. Rend. Fr. Acad. Sci.*, pp.435–8.
Vinothini, V., Singh, P. & Balasubramanian, M., 2006. Optimization of barium titanate nanopowder slip for tape casting. In *Journal of Materials Science*. pp. 7082–7087.
Vyas, A., Saraf, S. & Saraf, S., 2008. Cyclodextrin based novel drug delivery systems. *Journal of Inclusion Phenomena and Macrocyclic Chemistry*, 62(1–2), pp.23–42.
Wang, Q. et al., 2012. Super-tough double-network hydrogels reinforced by covalently compositing with silica-nanoparticles. *Soft Matter*, 8(22), p.6048.
Wang, S. et al., 2016. Polyelectrolyte coated $BaTiO_3$ nanoparticles for second harmonic generation imaging-guided photodynamic therapy with improved stability and enhanced cellular uptake. *RSC Adv.*, 6(46), pp.40615–40625.
Wang, T. et al., 2009. Bone marrow stem cells implantation with α-cyclodextrin/MPEG–PCL–MPEG hydrogel improves cardiac function after myocardial infarction. *Acta Biomaterialia*, 5(8), pp.2939–2944.
Wanka, G., Hoffmann, H. & Ulbficht, W., 1990. The aggregation behavior of poly-(oxyethylene)-poly-(oxypropylene)- poly-(oxyethylene)-block-copolymers m aqueous solution. *Colloid & Polymer Science*, 268(2), pp.101–117.
Watton, R., 1989. Ferroelectric materials and devices in infrared detection and imaging. *Ferroelectrics*, 91(1), pp.87–108.
Webster, J.G., 1999. *The measurement, instrumentation, and sensors handbook.* J. G. Webster, ed., CRC Press.
Weiner, S. & Wagner, H.D., 1998. The Material Bone: Structure-Mechanical Function Relations. *Annual Review of Materials Science*, 28(1), pp.271–298.
Wenz, G., 1994. Cyclodextrins as Building Blocks for Supramolecular Structures and Functional Units. *Angewandte Chemie International Edition in English*, 33(8), pp.803–822.
Wenz, G., Han, B.-H. & Müller, A., 2006. Cyclodextrin Rotaxanes and Polyrotaxanes. *Chemical Reviews*, 106(3), pp.782–817.
Whatmore, R.W., Osbond, P.C. & Shorrocks, N.M., 1987. Ferroelectric materials for thermal IR detectors. *Ferroelectrics*, 76(1), pp.351–367.
Wichterle, O. & Lím, D., 1960. Hydrophilic Gels for Biological Use. *Nature*, 185(4706), pp.117–118.
Williams, C.G. et al., 2005. Variable cytocompatibility of six cell lines with photoinitiators used for polymerizing hydrogels and cell encapsulation. *Biomaterials*, 26(11), pp.1211–1218.
Wintersgill, S., 2004. Production of tissue paper materials useful for making beverage infusion packages involves treating at least one of constitute fiber of tissue in such a manner that at least one cyclodextrin compound can permanently affix to it.
Wood, E., 2001. Improved aroma barrier properties in food packaging with cyclodextrins. *Paper, Film and Foil Converter*, 75(11).
Wood, E., Beaverson, N. & Kuduk, W., 2010. Maturation or ripening inhibitor release from polymer, fiber, film, sheet or packaging.

Wood, E. & Beaverson NJ, 2005. Amphoteric grafted barrier materials.
Wu, C.-J. et al., 2011. Mechanically Tough Pluronic F127/Laponite Nanocomposite Hydrogels from Covalently and Physically Cross-Linked Networks. *Macromolecules*, 44(20), pp.8215–8224.
Xu, B. et al., 2013. Nanocomposite hydrogels with high strength cross-linked by titania. *RSC Advances*, 3(20), p.7233.
Xu, G. et al., 2003. Design and construction of insulation configuration for ultra-high-temperature microwave processing of ceramics. *Journal of the American Ceramic Society*, 86(12), pp.2082–2086.
Yang, J. et al., 2014. Simple approach to reinforce hydrogels with cellulose nanocrystals. *Nanoscale*, 6(11), p.5934.
Yang, M.J. & Dan, Y., 2005. Preparation and characterization of poly(methyl methacrylate)/titanium oxide composite particles. *Colloid and Polymer Science*, 284, pp.243–250.
Yu, B.Y., Chung, J.W. & Kwak, S.-Y., 2008. Reduced Migration from Flexible Poly(vinyl chloride) of a Plasticizer Containing β-Cyclodextrin Derivative. *Environmental Science & Technology*, 42(19), pp.7522–7527.
Yu, L. & Ding, J., 2008. Injectable hydrogels as unique biomedical materials. *Chemical Society Reviews*, 37(8), p.1473.
Zeng, Y. & Lu, J.Q., 2014. Optothermally Responsive Nanocomposite Generating Mechanical Forces for Cells Enabled by Few-Walled Carbon Nanotubes. *ACS Nano*, 8(11), pp.11695–11706.
Zgonik, M. et al., 1994. Dielectric, elastic, piezoelectric, electro-optic, and elasto-optic tensors of BaTiO 3 crystals. *Physical Review B*, 50(9), pp.5941–5949.
Zhang, J. & Ma, P.X., 2013. Cyclodextrin-based supramolecular systems for drug delivery: Recent progress and future perspective. *Advanced Drug Delivery Reviews*, 65(9), pp.1215–1233.
Zhang, J. & Ma, P.X., 2010. Host–guest interactions mediated nano-assemblies using cyclodextrin-containing hydrophilic polymers and their biomedical applications. *Nano Today*, 5(4), pp.337–350.
Zhang, J., Wang, C. & Bowen, C., 2014. Piezoelectric effects and electromechanical theories at the nanoscale. *Nanoscale*, 6(22), pp.13314–13327.
Zhang, Q.M. et al., 2002. An all-organic composite actuator material with a high dielectric constant. *Nature*, 419, pp.284–287.
Zhang, X. et al., 2013. Polyaniline stabilized barium titanate nanoparticles reinforced epoxy nanocomposites with high dielectric permittivity and reduced flammability. *Journal of Materials Chemistry C*, 1(16), pp.2886–2899.
Zhang, X.B. et al., 2011. Optically- and Thermally-Responsive Programmable Materials Based on Carbon Nanotube-Hydrogel Polymer Composites. *Nano Letters*, 11(8), pp.3239–3244.
Zhang, Y. et al., 2014. Aligned porous barium titanate/hydroxyapatite composites with high piezoelectric coefficients for bone tissue engineering. *Materials Science and Engineering C*, 39(1), pp.143–149.
Zhao, L.Z. et al., 2015. Recent advances in clay mineral-containing nanocomposite hydrogels. *Soft Matter*, 11(48), pp.9229–9246.
Zhao, S.P., Zhang, L.M. & Ma, D., 2006. Supramolecular hydrogels induced rapidly by inclusion complexation of poly(ε-caprolactone)-poly(ethylene glycol)-poly(ε-caprolactone) block copolymers with α-cyclodextrin in aqueous solutions. *Journal of Physical Chemistry B*, 110(25), pp.12225–12229.
Zheng, Y. & Wyman, I., 2016. Supramolecular Nanostructures Based on Cyclodextrin and Poly(ethylene oxide): Syntheses, Structural Characterizations and Applications for Drug Delivery. *Polymers*, 8(5), p.198.
Zhou, J. & Ritter, H., 2010. Cyclodextrin functionalized polymers as drug delivery systems. *Polymer Chemistry*, 1(10), p.1552.

OBJECTIVES

OBJECTIVES

In the recent years the importance of nanomaterials, and particularly polymeric nanocomposites, is growing exponentially. They are taking over functions carried out by classic materials in many fields of science, as they present enhanced functionality derived from the possibility of combining the properties of the nanoparticles and the polymers. In addition to that, they open new possibilities of use, as they can be engineered at the structural level, developing properties of interest that were not reachable before.

Within this frame, the main objective of this thesis is the design, preparation and characterization of polymeric nanocomposites based on Barium Titanate and Cyclodextrins.

Barium Titanate ($BaTiO_3$, BT) is an inorganic ceramic that has been one of the most important materials of its kind. Because of its ferroelectric, dielectric and piezoelectric properties, BT has been at the forefront of many applications in areas such as microelectronics and electroceramics. While in the recent decades the number of applications of BT in microelectronics has decreased, newer promising applications of these ceramic applications are emerging within the biomaterials field. This project revolves around BT nanoparticles and our efforts to produce two different types of new BT-based polymeric nanocomposites: on one hand solid films based on a polymeric matrix (ethylene-vinyl acetate, EVA) for electrical applications; on the other hand, injectable hydrogel nanocomposites containing cyclodextrins (CDs) based on block copolymers of ethylenoxide and propylenoxide, more specifically poloxamines, for their use as biomaterials.

In order to achieve what we describe above, the following specific objectives have been proposed:

1. Structural characterization of BT nanoparticles of different sizes and crystalline structures. Design and optimization of a process to break the agglomeration of the nanoparticles in solid state. Design and preparation of nanocomposite films of EVA and Barium Titanate by means of High Energy Ball Milling (HEBM). (Chapter 1)

2. Modification of the surface of the BT nanoparticles with CDs seeking and improve in their stability in water without loss of properties, with the aim of preparing nanocomposites based on hydrosoluble polymers. (Chapter 3)

3. Preparation and characterization of nanocomposites based on thermoplastic (EVA) and hydrosoluble polymers (PEG, PEO and PPO/PEO poloxamers) with the modified

BT nanoparticles to test their homogeneity and uniformity upon casting. Exploration of the dielectrical response of the nanocomposite to ensure BT properties are sustained. (Chapter 3)

4. Design and study of the physicochemical properties of the inclusion complex of β-Cyclodextrin and Rhodamine B as a potential model for drug delivery, both in solution and in solid state. Evaluation of the capability of the complex to endure the preparation of the polymeric nanocomposites by means of HEBM. (Chapter 2)

5. Physicochemical and microbiological characterization of the modified nanoparticles, to evaluate their cytotoxicity against different cell lines in order to assess their use in biomaterial applications. (Chapter 3)

6. Study of the poloxamine Tetronic 1107 from a structural and rheological point of view. Analysis of the influence of pH, temperature and concentration on the micellization process tracked by DLS and SANS. (Chapter 4)

7. Preparation of hydrogel nanocomposites based on poloxamines and CD-modified BT nanoparticles. Design of the formulation to tailor the gelation properties for an injectable hydrogel. (Chapter 4)

8. Structural, rheological and cytotoxicity studies and characterization of the prepared hydrogel nanocomposites as a function of temperature and composition. (Chapter 4)

RESULTS

Chapter 1

Composites Based on EVA and Barium Titanate Submicrometric Particles: Preparation by High-Energy Ball-Milling and Characterization.

Polymer Composites
DOI: 10.1002/pc.22291

Abstract

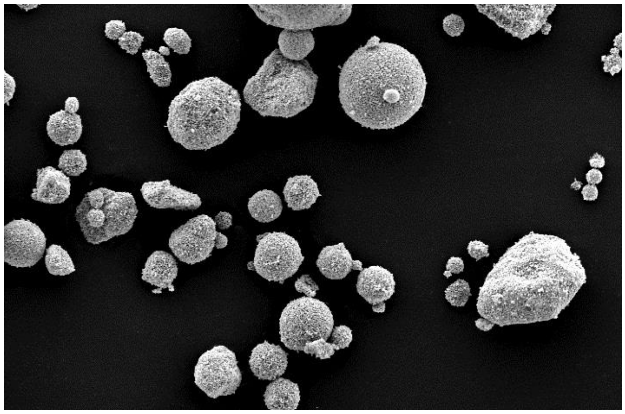

Ethylene vinyl acetate copolymer (EVA), a thermoplastic semicrystalline polymer, has been blended with barium titanate submicrometric particles ($BaTiO_3$) by means of high-energy ball milling (HEBM) for obtaining composites in the form of films by hot pressing. Two different milling conditions have been considered: i) milling at room temperature; and ii) milling under the temperature of the liquid nitrogen (cryomilling). The resulting composites have been fully characterized by spectroscopic and microscopic techniques to study the structure and morphology as a function of the processing conditions. A very good dispersion of the particles is attained under cryogenic conditions and, irrespective of the milling method, structural modifications were not observed in any of the materials used. Cross-contamination of iron from the milling tools is also reduced to acceptable values for HEBM standards, especially in the case of cryo-milling, an important issue for the use of these composites in electrical applications.

1. INTRODUCTION

One of the most important prerequisites to reach best performance in polymeric composite materials is to ensure a uniform dispersion of the particles, because the formation of particles agglomerates may lead to the unwanted discontinuity or deterioration of their properties (Pantaleón & González-Benito 2010). Up to now, several methods have been employed to achieve efficient dispersion of inorganic nanoparticles, either nano or submicron sized, in different matrices: i) modification of the surface of the particles(Yang & Dan 2005; Ash et al. 2004; Kim et al. 2007); ii) chemical modification of the filler with a monomer, to allow the subsequent polymerization when mixed with a co-monomer (Bikiaris et al. 2005); iii) "in situ" polymerization by dispersion of the particles in a monomer for subsequent polymerization (Reynaud et al. 2001); iv) by conventional sol-gel methods to generate nanoparticles within the polymer matrix; and v) addition of surfactants or other dispersant substances as phosphate esters (He et al. 2006). In general, these methods are based on material processing in solution or melted state. Typically, when the particle diameter is small (Ash et al. 2004), a uniform mixture is really difficult to obtain if the amount of filler is higher than 5 wt%, or if the polymer melt presents a high viscosity.

High-energy ball milling, HEBM, is a good approach of processing thermoplastic matrix nanocomposite materials, not only due to the results in terms of dispersion, but also from an economical point of view. Initially intended for the synthesis and processing of inorganic materials (Suryanarayana 2001; Benjamin 1970; Padella et al. 1998; Rowlands et al. 1994), this method has been successfully used to obtain polymer blends with improved mechanical properties and polymer nanocomposites with real dispersion of nanoparticles, as poly(methyl methacrylate)-silica (Castrillo et al. 2007; Gonzalez-Benito & Gonzalez-Gaitano 2008), acrylonitrile-butadiene-styrene, polystyrene and polypropylene (Shaw 1998; Incocciati et al. 2003) and high density polyethylene with TiO_2 nanoparticles (Olmos et al. 2009). However, due to the high energy involved in the process it may have adverse effects of wearing on the polymers by mechanisms of chain scission and sample oxidation, together with cross-contamination from the milling tools (Olmos et al. 2011).

The aim of this work has been to prepare by means of HEBM a new thermoplastic composite formed by ethylene vinyl acetate copolymer, EVA, blended with barium titanate submicrometric particles. $BaTiO_3$ has been chosen due to their ferroelectricity and high dielectric constant in its tetragonal structure (Lombardi et al. 2011), properties which make it useful for applications in the field of electronics as printed circuits or in capacitors, for

example. However, the high processing temperature as a ceramic material makes it unsuited for many practical uses. This problem may be overcome by its preparation in form of composites by making use of the low temperature processability of the polymer. EVA is a thermoplastic polymer with polar groups (vinyl acetate) and crystalline ethylene domains. When the amount of the ethylene comonomer is high enough, EVA copolymer can be easily processed in the form of films. The presence of polar vinyl acetate groups in the EVA copolymer may also favour its adhesion to $BaTiO_3$ particles, as observed in other fillers with polar surfaces (Chaudhary et al. 2005). In addition to that, the fact that the polymer is semicrystalline adds a potential interest because many of the final properties depend on the crystallinity of the composite matrix. The milling has been carried out under cryogenic and room temperature conditions, with the purpose of ascertaining the best way to achieve a uniform dispersion in the composite avoiding the degradation processes of the polymer and the phase change of the inorganic submicrometric particles. The characterisation of the $BaTiO_3$/EVA composites and the study of their morphology and particle dispersion according to the processing conditions are also presented in this work.

2. EXPERIMENTAL PART

2.1 Materials

Poly (ethylene-co-vinyl acetate), EVA (12 wt% in vinyl acetate, density 0.933 $g \cdot cm^{-3}$ at 25˚C, Vicat temperature ASTM D 1525 of 65 ˚C and melting point of 95 ˚C) was supplied by Sigma Aldrich. Inorganic submicrometric particles of barium titanate (BaTiO3) were supplied by Nanostructured and Amorphous Materials inc. Their average diameter according to the manufacturer is 200 nm, with 99.9% purity, density of 6.02 $g \cdot cm^{-3}$ and tetragonal crystalline structure.

2.2 Sample preparation

In order to make easier the subsequent blending process with the particles, EVA pellets were firstly ground in a MF 10 Basic IKA WERKE grinder at a rotation speed of 4500 rpm. The grinding time was short enough to avoid polymer melting due to the rise of temperature associated to the process. Two methods of processing were carried out to merge the $BaTiO_3$ with EVA:

i) HEBM at room temperature. $BaTiO_3$ was mixed with the ground EVA, 20 wt% of $BaTiO_3$ and introduced in a vial of stainless steel together with 11 stainless steel balls of 20-mm diameter. The vial was then hermetically closed and placed in a Pulverisette 5 Fritsch

apparatus where the powder was milled at 400 rpm for 2 hours at room temperature. Each 10 minutes of active milling was followed by 3 minutes of resting. After the first hour of active milling the equipment was left to rest for 20 minutes.

ii) Cryo-HEBM. A mixture of $BaTiO_3$ with EVA (20 wt%) was subjected to HEBM process under cryogenic conditions (cryomilling, Cryo) in a MM400 RETSCH miller. A vessel of 50 mL and one ball of 20 mm diameter made of stainless steel were used. The procedure consisted in 1 hour of active cryomilling divided into 12 cycles of 5 minutes of milling at 25 Hz (vessel oscillation) and 15 minutes of resting in liquid nitrogen.

Films of the composites were prepared by hot pressing. The milled powder was placed between two Teflon plates and pressed and heated in an oven at 150 ˚C for 20 min. After that, the prefilms were cooled inside the oven down to 40 ˚C. A small portion of the prefilm was placed between the two Teflon plates and sandwiched between two stainless steel plates fixed with clampers. A weight was placed on top of the sample as described by Olmos (Olmos et al. 2009) and put into an oven to be heated at 150 ˚C for 90 minutes. The film was slowly cooled down inside the oven to room temperature, avoiding any thermal stress in the sample. The thicknesses of the prepared films were of about 20 μm.

2.3 Techniques

The crystalline structure of the materials under study was characterized by X-ray diffraction, XRD, using a Philips X'PERT-MPD diffractometer with a copper anode emitting its typical $K\alpha_1$ radiation at a wavelength of 1.5405 Å applying a voltage of 40 kV. For randomly oriented powder preparations, the diffractograms were obtained scanning 2θ angles from 7˚ to 90˚ in steps of 0.02˚. The analysis of the X-ray diffraction patterns was carried out using the Philips X'Pert Graphics software.

Elemental analysis was carried out by atomic absorption spectroscopy, AAS, using a Perkin Elmer Analyst 800. The milled samples were subjected to a digestion process in a closed vessel with microwaves in concentrated nitric acid and hydrogen peroxide medium. The content in iron was deduced from interpolation in the calibration curve prepared with Fe standards.

The topography of the samples was inspected by SEM (Philips XL30 scanning electron microscope), with the signal coming from secondary electrons, SE, while the morphology and distribution of domains with different compositions were imaged using backscattered electrons, BSE. Finally, microanalysis at specific sites of the samples was performed with a DX4i coupled energy-dispersive X-ray spectroscopy (EDAX) detector. To avoid charge

accumulation on the surfaces under analysis, the samples were coated with Au by sputtering method.

FTIR spectra were recorded in transmission mode with a FTIR Spectrum GX (Perkin-Elmer). 40 scans with a resolution of 4 cm^{-1} were performed. The powders coming from the milling process were diluted in KBr (less than 1 wt%) and pressed in the form of discs. All samples had low enough amounts of EVA or EVA-$BaTiO_3$ as to satisfy the Lambert-Beer's law. On the other hand, the samples in the form of films were studied by attenuated total reflectance, FTIR-ATR using an FTIR-ATR Nicolette Avatar 360 spectrometer, with a resolution of 4 cm^{-1} and 32 scans per spectrum.

Thermogravimetric analysis was carried out in a Perkin Elmer STA 6000. The samples were subjected to a heating program from 30 ˚C to 800 ˚C at 30 ˚C per minute under a N_2 atmosphere.

The average size of the particles was determined by dynamic light scattering (DLS) using a DynaPro photon correlation spectrometer. The particles were dispersed in deionized water by sonication and diluted before the measurements without further filtration. The size distributions were calculated by the method of regularization with DynaLS 1.0 software, expressed in terms of the hydrodynamic radius, R_h.

3. RESULTS AND DISCUSSION

3.1 Characterization of the submicrometric particles

$BaTiO_3$ shows its typical piezoelectric response when its crystalline structure is tetragonal. XRD patterns of the commercial $BaTiO_3$ particles show the typical split of the tetragonal structure at 45˚ and 45.5˚ due to the planes (002) and (200), which come from the cubic cell distortion (Asiaie et al. 1996) according to the JCPDS chart #5-626. The DSC trace of the commercial $BaTiO_3$ shows also the Curie transition at 128.2 ˚C, due to the $BaTiO_3$ allotropic transformation from the tetragonal structure to the cubic one, in agreement with literature values (Baeten et al. 2006).

A SEM image of the commercial $BaTiO_3$ is shown in Figure 1.1. Spherical shape agglomerates of submicrometric particles can be observed. The mean hydrodynamic diameter that can be measured is close to the mean average particle size (APS) provided by the supplier (≈ 200 nm diameter).

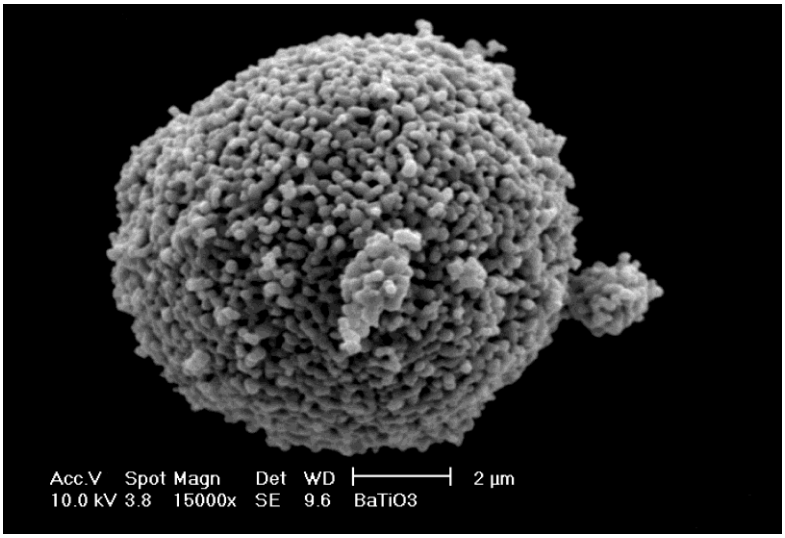

Fig. 1.1: SEM image of as received BaTiO3 nanoparticles.

DLS has been used to characterize more accurately the spectrum in size of the $BaTiO_3$. As seen on Figure 1.2 the distribution is bimodal. The first peak corresponds to the submicrometric particles dispersed in water while the second one is ascribed to aggregates (Table 1.1). The size distribution can be converted from scattered intensity to mass by assuming the particles have spherical shape. In terms of mass the distribution is quite monodisperse, with a negligible contribution of the aggregates (less than 1 wt%). When cryomilling the $BaTiO_3$, the average particle diameter results to be slightly smaller but practically the same within the experimental uncertainty (Table 1.1), the width of the distribution is reduced (i.e., particles more monodisperse) and also is the percentage of aggregates. This implies that the milling procedure does not affect significantly the average particle size of $BaTiO_3$, contributing to break the scarce existing agglomerates.

Table 1.1: DLS analysis for commercial and cryomilled $BaTiO_3$ particles.

	Peaks	**Intensity %**	**D_h (nm)**
Commercial	1	81	264 ± 80
	2	19	1524 ± 312
Cryomilled	1	85	212 ± 28
	2	15	1524 ± 226

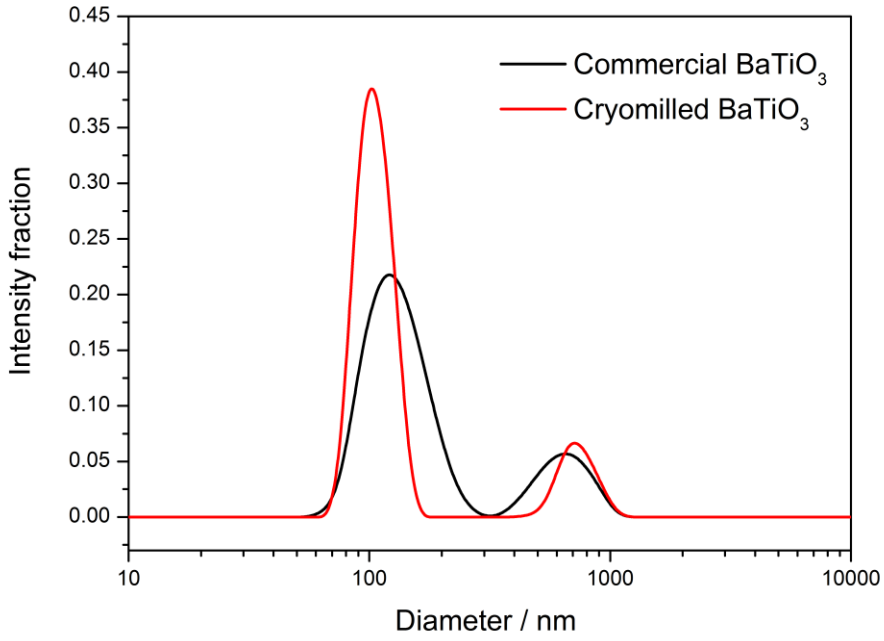

Fig. 1.2: Size distributions obtained by DLS of as received $BaTiO_3$ particles and after cryomilling.

3.2 Characterisation of the nanocomposites prepared by HEBM

Figure 1.3 shows the XRD patterns of the commercial and cryomilled EVA. The characteristic peaks of EVA with high fraction of ethylene comonomer appear at 21.3˚, 23.6˚ and 36.8˚, rising on the amorphous halo. These correspond to the orthorhombic crystal planes (110), (200) and (020). The intensity of these reflections decreases after milling, what suggests a reduction in the crystalline fraction of the EVA matrix, associated to the main ethylene part of the copolymer. This decrease is usually assigned to the change from the orthorhombic to the monoclinic phase in the ethylene fraction, represented by three peaks at 19.4˚, 21.3˚ and 27˚ respectively. Russell et al., (Russell et al. 1997) have pointed out that these changes in the crystal region cannot be obtained without a mechanical stress.

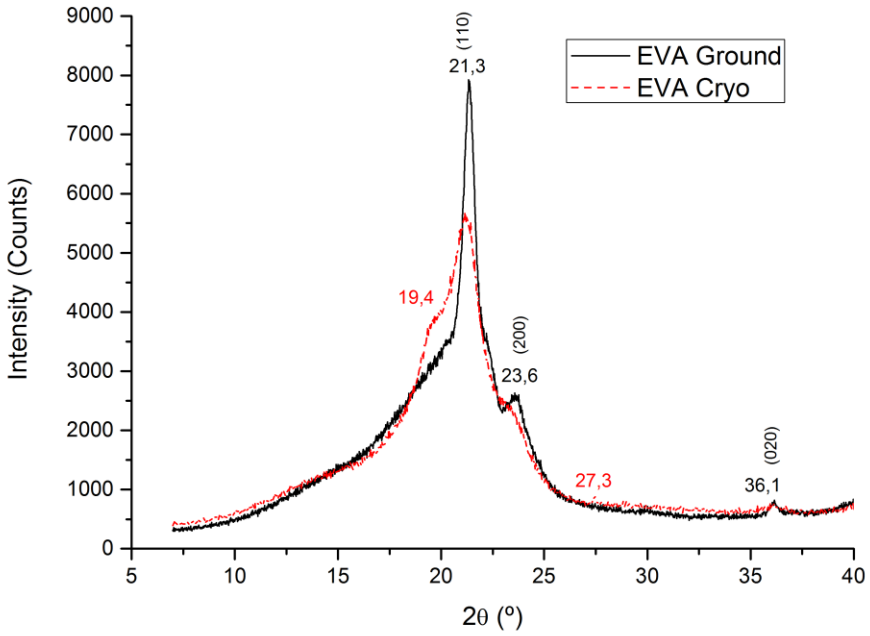

Fig. 1.3: XRD patterns of commercial and cryomilled EVA.

The X-ray diffraction patterns obtained for the samples EVA, commercial $BaTiO_3$ and cryomilled $BaTiO_3$ + EVA are shown in Figure 1.4. When comparing the diffractograms with those in Figure 1.3 it can be observed how the reduction of the crystalline fraction of EVA after cryomilling is even higher in presence of $BaTiO_3$. The higher reduction of crystallinity can be justified considering the additional mechanical stress imposed by the presence of $BaTiO_3$ particles, which do not see altered their size. On the other hand, the typical peaks of $BaTiO_3$ remain after milling with EVA (Figure 1.4), being slightly shifted to higher angles (0.5˚) and presenting a somewhat larger half peak width, which is indicative of smaller crystals (Kim et al., 1996). Finally, as seen in the inset of the Figure 1.4, the splitting of the peak at 45.5˚, representative of the $BaTiO_3$ tetragonal phase, is maintained when the particles are cryomilled with EVA. This result is really important in order to ensure the piezoelectric properties of the $BaTiO_3$ within the EVA matrix.

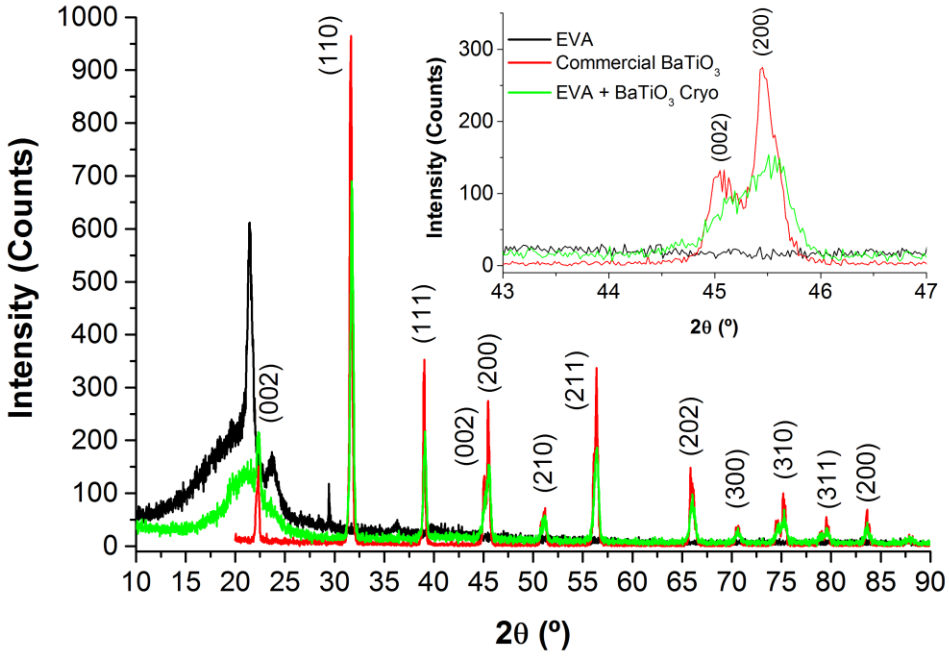

Fig. 1.4: X-ray diffractograms of EVA, commercial $BaTiO_3$, and cryomilled $BaTiO_3$ + EVA.

One of the main problems when HEBM is used is the cross-contamination from the milling tools, in this case made of stainless steel. The extent of such contamination largely depends on the milling time, the frequency and the hardness difference between the powder and the milling tools (Suryanarayana 2001; Olmos et al. 2011). In the case of a nanocomposite intended for electrical applications this undesired effect might be a drawback. Hence the milled powders have been analysed for iron by AAS, more sensible than TGA and X-ray microanalysis. The Fe content of the milled samples is given in Table 1.2.

Table 1.2: Fe content of the milled samples as determined by AAS.

Sample	HEBM	Fe (mg/kg)	wt%
EVA	RT	108.7	0.011
EVA	Cryo	30.1	0.003
EVA + $BaTiO_3$	RT	275.2	0.028
EVA + $BaTiO_3$	Cryo	128.4	0.013

In all cases the contamination is rather small, lower than 0.03 wt%. Cryomilling produces also a clearly less contamination than that attained with the milling process at room temperature (RT).

To evaluate the dispersion in EVA + $BaTiO_3$ nanocomposites, SEM images were obtained from BSE, which are sensible to the atomic mass of the elements imaged, ensuring that the domains observed are due to differences in elemental composition more than topography contrast. Brighter domains should correspond to regions with higher concentration of heavier atoms, in our case Ba and Ti arising from the particles. Figures 1.5 and 1.7 show representative SEM images of the milled samples. As can be observed in the samples of neat EVA, only contrast coming from the topography can be visualised (Figure 1.5). No contamination from the milling tools is observed, which has been confirmed with EDAX microanalysis shown in Figure 1.6, with the results of the cryomilled EVA (left) and of the EVA + $BaTiO_3$ (right). The unassigned peak corresponds to the gold coating of the samples. No differences were observed between the samples milled at room temperature (Figure 1.5 left) and that one milled under cryogenic conditions (Figure 1.5, right).

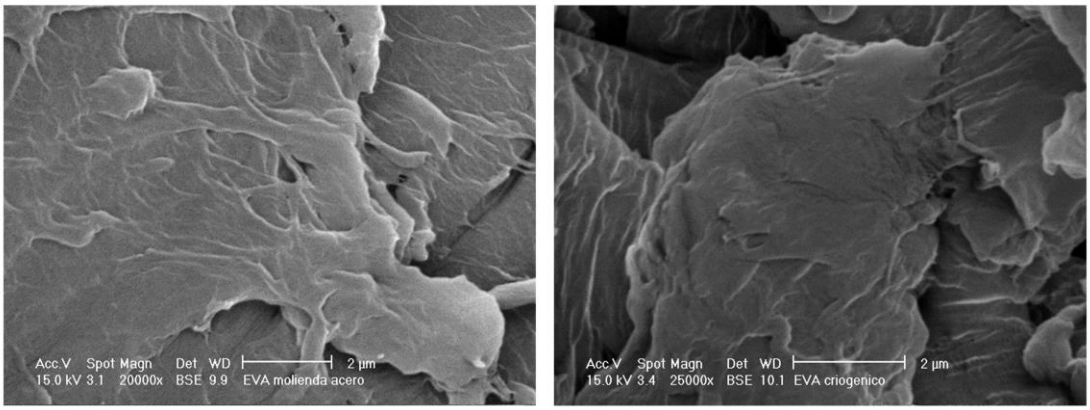

Fig. 1.5: SEM images obtained from BSE signal of EVA milled at room temperature (left) and cryogenically (right).

In addition to the topography, Figure 1.7 shows another contrast due to the presence of domains rich in Ba and Ti. This allows an easy evaluation of the dispersion of the $BaTiO_3$ particles. From a careful analysis of the images (in the inset of Figure 1.7 right, the particle size distribution has been represented) it can be observed that the sizes of the domains (246 ± 59 nm) coincide with those of the commercial $BaTiO_3$ particles determined by SEM image analysis and DLS.

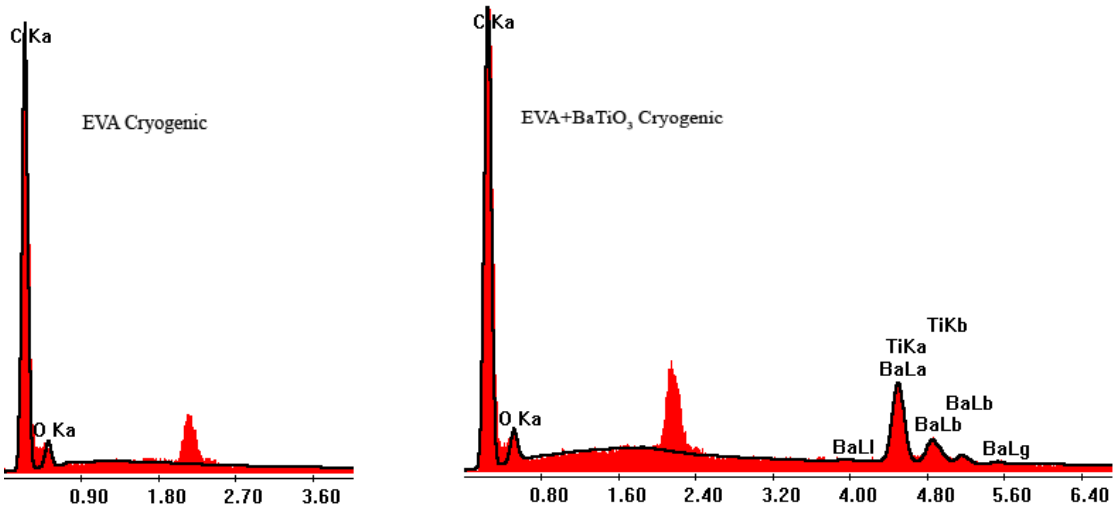

Fig. 1.6: EDAX analysis of cryomilled EVA (left) and cryomilled EVA + $BaTiO_3$ (right).

When HEBM is carried out at room temperature, low amounts of $BaTiO_3$ are observed near the surface of the milled powder (Figure 1.7, left). This suggests a non-uniform dispersion of $BaTiO_3$ particles within the EVA matrix. This is confirmed by EDAX microanalysis performed on different regions of the samples, showing different relative amounts of Ba and Ti. On the contrary, the cryo-milled sample shows large amounts of $BaTiO_3$ particles uniformly dispersed in the EVA polymer (Figure 1.7 right). Therefore, cryogenic conditions seem to be more effective to disaggregate the $BaTiO_3$ agglomerates and to adequately disperse the particles within the polymer matrix.

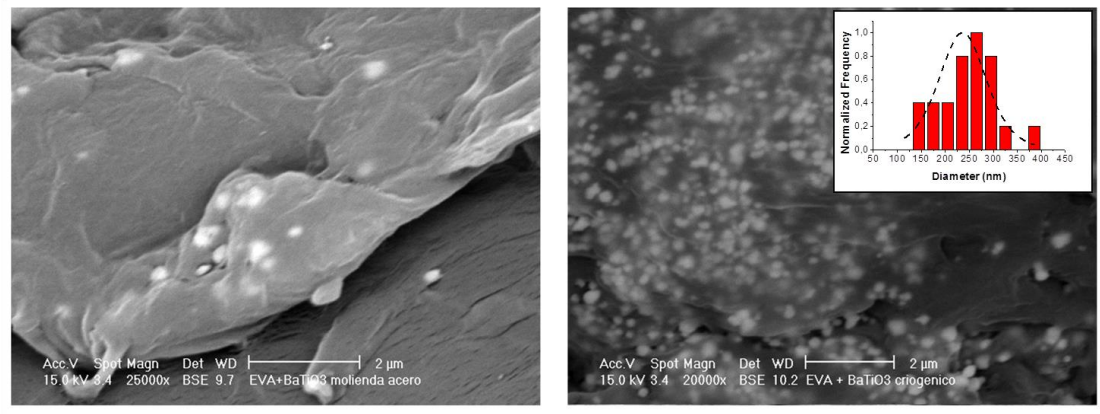

Fig. 1.7: SEM images obtained from BSE signal of EVA + BaTiO3 milled at room temperature (left) and cryogenically (right). Inset (right) represents the particle size distribution.

These materials will not be used typically in the form of powder but processed into films. Hence, SEM images have been also been taken on the film nanocomposites. Figure 1.8 shows SEM images from BSE of the films of EVA + $BaTiO_3$ milled at room temperature (left) and under cryogenic conditions (right). In both images the presence of $BaTiO_3$ particles is evidenced by the clear contrast observed in the BSE image, where the presence of Ba and Ti

elements produces brighter domains. When HEBM is carried out at room temperature the $BaTiO_3$ is not so well dispersed throughout the whole surface of observation, where a broad strip with lower concentration of $BaTiO_3$ can be seen from left to right (Figure 1.8 left). This is in accordance with what has been already observed in the milled powder at room temperature. On the contrary, the film coming from the powder sample milled under cryogenic conditions shows large amounts of $BaTiO_3$ particles uniformly dispersed in the EVA matrix (Figure 1.8 right).

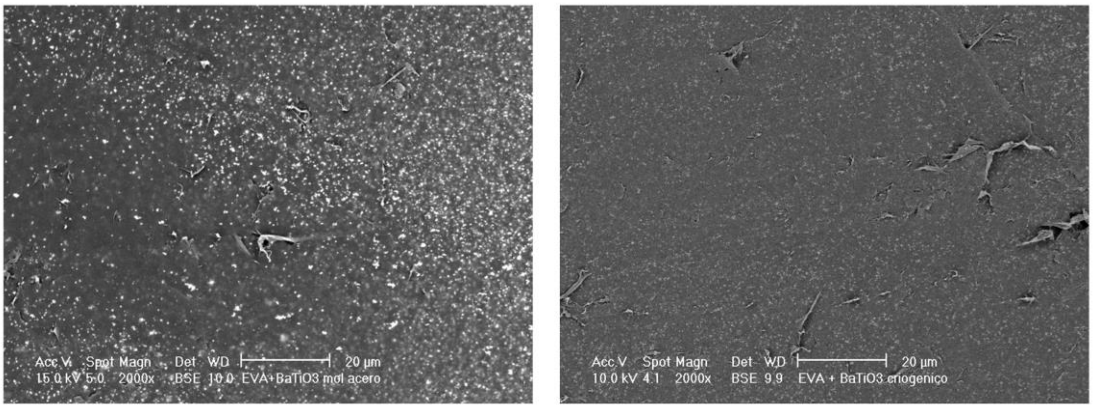

Fig. 1.8: SEM images obtained from the BSE signals of EVA + $BaTiO_3$ films milled at room temperature (left) and cryogenically (right).

Thus, uniform particle dispersion is preserved after processing the cryomilled powders by hot pressure to obtain thin films. The size of the particles agrees with that provided by the supplier and those determined initially by SEM and DLS. Figure 1.9 presents an image at higher magnification in the film obtained from the EVA+$BaTiO_3$ cryomilled powder, showing more clearly the proper dispersion of the filler.

The maximum amount of spherical particles that can be uniformly distributed within a polymer corresponds to a close-packing arrangement. For a certain amount of spherical particles uniformly dispersed within a matrix it seems reasonable to consider a similar arrangement in order to estimate the average distance between them. Taking into account this upper limit (in the case of the composite without the particles in contact with each other), for a certain volume of composite, overall composition and densities of filler and EVA, it is possible to estimate an average distance between $BaTiO_3$ particles of 600 nm.

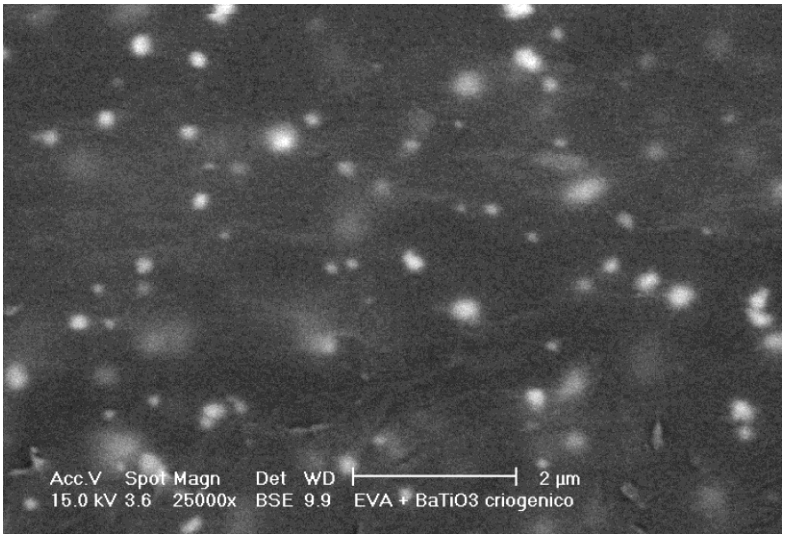

Fig. 1.9: SEM image obtained from the BSE signal of EVA + $BaTiO_3$ cryomilled films.

The analysis of the SEM image in Figure 1.9 yields an average distance between $BaTiO_3$ particles of 600 nm, matching the estimated and confirms the homogeneous dispersion of the submicrometric particles obtained using this method of processing.

Finally, in order to examine how the presence of $BaTiO_3$ affects the structure of the EVA polymer and the possible interactions between them, FTIR analysis of the powders and FTIR-ATR of the film samples has been carried out. The FTIR spectra of EVA as received, cryomilled and milled at room temperature are shown in Figure 1.10a, the most intense bands at 2915 cm^{-1} and 2855 cm^{-1} correspond respectively to the antisymmetric and symmetric stretching of the C-H bonds. The stretching of the carbonyl bond C=O from the EVA ester group can be seen at 1738 cm^{-1}, with a secondary band at 1238 cm^{-1}. The C-O stretching appears at 1020 cm^{-1}, also with a secondary band at 608 cm^{-1} that appears overlapped to the broad band of the Ti-O stretching at 559 cm^{-1}. Bending modes from the methyl and methylene groups can also be identified in the spectra at 1464 cm^{-1} and 1369 cm^{-1}. Other characteristic vibrations in the fingerprint region appear at 955 cm^{-1}, 720 cm^{-1} and 730 cm^{-1}. There are no significant differences between the spectra of the milled or neat products, in contrast with the degradation effect stated by Smith et al., when milling other polymers as poly(methyl methacrylate), polyisoprene and poly(ethylene-alt-propylene) (Smith et al. 2000). We must conclude then that the milling process does not affect to the EVA polymer structure.

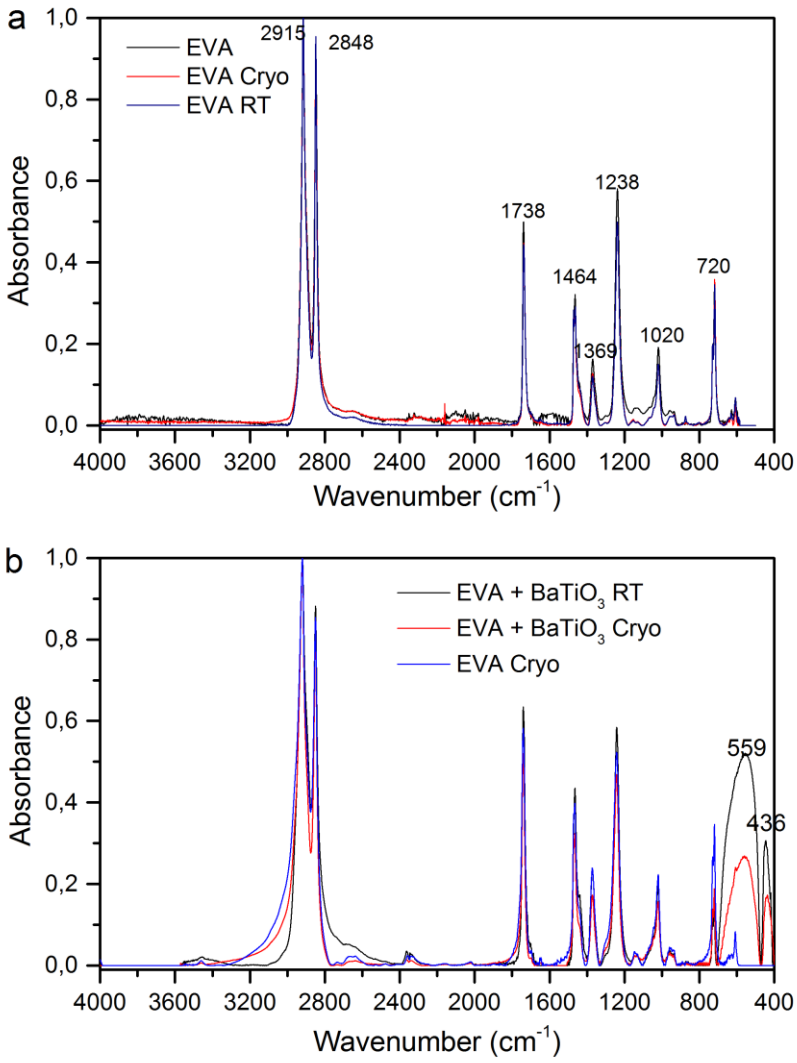

Fig. 1.10: (a) FTIR spectra of EVA: (i) as received (EVA); (ii) cryomilled (EVA Cryo); (iii) milled at room temperature (EVA RT). (b) FTIR-ATR spectra of cryomilled EVA and EVA blended with $BaTiO_3$ (under cryomilling conditions and at room temperature respectively).

The FTIR-ATR spectra of films made from cryomilled EVA and EVA blended with $BaTiO_3$ are shown in Figure 1.10b. The band associated to the carbonyl and to the ester group (1738 cm^{-1} and 1238 cm^{-1}, respectively) are the most probable candidates to interact specifically with the surface of $BaTiO_3$. However, no significant changes in the IR bands of EVA can be detected, which evidences a lack of strong interactions with the $BaTiO_3$ surface.

The thermal behaviour of the nanocomposites has also been studied. Figure 1.11 shows the thermogravimetric and differential thermogravimetric curves for all the samples

prepared: EVA before the milling (EVA), EVA cryomilled (EVA Cryo), EVA milled at room temperature (EVA RT), EVA and $BaTiO_3$ blended by cryomilling (EVA+$BaTiO_3$ Cryo), and EVA and $BaTiO_3$ blended by milling at room temperature (EVA+$BaTiO_3$ RT). The degradation process for the EVA takes place in two stages. In the first one, deacylation with the loss of acetic acid and the formation of double bonds occurs between 300 and 400 ˚C, with a maximum rate of degradation at around 370 ˚C. Radical and anionic beta-elimination mechanisms have been proposed for this reaction (Zanetti et al. 2001; Mcneill 1989; Camino et al. 2000).

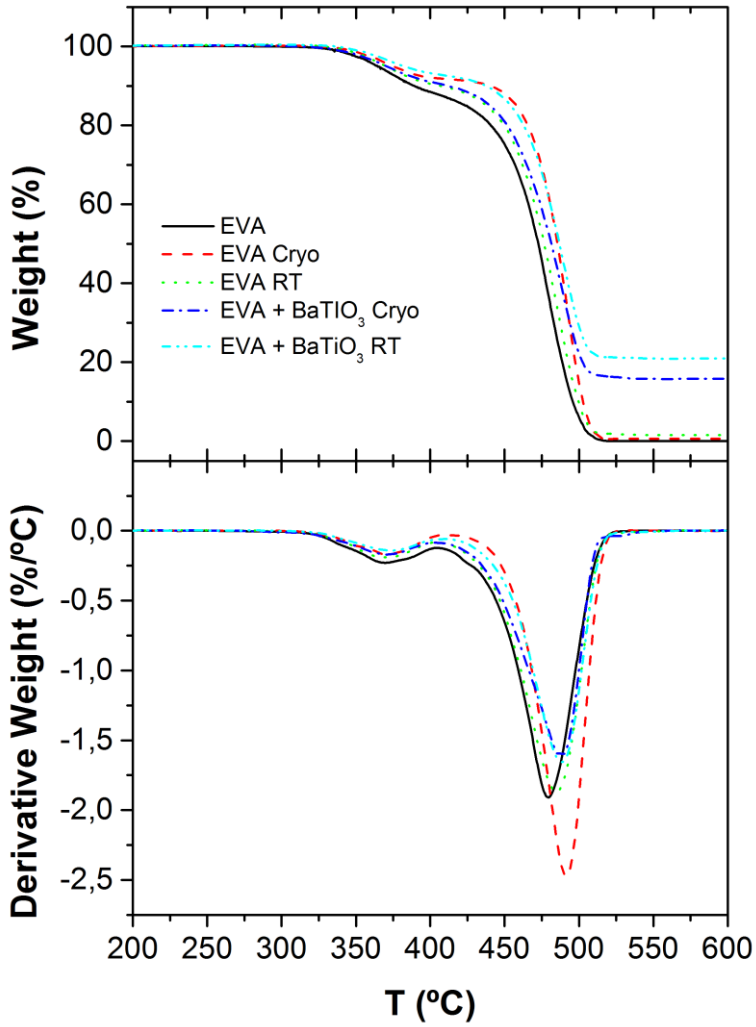

Fig. 1.11: Thermogravimetric and differential curves for powdered samples: EVA before milling (EVA), EVA cryomilled (EVA Cryo), EVA milled at room temperature (EVA RT), EVA and $BaTiO_3$ blended by cryomilling (EVA + $BaTiO_3$ Cryo), and EVA and $BaTiO_3$ blended by milling at room temperature (EVA + $BaTiO_3$ RT).

In the second step the olefinic degradation between 450 and 520 ˚C has been proposed (Zattera et al. 2005). In all cases the thermal profile is similar, which suggests that

the mechanism of thermal decomposition is not significantly altered either by the HEBM process or the introduction of $BaTiO_3$ modifies the thermal degradation in an inert atmosphere.

4. CONCLUSIONS

HEBM has been used to prepare nanocomposites based on the mixture of EVA and $BaTiO_3$ particles. The characterization of the samples as powders and films shows the lack of strong interactions between the matrix and the $BaTiO_3$, and that the cryogenic conditions are the most suitable to achieve a uniform dispersion of the nanofiller without altering the structural and morphological properties of the base materials. In this way both the processability of EVA and the tetragonal structure of $BaTiO_3$ are kept. Cryogenic milling also yields lower contamination levels of iron coming from the milling tools, lessening one of the main problems of the HEBM when used for the manufacture of nanocomposites.

5. REFERENCES

Ash, B.J., Siegel, R.W. & Schadler, L.S., 2004. Mechanical behavior of alumina/poly(methyl methacrylate) nanocomposites. Macromolecules, 37, pp.1358–1369.

Asiaie, R. et al., 1996. Characterization of submicron particles of tetragonal BaTiO3. Chemistry of Materials, 8, pp.226–234.

Baeten, F. et al., 2006. Barium titanate characterization by differential scanning calorimetry. Journal of the European Ceramic Society, 26, pp.589–592.

Benjamin, J.S., 1970. Dispersion strengthened superalloys by mechanical alloying. Metallurgical Transactions, 1, p.2943-.

Bikiaris, D.N. et al., 2005. Compatibilisation effect of PP-g-MA copolymer on iPP/SiO2 nanocomposites prepared by melt mixing. European Polymer Journal, 41, pp.1965–1978.

Camino, G. et al., 2000. Investigation of flame retardancy in EVA. Fire and Materials, 24(2), pp.85–90.

Castrillo, P.D. et al., 2007. Real dispersion of isolated fumed silica nanoparticles in highly filled PMMA prepared by high energy ball milling. Journal of Colloid and Interface Science, 308, pp.318–324.

Chaudhary, D.S. et al., 2005. Clay intercalation and influence on crystallinity of EVA-based clay nanocomposites. Thermochimica Acta, 433, pp.187–195.

Gonzalez-Benito, J. & Gonzalez-Gaitano, G., 2008. Interfacial conformations and molecular structure of PMMA in PMMA/silica nanocomposites. Effect of high-energy ball milling. Macromolecules, 41, pp.4777–4785.

He, J.P. et al., 2006. In situ preparation of poly(ethylene terephthalate)-SiO2 nanocomposites. European Polymer Journal, 42, pp.1128–1134.

Incocciati, E., Magini, M. & Padella, F., 2003. Mecanochemical process for treating plastic materials.

Kim, P. et al., 2007. Phosphonic acid-modiried barium titanate polymer nanocomposites with high permittivity and dielectric strength. Advanced Materials, 19, p.1001–+.

Lombardi, M. et al., 2011. Effect of the ceramic filler features on the properties of photopolymerized BaTiO3-acrylic composites. Polymer Composites, 32(8), pp.1304–1312.

Mcneill, I.C., 1989. Comprehensive Polymer Science and Supplements, Elsevier.

Olmos, D. et al., 2009. Crystallization and final morphology of HDPE: Effect of the high energy ball milling and the presence of TiO2 nanoparticles. Polymer, 50, pp.1732–1742.

Olmos, D. et al., 2011. Effect of the presence of silica nanoparticles in the coefficient of thermal expansion of LDPE. European Polymer Journal, 47(8), pp.1495–1502.

Padella, F. et al., 1998. Mechanically activated low temperature synthesis of Sr doped lanthanum manganite. Mechanically Alloyed, Metastable and Nanocrystalline Materials, Part 1, 269–2, pp.105–110.

Pantaleón, R. & González-Benito, J., 2010. Structure and thermostability of PMMA in PMMA/silica nanocomposites: Effect of high-energy ball milling and the amount of the nanofiller. Polymer Composites, 31(9), pp.1585–1592.

Reynaud, E. et al., 2001. Nanofillers in polymeric matrix: a study on silica reinforced PA6. Polymer, 42, pp.8759–8768.

Rowlands, S.A. et al., 1994. Destruction of toxic materials. Nature, 367, p.223.

Russell, K.E., Hunter, B.K. & Heyding, R.D., 1997. Monoclinic polyethylene revisited. Polymer, 38, pp.1409–1414.

Shaw, W.J.D., 1998. Current understanding of mechanically alloyed polymers. Mechanically Alloyed, Metastable and Nanocrystalline Materials, Part 1, 269–2, pp.19–29.

Smith, A.P. et al., 2000. High-energy mechanical milling of poly(methyl methacrylate), polyisoprene and poly(ethylene-alt-propylene). Polymer, 41(16), pp.6271–6283.

Suryanarayana, C., 2001. Mechanical alloying and milling. Progress in Materials Science, 46, pp.1–184.

Yang, M.J. & Dan, Y., 2005. Preparation and characterization of poly(methyl methacrylate)/titanium oxide composite particles. Colloid and Polymer Science, 284, pp.243–250.

Zanetti, M. et al., 2001. Synthesis and thermal behaviour of layered silicate–EVA nanocomposites. Polymer, 42(10), pp.4501–4507.

Zattera, A.J. et al., 2005. Characterization of EVA residues from the shoe industry and post-consumer urban-waste polyethylenes. Cellular Polymers, 24, pp.139–158.

Chapter 2

Rhodamine Solid Complexes as Fluorescence Probes to Monitor the Dispersion of Cyclodextrins in Polymeric Nanocomposites

Dyes and Pigments
DOI: 10.1016/j.dyepig.2012.02.009

Abstract

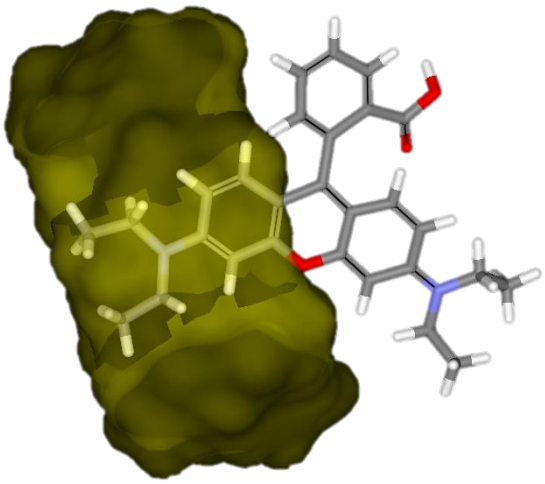

Rhodamines B and 6G (RhB and Rh6G) have been used to evaluate the dispersion of β-Cyclodextrin (β-CD) in a thermoplastic matrix, poly(ethylene-co-vinyl acetate), EVA, by high energy ball milling (HEBM). In a first stage, a study of the binding properties of β-Cyclodextrin with both fluorophores has been carried out, to determine which of them forms the most stable complex with the macrocycle, its topology and to check whether their fluorescence is kept after the milling process. Both systems have been fully characterized in solid state (FTIR and XRD, TGA and fluorescence spectroscopy), and in solution (ROESY, steady state and time-resolved fluorescence spectroscopy). Then, nanocomposites based on the thermoplastic matrix and the cyclodextrin complexes have been cryomilled and processed in the form of thin films. Only Rhodamine B forms a complex stable enough to track the nanofiller dispersion within the polymer. This labeled cyclodextrin is uniformly dispersed throughout the matrix after the milling and film forming, yielding a blue-shifted and remarkably enhanced fluorescent response when compared to the same material prepared with the simple mixture of Rhodamine B and β-Cyclodextrin without forming the complex.

1. INTRODUCTION

Polymer nanocomposites are generally built by homogeneous dispersion of a nanoscopic filler (nanofiller) into the polymeric matrix (Hussain 2006). In nanocomposites, because of the large surface to volume ratio of nanoparticles, the interphase formed between them and the polymer constitutes a greater fraction of the whole material than in common composites, even with small amounts of the nanofiller (less than 5% by weight), a feature that has important consequences on the final properties of the material (Zhao et al. 2008). Obtaining a perfectly homogeneous dispersion is critical for a nanocomposite to have the properties that are expected. However, regardless of the method used for the mixing, this issue becomes more decisive the smaller the nanofiller is. Recently, high energy ball milling (HEBM), a conventional method used for synthesis and processing of inorganic materials (Suryanarayana 2001; Padella et al. 1998; Rowlands et al. 1994), has revealed as a new way of processing thermoplastic matrix nanocomposite materials, not only due to its potential results in terms of nanoparticle dispersion, but also from an economical and clean point of view. While the mechanical action may have adverse effects of wearing on solid polymers by mechanisms of chain scission and sample oxidation, HEBM has been successfully used to obtain polymer blends with improved mechanical properties and polymer nanocomposites with a real dispersion of nanoparticles (Castrillo et al. 2007; Olmos et al. 2009; Gonzalez-Benito & Gonzalez-Gaitano 2008; Shaw 1998; Incocciati et al. 2003).

Cyclodextrins (CDs) are cyclic oligosaccharides composed of 6, 7 or 8 D-glucopyranose rings termed α, β and γ-CD respectively. Their sizes (ca. 1 nm) fall within the low limit of the nanometric scale so they can be considered as a limiting type of nanofiller. CDs are shaped like truncated cones, with a hydrophobic cavity and a hydrophilic exterior. The precise number of hydroxyl groups according to the number of glucose units makes it possible to establish strong interactions with certain polymeric matrices. CDs can also be easily modified with other functional groups that allow modulating such interactions according to the nature of the matrix, or can be grafted to common nanofillers (nanoparticles, layers…) for improving the properties of the material. The ability to form inclusion complexes with organic molecules inside the cavity, e.g. a monomer for its further polymerization (González-Gaitano & González-Benito 2008) also represents an added value to produce a material with features different from those of the single constituents of the nanocomposite. Yet, in spite of their exclusive properties the use of CDs in the field of nanocomposites is still very limited (Xu et al. 2010; Patel et al. 2008; Wu & Gao 2009).

A problem that arises when dispersing CDs in a polymer comes from the reduced size of these macrocycles, which makes it difficult to confirm that an adequate dispersion has taken place. AFM, SEM or TEM microscopy can be used to this purpose, but these are techniques which involve sample preparation processes that require a consistent amount of time and effort, more focused to a final product characterization and not convenient for regular checks. In addition to that, the electron beam can melt the matrix when thermoplastic polymers are being used.

A different approach may be to use fluorescence microscopy by previously tagging the CD by inclusion of a fluorophore in the cavity, provided it is stable enough. Rhodamine-based dyes present unique fluorescent properties and are therefore used in a wide variety of applications, ranging from applied chemistry and physics to biochemistry or microbiology (Gonzalez-Benito & Gonzalez-Gaitano 2008). Rhodamines are known to interact with βCD in different ways, depending on the state of aggregation of the fluorophore and its molecular form (Liu et al. 2001; Saenger et al. 1998), increasing or decreasing the fluorescence quantum yield as a result of their interaction. In the solid state, however, the number of investigations is limited, most of them related to the development of solid state dye lasers (O'Connell & Saito 1983; Peterson & Snavely 1968) or to the use of CD-based resins to adsorb organic dyes (Crini 2008).

In this work we propose the use of the fluorescent properties of Rhodamine B and Rhodamine 6G (RhB and Rh6G), (Figures 2.1a and 2.1b) and their ability to form complexes with βCD (Figure 2.1c), to produce a solid complex that acts as a fluorescent probe to evaluate the dispersion of these oligosaccharides into a thin-film polymeric nanocomposite material prepared by HEBM. The polymeric matrix used here is ethylene vinyl acetate (EVA), a thermoplastic polymer with polar vinyl acetate groups and crystalline ethylene domains. EVA copolymers are a good choice to combine with these fluorophores, as they present optical homogeneity and organic dyes usually show good compatibility with polymeric matrices. In addition, their easy processability makes them excellent for miniaturization and to be included in other composite systems (Arbeloa et al. 1997).

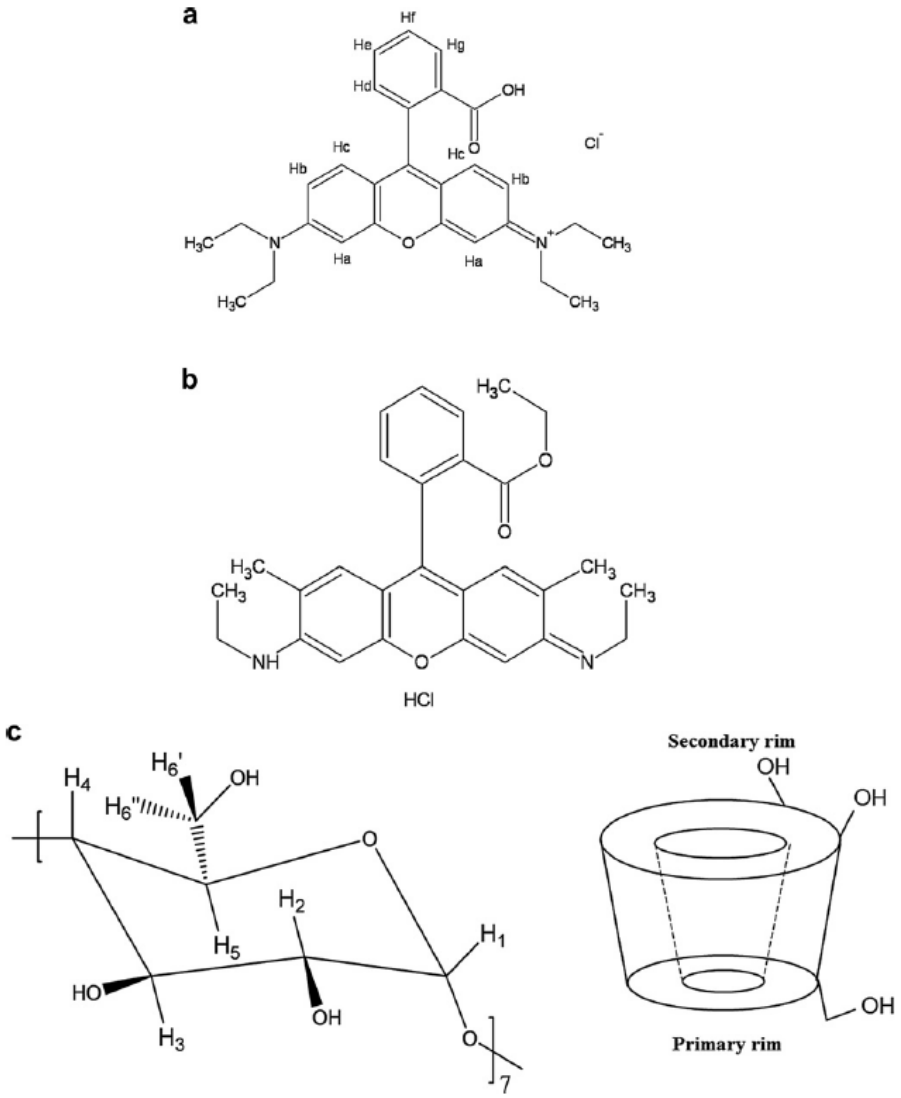

Fig. 2.1: a) Rhodamine B; b) Rhodamine 6G; c) Scheme of β-Cyclodextrin.

In this research we have focused on the dispersion of the macrocycle as the nanofiller in the polymer, leaving the grafting of the βCD to nanoparticles and further nanocomposite synthesis for future projects. The first step is to evaluate that the complexes between the fluorophore and the CD do form and are stable enough to endure the HEBM process, that they have a different fluorescent response when attached to the βCD compared to the free form and that they can be dispersed homogenously, so they can be used as dispersion fluorescence probes in nanomaterials. For this purpose the systems have been previously studied in solution to characterize their complex formation characteristics (stability, temperature dependence, stoichiometry and topology) and the fluorescent emission. Finally, the solid state products are tested and combined with the polymer using the HEBM method, to verify their adequate dispersion and whether their properties are retained along the nanocomposite processing.

2. MATERIALS AND METHODS

2.1 Materials

Rhodamine B 99% pure (Basic Violet 10; C.I. 45170; 9-(2-Carboxyphenyl)-3,6-bis(diethylamino)xanthylium chloride) and Rhodamine 6G 99% pure (Basic Red 1, C.I. 45160, ethyl 2-(6-(ethylamino)-3-(ethylimino)-2,7-dimethyl-3H-xanthen-9-yl)benzoate monohydrochloride) were purchased from Acros Organics. β-Cyclodextrin was bought from Wacker Chemicals (Cavamax Pharma, 99.5% pure). Polyethylene-co-vinyl acetate (composition 12 wt% in vinyl acetate, density 0.933 g/cm^3 at 25 ˚C, Vicat temperature ASTM D 1525 of 65 ˚C and melting point of 95 ˚C), was supplied by Sigma Aldrich.

2.2 Sample Preparation

RhB:βCD complex was prepared by mixing a RhB 2.5x10^{-3} M aqueous solution with βCD at an equimolar ratio followed by stirring for 10 minutes, poured into a crystallizer and placed in the stove at 70 ˚C until solvent evaporation. The resulting solid is a dark red flaked product. The physical mixture of RhB and βCD was prepared by weighing the same amounts used for the complex preparation and mixing them in a vortex shaker, resulting in a greenish powder mixture. The same procedure was carried out with Rh6G. In this case the solid mixture and the compound prepared by crystallization did not show any visual differences.

A mixture of 5 wt% of RhB:βCD and EVA was subjected to HEBM under cryogenic conditions (cryomilling) in a MM400 RETSCH miller. Stainless steel milling tools (a vessel of 50 mL of capacity and one ball of 20 mm diameter) were used. The process was carried according to the following protocol: 1 hour of active cryomilling divided into 12 cycles of 5 minutes of milling at 25 Hz and 15 minutes of resting in liquid nitrogen. Another vessel endured the same procedure with the physical mixture of RhB and βCD and the EVA at the same proportions (95 wt% of EVA).

Thin films were prepared by hot pressing. The powder obtained from the milling processes was deposited between two Teflon plates and then pressed and heated in an oven at 150 ˚C for 20 min. After that, the prefilms obtained were cooled inside the oven down to 40 ˚C. A small portion of the prefilm (about 9 mm^2) was then sandwiched between the two Teflon plates and clamped within two stainless steel plates, introduced in a preheated oven at 150 ˚C and heated for 120 min. The film was slowly cooled down inside the oven to room temperature, thus avoiding any thermal stress in the sample.

2.3 Characterization Techniques

The crystalline structure of materials under study was characterised by X-ray diffraction, XRD, on randomly oriented powder preparations using a Bruker D8 Advance diffractometer with a X Kristalloflex K760 X-Rays generator, with a copper anode emitting typical X radiation $K_{\alpha 1}$=1.5417 Å at 40 kV and 30 mA. Diffraction angles were monitored from 2θ = 2˚ to 40˚ at a rate of 3 s/step (0.02˚ in 2θ). Analysis of the XRD patterns was carried out with XRD Wizard 2.4.11 software (Bruker GmbH). FTIR-ATR analyses of powder and films were performed with a FTIR-ATR Nicolette Avatar 360, using a resolution of 2 cm^{-1} and averaging 32 scans. Spectral analysis treatment was undertaken with the OMNIC E.S.P. v5.1 software (Nicolet). Thermogravimetric analysis, TGA, was carried out in a TGA-SDTA 851 Mettler Toledo. Samples were subjected to a heating program from 25 ˚C to 600 ˚C at a heating rate of 10 ˚C/min under a N_2 atmosphere.

Fluorescence studies were undertaken using an Edinburgh Instruments FLS920 spectrofluorimeter equipped with a 450 W Xenon arc lamp. Samples were excited at 553 nm and the emission recorded from 560 to 750nm under constant stirring, averaging 5 scans with a 1 nm step and 0.1 s dwell time. Excitation and emission slits were 2 nm and 3 nm, respectively. Measurements in solution were carried out at 15 ˚C, 25 ˚C, 35 ˚C and 45 ˚C in a 10 mm path length quartz cuvettes controlled by a Lauda Ecoline RE104 thermostat. Each isotherm was repeated three times. For the solid samples the powder or a portion of the film was sandwiched between two quartz glasses in the instrument sample holder. Fluorescence lifetimes were measured with the same equipment using as the radiation source a PDL800-B Picoquant pulse diode driver and 455 nm and 500 nm diodes, with full width at half maximum (FWHM) of 1600 and 1700 ps, respectively. The instrument response was measured by using a Ludox 30% aqueous suspension, purchased from Aldrich. Data treatment of the lifetime measurements were performed with Fast v1.8.1 software (Edinburgh). The films were observed with an Olympus CH40 fluorescence microscope equipped with a ColorView camera (Soft Imaging Systems).

NMR experiments were performed in in a Bruker Avance 700 Ultrashield (700 MHz). The samples were prepared in D_2O (99.9% in deuterium purchased from Sigma Aldrich), with no buffers added, using the HDO signal as the reference. Monodimensional experiments were done by averaging 256 scan. ROESY experiments were carried out on 32 scans with presaturation of the solvent signal (Hwang et al,. 1995) by using the pulse sequence described in the literature (Bax & Davis 1985), with an optimal mixing time of 600ms. Temperature was set to 25 ˚C in all cases.

3. RESULTS AND DISCUSSION

3.1 Complexes in solution: stoichiometry, stability and structure

As a first stage, the complexes between rhodamines and βCD have been investigated. The analysis of the chemical shifts of the ^{1}H-NMR signals of the complex in relation to the signals from the pure RhB and βCD (Table 2.1 and Figures 2.2 and 2.3) are the main indication of the extent of the complex formation. For the β-CD, the protons undergoing the most important changes are the H_6 and H_5, i.e., those located at the mid-bottom inner side of the cavity and at the narrower rim of the macrocycle, respectively. Less significant changes were noted for the inner H_3, at the mid-upper part of the CD. Finally, tiny shifts are detected in the outer protons H_1, H_2 and H_4. All these resonances, except the H_4, shift upfield. If we consider now the guest molecule, RhB, the protons of the substituents CH_3- and CH_2- (downfield) and the H_D (upfield) experience the larger shifts.

Table 2.1: Changes in the chemical shifts of protons of β-CD and RhB.

H	Free δ(ppm)	Δδ(ppm)
β-Cyclodextrin		
H_1	4.949	0.039
H_2	3.541	0.006
H_3	3.856	0.074
H_4	3.478	-0.015
H_5	3.748	0.155
H_6	3.769	0.101
Rhodamine B		
H_{CH3}	1.115	-0.059
H_{CH2}	3.455	-0.079
H_A	6.624	-0.028
H_{B1}	6.772	-0.019
H_{B2}	6.786	-0.018
H_C	7.100	-0.013
H_D	7.313	0.068
H_E	7.608	-0.013
H_F	7.608	-0.013
H_G	7.834	-0.008

These results prove unambiguously the inclusion of the RhB in the CD, which involves the ethyl amino groups (Bernini et al. 2004).

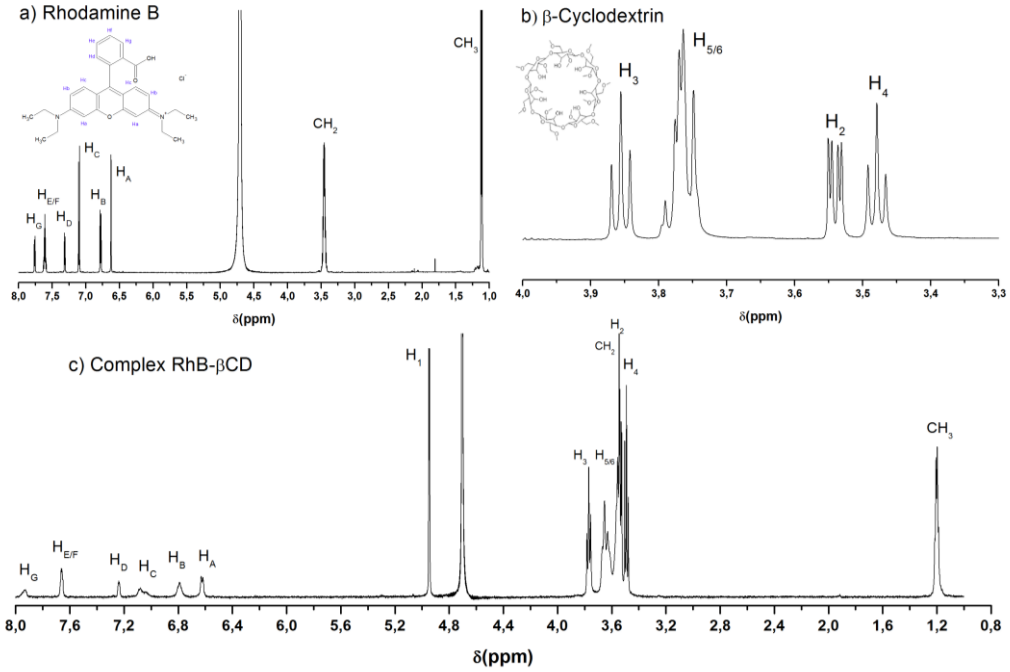

Fig. 2.2: ^{1}H RMN spectra in D_2O of a) Rhodamine B, b) β-Cyclodextrin and the c) complex RhB-βCD at a molar ratio 1:1.

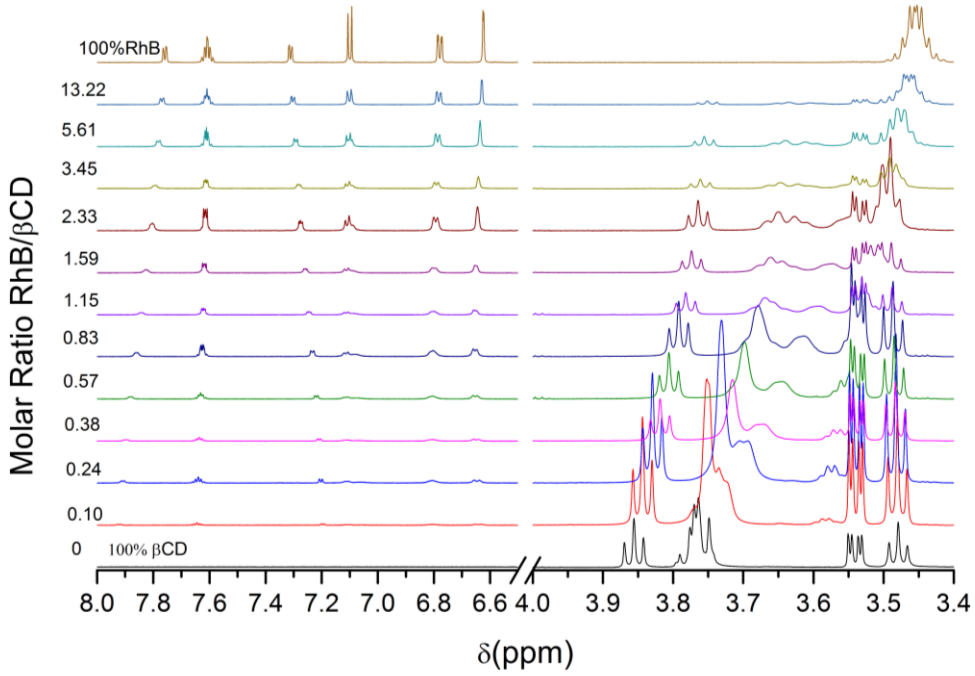

Fig. 2.3: ^{1}H RMN Chemical Shifts of different molar ratios RhB and β-CD. Concentrations of β-CD and RhB are in the range from 0 to $5x10^{-4}$ M.

^{1}H ROESY experiments can provide more detailed information about the inclusion mode through the intensity of the cross-peaks in the 2D spectrum, related to the closeness between protons of host and guest molecules.

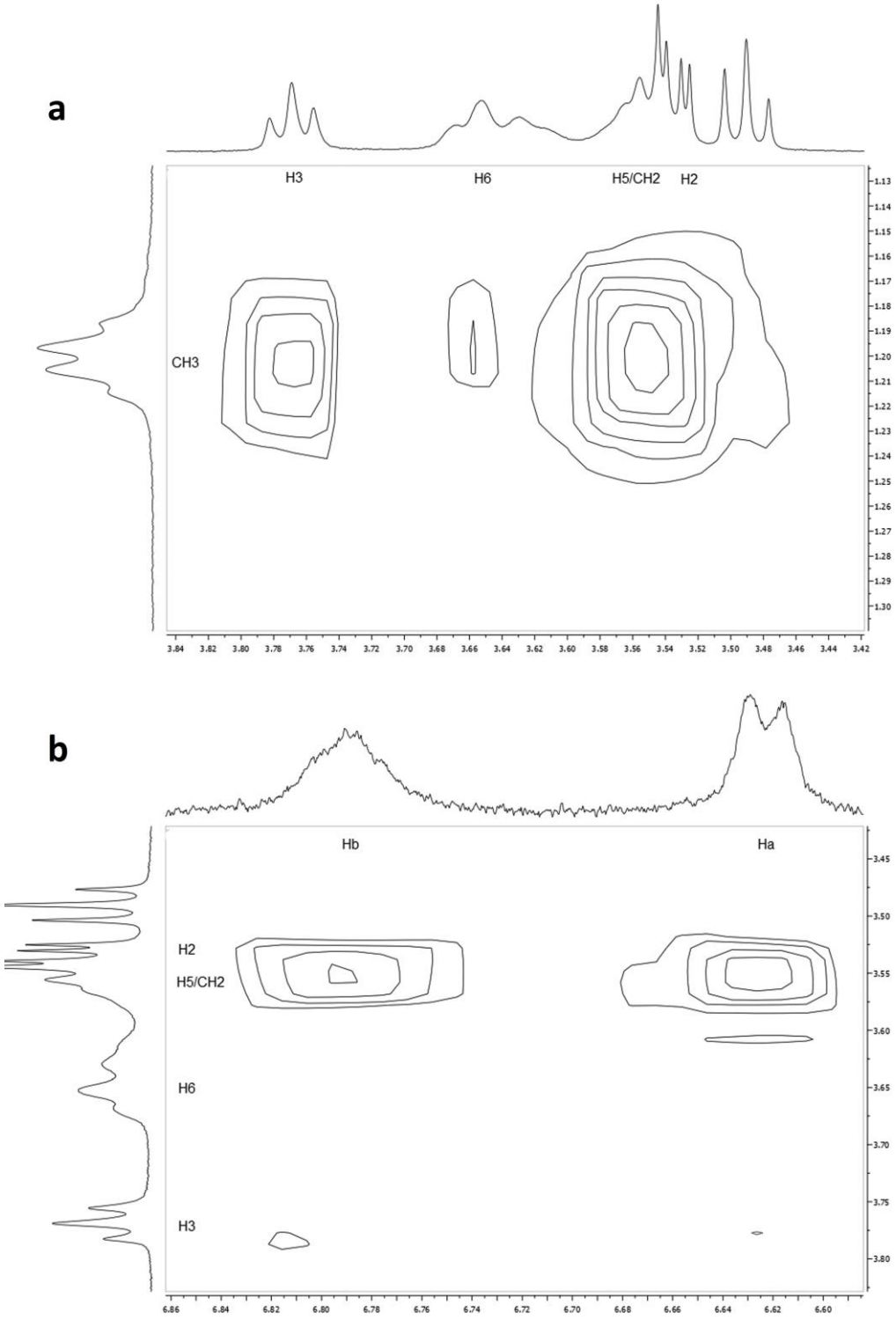

Fig. 2.4: Zoomed view of the ROESY spectrum of RhB:βCD (1:1).

Figure 2.4 shows expanded views of the correlation between the aromatic region of RhB with the CD and the methyl and methylene groups of the guest with the CD. Strong ROE cross-peaks arise between the H_3 and H_5 of the CD (3.76 ppm and 3.52 ppm) with the CH_3 group of the RhB, that of H_3 being the most intense. This double interaction of the CH_3 with both H_3 and H_5 at the wide and narrow borders of the βCD respectively, implies that RhB is entering the cavity by the secondary hydroxyl rim. At 6.61 ppm and 6.77 ppm two more interactions arise, corresponding to the H_a and H_b from the RhB xanthene rings with the H_6 and H_5 of the βCD. The intermolecular interaction with the CH_2- can be ruled out, as there are no cross-peaks in the spectrum for the RhB. Finally, the intramolecular interactions of the RhB H_a and H_b with the CH_3 can be detected at 6.63 ppm and 6.77 ppm. As the -CH_3 undergoes changes, it is reasonable to think that the -CH_2 will experience them too; unfortunately these cannot be clearly observed as the -CH_2 signal (around 3.50 ppm) overlaps with those of the H_2 and H_4 so it has not been possible to track the signal through the experiments.

The fact that the interaction is taking place, not in the central carboxyphenyl ring, but in one of the diaminoethyl groups, opens the possibility of a 2:1 complex, i.e. two CDs per guest, and not the 1:1 expected. Job's continuous variation analysis (Job, 1928) has been used to determine the actual stoichiometry. For this purpose samples at different molar ratios prepared with βCD and RhB concentrations ranging from 0 to $5x10^{-4}$ M were prepared in D_2O and analyzed by ^1H NMR spectroscopy.

The Job plot for protons H_3, H_2 of βCD and CH_3, H_G and H_D of RhB are shown in Figure 2.5, thus a proton from inside the βCD cavity and one from outside can be seen. The maximum change in the chemical shift takes place when the molar ratio is 0.5, inferring that the stoichiometry of the complex is 1:1.

As seen in Table 1, the protons of the carboxyphenyl ring also shift, although no NOE signals are detected. A possible explanation to the fact the stoichiometry sticks to 1:1 when having two diaminoethyl groups in the molecule, is that when the βCD approaches one of the diaminoethyl branches, it might induce the movement of the carboxyphenyl ring to the opposite side, as seen by the shift in H_D, and thus the molecule is not receptive to dock with another βCD molecule in the other ring because of steric effects. Those same experiments were performed on the Rh6G-βCD system, but neither significant changes in the chemical shifts nor cross peaks in the ROESY spectrum were detected. These results confirm that only RhB forms a suitable stable inclusion complex with a 1:1 stoichiometry, where the βCD enters the RhB by one of its diethylamine sides.

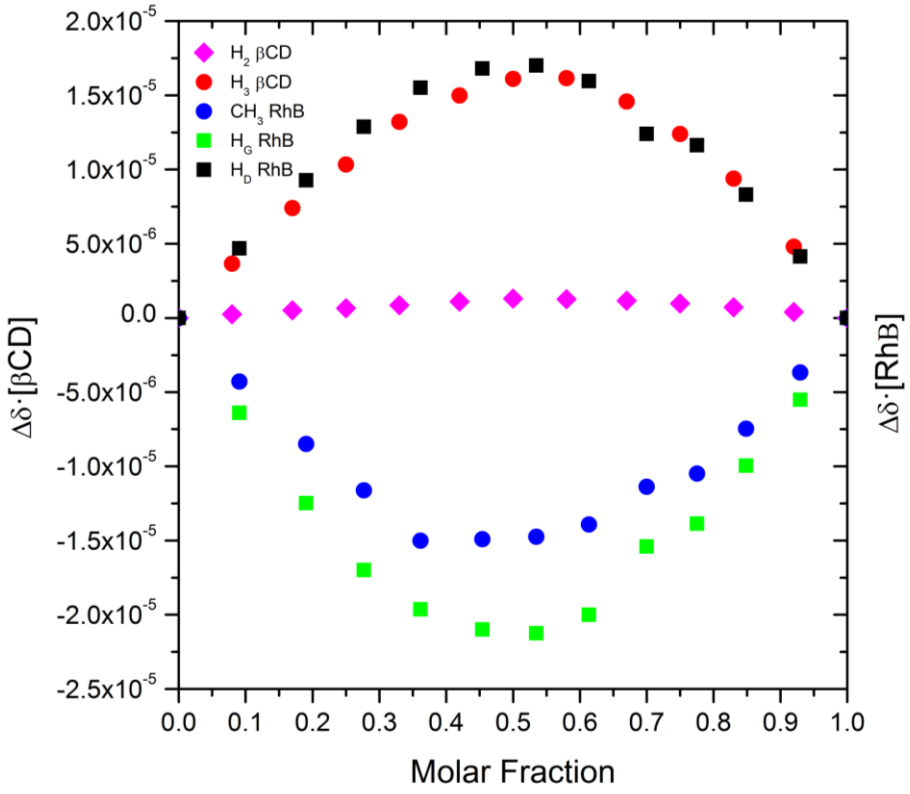

Fig. 2.5: Job's Plot for the H_3 and H_2 (βCD) and CH_3, H_D and H_G (RhB) signals.

Fluorescence emission can be used to gather precise information about the stability of the association. RhB presents a high fluorescence quantum yield, but it easily aggregates forming dimers and other species, especially in aqueous solution (Mchedlov-Petrosyan & Kholin 2004). This process manifests as a quenching in the emission attributed to the long range dipole-dipole energy transfer from the monomer excited state to the aggregates (Saenger et al. 1998) and also in bathochromic shifts from 587 nm to 650 nm in 10^{-3} M RhB solutions. Rhodamines and βCD may interact in different ways depending on the fluorophore concentration and its aggregation state. Thus, in dilute solutions of RhB, the βCD causes a decrease in emission due to the formation of the complex, less fluorescent than the free RhB. However, in conditions at which RhB is in the form of aggregates and its fluorescence quenched, the addition of βCD produces the opposite effect, yielding a fluorescent enhancement (Degani et al. 1984). On the other hand, Rh6G does not aggregate as easily as the RhB (Politzer et al. 1989), because of the bulkiness of the ester group in the phenyl ring and the methyl and ethyl substituents, which hinder the molecule stacking. Consequently, the presence of βCD enhances the emission in the case of Rh6G in aqueous solution.

The effect of successive additions of βCD to RhB $8x10^{-6}$ M is shown in Figure 3.6. Free RhB has its maximum fluorescent emission at 582 nm, and experiences a slight blue shift of ca. 4 nm when βCD is added, along with a quenching in its fluorescence. Under our instrumental conditions, the linear response of the fluorescence for the RhB ranges up to $8x10^{-6}$ M, free of aggregation effects.

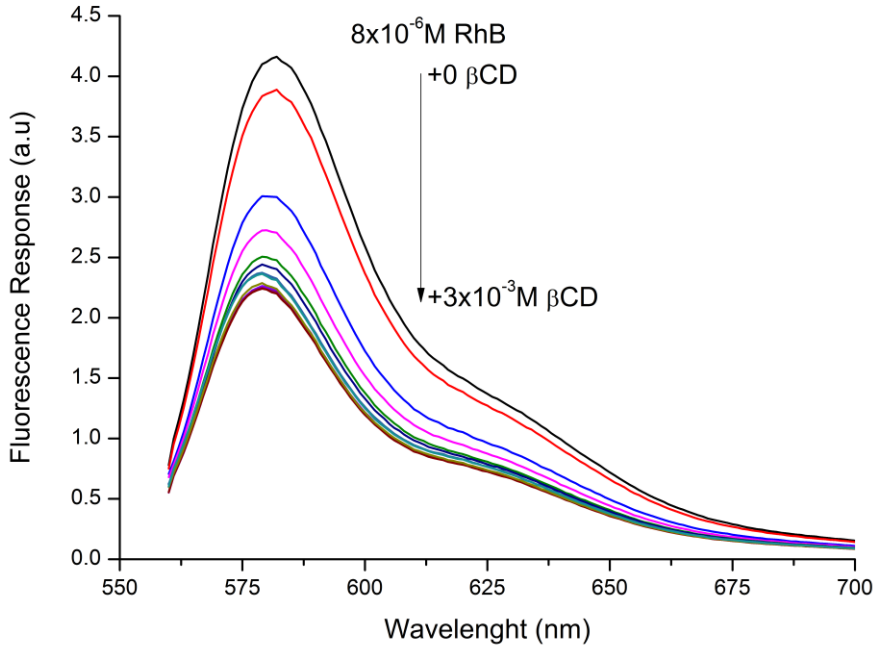

Fig. 2.6: Effect of the βCD successive additions on the fluorescence emission of a $8x10^{-6}$M RhB solution.

As the stoichiometry for the βCD complex is 1:1, its formation constant at a certain temperature can be expressed by the action mass law as:

$$[1] \qquad K = \frac{[R:CD]}{[R][CD]}$$

being *R* the free fluorophore, *CD* the free βCD and *R:CD* the complex. In the experiments, the concentration of *R* is kept constant, varying that of *CD*. By combining the action mass law with the concentration mass balance for host and guest we get for [*R*] the following quadratic equation:

$$[2] \qquad [R]^2 + \left(CD_0 - R_0 + \frac{1}{K}\right)\left[R - \frac{R_0}{K}\right] = 0$$

The measured fluorescence at a certain wavelength, F_λ, is the result of the contributions of the two fluorescent species, *R* and *R:CD*, so thus:

$$[3] \qquad F_\lambda = F_\lambda^R + F_\lambda^{R:CD} = a_\lambda [R] + b_\lambda [R:CD]$$

where a_λ and b_λ are constants related to the fluorescence quantum yield and molar absorptivity of each fluorescent species at the excitation wavelength, λ, and to experimental conditions (source intensity, slit width and path-length of the cell).

Dividing the above expression by $F_0 = a_\lambda R_0$, i.e., the fluorescence in the absence of cyclodextrin, eq. 3 can be written as:

$$[4] \qquad \left(\frac{F}{F_0}\right)_\lambda = \frac{[R]}{[R_0]} + \varphi \frac{[R:CD]}{R_0}$$

Where $\phi = b_\lambda / a_\lambda$. The experimental data at a certain emission wavelength can thus be fitted by a non-linear least-squares procedure to the above equation, in which ø and *K* are left as adjustable parameters. It is possible to improve the fitting using a wider set of data by taking into account the emission measured at each wavelength, and not only at λ_{max}. A multivariable analysis can be performed by imposing the condition that the binding constants are the same for each wavelength. The error function to be minimized becomes

$$[5] \qquad E = \sum_\lambda \sum_i \left(\left(F_i / F_{0,\lambda} \right)^{cal} - \left(F_i / F_{0,\lambda} \right)^{meas} \right)^2$$

Where *i* sums over all the concentrations of CD and λ over all the wavelength range. The input parameter is a vector that contains the initial guess for the binding constants and ϕ_i, and the output is the estimation of the parameters with their error bounds, defined as the confidence intervals corresponding to a significance level α=0.16. A weight factor, ω_λ, taken as the absolute value of the difference between $F_{0,\lambda}$, and the maximum value reached in the binding, is introduced at each wavelength in Eq (5), to give a higher statistical weight to those λ's at which the changes in intensity are higher (Sainz-Rozas et al. 2005). The enthalpy and the entropy obtained from the *K* dependence on the temperature through Van't Hoff equation and a weighted least-square method (Table 2.2).

Table 2.2. Binding constants for the complex βCD:RhB ([RhB]=8x10^{-6}M).

	15˚C	**25 ˚C**	**35 ˚C**	**45 ˚C**	**Δ*H*** **(kJ·mol^{-1})**	**Δ*S*** **(J·mol^{-1}·K^{-1})**
K·10^{-3}L·mol^{l-1}	5.1±0.5	4.8±0.2	4.1±0.2	3.1±0.2	-15±3	21±10

The binding constants of RhB in water are relatively high, which indicates a stable association. The increasing temperature produces the diminution of *K*, as expected in an exothermic process. This same trend has been obtained by measuring at lower concentrations of RhB (data not shown). This stability with the temperature is important, considering that the formation of the nanocomposites requires conditions that, depending on the type of polymer, must be higher than 120 ˚C. As for the Rh6G:βCD system, it barely experiences changes in the emission by adding CD, resulting in the non-convergence of the fitting towards very low constants. This is a confirmation that there is no significant complex formation, in accordance with NMR data. It is worth to mention that the enthalpy is not too high for these types of complexes, being the process controlled mainly by the entropy. According to ROESY data and considering the bulkiness of RhB and the size of the cavity, the inclusion is shallow and only part of the guest is included. Although the association constant is in good agreement with the one stated by Liu et al. (Liu et al. 2001), the enthalpy and entropy values are considerably different, as they obtain a non-expected positive ΔH=40.8 $kJ \cdot mol^{-1}$ and ΔS=0.21 $kJ \cdot mol^{-1}K^{-1}$ at 25 ˚C. These unusual values are reasoned in terms of the extra desolvation due to the lactonization of the hydrated benzoate moiety at the conditions of the experiment. It must be noticed that the constants obtained by this method are apparent constants, as the equilibrium between the cationic, lactone and zwitterionic form exists. However, as stated by Mchedlov-Petrosyan et al. (Mchedlov-Petrossyan et al. 2003) the fraction of the RhB molecules converting to the colorless lactone form in water at our concentration is less than 1%, so in our case we can rule out the lactonization effect mentioned before as being responsible for the different values. The use of a phosphate buffer 0.1 M to maintain the pH at 7.20 may be one of the reasons for this difference, as the ionic strength of the solution with this precise buffer is considerable and it is well known the quenching effect of some buffers on the fluorescence of rhodamines (Schulman, 1976). In our case, the pH has not been controlled by addition of buffers and the low concentration of RhB makes the ionic strength virtually zero.

In order to check the state of aggregation of the RhB at different concentrations and the effect the CD may have, fluorescence lifetime analyses were carried out upon these samples. In the experiments, RhB concentration was fixed at $1x10^{-4}$ M, $1x10^{-5}$ M and $1x10^{-6}$ M, and aliquots of a $5x10^{-3}$ M βCD stock solution were added to gradually increase the βCD concentration and induce the complex formation. The decay curves were processed by reconvolution distribution analysis at 200 intervals between 0 and 50 ns. Free RhB has a

lifetime response around 1.7±0.2 ns (Figure 2.7), which correlates with the values found in the literature, 1.52 ns with emission at 400 nm and 1.68 ns at 560 nm (Magde et al. 1999). Upon addition of βCD, a new mode appears with fluorescence lifetime of around 0.75±0.04 ns, which is retained upon successive additions (Figure 2.7), its fraction increasing with the βCD concentration, accordingly to the shift of the equilibrium. When RhB $1x10^{-4}$ M is tested at 500 nm in the absence of βCD, a considerable fraction appears at approximately the same lifetime than the complex 0.97±0.03 ns, which is attributable to the RhB aggregation effect at high concentrations. When the concentration of RhB is low, from $1x10^{-5}$ M to $1x10^{-7}$ M, and βCD is absent, this fraction does not appear in the system and that corresponding to the free RhB is close to 100%. These results indicate the aggregation limit is within 10^{-4} M and 10^{-5} M for aqueous solutions, in good agreement with the literature values (Ferreira & Costa 2005).

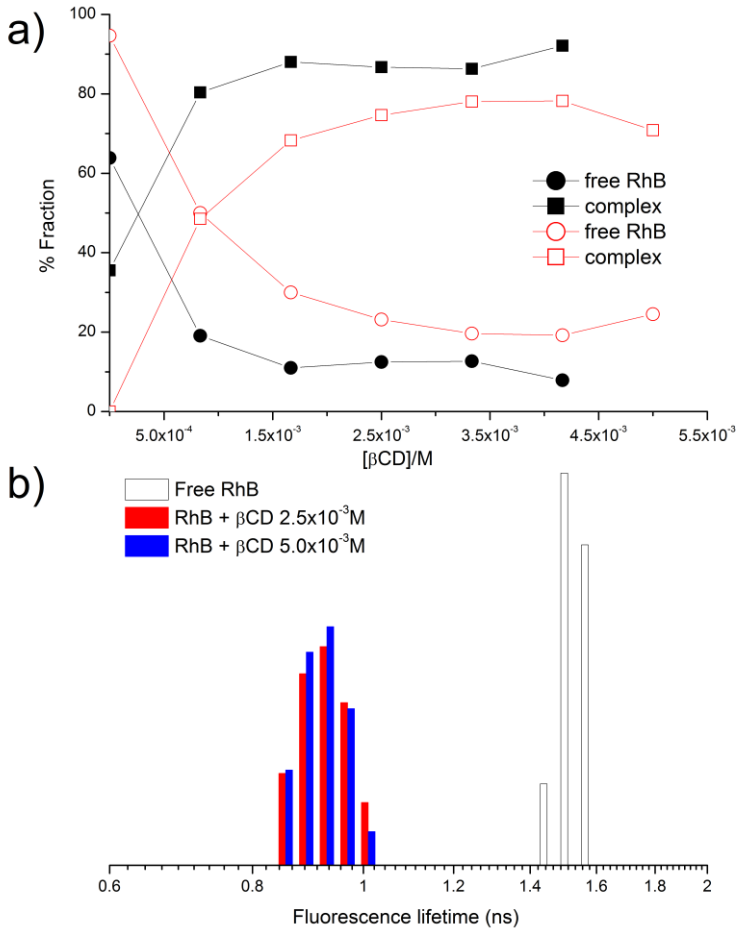

Fig. 2.7: Lifetime analysis: a) Fraction of the species found on $1x10^{-4}$ M and $1x10^{-5}$ M of RhB upon addition of βCD; b) Lifetime distribution of the species.

3.2 Solid complexes

The thermogravimetric analysis of the powder samples (Figure 2.8) shows how the RhB presents at least a three-step decomposition process, starting around 180 ˚C and ending at 500 ˚C, and so does the physical mixture RhB-βCD. However, as confirmed by the first derivative trace, once the RhB:βCD complex is formed the decomposition process changes to a single step process, confirming that the inclusion yields a product with a different thermal behavior. This difference can be seen by the absence of the first minimum around 180 ˚C and the shift of the degradation temperature to 257 ˚C. When the same analysis is carried out with the Rh6G, only a slight shift in the temperature can be seen, but there is no evidence concerning the formation of a different product.

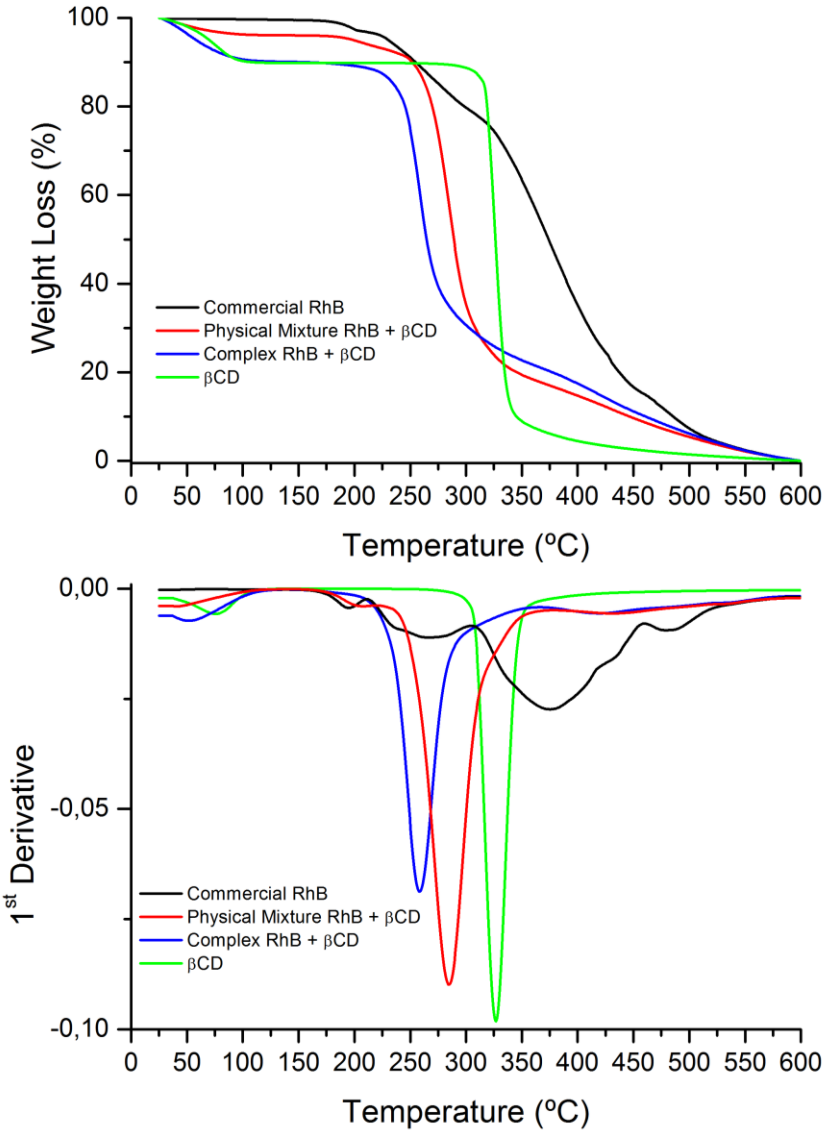

Fig. 2.8: TGA curves (top) and 1st derivative (bottom) of the RhB samples.

Confirming the results revealed above, FTIR-ATR analysis of the compounds shows that the RhB-βCD system presents important differences in the spectra compared to the physical mixture, whereas the Rh6B-βCD cannot be distinguished from the mixture. The strong band at 1587 cm^{-1} of RhB is assigned to the aromatic ring C-C vibrations and remains when forming the complex (data not shown). The rest of the RhB bands in the aromatic region persist in the complex, while in the physical mixture they lose shape and are hidden in the baseline. Taking into account that the solid complex is formed from the aqueous solution, and with the previous data confirming that the Rh6G does not form complex with the βCD, we must conclude that the precipitate will be a bare physical mixture of both components.

X-Ray diffraction patterns (Figure 2.9) corroborate the above feature. The analysis shows a decrease in the crystallinity, as seen by the absence of peaks and the amorphous

halo when the complex is formed in comparison to the commercial RhB and the physical mixture. The latter itself matches the sum of the RhB and the βCD diffractograms. As expected, Rh6G shows no evidence of complex formation.

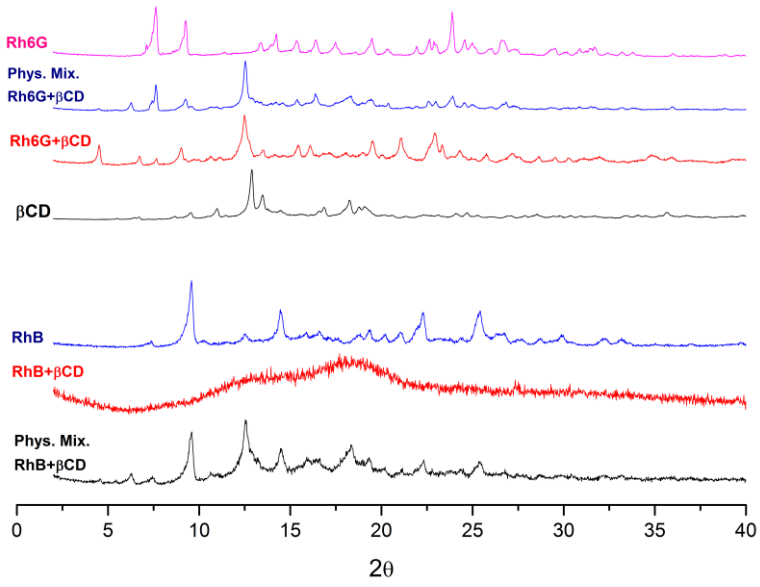

Fig. 2.9: X-Ray diffractograms of the solid samples.

Finally, solid state fluorescence measurements were also recorded on the commercial RhB, the physical mixture RhB-βCD and the RhB:βCD complex. The emission spectra show a 20 nm blue-shift upon complex formation. Commercial RhB shows an emission band at 690 nm, and the complex at 670 nm. The physical mixture behaves exactly like the commercial RhB (Figure 2.10).

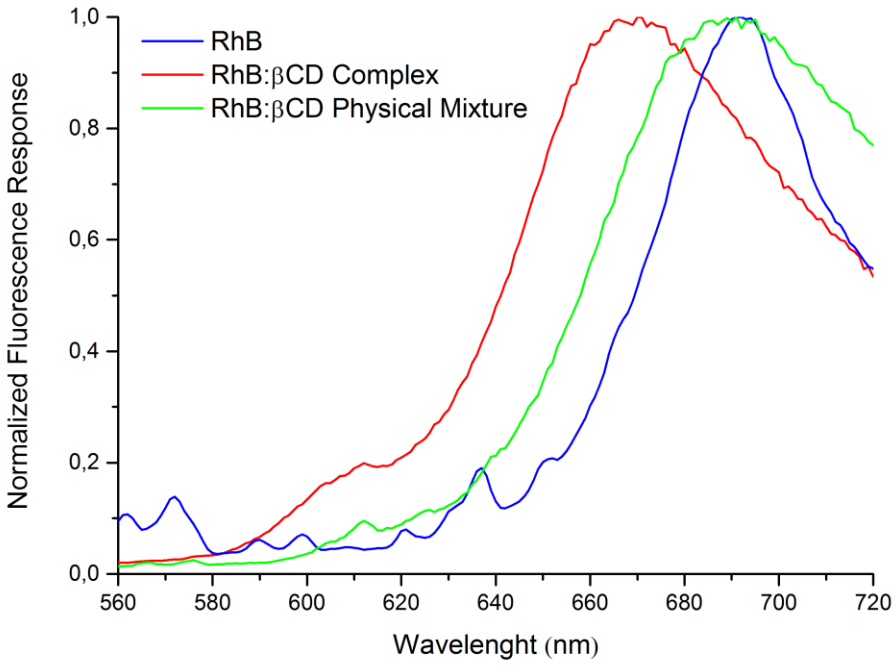

Fig. 2.10: Fluorescence emission of the solid samples.

3.3 Effect of Milling

The last step of the nanocomposite preparation is the milling of the fluorescent probe in its complex form with the polymeric matrix trying to ensure that the inclusion complex is kept after the HEBM and that the probe is homogeneously distributed throughout the matrix. It is known that the severe mechanical conditions occurring in these processes may break bonds or produce free radicals (Shaw 1998). For this reason, the β-CD has been milled alone under the same conditions as those of the films. According to ^{1}H NMR data, no changes are perceived in the spectrum after milling, which indicates that the process does not alter the chemical structure of the macrocycle. Regarding to the nanocomposites, after the products were milled and processed into thin films, the fluorescence response of the film containing the RhB:βCD complex presented a four-fold fluorescence enhancement (Figure 2.11 bottom) compared to the physical mixture and a blue shift of 40 nm (Figure 2.11 top), which is in good agreement with the results of the solid samples before milling. It is worthy to mention that the trend is the same as in a concentrated solution of RhB, where the fluorophore is extensively aggregated and the addition of βCD produces an enhancement on the fluorescent response, as explained above. All these confirms that the RhB:βCD complex can be used as a probe to monitor the dispersion of the oligosaccharide alone or attached to other nanostructure, as nanoparticles, as RhB behaves differently when

bound to the βCD than when it is free in the matrix and that the complex is capable of enduring the extreme conditions of the HEBM process without losing its properties.

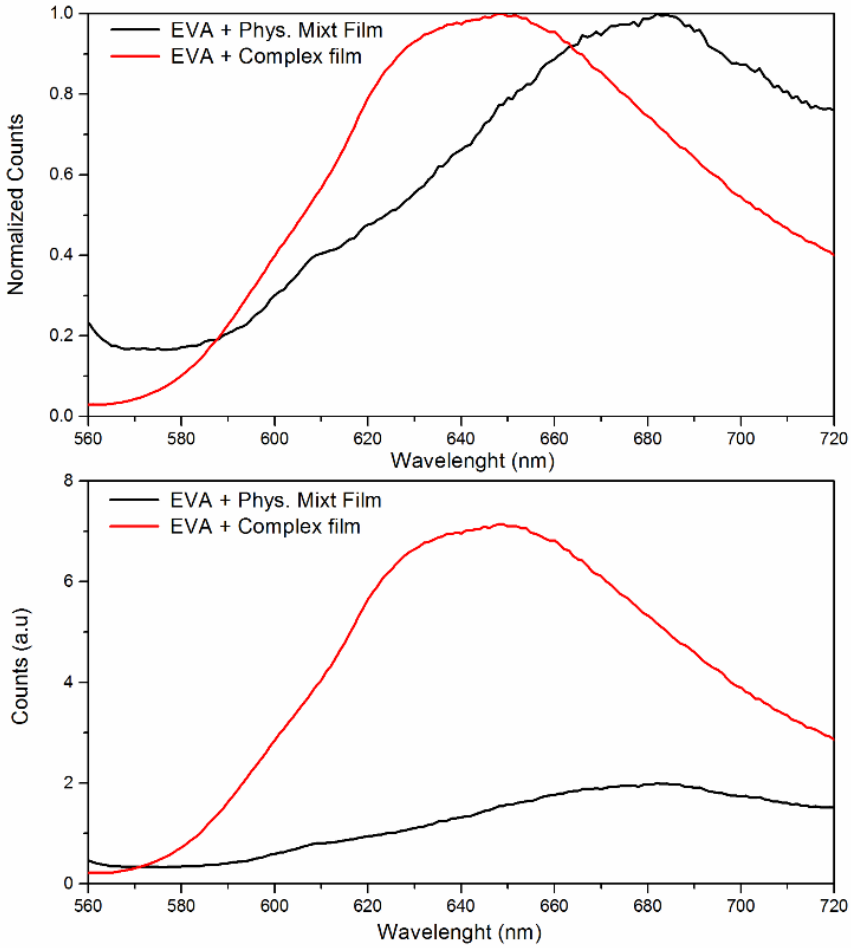

Fig. 2.11: Solid State Fluorescent Response.

The films are shown in Figure 2.12. The one containing the complex presents a uniform and homogeneous appearance in contrast to the film with the simple physical mixture, also prepared by HEBM. The latter presents a darker color with white spots corresponding to macroscopic domains of aggregated βCD. As the complex lacks a crystalline structure, as XRD experiments have shown, it seems that in order to achieve a good dispersion of the βCD in solid phase it is necessary to break its crystalline arrangement and convert it to an amorphous form.

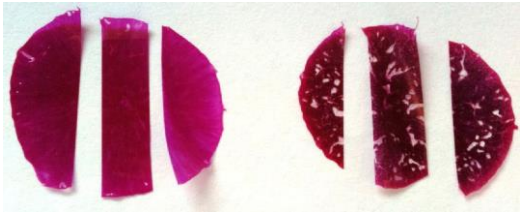

Fig. 2.12: Complex film (left) and physical mixture film (right).

Images at different scales of the films with the RhB:βCD complex and the physical mixture were taken with a fluorescence microscope. As it can be seen in Figures 2.13 and 2.14, using the same diaphragm and magnification conditions (10x, 20x 40x and 100x), the RhB:βCD film clearly shows an enhanced fluorescent response in relation to the other when excited at 510 nm. Although both films are visually colored, the βCD decreases the emission of the RhB in the physical mixture, while in the complex, RhB is included in the cavity and the fluorescence is enhanced. In addition to that, the complex shows an excellent dispersion throughout the matrix, whereas the mixture presents local domains of RhB at the bottom section and other sectors that are richer in βCD, where there is no fluorescence response at all resulting in a dark image.

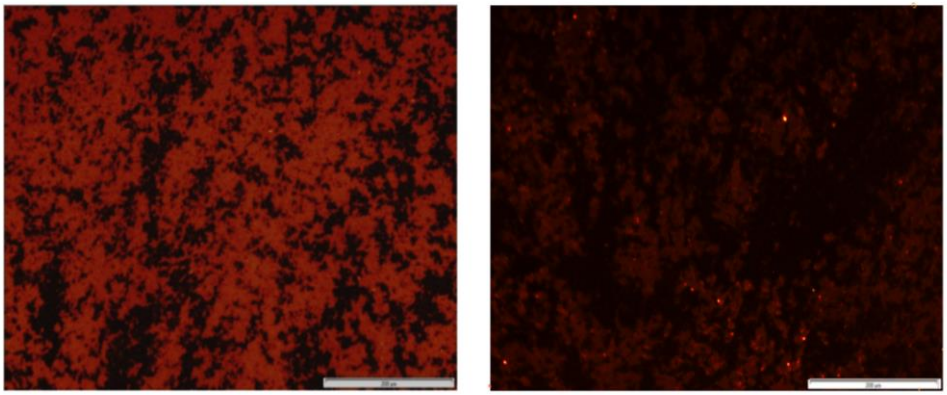

Fig. 2.13: 20x Fluorescent microscope image of the RhB-βCD Complex film (left) and Physical Mixture (Right). Scale bar 200 µm. λex = 510 nm.

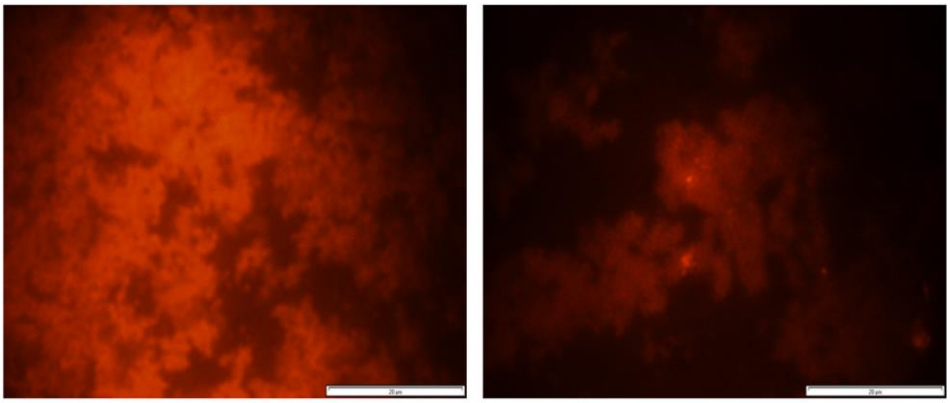

Fig. 2.14: 100x Microscope image of the RhB-βCD Complex film (left) and Physical Mixture (Right). Scale bar 20 µm.

4. CONCLUSIONS

The association between βCD and RhB and Rh6G has been studied both in solution and solid state by different techniques. ^{1}H-NMR results combined with fluorescence spectroscopy confirm the formation of a stable complex of RhB of 1:1 stoichiometry, with a binding constant of the order of 10^{4} M^{-1} on a wide range of temperatures. The mode of inclusion has been elucidated with the aid of ROESY spectra, proving that the RhB enters the βCD by any of the ethylamonium substituents towards the wider rim of the macrocycle, leaving exposed to the solvent the moiety of the RhB that bears the carboxylic group. Analysis of the solid products show that the complex of RhB retains its stability in the solid phase, as stated by the disappearance of the endothermic peak at 200 ˚C in TGA, characteristic of the RhB, and to the blue shift and emission enhancement observed by fluorescence. On the other hand, Rh6G does not form complexes either in aqueous solution or in solid phase.

The RhB complex mixed by cryo HEBM with the polymer, EVA, after the subsequent film production is homogeneously scattered through the matrix, undergoing a four-fold enhancement in its fluorescence, that is not observed with the physical mixture. The use of a fluorescent complex with β-CD has thus the double effect of breaking the crystalline structure of the β-CD by forming an amorphous phase that makes possible the proper dispersion of the macrocycle, and to enhance the “visibility” of the macrocycle. These results, apart from eliminating the need of using more sophisticated techniques as SEM or AFM, are important for subsequent investigations of nanocomposites based in CDs, either as nanofillers by themselves or attached to other nanostructures.

5. REFERENCES

Arbeloa, F.L. et al., 1997. Relations between photophysical and lasing properties of rhodamines in solid polymeric matrices. *Applied Physics B-Lasers and Optics*, 64(6), pp.651–657.

Bax, A. & Davis, D.G., 1985. Practical aspects of two-dimensional transverse NOE spectroscopy. *Journal of Magnetic Resonance (1969)*, 63(1), pp.207–213.

Bernini, A. et al., 2004. NMR studies of the inclusion complex between beta-cyclodextrin and paroxetine. *European journal of pharmaceutical sciences : official journal of the European Federation for Pharmaceutical Sciences*, 22(5), pp.445–50.

Castrillo, P.D. et al., 2007. Real dispersion of isolated fumed silica nanoparticles in highly filled PMMA prepared by high energy ball milling. *Journal of Colloid and Interface Science*, 308, pp.318–324.

Crini, G., 2008. Kinetic and equilibrium studies on the removal of cationic dyes from aqueous solution by adsorption onto a cyclodextrin polymer. *Dyes and Pigments*, 77(2), pp.415–426.

Degani, Y., Willner, I. & Haas, Y., 1984. Lasing of rhodamine B in aqueous solutions containing β-cyclodextrin. *Chemical Physics Letters*, 104(5), pp.496–499.

Ferreira, J.A.B. & Costa, S.M.B., 2005. Non-radiative decay in rhodamines: Role of 1 : 1 and 1 : 2 molecular complexation with beta-cyclodextrin. *Journal of Photochemistry and Photobiology A-Chemistry*, 173(3), pp.309–318.

Gonzalez-Benito, J. & Gonzalez-Gaitano, G., 2008. Interfacial conformations and molecular structure of PMMA in PMMA/silica nanocomposites. Effect of high-energy ball milling. *Macromolecules*, 41, pp.4777–4785.

González-Gaitano, G. & González-Benito, J., 2008. Pseudorotaxanes of Cyclodextrin and Diglycidyl Ether of Bisphenol A as Precursors of New Intramolecularly Reinforced Epoxy-based Thermosets. *Supramolecular Chemistry*, 20(3), pp.335–344.

Hussain, F., 2006. Review article: Polymer-matrix Nanocomposites, Processing, Manufacturing, and Application: An Overview. *Journal of Composite Materials*, 40(17), pp.1511–1575.

Incocciati, E., Magini, M. & Padella, F., 2003. Mecanochemical process for treating plastic materials.

Liu, Y. et al., 2001. Cooperative multipoint recognition of organic dyes by bis(beta-cyclodextrin)s with 2,2 ’-bipyridine-4,4 '-dicarboxy tethers. *Chemistry-a European Journal*, 7(12), pp.2528–2535.

Magde, D., Rojas, G.E. & Seybold, P.G., 1999. Solvent Dependence of the Fluorescence Lifetimes of Xanthene Dyes. *Photochemistry and Photobiology*, 70(5), pp.737–744.

Mchedlov-Petrossyan, N.O., Vodolazkaya, N.A. & Doroshenko, A.O., 2003. Ionic equilibria of fluorophores in organized solutions: The influence of micellar microenvironment on protolytic and photophysical properties of rhodamine B. *Journal of Fluorescence*, 13(3), pp.235–248.

Mchedlov-Petrosyan, N.O. & Kholin, Y. V, 2004. Aggregation of rhodamine B in water. *Russian Journal of Applied Chemistry*, 77(3), pp.414–422.

O’Connell, R.M. & Saito, T.T., 1983. Plastics for high-power laser applications-: A review. *Optical Engineering*, 22(4), p.224393.

Olmos, D. et al., 2009. Crystallization and final morphology of HDPE: Effect of the high energy ball milling and the presence of TiO2 nanoparticles. *Polymer*, 50, pp.1732–1742.

Padella, F. et al., 1998. Mechanically activated low temperature synthesis of Sr doped lanthanum manganite. *Mechanically Alloyed, Metastable and Nanocrystalline Materials, Part 1*, 269-2, pp.105–110.

Patel, K. et al., 2008. Enzyme-responsive snap-top covered silica nanocontainers. *Journal of the American Chemical Society*, 130(8), pp.2382–3.

Peterson, O.G. & Snavely, B.B., 1968. STIMULATED EMISSION FROM FLASHLAMP-EXCITED ORGANIC DYES IN POLYMETHYL METHACRYLATE. *Applied Physics Letters*, 12(7), p.238.

Politzer, I.R. et al., 1989. Effect of β-cyclodextrin on the fluorescence, absorption and lasing of rhodamine 6G, rhodamine B and fluorescein disodium salt in aqueous solutions. *Chemical Physics Letters*, 159(2-3), pp.258–262.

Rowlands, S.A. et al., 1994. Destruction of toxic materials. *Nature*, 367, p.223.

Saenger, W. et al., 1998. Structures of the Common Cyclodextrins and Their Larger Analogues-Beyond the Doughnut. *Chemical reviews*, 98(5), pp.1787–1802.

Sainz-Rozas, P.R., Isasi, J.R. & González-Gaitano, G., 2005. Spectral and photophysical properties of 2-dibenzofuranol and its inclusion complexes with cyclodextrins. *Journal of Photochemistry and Photobiology A: Chemistry*, 173(3), pp.319–327.

Shaw, W.J.D., 1998. Current understanding of mechanically alloyed polymers. *Mechanically Alloyed, Metastable and Nanocrystalline Materials, Part 1*, 269-2, pp.19–29.

Suryanarayana, C., 2001. Mechanical alloying and milling. *Progress in Materials Science*, 46, pp.1–184.

Wu, J. & Gao, C., 2009. Click Chemistry Approach to Rhodamine B-Capped Polyrotaxanes and their Unique Fluorescence Properties. *Macromolecular Chemistry and Physics*, 210(20), pp.1697–1708.

Xu, M. et al., 2010. Cyclodextrin Supramolecular Complex as a Water-Soluble Ratiometric Sensor for Ferric Ion Sensing. *Langmuir*, 26(6), pp.4529–4534.

Zhao, R., Torley, P. & Halley, P.J., 2008. Emerging biodegradable materials: starch- and protein-based bio-nanocomposites. *Journal of Materials Science*, 43(9), pp.3058–3071.

Chapter 3

Cyclodextrin-Grafted Barium Titanate Nanoparticles for Improved Dispersion and Stabilization in Water-Based Systems

Journal of Nanoparticle Research
DOI: 10.1007/s11051-015-3321-x

Abstract

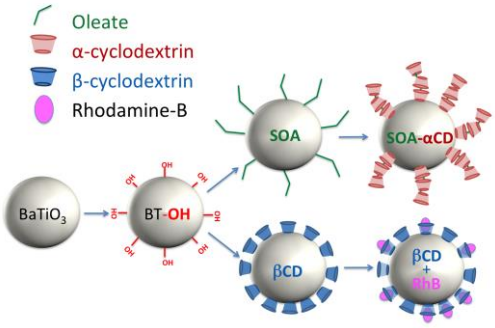

Ceramic nanoparticles with piezoelectric properties, as $BaTiO_3$ (BT), constitute a promising approach in the fields of nanocomposite materials and biomaterials. In the latter case, the drawback of their fast aggregation and practically null stability in water has to be overcome to succeed in their preparation. The objective of this investigation has been the surface functionalization of $BaTiO_3$ nanoparticles with cyclodextrins (CDs) as a way to break the aggregation and improve the stability of the nanoparticles in water solution, preventing and minimizing the fast precipitation. As a secondary goal, we are able to achieve extra-functionality, bestowed from the hydrophobic cavity of the macrocycle, which is able to lodge guest molecules that can form inclusion complexes with the oligosaccharide. The nanoparticle functionalization has been fully tracked and characterized, and the cytotoxicity of the modified nanoparticles with fibroblasts and pre-osteoblasts cell lines assessed with excellent results in a wide range of concentrations. The modified nanoparticles resulted suitable for the easy preparation of nanocomposite hydrogels, by dispersion in hydrophilic polymers of typical use in biomedical applications (PEG, Pluronics and PEO), and further processed in the form of films by water casting, showing very good results in terms of homogeneity in the dispersion of the filler. Likewise, as examples of application and with the aim of exploring a different range of nanocomposites, Rhodamine B was included in the macrocycles as a model molecule, and films prepared from a thermoplastic matrix (EVA) by high energy ball milling have been tested by impedance spectroscopy to discuss their dielectric properties, which indicated that even little modifications in the surface of the nanoparticles involve a

different kind of interaction with the polymeric matrix. The CD-modified nanoparticles are thus suitable for easy preparation either of water-based nanocomposites as hydrogels or nanocomposites based on thermoplastic matrices.

1. INTRODUCTION

Nanocomposite materials, composed of polymers and nanostructures, lay behind most of the biomaterials being developed at the moment, as a small amount of nanoparticles can dramatically modify the properties of the matrix, empowering tailored compositions for different uses (Gaharwar et al. 2011). Recently, a wide range of inorganic materials as barium titanate ($BaTiO_3$, BT), hydroxyapatite or synthetic silicates such as laponites have started to gain consideration for their prospective use in bioengineering due to their unique mechanical and chemical properties (Wang et al. 2013; Gaharwar et al. 2013; Mamana & Pellegri 2015). Specifically, biocompatible nanocomposites have a key role in important fields of medicinal, chemical and biological research, arousing important innovations for bone regeneration, tissue engineering, implants or drug delivery systems (Shi et al. 2010).

BT is a perovskite-type ceramic, ferroelectric in all its crystalline phases except the cubic one. It possesses a high dielectric constant with piezoelectric properties on its tetragonal, orthorhombic and rombohedral crystalline phases. These properties make BT useful for applications other than bioengineering, such as in electronics as printed circuits, piezoelectric sensors for ultrasonic transducers, capacitors and random access memories as some examples (Ring & Kavanagh 2003; Yu et al. 2011). However, BT has been replaced in some of these applications by multiceramic materials as lead zirconate titanates, or PZTs (Park & Shrout 1997). On the other hand, the high processing temperature of these ceramic materials makes them unsuitable for many practical uses where polymeric materials are involved as in printed circuit boards (PCBs). This problem may be overcome by its preparation in form of polymeric nanocomposites, which are easily processable and with tuneable properties, and in order to do that, the first and most important requisite is to ensure a uniform dispersion of the filler, since the formation of particles agglomerates may lead to the unwanted discontinuity or deterioration of their properties. In some previous works we have described an easy, inexpensive and solvent-free way of achieving a good dispersion of the filler in thermoplastic-matrix nanocomposites, based on solid state methods as high-energy ball milling (HEBM) (R Serra-Gómez et al. 2012). Nonetheless, biocompatible nanocomposites mostly require that their components are soluble in water, or at least stable in suspension in order to achieve an adequate dispersion of the filler. As PZTs are not suitable materials for most biomedical applications, due to the high toxicity of the lead components (Sakai et al. 2006; Tsuchiya et al. 2011), BT has been pointed as a good alternative provided that the stability issue is overcome; some examples are as second harmonic generators for imaging (Dempsey et al. 2013; Hsieh et al. 2010), as drug and gene

delivery carriers (Ciofani, Danti, D'Alessandro, et al. 2010; Jeong et al. 2013), or as ceramic fillers in bone defects to promote its regeneration (Feng et al. 1997; Baxter et al. 2009). All the more, these nanomaterials have often been used as fillers in polymers and hydrogels that do not present the desired mechanical properties for the use they were intended for (Huang et al. 2007; Schexnailder & Schmidt 2008; Knauert et al. 2007). Yet, the main difficulty to use BT in biocomposites is to achieve a uniform and stable dispersion in aqueous media since the nanoparticles tend to aggregate as a result of their high area-to-volume ratio (Blanco-Lopez et al. 1997; Paik et al. 2002). These aggregates can reach sizes of a few micrometres (R Serra-Gómez et al. 2012; Gao et al. 2015) and are a main drawback because of their high tendency to precipitate. The modification of the surface of the nanoparticles is a possible approach to improve the stability of the dispersions, either by adsorption on the surface of different substances like polyethylene glycol, PEG (Čulić-Viskota et al. 2012), polyacrylic acid ammonium salts, PAA-ammonium (Jean & Wang 2005) and polyalcohols or by covalent bonding by first generating either amine (FarrokhTakin et al. 2012), phosphonic (Kim et al. 2007) or hydroxyl (Chang et al. 2009) groups on the surface for further grafting of molecules of interest.

Cyclodextrins (CDs) are cyclic oligosaccharides composed of 6, 7 or 8 D-glucopyranose rings termed α, β and γ-CD respectively. Their sizes (ca. 1 nm) fall within the low limit of the nanometric scale so they can be considered as a limiting type of nanofiller. CDs are shaped like truncated cones, with a hydrophobic cavity and a hydrophilic exterior. The definite number of hydroxyl groups, according to the number of glucose units, makes it possible to establish strong interactions with certain polymeric matrices. One of the few applications of CDs with ceramic nanoparticles as TiO_2 and BT has to do with the stabilization of nanocrystals and nanoparticles in their hydrothermal-synthesis steps to provide a shell for the nanocrystals to grow, allowing the sizes to be precisely controlled (2-10 nm) and therefore a better stabilization as the aggregation is supressed (Shiraishi et al. 2015; Sun et al. 2008; Li et al. 2006).

In this paper we report on a novel method of disaggregation and water stabilization of commercially available BT nanoparticles of different sizes (50, 100 and 200 nm in diameter) by coating them with β-CD attached by hydrogen bonding forces to the previously generated –OH groups via the hydroxylation of the surface through reaction with H_2O_2 (Choudhury 2012; Hiroki & Laverne 2005). As a consequence of that, the addition of the macrocycles on the surface opens the possibility of adding extra-functionality to the nanoparticles, as they can include different types of molecules and drugs of interest in their cavity (Städe et al.

2015). Another type of covalent modification via conjugation with oleate (SOA) as proposed by Chang et al. to improve the dispersion in organic solvents has been used, followed by the addition of α-cyclodextrin (α-CD), which is known to form supramolecular complexes via the inclusion of the hydrocarbon tail of the surfactant (Gonzalez-Gaitano et al. 2000) proving by this method that the water stability is also enhanced when incorporating the CD to the surface of the nanoparticle.

With the modified nanoparticles, and as examples of possible applications, various types of nanocomposites have been prepared by changing the polymeric matrix and have been tested for their use in solid and in solution, confirming that the modified surface is able to endure both solid-state methods of dispersion (high energy ball milling, HEBM) as well as water casting methods. The cytotoxicity of the modified nanoparticles has been evaluated in different concentrations and cell lines and films have been casted from different polymeric solutions prepared with matrices like poly (ethylene-co-vinylacetate), EVA, polyethylene oxide (PEO), PEG and Pluronic® F127 (an amphiphilic PEO-PPO-PEO block copolymer) to show the ability of the nanoparticles to form stable suspensions and hydrogels to be used in biomedical applications. The samples have been fully characterized by means of FTIR-ATR spectroscopy, thermogravimetric analysis, dynamic light scattering, X-ray diffraction and electron microscopy. The dielectric response of the films has also been evaluated to study the influence of the filler modification on the dielectric properties of the nanocomposites, showing that the individual properties of the components are maintained after the solid-state treatments.

2. MATERIALS AND METHODS

2.1. Materials.

Inorganic submicrometric particles of barium titanate (BT), with an average diameter size of 200 nm (99.9% purity, ρ=6.02 $g \cdot cm^{-3}$ and tetragonal crystalline structure) and nanoparticles of 100 nm (99.9% purity, ρ=5.85 $g \cdot cm^{-3}$ and cubic crystalline structure) were supplied by Nanostructured and Amorphous Materials Inc. BT of 50 nm in diameter was provided by Sigma-Aldrich (99.9% purity, ρ=6.08 $g \cdot cm^{-3}$ and cubic crystalline structure). Sodium oleate (≥82% fatty acids, as oleic acid) was supplied by Aldrich and αCD and βCD were provided by Wacker as Cavamax®, W6 and W7, respectively. PEO with $4x10^{6}$ $g \cdot mol^{-1}$ from Aldrich, polyethylene glycol, PEG, Mw of 10.000 $g \cdot mol^{-1}$ from Fluka, and Pluronic® F127 with an average Mw. of 12600 $g \cdot mol^{-1}$, have been used for the preparation and casting of water based composites. Poly (ethylene-co-vinyl acetate), EVA (12% w/w in vinyl acetate,

density 0.933 g·cm^{-3} at 25 ˚C, Vicat temperature of 65 ˚C and melting point of 95 ˚C) was supplied by Sigma Aldrich.

2.2 Sample preparation

i) Surface Modification. The process used for the modification of the nanoparticles consisted of three steps: a) Hydroxylation of BT by oxidation with H_2O_2 in a reflux setup for 4 h at 106 ˚C; b) covalent bonding of SOA to the hydroxyl groups generated in the previous step by stirring a suspension of nanoparticles (2 wt%) in a SOA aqueous solution (0.5 wt%) for 3 h at 90 ˚C; c) reaction with α-CD for 3 h at room temperature under vigorous stirring. Three washing and rinsing cycles were done in each step. In the case of the modification only with CD, the second step was skipped and the reaction with α-CD and βCD was directly done on the hydroxylated surface. The resulting modified nanoparticles were freeze-dried and characterized.

ii) Cryo-HEBM. In order to make easier the subsequent blending process with the particles in the case of EVA pellets, the polymer was first ground in a MF 10 Basic IKA WERKE grinder at a rotation speed of 4500 rpm. A mixture of BT with EVA (20 wt%) was subjected to cryo-HEBM as described in our previous work (R Serra-Gómez et al. 2012), followed by the film preparation as described by (Olmos et al. 2011).

The nomenclature used for the samples during the synthesis and characterization is as follows: *BT* plus a number depending on the diameter size of the nanoparticles (1 for 100 nm and 2 for 200 nm) plus the coating applied; *-OH* for the hydroxyl generation, *-SOA* for the oleate, *-SOA-αCD* for the oleate plus cyclodextrin and *-αCD* and – β*CD* for the alpha and beta cyclodextrins, respectively.

2.3 Techniques

Attenuated total reflectance was used for the IR characterisation, using an FTIR-ATR Nicolette Avatar 360 spectrometer, with a resolution of 2 cm^{-1} and 32 scans per spectrum. Thermogravimetric analysis, TGA, was carried out in a TGA-SDTA 851 Mettler Toledo with a heating program from 25 ˚C to 600 ˚C at 10 ˚C/min under a N_2 atmosphere.

Fluorescence studies on the modified nanoparticles tagged with Rhodamine B (RhB) were done using an Edinburgh Instruments FLS920 spectrofluorimeter. Samples in a quartz cuvette of 10 mm of path length were excited at 553nm and the emission recorded from 560 to 700 nm under constant stirring, averaging 5 scans with a 1 nm step and 0.1 s dwell time. Excitation and emission slits were set at 2 nm. 30 mg of CD-modified nanoparticles were put in contact with a 4·10^{-6} M RhB solution and stirred for 1 h. Then they were

centrifuged at 8000 rpm for 30 min and the nanoparticles were separated from the supernatant and dried at 80 °C for 24 h.

The size distribution of the different particles was determined by dynamic light scattering (DLS) using a DynaPro photon correlation spectrometer. The particles were dispersed in deionized water by sonication and diluted before the measurements without further filtration. The intensity size distributions, expressed in terms of the hydrodynamic radius, $R_{h,}$ were calculated by the method of regularization with DynaLS 1.0 software.

For the Zeta potential measurements, an electroacoustic-based zeta potential analyser (ZetaProbe of Colloidal Dynamics), specifically designed for the study of concentrated suspensions, was used. Alkaline pH was reached by addition of NaOH 0.1 M and the titration from pH=12 to pH=3 conducted with HCl 0.1 M. For the Transmission Electron Microscopy (TEM) images the samples were treated with osmium tetroxide 1% and were kept at 4 ˚C for 1 h. Then a drop of the suspension was placed in a copper grid and phosphotungstic acid 2% as a negative contrast agent was applied. Samples were analyzed using a LIBRA 120 energy-filtering TEM (Zeiss) operated at 80 KV.

The cytotoxicity of the modified BT nanoparticles was tested on the fibroblast cell line NIH3T3 and MC3T3-E1 pre-osteoblasts. The Tetrazolium assay (MTT) was used to assess the viability of the cells, and therefore the cytotoxicity established by the loss of viable cells upon treatment with the compounds of interest. The cells were incubated in Dulbecco's modified eagle medium from Life's Technologies, supplemented with 10% of fetal bovine serum and 0.1% of penicillin/streptomycin at 37 °C and 5% CO_2. Cells were seeded into 96-well plates at a concentration of $5x10^4$ cells/mL and 24 hours later the nanoparticles were added at different concentrations. MTT tests were conducted on day 3 and day 7 by addition of MTT 1 mg/ml and incubation of 3 h. The formazan absorbance at 540 nm was measured with a Thermo Scientific Multiscan EX microplate reader. DMSO was used as a positive control, and the appropriate negative controls were performed.

Impedance measurements in the frequency range 1 Hz–1 MHz were carried out at room temperature using an impedance analyzer SOLARTRON 1260A. A 3V sinusoidal voltage signal was applied, measuring the current to finally obtain the complex impedance with its amplitude and phase over a range of frequencies (20 points per decade). Zview® software (Scribner Associates, Inc.) was used for the numerical fitting of the impedance data by considering a specific equivalent circuit. The measurements were performed on capacitors made by a dielectric film consisting on each sample in between two plate electrodes with circular surfaces of 1.25 cm in diameter. The thicknesses of the dielectrics

were measured with a thickness meter Easy-Check FN of NEURTEK Instruments with an accuracy of ± 1 µm.

3. RESULTS AND DISCUSION

3.1. Characterization of the surface modification of the BT nanoparticles.

The surface modification consists of a three-step process that can be easily tracked by FTIR-ATR spectroscopy. Fig. 3.1 shows the spectra of the as received nanoparticles (BT, black trace) where the Ti-O stretching band can be seen in the fingerprint region starting at 600 cm^{-1}; the C-O band at 1452 cm^{-1} corresponds to vibrations coming from residual $BaCO_3$ from the synthesis method of the nanoparticles, usually deposited on the surface (Chaudhary et al. 2011). After the H_2O_2 treatment (BT-OH, red trace) the particles start showing the typical broad band of hydroxyl groups around 3300 cm^{-1}. On the other hand, when incorporating hydrophobic chains after the SOA reaction (BT-SOA, green trace), the characteristic bands at 2850-2910 cm^{-1} corresponding respectively to the antisymmetric and symmetric stretching of the C-H bonds, together with their bending modes at 1510-1430 cm^{-1} are clearly seen. The spectrum of BT-SOA-αCD (navy blue trace) shows the inclusion complex of the αCD, as seen by the growth of the –OH band due to the CD hydroxyl groups and the 1154 cm^{-1} bands of the C-O-C vibrations. From 1700 to 1300 cm^{-1} the skeletal C-C vibrations appear, along with the stretching vibrations of C-H and C-O bonds at 1082 cm^{-1}. Lastly, the BT-βCD trace (light blue), shows how the –OH band and vibrations of the CD groups appear at the same wavenumbers than the previous one, but with considerable lower intensities, as expected due to the different proportions between the bulk of the nanoparticle and the CD on the surface.

Due to the proportions between the nanoparticle and amount of modifier bound to the surface it can be challenging to fully characterize the three different steps of the modification process. In order to facilitate that, an estimation of the hydroxyl (-OH) groups that are generated on the surface can be calculated from the weight loss of the samples analyzed by thermogravimetry. As the stoichiometry of the reaction between SOA and the OH is 1:1, we can estimate the maximum number of bound SOA molecules per nanoparticle, and compare it to the experimental results to assess the extent of the functionalization. On the other hand, considering the size of the αCD (4.7-5.3 Å), its height (7.1 Å) (Saenger et al. 1998) and the length of the SOA chains (≈2 nm) (Lingley et al. 2013), it is expected that each SOA molecule can host a maximum of 3 α-CD molecules; however, steric effects as the bending of the oleate due to the double bond and the proximity of other chains already including CDs might reduce that number.

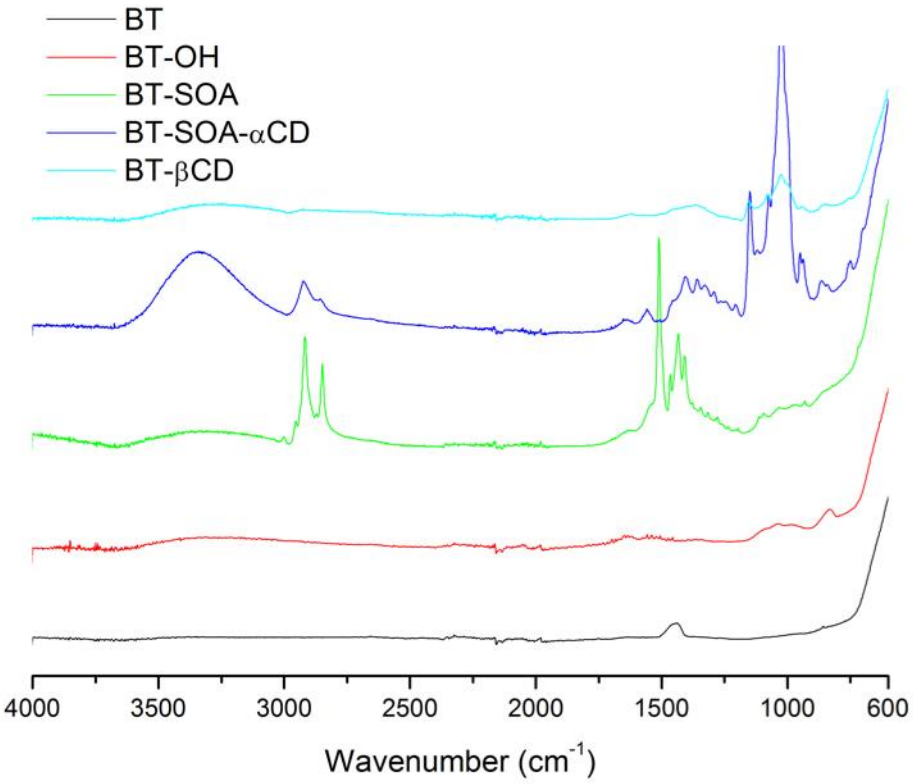

Fig. 3.1: FTIR spectra of the BT nanoparticles along the different surface modification steps. BT as received (black), BT-OH (red), BT-SOA (green), BT-SOA-αCD (navy blue) and BT-βCD (light blue).

Table 3.1 shows the results of the calculations as well as the experimental values obtained by TGA on the different nanoparticles for the SOA modification. As expected, the weight percentage decreases as the nanoparticle diameter increases, but always within the limits of the theoretical estimations.

Table 3.1: Theoretical and experimental values estimated by TGA of the wt% of OH and oleate groups upon modification of BT 50 nm nanoparticles (BT50), BT 100 nm nanoparticles (BT100) and BT 200 nm nanoparticles (BT200).

Sample	OH (TGA loss)	Theoretical Maximum SOA (1:1)	Experimental SOA
BT50	3.4%	55%	14%
BT100	3.4%	53%	3.0%
BT200	2.2%	37%	1.8%

The composition of the coating can be examined by TGA as SOA and the CD decompose around 300 °C, while the ceramic nanoparticles remain intact; therefore the weight loss should indicate the weight percentage of the coating. The decomposition of the CD can be attributed to the weight loss occurring between 315 ˚C and 350 ˚C, being the lower end of the range for the decomposition of CDs adsorbed in the surface and the higher value for the CDs with oleate chains included in them. The oleate loss takes place from approximately 368˚ C to 507 ˚C, which corresponds to the oleate chains that are covalently attached to the surface. when free or weekly attached chains are considered, decomposition occurs at lower temperatures around 290 ˚C, as described by Ozel (Ozel et al. 2013). As expected, the amount of SOA on the surface varies due to the differences on the surface-volume relation between the three sizes of nanoparticles. Fig. 3.2 shows the TGA thermograms of the BT100 and BT200 samples, exhibiting a coating well within the limits of the estimation done before for the SOA treatment. The weight loss values of the CDs and oleate thermal degradation are shown in Table 3.2.

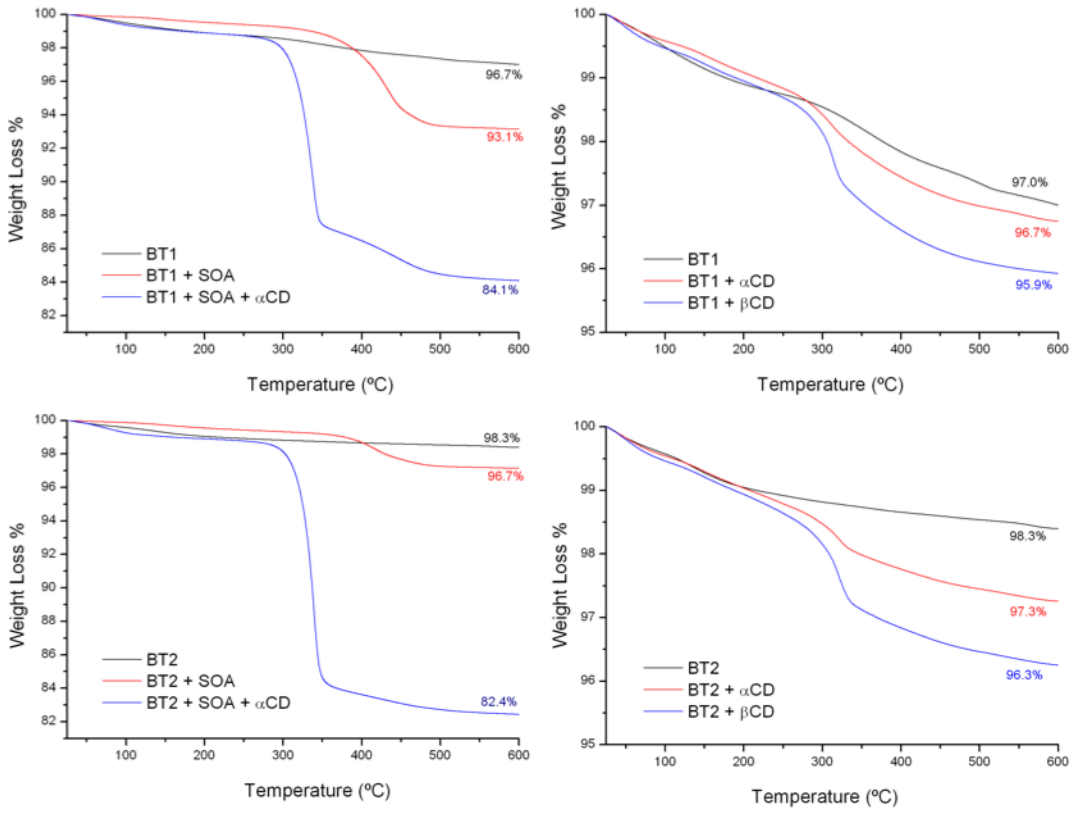

Fig. 3.2: TGA of the modified nanoparticles 100 nm (top) and 200 nm (bottom) with SOA and αCD (Left) and modified with αCD and βCD (right).

Table 3.2: Weight loss percentage calculated from TGA of the modified BT nanoparticles in the temperature region of the CDs and oleate degradation.

Samples BT	αCD	SOA	BT samples	αCD	βCD	CDs monolayer estimation
BT50-SOA		13.1%	**BT50-αCD**	0.56%		0.23%
BT50-SOA-αCD	21.1%	3.73%	**BT50-βCD**		0.59%	0.21%
BT100-SOA		5.21 %	**BT100-αCD**	0.75%		0.12%
BT100-SOA-αCD	11.0%	2.88 %	**BT100-βCD**		1.31%	0.11%
BT200-SOA		1.84 %	**BT200-αCD**	0.58%		0.06%
BT200-SOA-αCD	14.2%	1.31 %	**BT200-βCD**		1.20%	0.05%

In the case of the modification only with CD the values are considerably higher than the ones expected from the previous estimation, so it is clear that there is not only a monolayer on the surface of the nanoparticle. It is known that CDs self-aggregate in water, both in native form or when forming complexes (González-Gaitano et al. 2002), so it is likely that a multilayer of CDs is formed on the surface of the nanoparticles, especially when the treatment involves having the precursors in solution at relatively high concentration and after further drying. In both cases, BT100 and BT200, the adhesion of CDs to the surface of the nanoparticles is larger when βCD is the one involved, which confirms the stated above since the βCD self-aggregation tendency is much higher than that of αCD (González-Gaitano et al. 2002).

However, the thermogravimetry results of the CD modified samples fall within the sensitivity range of the technique (1 wt%). In order to confirm the presence of the CD layer, given that the values from TGA are relatively low and that the amount of CD is scarce for a reliable FTIR quantification, an alternative procedure was used, taking advantage of the inclusion complex formation between Rhodamine B (RhB) and βCD, reported in the preceding chapter (R. Serra-Gómez et al. 2012). The RhB solution was put together with the modified nanoparticles and both the fluorescence signal emitted by the solid samples as well as the fluorescence loss in the solution were measured.

After mixing the nanoparticles with the RhB solution an extensive adsorption of the RhB in the surface takes place, seen by the pinkish color in the samples. Fluorescence measurements on the supernatant of the modified nanoparticles (Fig. 3.3) show a decrease in the emission of a 6% in relation to the untreated BT as well as an increase in the

fluorescence of the solid (not shown), evidencing the formation of the inclusion complex between the RhB and the adsorbed CDs. It is also remarkable the decrease of the fluorescence yield of the BT-SOA modification, being a 35% loss over the native BT. In the case of the BT-SOA-αCD the long oleate chains are capped with the CDs and the fluorescence values show that, as the oleate chains are trapped by the CDs, the RhB molecules are hindered towards the long alkyl chains, with the subsequent reduction in the amount of RhB attached to the nanoparticle and therefore a concentration increase in the supernatant. The last result is not only important because it provides evidence of the attachment of the CDs to the surface, but it opens a wide array of possible molecules that can be successfully carried and released from the CDs, being able to use the BT as a nanocarrier in the body.

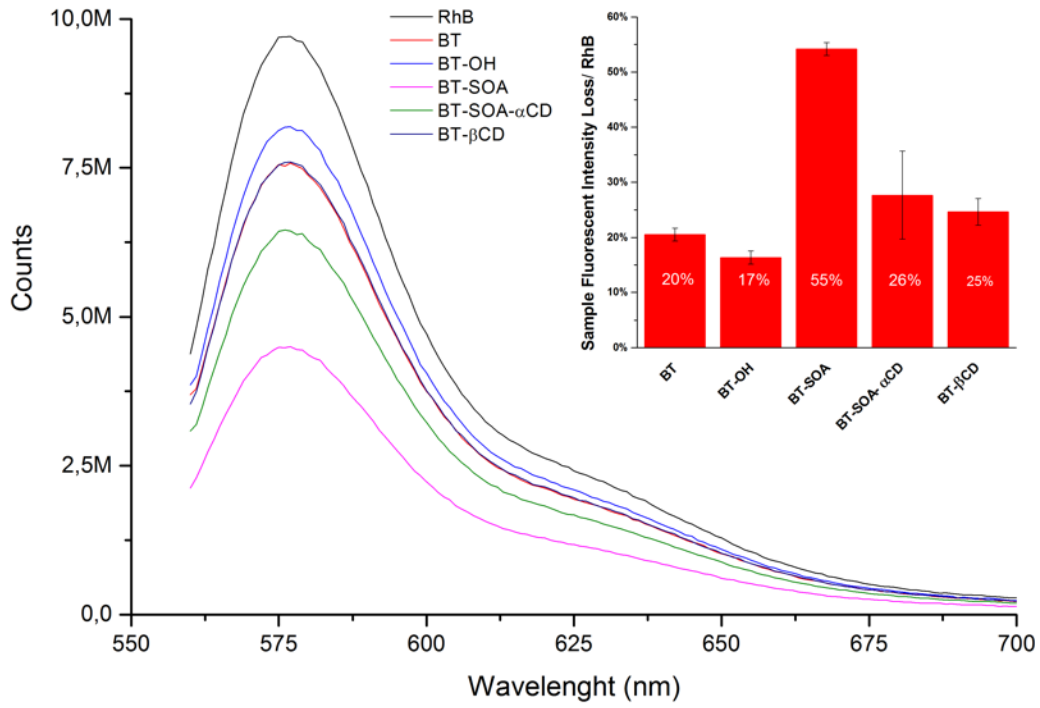

Fig. 3.3: Fluorescence emission of the supernatant of RhB $1.25 \cdot 10^{-7}$ M aqueous solution containing modified nanoparticles. The inset shows the fluorescence signal loss of the samples in relation to RhB.

The aggregation behavior of all the samples has been tested by DLS. Figure 3.4 shows the intensity size distributions for the 50 nm nanoparticles (the corresponding peak analyses are shown in Table 3.3).

A strong aggregation of the native nanoparticles (black trace) can be perceived, with an important contribution of agglomerates of around 300 nm and >1000 nm in diameter.

However, with the SOA-αCD complex (green trace in Fig. 3.4), as well as with βCD (blue trace in Fig. 3.4), the disaggregation is notably improved (50-80 nm). This corroborates that the first step to achieve a proper dispersion for an improved suspension in water is to break up the aggregates.

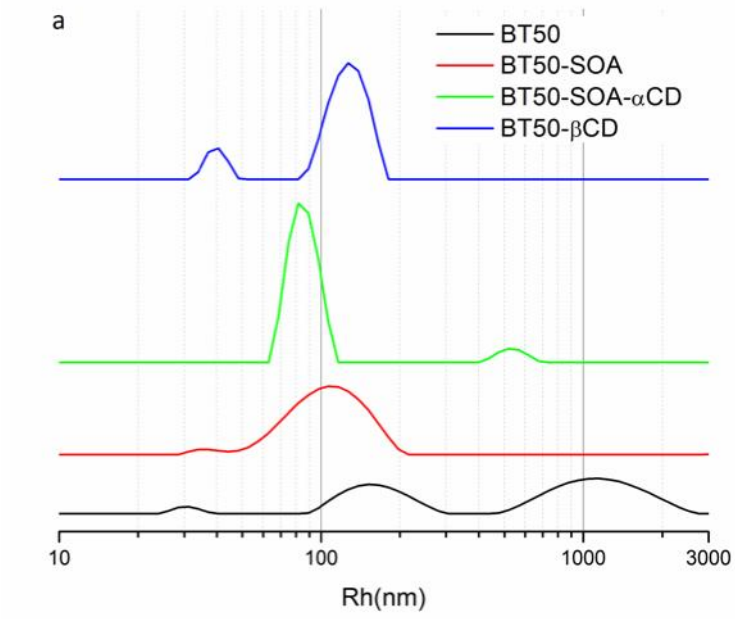

Fig. 3.4: Intensity size distributions of as received and modified BT50 nm nanoparticles.

Table 3.3: Area and position analysis of the intensity size distributions by DLS.

Sample	Peak	Area	Size (nm)
BT50	1	0.03	31
	2	0.33	170
	3	0.56	1258
BT50-SOA	1	0.03	37
	2	0.91	113
BT50-SOA-αCD	1	0.85	88
	2	0.07	444
B50-βCD	1	0.12	41
	2	0.79	133

The stability in suspension of these samples was tested by Z-potential measurements on the pH range from 3 to 12. Figure 3.5 shows a significant change in the modified samples

reaching potentials -200 mV for the BT50-βCD (green trace upper graph) and -100 mV for the BT200-βCD (green trace bottom graph) when the pH is in the physiological range between 7 and 11.

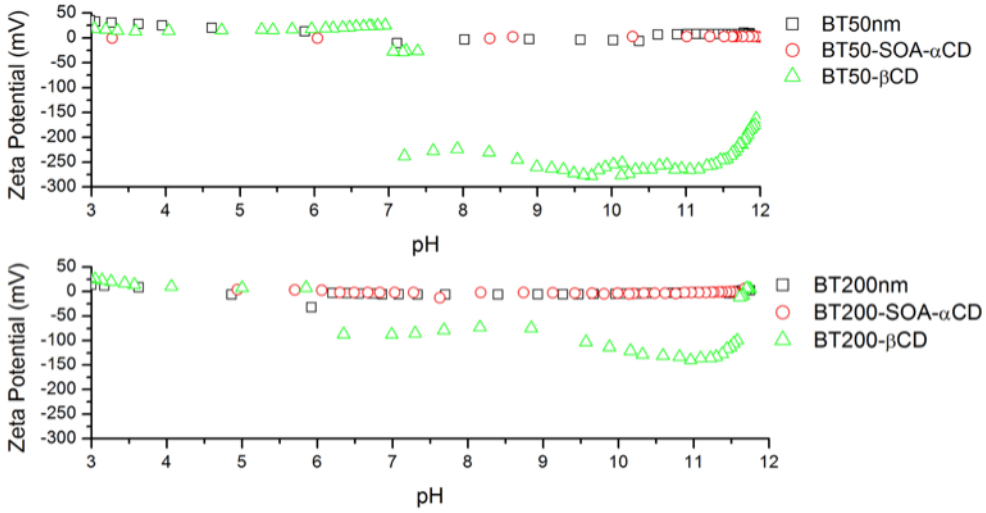

Fig. 3.5: Z-potential measurements of 1 wt% suspension of native and modified BT samples.

These Z potential values, together with the above presented data suggest that the modified nanoparticles with oleate and CDs, as well as the ones with βCD, present a stability improvement in this pH range, as the modifications involve enough change in the surface charge to prevent their aggregation, in contrast to the untreated nanoparticles, as a result of the presence of the high density of hydroxyl groups on the βCD. The difference in Z-potential values is in accordance with Paik (Paik et al. 1998), they stated the direct dependence on the percentage of BT surface covered with the solution stability. As previously indicated, the modification with CDs alone yields a multilayer due to the CD stacking and therefore a higher percentage of surface coverage than when the SOA treatment is applied. An example of the improved dispersion of the nanoparticles in water can be seen in the following photographs of samples after 4 hours (Fig 3.6).

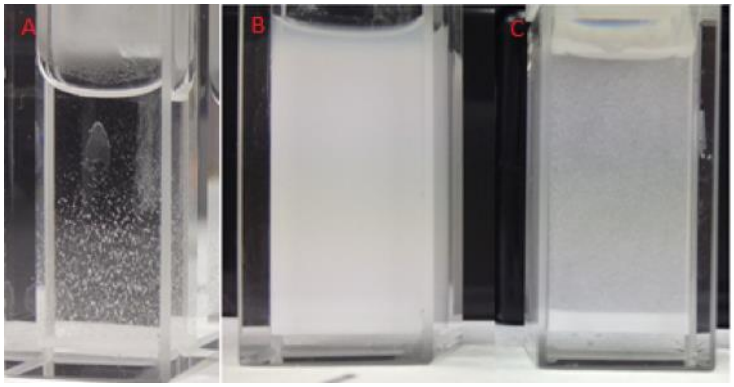

Fig. 3.6: Water dispersions after 4h of (a) 50mg/mL BT, (b) BT-SOA-αCD and (c) BT-βCD.

TEM microscopy was performed upon selected samples, to show the difference in the nanostructure upon functionalization. The untreated nanoparticles (Fig 3.7 left) present a homogeneous surface, while the –SOA-αCD modified ones (Fig 3.7 right), display a surface with a variation of dark tonalities resulting from the osmium oxide reaction with the SOA unsaturation, which proves the presence of the functionalization all over the surface.

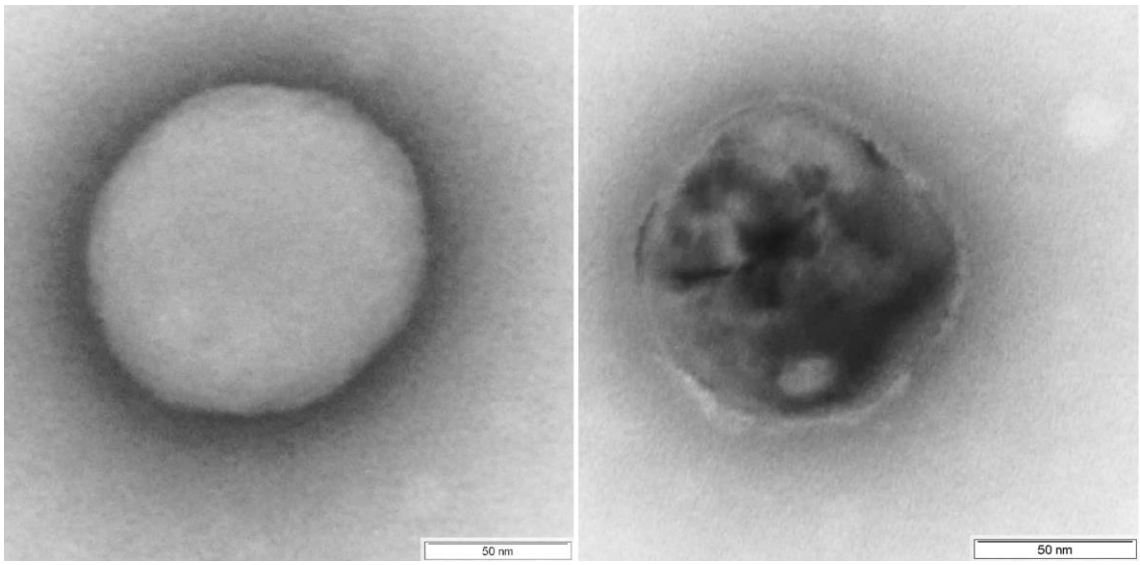

Fig. 3.7: TEM image of the commercial BT100 nm (left) and the BT-SOA-αCD modified nanoparticles (right).

3.2 Cytotoxicity

The cytotoxicity of the CD's modified BT has been assessed in a wide range of concentrations from 0 to 200 µg/ml. By reviewing the literature on BT cytotoxicity, mainly the studies of Dempsey and Ciofani (Dempsey et al. 2013; Ciofani, Danti, Moscato, et al. 2010; Ciofani et al. 2013), it seems clear that the coating plays a crucial role as it can notably change the way the cells interact with the BT, and represent the main contribution to the cytotoxicity. In our case, the CD coating seems to allow higher concentrations of nanoparticles without any negative effect in the cell viability. Figure 3.8 shows the MTT assay results for the BT-CD, which show excellent viability of the cells even up to concentrations of 200 µg/mL after a week of treatment, with significant improvements in the cell proliferation at concentrations of 100 µg/mL and 200 µg/mL according to the ANOVA and Student's T test ($p<0.01$; $n=12$).

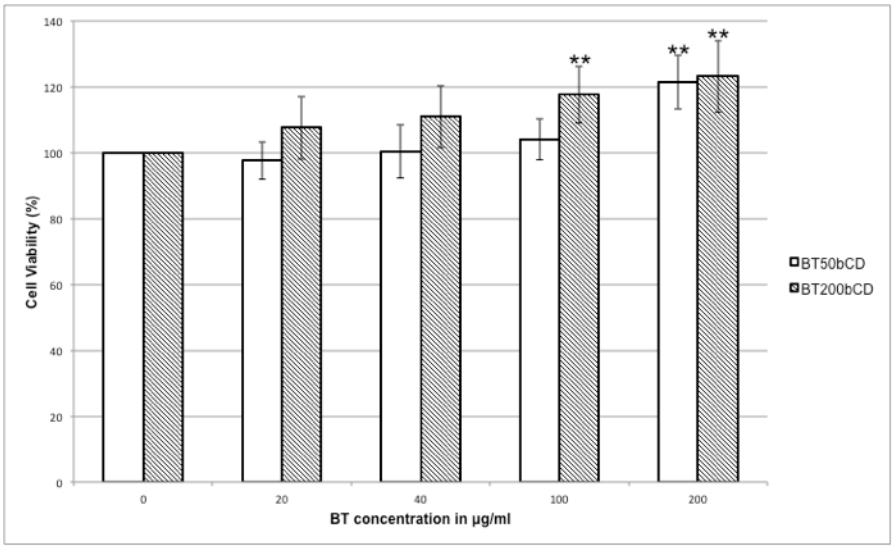

Fig. 3.8: MTT results for NIH3T3 cells and Barium Titanate nanoparticles modified with βCD. Notes: ** denotes p<0.01 by ANOVA variance test and Student's T Test. The confocal image (Right) shows the MC3T3-E1 cells after 14 days of culture. Cell nuclei are stained blue, actin in green and the BT-βCD appears in red.

The same nanoparticles were tested against the MC3T3-E1 cell line and phase contrast (Fig. 3.9) and confocal images (Fig. 3.10) were taken at days 3, 7 and 14 after treatment.

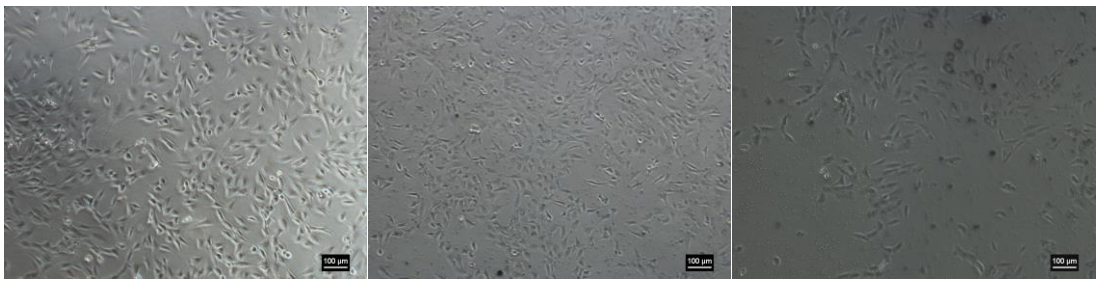

Fig. 3.9: MC3T-E1 cells with BT-βCD NP after 3 days of culture at 0µg/ml (left), 100µg/ml (center) and 200µg/ml (right).

The confocal image shows how, after 14 days of treatment the nanoparticles (200 µg/ml, red tones) are internalized in the tissue formed by the cells that grew normally. The βCD modification, as opposed to other coatings used to disperse BT, does not present a cytotoxic effect at the studied concentrations up to 200µg/ml.

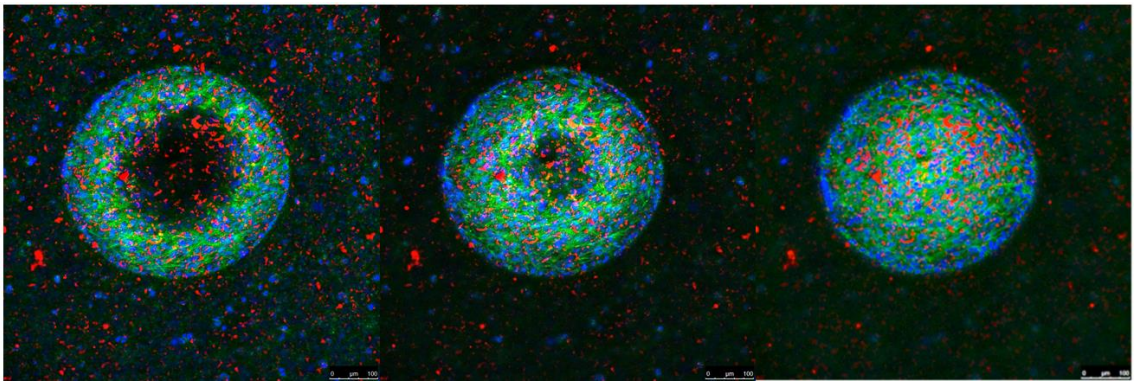

Fig. 3.10: MC3T3-E1 cells with BT-βCD NP growing sequence for 14 days of culture at 200µg/ml.

3.3 Examples of application.

As examples of the improvement achieved by the surface modifications, two cases will be shown in which the nanoparticles have been used to prepare different types of nanocomposites: one by water casting with EO-based polymers to obtain nanocomposite hydrogels, and another one by cryo-HEBM as the processing method from a thermoplastic matrix. Lastly, the outcomes of these two examples of application will be tested by impedance spectroscopy to study the effect of the BT modification on some electrical properties of the composites. This is a common technique to study the capacitance and the relaxation behavior of the nanocomposite films, particularly in those containing nanofillers with ferroelectric or piezoelectric properties, for their use as capacitors or as sensors and actuators (Beier et al. 2010).

a) Interaction of the modified nanoparticles with water-soluble hydrogel matrices.

Firstly, in order to test the preparations based on the modified NP with polymers, 15 wt% solutions of PEG and Pluronic® F127 were prepared and mixed with 10 wt% of commercial and modified nanoparticles. These two polymers have been chosen as they are commonly used as hydrogel substrates and have a similar average molecular weight. Therefore the different interactions with the surface of the nanoparticles should be mainly derived from their structures and the modifications applied. The difference in coatings of the nanoparticles produces different kinds of interactions with polymers. It can be seen in Figure 3.11 how the Pluronic® F127 presents a higher interaction than the PEG chains as seen by the weight loss in the 300-400 ˚C range. The effect is even more noticeable when αCD is on the surface, as this CD is known to form stable inclusion complexes with the PEO chains of the F127, as opposed to the βCD, that due to its wider size, is able to enter the chain and form the complex with the inner PPO chain (Larrañeta & Isasi 2012). As another interesting

result, the interaction of the particles with the hydrogel matrix can be tailored to some extent by the type of CDs attached to the surface.

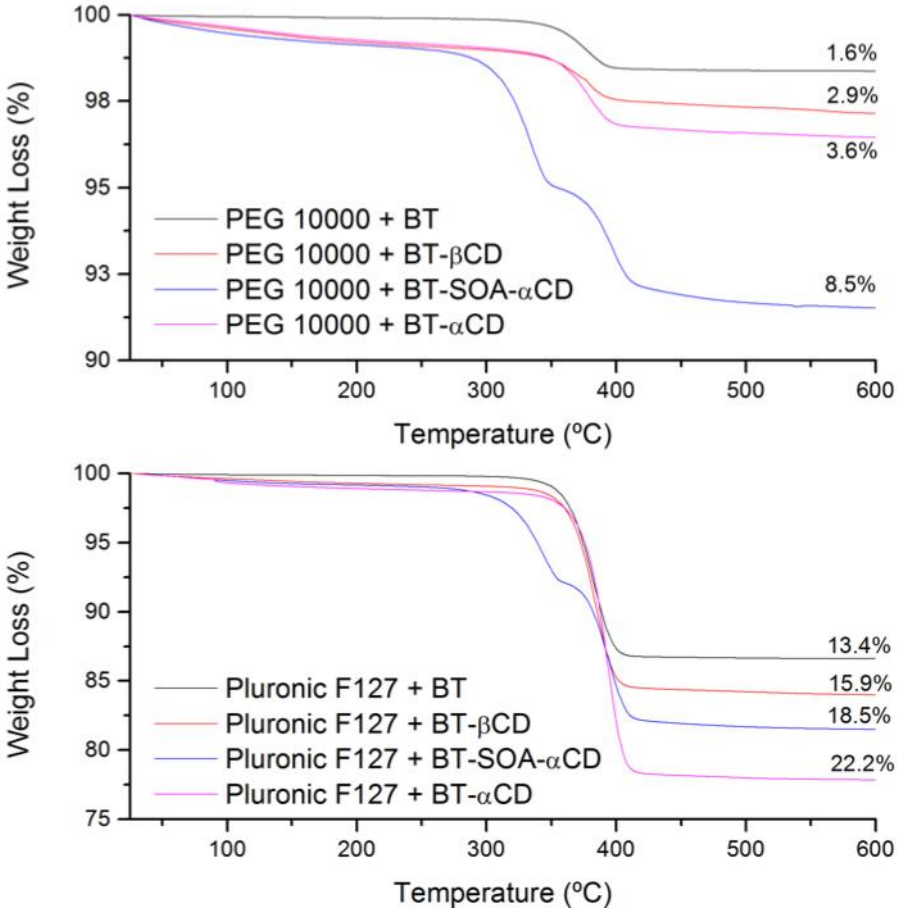

Fig. 3.11: Coating of PEG and Pluronic® F127 on the BT nanoparticles before and after the different surface treatments.

b) Interaction of the modified nanoparticles with thermoplastic polymers and solid state dispersion methods.

On a second step we mixed by cryo-HEBM the modified BT with EVA at a 20 wt% proportion to ensure the surface modifications applied are kept and contribute to achieve a good dispersion in the solid state preparations. The powders were processed into films and characterized by FTIR-ATR and TGA to evaluate the effect the HEBM produces on the nanoparticles and its surface modifications.

The main bands of the EVA polymer are in the same positions as the SOA ones (Fig. 3.12), as they mainly consist of $-CH_2-$ groups. However in the samples where αCD is added an absorbance increase of the -OH band over 3000 cm^{-1} can be observed, as well as that of the characteristic bands of the CD at 1000, 1078 and 1150 cm^{-1}.

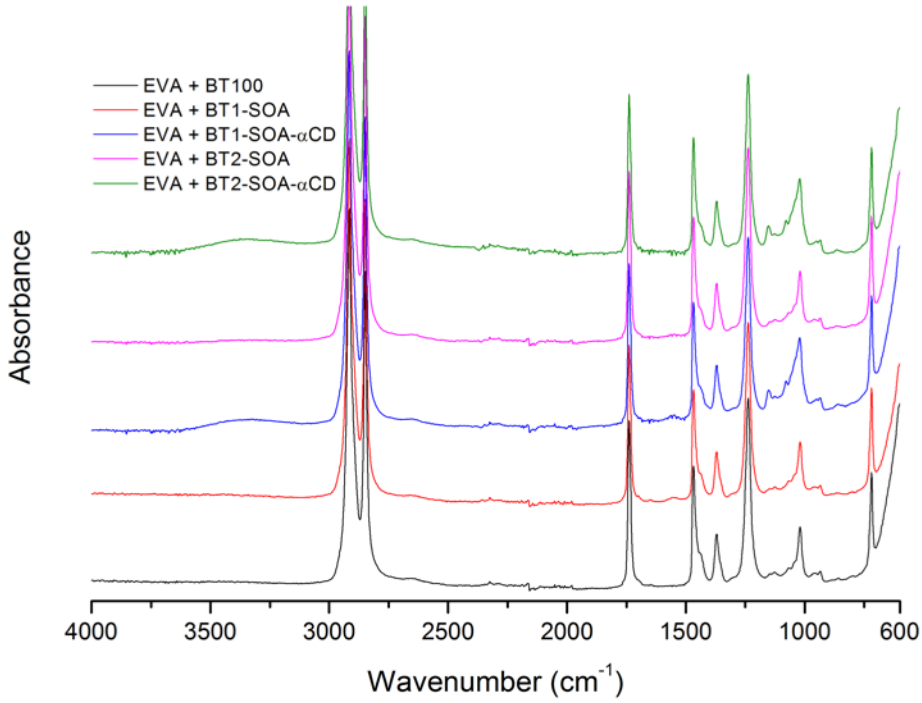

Fig. 3.12: FTIR-ATR spectra of the SOA-αCD modified samples after HEMB with EVA.

In the samples where only the CDs are attached to the nanoparticles their characteristic bands in FTIR cannot be seen well (Fig. 3.13 top), being hidden under the EVA ones due to the low amount of oligosaccharide (the CDs represent just 1% of the filler in this case, which corresponds to the 20 wt% of the composite with EVA, accounting for the small contribution of the small band from the CDs OH groups above 3000 cm^{-1}).

Similar conclusions can be extracted from the TGA analysis (Fig. 3.14). The EVA thermodegradation occurs within the same temperature range than the SOA and CD. The degradation process for the thermoplastic takes place in two stages. In the first one, deacylation with the loss of acetic acid and the formation of double bonds occurs between 300 and 400 ˚C, with a maximum rate of degradation at around 370 ˚C. In the second step the olefin degradation between 450 and 520 ˚C takes place (Zattera et al. 2005). Both processes overlap the SOA and CD ones, so only the proportion between the total amount of filler and the polymeric matrix can be deduced from the thermal analysis.

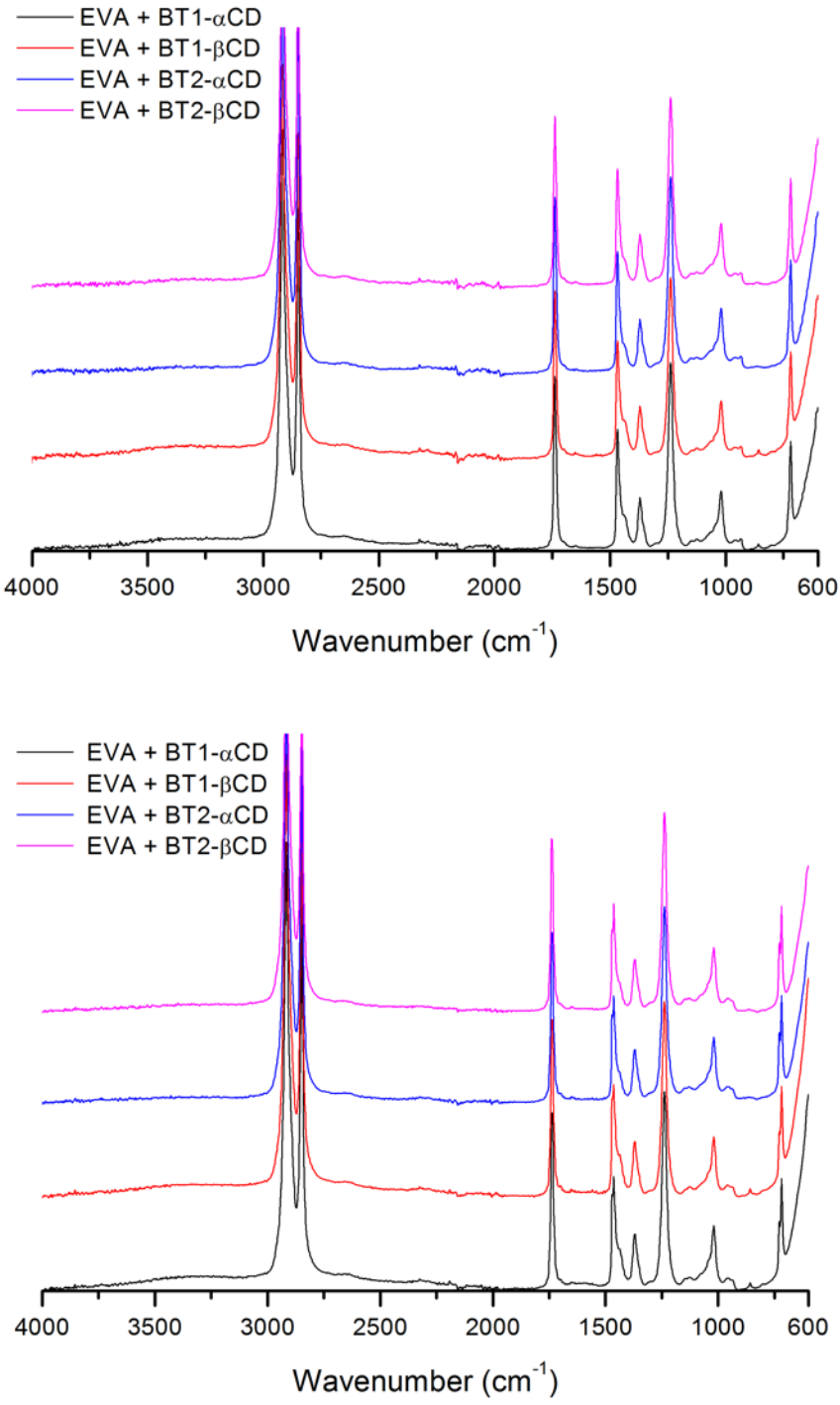

Fig. 3.13: FTIR-ATR spectra of the CD modified samples after HEBM with EVA and film casting.

Lastly, as another example of the dispersion from water casting, the nanoparticles were dispersed in a 1% (w/v) polyethylene oxide aqueous solution. As a result thin films were obtained as shown in Fig. 3.14 (right), where the uniform dispersion achieved is comparable to that obtained by solid-state methods (Fig. 3.14 left).

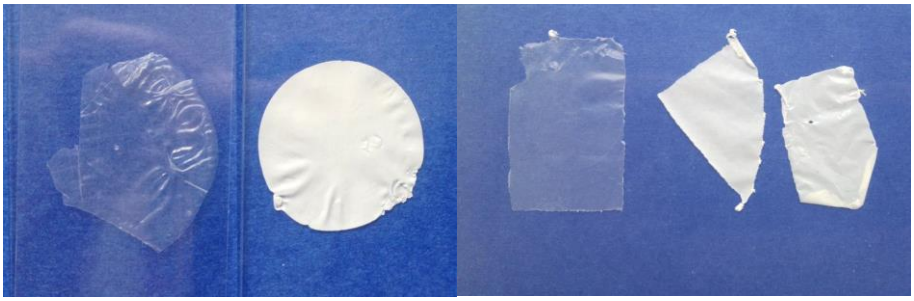

Fig. 3.14: Films casted from EVA samples prepared by HEBM (left) and PEO samples prepared by water suspension (right).

c) Impedance Spectroscopy tests on films prepared from solid and water based precursors.

In the frequency response analysis (FRA, impedance spectroscopy) the magnitude being measured is the complex impedance of the samples. The dielectric parameters as a function of frequency are described by the complex impedance in the form of (Tripathi et al. 2012):

[1] $$Z = Z' + iZ''$$

where *Z'* and *Z''* are real and imaginary part of the complex impedance.

[2] $$\mathrm{Z}(\omega) = \mathrm{U}(\omega)\mathrm{I}\omega = 1\mathrm{i}\omega\mathrm{C}\omega$$ [3] $$\mathrm{C}(\omega) = \frac{\mathrm{A}}{\mathrm{d}}\varepsilon(\omega)$$

The capacitance is defined by [3]. Where *A* is the area of the dielectric and *d* the thickness of the sample. The polarization phenomenon exerted by the oscillatory electric field applied during the FRA measurement can be modeled in many dielectric materials using a series RC circuit connected in parallel with another capacitor, which has been the model to fit the experimental (Fig. 3.15).

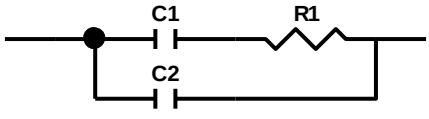

Fig. 3.15: Equivalent circuit for the measured samples.

From this equivalent circuit and taking into account the Debye model (Scaife 1998) the following parameters can be deduced (Jonscher 1983):

[4] $\varepsilon_s = \frac{C_1 + C_2}{\frac{A}{d}}$ [5] $\varepsilon_\infty = \frac{C_2}{\frac{A}{d}}$ [6] $\tau = R_1 C_1$

Where C_1 and C_2 are the capacities values associated to the bulk and the interphase, respectively, as C_1 relates to the atomic polarization and C_2 to the fastest dipoles, and from them, the real and imaginary parts of the permittivity as well as the loss factor can be obtained. The values thus calculated have been gathered in Table 4, where the low error values indicate the goodness of fit.

Table 3.4: C1, C2 and R-values calculated from Impedance Spectroscopy on selected samples.

Sample	C1 (nF)	R1 (MΩ)	τ (x10^2 s)	C2 (pF)
EVA	9.3 ± 0.2	9.01 ± 0.09	8.4± 0.1	54.1 ± 0.4
EVA + BT100	9.3 ± 0.2	8.92 ± 0.08	8.3± 0.1	52.4 ± 0.4
EVA + BT1-SOA-αCD	9.3 ± 0.2	8.92 ± 0.08	8.3± 0.1	66.3 ± 0.5
EVA + BT2-SOA-αCD	9.3 ± 0.2	9.00 ± 0.09	8.3± 0.1	65.3 ± 0.5
EVA + BT1-αCD	9.3 ± 0.2	8.94 ± 0.08	8.3± 0.1	47.0 ± 0.4
EVA + BT2-αCD	9.3 ± 0.2	8.93 ± 0.08	8.3± 0.1	58.6 ± 0.5
EVA + BT1-βCD	9.3 ± 0.2	8.92 ± 0.08	8.3± 0.1	47.5 ± 0.4
EVA + BT2-βCD	9.3 ± 0.2	8.93 ± 0.08	8.3± 0.1	52.4 ± 0.4
PEO	26 ± 2	2.65 ± 0.07	6.8± 0.1	113 ± 3
PEO + BT-αCD	11.6 ± 0.4	6.40 ± 0.09	7.4± 0.1	119 ± 2

The two sets of samples present significant differences. In the case of the samples prepared by HEBM there is no difference in the capacity of the bulk (C1), when comparing the pure polymer with composites, which is also expected due to the low relative amount of filler. However, in the case of the capacity associated to the interphase there are differences that can be attributed solely to the different modifications of the nanoparticles since they are higher than the defined errors. While EVA and EVA+BT100 (without modification) present the same values, in the case of the nanoparticles have been modified with oleate and CD there is a 20% increase. For the samples modified only with CDs the difference appears for the samples of BT 100 nm with higher changes than those obtained for BT 200 nm, regardless the type of CD probably because a higher polar surface area is facilitating the

polarization. In the case of the water casted PEO the opposite trend is seen, a dramatic decrease in the C1 contribution when the nanoparticles are dispersed in the polymer and a two-fold increment of the resistance, however, the interphase contribution remains practically the same. In this case, the effect of the nanoparticles on the PEO system is by far more important than that exerted on the EVA polymer. The particles may intercalate in the PEO chains and therefore change their structure, crystallization and rearrangement capacity in the system, similar to what Scrosati et al., mention in their study of PEO nanocomposites with polymer electrolytes (Scrosati et al. 2000).

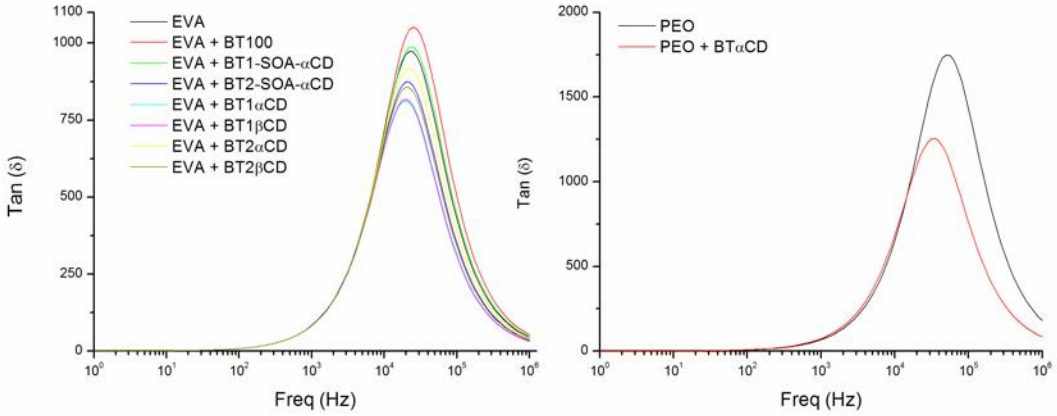

Fig. 3.16: Impedance spectroscopy loss factor measurements on selected samples with BT: EVA samples (left) and PEO samples (right).

These different behaviors can be better visualized in the loss tangent plots (Fig 3.16) showing a decrease in the height of the peaks as well as a shift to lower frequencies upon addition of the BT. As the relaxation behavior in polymeric nanocomposites depends on the interaction of the filler with the polymeric matrix, it can be concluded that the observed shifts are the result of the modifications made to the BT leading to slightly different interactions between the matrix and the nanoparticles surface. The differences also show that the modifications produced on the nanoparticles are kept despite the high-energy conditions of the HEBM or the milder ones of the water casting process.

The results described herein, particularly the chemical modification of the nanoparticles with CDs and their good cytocompatibility, encourages us to further pursue technological applications for them. The multifunctionality of the nanoparticles acquired by grafting different types of CDs to the surface could allow for selective delivery platforms in addition to the ones explored by Genchi and Dempsey (Genchi et al. 2016; Dempsey et al. 2013). Moreover, it opens the possibility of preparing nanocomposite hydrogels with

enhanced mechanical properties, thanks to the improvement of the stability in water of the nanoparticles and, in the case of the piezoelectric $BaTiO_3$, the production of stimuli-responsive hydrogels (Stuart et al. 2010). These hydrogels are bound to respond to external stimuli, such as thermal, chemical (pH, for example), electrical or magnetic ones, with the subsequent triggering of structural changes. Advantage can be taken from these changes for the release of active compounds, of utmost interest for tissue engineering, drug delivery and microfluidic applications, among others (Koetting et al. 2015).

4. CONCLUSIONS

A novel way of modification of barium titanate nanoparticles has been achieved by the incorporation of cyclodextrins to their surface, with the aim of using them as nanofillers in nanocomposites. While oleate-modified particles also present some degree of aggregation in water, due to the hydrophobicity of the chains, once the hydrocarbon tails have been included in the cavity of the αCDs the stability of the suspension over time is increased. However, when incorporating αCD and βCD directly on the surface the disaggregation takes place much faster and is maintained through the same period of time, becoming an easier, faster and cleaner way of modification. Moreover, the addition of CDs bestows the nanoparticles extra-functionality due to the wide array of host-guest interactions that can be formed within the CD cavity, as tested by analyzing the fluorescence of rhodamine B that is included in the macrocycles, attached to the nanospheres surface. This opens a whole range of potential uses for these nanoparticles by their combination with drugs and molecules that could be transported and released in a controlled way, particularly in the case of biocomposites. The cytotoxicity of the modified nanoparticles with fibroblasts and pre-osteoblasts cell lines has been assessed with excellent results in a wide range of concentrations. The surface modification with CDs allows the nanoparticles to be suspended in aqueous solutions of different polymers (PEO, PEG and Pluronic F-127) and the further casting of films, with very good results in terms of particle dispersion. The same conclusion is reached with the films obtained from the solid mixtures produced by HEBM with a thermoplastic polymer (EVA). In the latter case, the data obtained by impedance spectroscopy suggest that even little modifications in the surface of the nanoparticles involve a different kind of interaction with the polymeric matrix, as seen by the changes in the dielectric behavior. The modified nanoparticles are thus suitable for easy preparation either of water-based nanocomposites as hydrogels or nanocomposites of thermoplastic matrices.

5. REFERENCES

Baxter, F.R. et al., 2009. An in vitro study of electrically active hydroxyapatite-barium titanate ceramics using Saos-2 cells. *Journal of materials science. Materials in medicine*, 20(8), pp.1697–708.

Beier, C.W., Cuevas, M. a & Brutchey, R.L., 2010. Effect of surface modification on the dielectric properties of BaTiO3 nanocrystals. *Langmuir : the ACS journal of surfaces and colloids*, 26(7), pp.5067–71.

Blanco-Lopez, M.C., Rand, B. & Riley, F.L., 1997. The properties of aqueous phase suspensions of barium titanate. *Journal of the European Ceramic Society*, 17(2–3), pp.281–287.

Chang, S.-J. et al., 2009. An efficient approach to derive hydroxyl groups on the surface of barium titanate nanoparticles to improve its chemical modification ability. *Journal of colloid and interface science*, 329(2), pp.300–5.

Chaudhary, Y.S., Bhatta, U.M. & Khushalani, D., 2011. Octyl-β-D-glucopyranoside mediated synthesis of nanocrystalline BaTiO3 using a single-source precursor. *Journal of Materials Research*, 23(3), pp.842–848.

Choudhury, A., 2012. Preparation, characterization and dielectric properties of polyetherimide nanocomposites containing surface-functionalized BaTiO3 nanoparticles. *Polymer International*, 61(5), pp.696–702.

Ciofani, G., Danti, S., D'Alessandro, D., et al., 2010. Barium Titanate Nanoparticles: Highly Cytocompatible Dispersions in Glycol-chitosan and Doxorubicin Complexes for Cancer Therapy. *Nanoscale research letters*, 5(7), pp.1093–101.

Ciofani, G. et al., 2013. Effects of barium titanate nanoparticles on proliferation and differentiation of rat mesenchymal stem cells. *Colloids and surfaces. B, Biointerfaces*, 102, pp.312–20.

Ciofani, G., Danti, S., Moscato, S., et al., 2010. Preparation of stable dispersion of barium titanate nanoparticles: Potential applications in biomedicine. *Colloids and surfaces. B, Biointerfaces*, 76(2), pp.535–43.

Čulić-Viskota, J. et al., 2012. Surface functionalization of barium titanate SHG nanoprobes for in vivo imaging in zebrafish. *Nature protocols*, 7(9), pp.1618–33.

Dempsey, C. et al., 2013. Coating barium titanate nanoparticles with polyethylenimine improves cellular uptake and allows for coupled imaging and gene delivery. *Colloids and surfaces. B, Biointerfaces*, 112, pp.108–12.

FarrokhTakin, E. et al., 2012. Synthesis and characterization of new barium titanate core–gold shell nanoparticles. *Colloids and Surfaces A: Physicochemical and Engineering Aspects*, 415, pp.247–254.

Feng, J., Yuan, H. & Zhang, X., 1997. Promotion of osteogenesis by a piezoelectric biological ceramic. *Biomaterials*, 18(23), pp.1531–4.

Gaharwar, A.K. et al., 2013. Bioactive silicate nanoplatelets for osteogenic differentiation of human mesenchymal stem cells. *Advanced materials*, 25(24), pp.3329–36.

Gaharwar, A.K. et al., 2011. Highly extensible, tough, and elastomeric nanocomposite hydrogels from poly(ethylene glycol) and hydroxyapatite nanoparticles. *Biomacromolecules*, 12(5), pp.1641–50.

Gao, J. et al., 2015. Factors influencing formation of highly dispersed BaTiO3 nanospheres with uniform sizes in static hydrothermal synthesis. *Journal of Nanoparticle Research*, 17(7), p.286.

Genchi, G.G. et al., 2016. Barium titanate nanoparticles: promising multitasking vectors in nanomedicine. *Nanotechnology*, 27(23), p.232001.

González-Gaitano, G. et al., 2002. The aggregation of cyclodextrins as studied by photon correlation spectroscopy. *Journal of Inclusion Phenomena*, 44, pp.101–105.

Gonzalez-Gaitano, G., Crespo, A. & Tardajos, G., 2000. Thermodynamic Investigation (Volume and Compressibility) of the Systems -Cyclodextrin + n- Alkyltrimethylammonium Bromides + Water. *Journal of Physical Chemistry B*, 104(8), pp.1869–1879.

Hiroki, a & Laverne, J. a, 2005. Decomposition of hydrogen peroxide at water-ceramic oxide interfaces. *The journal of physical chemistry. B*, 109(8), pp.3364–70.

Hsieh, C.-L. et al., 2010. Bioconjugation of barium titanate nanocrystals with immunoglobulin G antibody for second harmonic radiation imaging probes. *Biomaterials*, 31(8), pp.2272–7.

Huang, T. et al., 2007. A Novel Hydrogel with High Mechanical Strength: A Macromolecular Microsphere Composite Hydrogel. *Advanced Materials*, 19(12), pp.1622–1626.

Jean, J.-H. & Wang, H.-R., 2005. Dispersion of Aqueous Barium Titanate Suspensions with Ammonium Salt of Poly(methacrylic acid). *Journal of the American Ceramic Society*, 81(6), pp.1589–1599.

Jeong, C.K. et al., 2013. Virus-Directed Design of a Flexible BaTiO3 Nanogenerator. *ACS Nano*, 7(12), pp.11016–11025.

Jonscher, A.K., 1983. *Dielectric Relaxation in Solids*, London: Chelsea Dielectric Press.

Kim, P. et al., 2007. Phosphonic Acid-Modified Barium Titanate Polymer Nanocomposites with High Permittivity and Dielectric Strength. *Advanced Materials*, 19(7), pp.1001–1005.

Knauert, S.T. et al., 2007. The Effect of Nanoparticle Shape on Polymer-Nanocomposite Rheology and Tensile Strength. *Journal of Polymer Science: Part B: Polymer Physics*, 45, pp.1882–1897.

Koetting, M.C. et al., 2015. Stimulus-responsive hydrogels: Theory, modern advances, and applications. *Materials Science and Engineering R: Reports*, 93, pp.1–49.

Larrañeta, E. & Isasi, J., 2012. Self-assembled supramolecular gels of reverse poloxamers and cyclodextrins. *Langmuir*, (28), pp.12457–12462.

Li, L. et al., 2006. Synthesis of anatase TiO2 nanoparticles with beta-cyclodextrin as a supramolecular shell. *Chemistry - an Asian journal*, 1(5), pp.664–668.

Lingley, Z. et al., 2013. Nanocrystal-semiconductor interface: Atomic-resolution cross-sectional transmission electron microscope study of lead sulfide nanocrystal quantum dots on crystalline silicon. *Nano Research*, 7(2), pp.219–227.

Mamana, N. & Pellegri, N., 2015. Functional BaTiO3 nanostructures immobilized onto si-based substrates using sol–gel and reverse micelle techniques. *Journal of Nanoparticle Research*, 17(3), p.115.

Olmos, D. et al., 2011. Effect of the presence of silica nanoparticles in the coefficient of thermal expansion of LDPE. *European Polymer Journal*, 47(8), pp.1495–1502.

Ozel, F. et al., 2013. Superparamagnetic iron oxide nanoparticles: effect of iron oleate precursors obtained with a simple way. *Journal of Materials Science: Materials in Electronics*, 24(8), pp.3073–3080.

Paik, U. et al., 2002. Dissolution and reprecipitation of barium at the particulate BaTiO3–aqueous solution interface. *Materials Research Bulletin*, 37(9), pp.1623–1631.

Paik, U. et al., 1998. The effect of electrostatic repulsive forces on the stability of BaTiO3 particles suspended in non-aqueous media. *Colloids and Surfaces A: Physicochemical and Engineering Aspects*, 135(1–3), pp.77–88.

Park, S.-E. & Shrout, T.R., 1997. Ultrahigh strain and piezoelectric behavior in relaxor based ferroelectric single crystals. *Journal of Applied Physics*, 82(4), p.1804.

Ring, K.M. & Kavanagh, K.L., 2003. Substrate effects on the ferroelectric properties of fine-grained BaTiO[sub 3] films. *Journal of Applied Physics*, 94(9), p.5982.

Saenger, W. et al., 1998. Structures of the Common Cyclodextrins and Their Larger Analogues-Beyond the Doughnut. *Chemical reviews*, 98(5), pp.1787–1802.

Sakai, T., Hoshiai, S. & Nakamachi, E., 2006. Biochemical compatibility of PZT piezoelectric ceramics covered with titanium thin film. *Journal of Optoelectronics and Advanced Materials*, 8(4), pp.1435–1437.

Scaife, B.K.P., 1998. *Principles of Dielectrics*, New York: Oxford University Press.

Schexnailder, P. & Schmidt, G., 2008. Nanocomposite polymer hydrogels. *Colloid and Polymer Science*, 287(1), pp.1–11.

Scrosati, B., Croce, F. & Persi, L., 2000. Impedance Spectroscopy Study of PEO-Based Nanocomposite Polymer Electrolytes. *Journal of The Electrochemical Society*, 147(5), p.1718.

Serra-Gómez, R. et al., 2012. Rhodamine solid complexes as fluorescence probes to monitor the dispersion of cyclodextrins in polymeric nanocomposites. *Dyes and Pigments*, 94(3), pp.427–436.

Serra-Gómez, R., Gonzalez-Gaitano, G. & González-Benito, J., 2012. Composites based on EVA and barium titanate submicrometric particles: Preparation by high-energy ball milling and characterization. *Polymer Composites*, 33(9), pp.1549–1556.

Shi, J. et al., 2010. Nanotechnology in drug delivery and tissue engineering: From discovery to applications. *Nano Letters*, 10, pp.3223–3230.

Shiraishi, Y. et al., 2015. Effect of Particle Size on Electro-Optic Properties of Liquid Crystal Devices Doped with γ-Cyclodextrin Stabilized Barium Titanate Nanoparticles. *Molecular Crystals and Liquid Crystals*, 611(1), pp.100–108.

Städe, L.W. et al., 2015. Nonfouling Tunable βCD Dextran Polymer Films for Protein Applications. *ACS Applied Materials & Interfaces*, 7, pp.4160–4168.

Stuart, M.A.C. et al., 2010. Emerging applications of stimuli-responsive polymer materials. *Nature Materials*, 9(2), pp.101–113.

Sun, X. et al., 2008. Synthesis of BaTiO3 nanocrystals with beta-cyclodextrin as a supramolecular shell. *Wuji Huaxue Xuebao*, 24(1), pp.93–97.

Tripathi, S.K., Gupta, A. & Kumari, M., 2012. Dielectric and Modulus spectra_____Studies on electrical conductivity and dielectric behaviour of PVdF–HFP–PMMA–NaI polymer blend electrolyte. *Bulletin of Materials Science*, 35(6), pp.969–975.

Tsuchiya, K. et al., 2011. Design of biocompatible high-piezoelectric BaTiO3 with additives. In S. Juodkazis & M. Gu, eds. *Smart Nano-Micro Materials and Devices*. International Society for Optics and Photonics, p. 82042A.

Wang, H. et al., 2013. Development of injectable organic/inorganic colloidal composite gels made of self-assembling gelatin nanospheres and calcium phosphate nanocrystals. *Acta biomaterialia*, 10(1), pp.508–519.

Yu, C.-R. et al., 2011. Electrical and dielectric properties of polypropylene nanocomposites based on carbon nanotubes and barium titanate nanoparticles. *Composites Science and Technology*, 71(15), pp.1706–1712.

Zattera, A.J. et al., 2005. Characterization of EVA residues from the shoe industry and post-consumer urban-waste polyethylenes. *Cellular Polymers*, 24, pp.139–158.

Chapter 4

Structure and Rheology of Poloxamine T1107 and its Nanocomposite Hydrogels with Cyclodextrin-Modified Barium Titanate Nanoparticles

Langmuir
DOI: 10.1021/acs.langmuir.6b01544

Abstract

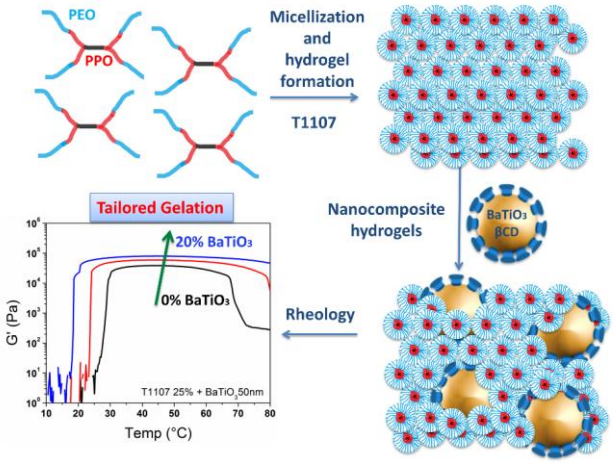

We report the preparation of a nanocomposite hydrogel based on a poloxamine gel matrix (Tetronic® T1107) and cyclodextrin (CD)-modified Barium Titanate (BT) nanoparticles. The micellization and sol-gel behaviour of pH-responsive block-copolymer T1107 were fully characterised by small-angle neutron scattering (SANS), dynamic light scattering (DLS), and FTIR-ATR spectroscopy as a function of concentration, pH and temperature. SANS results reveal that spherical micelles in the low concentration regime present a dehydrated core and highly hydrated shell, with a small aggregation number and size, highly dependent on the degree of protonation of the central amine spacer. At high concentration, T1107 undergoes a sol-gel transition, which is inhibited at acidic pH. Nanocomposites were prepared by incorporating CD-modified BT of two different sizes (50 nm and 200 nm) in concentrated polymer solutions. Rheological measurements show a broadening of the gel region, as well as an improvement of the mechanical properties, as assessed by the shear elastic modulus, G' (up to 200% increase). Initial cytocompatibility studies of the nanocomposites show that the materials are non-toxic with viabilities over 70% for NIH3T3 fibroblast cell lines. Overall, the combination of Tetronics and modified $BaTiO_3$ provides easily customizable systems with promising applications as soft piezoelectric materials.

1. INTRODUCTION

Nanocomposite hydrogels are emerging as an attractive concept to craft materials with tailored properties, such as mechanical, optical, electrical, as well as promoting a specific biological response (self-healing materials, mechano-actuators, triggered delivery, etc.) (da Silva & Dreiss 2016). The combination of a polymer gel matrix (which affords mechanical support, phase modulation and a hydrated environment) with nanoparticles (bringing specific functionalities, such as optical, magnetic, piezoelectric, antimicrobial…) is the basis of obtaining fascinating properties, that may result from a synergistic interplay between matrix and filler (da Silva & Dreiss 2016).

A promising type of matrix to produce nanocomposite hydrogels are poloxamines, also known by the commercial name of Tetronics® (BASF). They are amphiphilic block copolymers, presenting an original X shape, where each of the four arms is made of a poly(propylene oxide) (PPO) and a poly(ethylene oxide) (PEO) block connected by a central ethylene diamine spacer. The number of PO and EO units that form the arms can be varied, offering a wide range of Mw and HLB values, and hence a rich phase behaviour and custom-made properties, both in terms of thermal and pH response (Gonzalez-Lopez et al. 2008; Larrañeta & Isasi 2013; González-Gaitano, da Silva, et al. 2015). PEO-PPO-based polymeric micelles are now emerging as promising formulation candidates in the biomedical field, being available in large quantities in a large array of architectures, at low-cost, and also showing biological inhibitory activity of drug efflux pumps (Cuestas et al. 2011; Alvarez-Lorenzo et al. 2011). The more well-known linear counterparts of Tetronics - Pluronic – are currently undergoing clinical trials with the cancer drug doxorubicin (Alakhova & Kabanov 2014) and the recent demonstration of the ability of Tetronics to also inhibit ATP-binding cassette transporters in cancer cell lines, responsible for multidrug resistance (Cuestas et al. 2011), added to their pH-responsiveness, has recently brought them into the spotlight as serious contenders in the biomedical field (Alvarez-Lorenzo et al. 2011). Indeed, they have been proposed as water-soluble copolymers for injectable formulations (Annaka et al. 2011), nanocarriers for drug and gene delivery (Alvarez-Lorenzo et al. 2010; Zhang et al. 2014) and in tissue engineering for bone regeneration (Rey-Rico et al. 2011).

The introduction of different types of nanoparticles into hydrogels is a successful way to not only improve existing characteristics (such as gel elasticity and toughness), but also add extra functionalities to the hydrogels (Balazs et al. 2013; Schexnailder & Schmidt 2008; Chu et al. 2013), resulting in new, functional materials. Extensive research is being carried out in this field covering a wide range of nanofillers, which, used in relatively low amounts,

can yield remarkable changes in the final properties. Some examples are clays as natural and synthetic laponites (Wu et al. 2011), ceramics as hydroxyapatite (HA) or beta-tricalcium phosphate (β-TCP) for bone regeneration (Gaharwar et al. 2011; Chen et al. 2012) and delivery of growth factors (Nguyen et al. 2012). Metallic nanoparticles such as silver and gold constitute other approaches, chosen for their antimicrobial properties (Fan et al. 2014), as well as multi-wall carbon nanotubes (MWCNT) and graphene oxide (GO), which are also exploited to create electrically active hydrogels mimicking cardiac tissue with mechano-actuation (Shin, Aghaei-Ghareh-Bolagh, et al. 2013), and polymer colloids to develop hydrogels for adhesives and surgical sealants (Cho et al. 2012).

A substantial amount of work is focusing on inorganic nanoparticles and ceramics as bioactive components in bioengineering (Wang et al. 2013; Pina et al. 2015), such as bioactive silica nanoparticles for improved osteogenesis (Schiraldi et al. 2004; Gaharwar et al. 2013) or TiO_2 for antibacterial biodegradable hydrogels (Si et al. 2013). In this work, we focus on Barium Titanate ($BaTiO_3$, BT) nanoparticles, a perovskite-type ferroelectric ceramic that possesses a high dielectric constant with piezoelectric properties (in its tetragonal, orthorhombic and rhombohedral crystalline phases). BT has been replaced in some - mainly electric - applications by multiceramic materials, such as lead zirconate titanates, or PZTs. However, PZTs are not appropriate for biomedical applications due to the high toxicity of the lead component, and BT has been suggested as a good piezoelectric alternative due its better biocompatibility (Jeong et al. 2013; Sakai et al. 2006; Tsuchiya et al. 2011). Some examples are as second harmonic generators for imaging applications (Dempsey et al. 2013; Hsieh et al. 2010) and in drug and gene delivery as nanocarriers and vectors (Ciofani, Danti, Moscato, et al. 2010; Jeong et al. 2013). In bone regeneration in particular, BT presents potential as a ceramic filler; its piezoelectricity and interaction with the dipoles formed on the collagen fibres of the inner bone have been shown to promote bone regeneration, as they are able to generate small electrical impulses under minimal mechanic stress, enhancing the cellular and tissue stimulation for the healing process (Barrère et al. 2008; Feng et al. 1997; Baxter et al. 2009).

The main problem to overcome is that ceramic nanoparticles usually present poor processability and high aggregation due to their high area-to-volume ratio (Blanco-Lopez et al. 1997; Paik et al. 2002). This problem may be overcome by surface modification of the nanoparticles. Based on our substantial work on cyclodextrins (González-Gaitano, da Silva, et al. 2015; Serra-Gómez et al. 2012), we explore here the effect of surface modification of BT with cyclodextrins (CDs)(Serra-Gómez et al. 2016) prior to their introduction in the

hydrogel matrix. Once the nanocomposite hydrogel has been prepared, the physical and chemical interaction between the matrix and the nanofiller is a determining factor for modulating the properties, which in our case are the changes in the sol-gel transition temperature and the improvement of the mechanical response of the hydrogels.

While it is clear that the introduction of nanoparticles inside a gel matrix may improve the mechanical properties and generally the functionality of the material, there are still few fundamental studies aiming at elucidating structural changes induced by the presence of the nanoparticles, in particular using techniques such as small-angle neutron scattering (SANS). A few exceptions are the studies by Namban and Philip's on the influence of Fe_3O_4 nanoparticles in a matrix of Pluronics (Nambam & Philip 2012), the introduction of clays such as laponite nanoparticles into Pluronic gels (Sun & Raghavan 2010) and other ABA-type triblock copolymer hydrogels (Agrawal et al. 2008), Annaka et al (Annaka et al. 2012). reported SANS studies where the introduction of hydrophilized silica nanoparticles (to match the refractive index of the natural lens) impacted the temperature and concentration regime of gel formation; SANS measurements showed that the silica particles did not affect micellar size but decreased their effective volume fraction. Tamborini et al (Tamborini et al. 2012) also used SANS to study the nanocomposite structure of Pluronic crystals and silica nanoparticles as a function of the temperature rate used during preparation, where the volume fraction of the silica nanoparticles is kept low and their size are similar to the micelles.

Within this framework, the objective of this work was to develop soft nanocomposites, using naturally gelling, low-cost poloxamines as a gel matrix, combined with piezoelectric $BaTiO_3$ nanoparticles, chemically modified with cyclodextrins (Serra-Gómez et al. 2016) for improved compatibility. The $BatiO_3$ particles are relatively large compared to the micelles and introduced up to high volume fraction (20 wt%). In the first part of this work, we perform a thorough characterisation of the structural changes that lead to T1107 micellization and sol-gel transition, as a function of concentration, pH and temperature, using a combination of techniques (SANS, DLS and FTIR-ATR). Following this, cyclodextrin-modified BT nanoparticles of two different sizes are introduced in the polymer matrix to produce nanocomposite gels, which are characterised both rheologically and spectroscopically, with particular focus on the structural and mechanical changes induced by the addition of the nanofiller. Finally, cytotoxicity and cytocompatibility assays of the nanocomposites at different concentrations, in solution as well as in the gel phase, are performed, as an initial evaluation of their suitability as biomaterials.

2. MATERIALS AND METHODS

2.1. Materials

Tetronic 1107 (T1107) was a gift from BASF, with a reported composition per arm of 60 EO and 20 PO, HLB 18-23 and average molecular weight 15.000 $g \cdot mol^{-1}$. Inorganic nanoparticles of barium titanate (BT, $BaTiO_3$), with an average diameter of 200 nm were supplied by Nanostructured and Amorphous Materials Inc. (tetragonal crystalline structure, 99.9% purity, ρ = 6.02 $g \cdot cm^{-3}$), while nanoparticles of 50 nm in diameter were supplied by Sigma-Aldrich (cubic crystalline structure, 99.9% purity, ρ = 6.08 $g \cdot cm^{-3}$).

2.2. Preparation of $BaTiO_3$ NPs

BT nanoparticles present strong aggregation that leads to rapid precipitation in water. Surface modification of the NPs with β-cyclodextrin (CD) was performed to overcome this problem, according to the two-step procedure described in a previous work (Serra-Gómez et al. 2016), consisting in the generation of hydroxyl groups on the surface by reaction with H_2O_2, followed by mixing with a 10 mM β-CD solution under vigorous stirring. The resulting nanoparticles are centrifuged and washed three times to remove reagents in excess and freeze-dried for storage.

2.3. Small-Angle Neutron Scattering (SANS)

Small-angle neutron scattering (SANS) experiments were carried out on LOQ instrument at ISIS spallation neutron source (ISIS, Rutherford-Appleton Laboratory, STFC, Didcot, Oxford). LOQ uses incident wavelengths from 2.2 to 10.0 Å, sorted by time-of-flight, with a fixed sample-detector distance of 4.1 m, which provides a range of scattering vectors (q) from 0.009 to 0.29 $Å^{-1}$. The samples were prepared in D_2O (Aldrich, > 99.9% in D) and placed in clean disc-shaped quartz cells (Hellma) of either 1 or 2 mm path length, controlling the temperature from 20 to 50 °C with an external thermostat. In the case of experiments in acidic solutions, the necessary volume of concentrated HCl was added to the samples to reach the desired pH. All scattering data were first normalised for sample transmission and then background-corrected using a quartz cell filled with D_2O to compensate for the inherent instrumental background, and finally corrected for the linearity and efficiency of the detector response using instrument-specific software package. The data were then converted to differential scattering cross-sections expressed in absolute units of cm^{-1} using the standard procedures at ISIS. Some additional samples (Fig. 4.6) were measured on D22 at the Institut Laue-Langevin (ILL), The wavelength λ was set at 6 Å, the peak flux of the cold source. The sample-to-detector distance was 4 m with a collimation at 5.6 m and a detector

offset of 400 mm to maximize the available q-range using rectangular cells of 1mm of path length. All samples for SANS analysis were made in D_2O to ensure sufficient contrast between the polymer and the solvent.

SANS curves were fitted using the SasView 3.1.0 software and a brief explanation of the models can be found in the SI.(Anon n.d.) Scattering curves from T1107 in its unimer form were fitted with a four-arm star-shape polymer model (Benoit 1953), while micelles were fitted to a core-shell sphere (CSS) model combined with a hard-sphere structure factor. When letting the scattering length density (sld) of the micellar core float, this value converged consistently to values similar to that of pure PO (ρ_{PO} = 3.44×10^{-7} Å^{-2}), therefore this parameter was fixed in the fits, reflecting the fact that the micellar core is largely dehydrated, as observed with other poloxamines under dilute conditions (González-Gaitano, da Silva, et al. 2015; González-Gaitano, Müller, et al. 2015). Instead, the shell is extensively hydrated, and the level of hydration can be estimated from the fitted value of the sld of the PEO shell, ρ_{shell}. The volume fraction (occupied volume divided by the total volume) of solvent in the corona, x_{solv}, is related to the sld of the shell, PEO block and D_2O by:

$$x_{solv} = \frac{\rho_{shell} - \rho_{EO}}{\rho_{D_2O} - \rho_{EO}} \quad \text{Eq. 1}$$

The number of water molecules, n_{solv}, in the shell is obtained from:

$$n_{D_2O} = x_{solv} \frac{V_{shell}}{V_{D_2O}} \quad \text{Eq. 2}$$

where v_{D_2O} is the volume of a molecule of solvent. The number of water molecules per EO group, n_{solv}/EO, can then be obtained from Eq. 2 and the value of the aggregation number, N_{agg}, is obtained from the hydration of the shell and the structural parameters of the core-shell model. Provided that the amount of water inside the core is negligible, the volume of the micelle is:

$$V_m = N_{agg} V_s + x_{solv} V_{shell} \quad \text{Eq. 3}$$

where v_s is the volume of a surfactant molecule. N_{agg} can be extracted by introducing into the equation the volume fraction of solvent in the shell, x_{solv}, deduced from Eq. 1.

SANS data for the nanocomposites were analysed by a combination of the CSS and a generic power law model (CSS+PL), as well as the combination of different types of paracrystals (SC, BCC and FCC) and the PL model. In all the calculations, the polydispersity of the micelles was taken into account 0.20 by assuming a Gaussian size distribution either of core radii (dilute regime) or overall micellar radii (gel region).

2.4. Dynamic light scattering (DLS)

Size distributions of the poloxamine in water were obtained with a photon correlation spectrometer Malvern Zetasizer Nano, with a laser wavelength of 633 nm. The samples were filtered prior to the measurements by 0.22 μm Millex syringe PVDF filters onto semi-micro glass cells, and the temperature of the samples was controlled with 0.1˚C accuracy by the built-in Peltier in the cell compartment. The viscosity and refractive index of the solvent at different temperatures were taken into account to obtain the particle size distribution from the analysis of the autocorrelation function, which was performed with the Zetasizer software in the high-resolution mode to better distinguish overlapping distributions.

2.5. Infrared spectroscopy

The gelation processes were studied by attenuated total reflectance infrared spectroscopy (FTIR-ATR), using a Nicolette Avatar 360 spectrometer, equipped with a Golden-Gate temperature controlled ATR. The spectra were collected on 0.1 mL samples placed directly on the diamond, at 2 cm^{-1} resolution and 32 scans per spectrum, in the temperature range from 20 to 60 ˚C.

2.6. Rheology

Small-amplitude shear oscillatory experiments were performed on a dynamic strain-controlled rheometer ARES (TA Instruments) using plate-plate geometry (25 mm), with a temperature-controlling Peltier unit and a solvent trap. All solutions were left to rest at least one day at room temperature after preparation before conducting the rheological measurements. After loading, a thin layer of low viscosity paraffin oil was added to the geometry edge in order to prevent evaporation. Samples were allowed to rest for a few minutes before the start of the experiments to ensure dissipation of any pre-shearing due to manipulation and loading. Temperature sweeps at constant angular frequency of 6.28 $rad \cdot s^{-1}$ and 1% strain amplitude, within the limit of the linear viscoelastic range as measured by strain amplitude experiments, were conducted at a heating rate of 2 °C/min covering the temperature range from 20 to 80 °C. The gel points are calculated by monitoring the elastic modulus, G', along the temperature sweeps and identifying the gel point as the onset of the region in which G' reaches values corresponding to a solid-like behavior.

2.7. Preparation of the Nanocomposite Hydrogels

Concentrated solutions of T1107 and NPs were prepared by weighting the required amounts of Tetronic, modified $BaTiO_3$ nanoparticles (50 nm and 200 nm in diameter) and water, D_2O or PBS, followed by mixing. To ensure appropriate dispersion of the NPs in the gel matrix, cycles alternating magnetic stirring, vortex mixing and cooling to 4 ˚C were performed, facilitating the dissolution of the polymer, while keeping the viscosity low (the viscosity of poloxamines increases with temperature).

2.8. Cytotoxicity Studies

The cytocompatibility of the nanocomposite gels of T1107 and BT was tested on the fibroblast cell line NIH3T3 by means of the tetrazolium assay (MTT), in which the viability of the cells is assessed by the loss of viable cells upon treatment with the compounds of interest. The cells were incubated at 37 ˚C and 5% CO_2 in Dulbecco's modified eagle medium from Life's Technologies, supplemented with 10% fetal bovine serum and 0.1% of penicillin/streptomycin. T1107 solutions were prepared in PBS and filtered through 0.22 µm for sterilization. Cells were seeded into 96-well plates at a concentration of 5×10^4 cells·mL^{-1} and 24 hours later the nanocomposite was introduced into the wells. MTT tests were conducted on day 3 by the addition of MTT 5 mg/mL and incubation for 4 hrs. The formazan absorbance at 540 nm was measured with a Thermo Scientific Multiscan EX microplate reader. DMSO was used as a positive control, and the appropriate negative controls performed by incubating the cells in the absence of the nanocomposite.

3. RESULTS AND DISCUSION

3.1. Self-aggregation of T1107 and phase behaviour: the dilute regime

The phase beahvior of T1107 in water at its natural pH (ca. 7.8) is shown in Table 4.1. At 20% and 40 ˚C, the solution becomes gel-like up to 50 ˚C, with a wider gel region at higher concentrations (spanning 30 ˚C to 80 ˚C at 30%). Gel formation is impeded at acidic pH, due to the protonation of the di-amino middle block. For example, at pH 6, no gel is detected from 25 to 80 ˚C for a 20% mixture. A similar behaviour has been observed with poloxamine T1307, which has a larger molecular weight (18,000 g·mol^{-1}) and higher HLB (> 24); however with this larger poloxamine, at 20% and pH = 6 a gel phase still exists between 40 and 50 ˚C (González-Gaitano, da Silva, et al. 2015). More acidic pH totally hinders gel formation. Replacement of H_2O by D_2O slightly shifts the gel phase boundary to higher concentration and temperature (Table 4.1).

Table. 4.1. Phase behaviour of T1107 in H_2O and in D_2O. ○ Solution; □ viscous solution; ● gel.

H_2O	T (˚C)												
T1107 wt%	**20**	**25**	**30**	**35**	**40**	**45**	**50**	**55**	**60**	**65**	**70**	**75**	**80**
5	○	○	○	○	○	○	○	○	○	○	○	○	○
10	○	○	○	○	○	○	○	○	○	○	○	○	○
15	○	○	○	○	○	○	○	○	○	○	○	○	○
20	□	□	□	□	●	●	●	□	□	□	○	○	○
25	□	□	□	●	●	●	●	●	●	●	●	●	●
30	□	●	●	●	●	●	●	●	●	●	●	●	●

D_2O	T (˚C)						
T1107 wt%	10	15	20	25	30	35	40
5	○	○	○	○	○	○	○
10	○	○	○	○	○	○	○
15	○	○	○	○	○	○	○
20	○	○	○	○	○	○	○
25	○	○	○	□	□	□	●
30	○	□	□	□	●	●	●
35	●	●	●	●	●	●	●
40	●	●	●	●	●	●	●

Fig. 4.1A shows the intensity size distribution of 1% T1107 at different temperatures obtained from DLS measurements. Unimers are detected at 20 ˚C, with a hydrodynamic radius, R_h, of 3.2 nm. Between 30 and 35 ˚C, the distribution broadens and shifts toward higher sizes, reflecting the micellization process. Micelles are fully formed at 40 ˚C, with a R_h nearly constant above that point (7.8 nm). The relative size of the micelles compared to that of the unimers, R_{mic}/R_{unim}, is 2.4, which is intermediate between the larger T1307 (1.6, with N_{EO} = 72, N_{PO} = 23)(Gonzalez-Lopez et al. 2008) and the more hydrophobic T904 (2.8, N_{EO} = 15, N_{PO} = 17) (Larrañeta & Isasi 2013), suggesting that the micelles of T1107 must contain a relatively low number of unimers as found for T1307 (González-Gaitano, da Silva, et al. 2015) and also reported with Pluronic of high HLB, such as P85 (Kabanov et al. 2002). At pH 2.8 (Fig. 4.1B), the formation of micelles is hindered, resulting in a smaller micellar size of 6.9 nm at 50 ˚C.

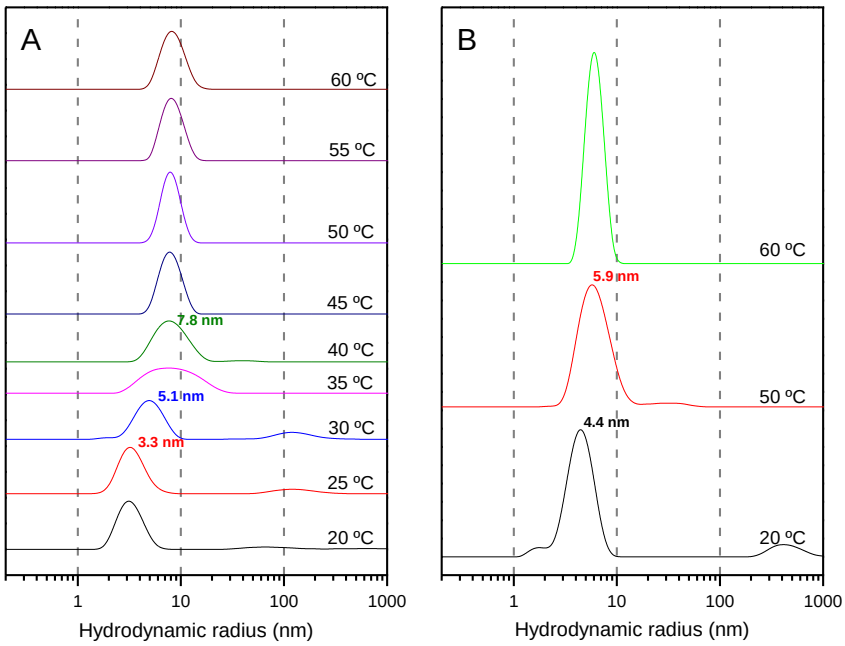

Fig. 4.1: Intensity size distributions as a function of temperature obtained by DLS for a 1% aqueous solution of T1107 at (A) pH 7.8 and (B) pH 2.8 in H_2O.

More detailed structural information on the unimers and micelles can be obtained from small-angle neutron scattering measurements (SANS); combining these data with DLS enables one to unambiguously identify concentration regimes where unimers, micelles, or both, are present, thus directing the choice of a suitable fitting model. Fig. 2A shows the scattering curves for a 2% T1107 solution in D_2O. Below 30 ˚C, the poloxamine is in the form of unimers (as established by DLS), whereas at 40 ˚C and 50 ˚C micelles are the dominant species, and the overall scattering increases accordingly. A four-arm star-shape polymer model was shown to successfully describe the unimers (Benoit 1953). With this model, the radius of gyration, R_g, at 20 ˚C decreases with concentration, from 3.6 nm at 0.5%, to 2.9 nm at 2% and 1.9 nm at 5%; the first value is close to 3.2 nm obtained by DLS for R_h at 1%.

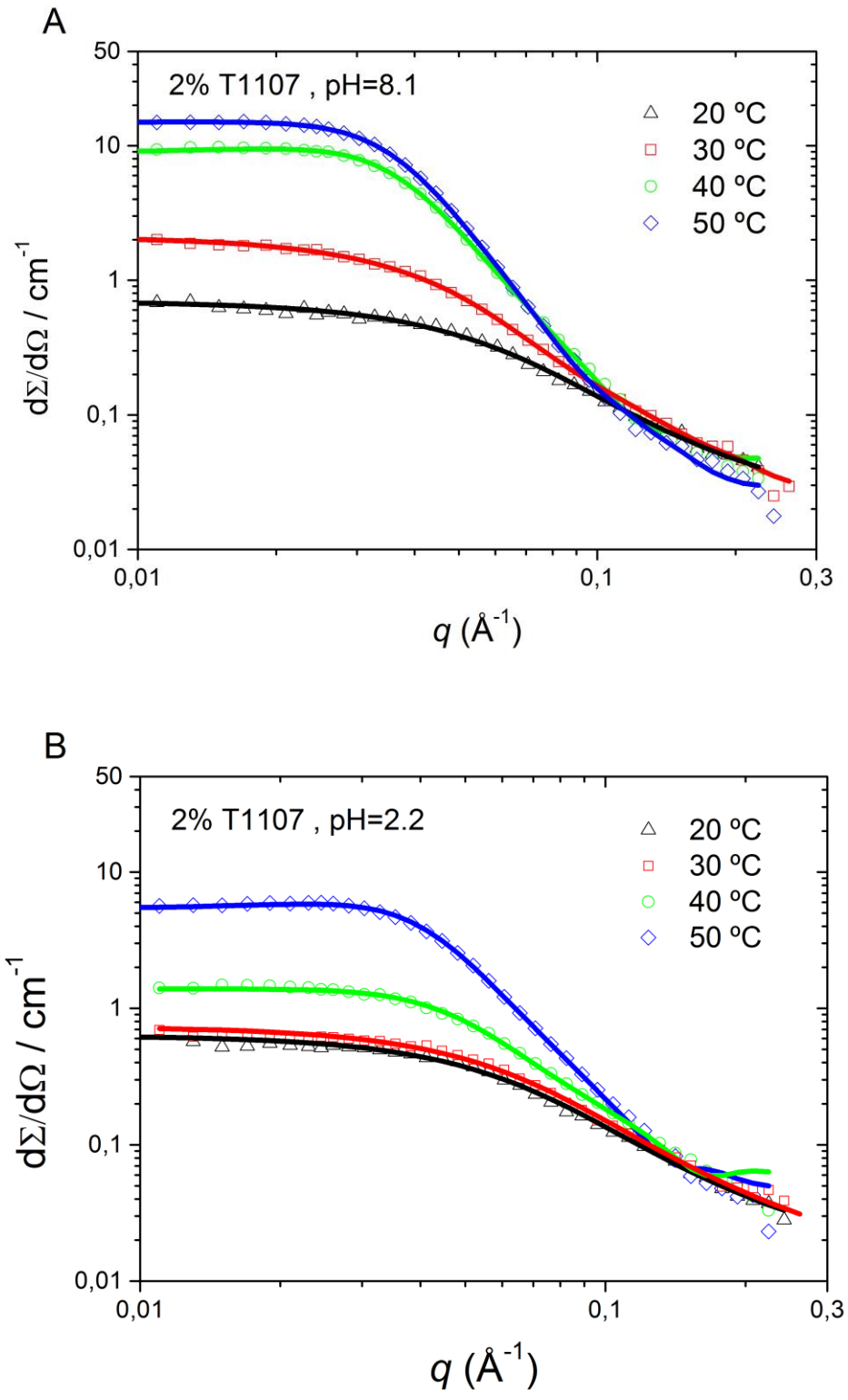

Fig. 4.2: SANS curves for 2% T1107 solutions in D2O as a function of temperature at pH 8.1 (A) and pH 2.2 (B). Solid lines are fits to the different models described in the text.

At 40 and 50 ˚C, micelles dominate the scattering, and hence a core-shell sphere model (CSS) combined with a structure factor for hard spheres (HS) was used. The fitted and

calculated parameters in the dilute regime (2 %) are collected in Table 4.2 (top) for two values of the pH (data at 0.5% and 5% are provided in Table 4.2, bottom).

Table 4.2. Micellar parameters of 2% (top) and 0.5% and 5% (bottom) T1107 in D_2O deduced from fits to the SANS data (core-shell model with a hard-sphere structure factor): *Rc* (core radius), *t* (shell thickness), ϕ (volume fraction from the hard-sphere potential), ρ_{shell} (scattering length density of the hydrophilic corona), N_{agg} (aggregation number), nsolv/EO (number of solvent molecules per EO in the shell).

pH	*T / °C*	R_c / Å	*t* / Å	ϕ	$\rho_{shell}\times10^6$ / Å^{-2}	N_{agg}	n_{solv}/EO
8.1	40	34	47	0.08	5.95	14	20
	50	34	46	0.08	6.06	12	23
2.2	50	30	43	0.08	5.99	9	22

wt %	*T / °C*	R_c / Å	*t* / Å	ϕ	$\rho_{shell}\times10^6$ / Å^{-2}	N_{agg}	n_{solv}/EO
0.5	40	32	53	0.02	6.05	12	28
	50	35	48	0.02	6.03	13	22
5	40	34	44	0.19	5.92	13	18
	50	36	45	0.19	6.05	14	20

Micellar size is fairly insensitive to temperature or concentration up to 5% (Table 4.2), with a total radius around 8 nm (in agreement with DLS, Fig. 4.1A). The sld of the shell, ρ_{shell}, takes values close to that of D_2O (6.36×10^{-6} Å^{-2}), indicating an extensive solvation of the hydrophilic corona, reflected in the high number of solvent molecules per EO. The aggregation number, N_{agg}, does not vary much with temperature or concentration, while the hydration of the shell (n_{solv}/EO) decreases slightly with concentration, suggesting a more compact micellar structure.

In contrast to temperature and concentration, pH has a strong impact on micellar structure (Fig. 4.2B, Table 4.2 top). At pH 2.2, the low scattering at 20 ˚C and 30 ˚C reflects the presence of unimers with R_g = 2.7 nm (similar to 2.8 nm, at natural pH). At 40 ˚C, both aggregates and micelles coexist (as shown by DLS). At 50 ˚C, the micelles are substantially smaller than at neutral pH (Table 4.2 top), in agreement with DLS results (Fig. 4.1B). N_{agg} is of only 9 molecules per aggregate, comparable to the value of 4 reported in water by static light scattering at pH 2 (37 °C) (Gonzalez-Lopez et al. 2008). Thus, a drop in pH can be envisaged as a trigger for the release of a cargo from the interior of the micelles, which do not break fully, thus enabling delivery in a stepwise fashion.

IR spectroscopy can provide information on changes occurring in the chemical surroundings of specific functional groups, such as those in micellization processes or temperature induced sol-gel transitions. There is a precedent of this type of study in the literature, where the aggregation of Pluronic F127 (Su et al. 2002) and reverse Tetronic 10R5 (Larrañeta & Isasi 2013) was followed by monitoring the band at 1085 cm^{-1} (corresponding to the combination of stretching and vibration of the C-O-C from PEO and PPO blocks). The same approach applied to 10% T1107is shown in Figure 4.3. When increasing the temperature from 20 to 60 ˚C, a shift of the 1085 cm^{-1} band towards higher wavenumbers (blue shift) is observed, as well as a broadening in the bandwidth (FWHM). There is no clear breakpoint in any of the plots, but a smooth change of slope at around 30 ˚C (shown with the linear fits) in the maximum of the band, suggesting a small degree of dehydration once micelles form (above the cmc). The broadening of the IR band also points to the coexistence of different environments or states of dehydration. This pattern is qualitatively similar to that obtained for Pluronic F127 (Su et al. 2002), although in that previous study the breakpoint was sharper. The more open structure of the T1107 compared to that of the Pluronics might explain that changes in hydration occur in a continuous manner, with less of a sharp change, as the micelles are comparatively less compact, with looser unimers.

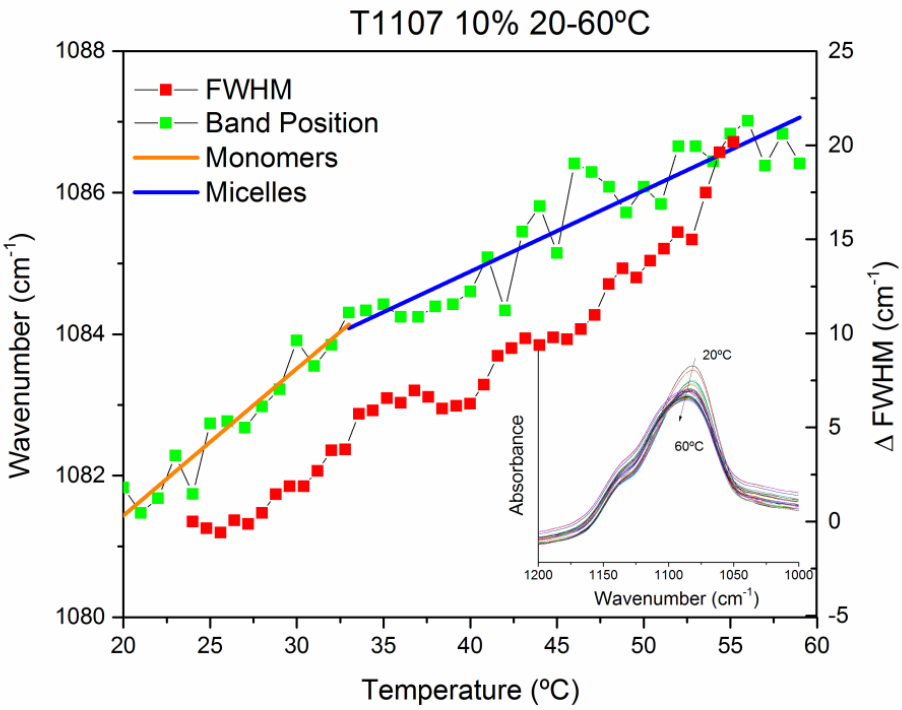

Fig. 4.3: FTIR-ATR analysis of the position and FWHM of the 1085 cm^{-1} band of T1107 samples at 10%. The lines are the linear fits in the monomer region (orange) and micelles region (blue).

3.2. The concentrated regime: T1107 gels

Raising the temperature and increasing the concentration of T1107 induces the formation of physical gels (Table 4.2 top). Fig. 4.5A shows the SANS data obtained at 25% T1107 when gradually increasing the temperature from 20 to 50 ˚C; samples turn to gels at 40 ˚C and 50 ˚C (Table 4.2 bottom for the phase diagram in D_2O). Up to 30 ˚C the solution is viscous and the system consists of a concentrated solution of micelles, whose interactions are reflected by a strong peak in the mid-*q* range. At 20 ˚C, a fit to the CSS model reveals micelles of 26 Å core and 33 Å shell (Table 4.3). Despite the considerably higher concentration, N_{agg} is lower than for 2% micelles at 40 or 50 ˚C, and the shell contains more solvent molecules per EO unit (Table 4.2 top), showing that temperature more readily enhances aggregation than concentration. At 30 ˚C, the solution becomes very viscous, producing a high intensity peak around 0.06 $Å^{-1}$ (Fig. 4.5A), as seen in physical gels consisting of packed micelles.(Okabe et al. 2003) In the gel phase (40 and 50 ˚C), good fits were obtained by using the CSS model with a structure factor for hard spheres (HS), with the sld of the core fixed to that of PO (as for dilute micelles), rather than the paracrystal model used elsewhere for Pluronic gels (Dreiss et al. 2009; Okabe et al. 2003).

Table 4.3. Micellar parameters of 25% T1107 in D_2O deduced from SANS data analysis. *Rc* (core radius), *t* (shell thickness), ϕ (volume fraction from the hard-sphere potential), ρ_{shell} (scattering length density of the hydrophilic corona), N_{agg} (aggregation number), n_{sol}/EO (number of solvent molecules per EO in the shell).

pH	*T / °C*	*Phase*	R_c / Å	*t* / Å	ϕ	$\rho_{shell} \times 10^6$ / $Å^{-2}$	N_{agg}	n_{sol}/ *EO*
8.8	20	Sol	26	33	0.39	6.29	4	31
	30	Sol-Gel	30	36	0.52	5.98	8	18
	40	Gel	32	36	0.53	5.92	10	16
	50	Gel	33	36	0.53	5.94	10	15
2.1	30	Sol	23	25	0.29	6.05	3	18
	40	Sol	26	27	0.41	5.90	5	14
	50	Sol	28	28	0.44	5.80	7	12

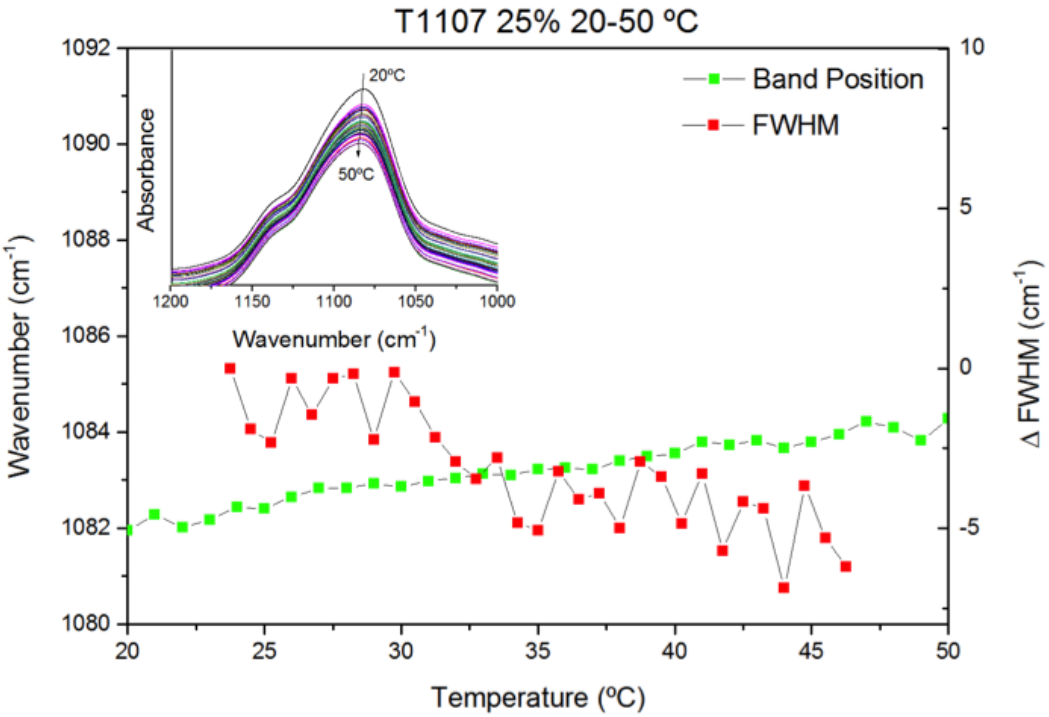

Fig. 4.4: Position and FWHM (Full Width at Half Maximum) of the 1085 cm^{-1} band of T1107 at 25% wt. from 20 to 50 ºC obtained by FTIR-ATR.

Band position and FWHM for the for the C-O-C vibration band of T1107 gels (Fig. 4.4), unlike what has been observed at 10%, shows very little change, suggesting that the chemical environment (i.e., hydration state) of the EO and PO groups remains very similar over the sol-to-gel transition, while it increases more noticeably as a result of micellization (Fig. 4.3).

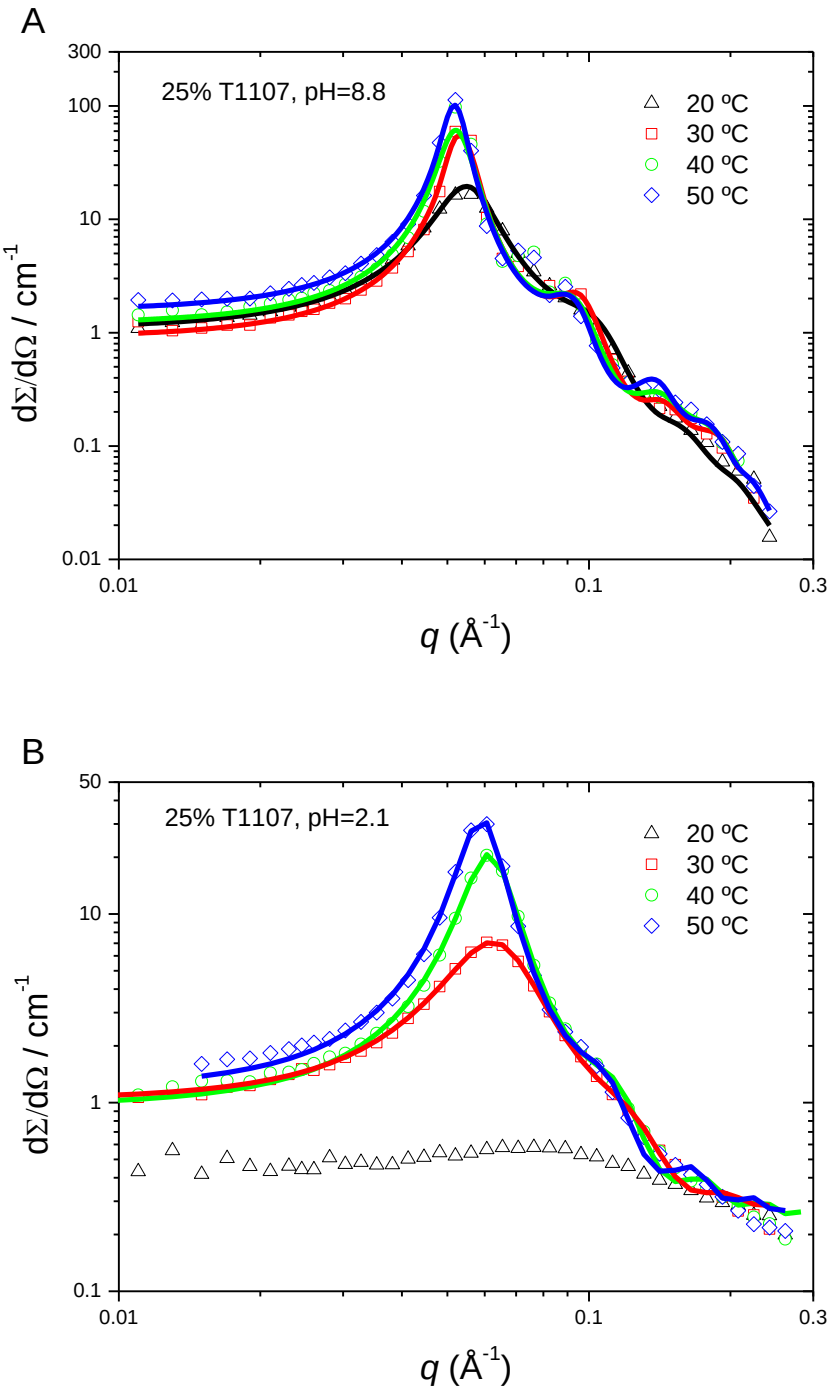

Fig. 4.5: SANS curves from 25% T1107 solutions in D_2O as a function of temperature at pH 8.8 (A) and at pH 2.1 (B). Solid lines are fits to the models described in the text.

As acidic pH hinders the formation of the micelles, or results in smaller micelles (as observed in the dilute regime), this must have direct consequences on the structure of the T1107 gel (Fig. 4.5B). Clearly, the overall scattering is much lower than at natural pH (Fig. 4.5A). At 20 ˚C, the lower intensity suggests a transition state, corresponding to a mixture of unimers and micelles, while at higher temperatures (30 ˚C, 40 ˚C, 50 ˚C) the scattering

reflects the presence of strongly interacting aggregates, whose structural parameters have been calculated according to a model of CSS with a HS structure factor. The resulting aggregation numbers are low compared to the gels at natural pH, but the trend with temperature is the same: a dehydration of the shell and increase of N_{agg}, along with an increase in the dimensions of the aggregates. Finally, the volume fractions and sizes are smaller than at natural pH, in agreement with the reduced N_{agg} under acidic conditions.

The volume fraction returned from the fits gives some valuable insights into the structural changes occurring with temperature. At 20 ˚C and natural pH, where the solution is still viscous but no gelation has occurred, a value of 0.39 reflects the concentration of strongly interacting particles. This value increases with temperature and becomes practically constant within the gel region at 0.53. The theoretical volume fraction for a compact packing of spheres fcc is 0.74, 0.68 for a bcc, and 0.52 for a scc arrangement, hence the value obtained would correspond to a simple cubic paracrystal arrangement, as for Pluronic F127 (Dreiss et al. 2009). The estimated fraction volume of 0.53, suggests that the arrangement, although displaying some long-range order responsible for the intense diffraction peaks, might rather be a dense mixture of micelles, in close contact, which do not form a completely ordered structure.

In order to test this hypothesis further, a wider range of concentrations of T1107 (10%, 20%, and up to 30%) were measured at 40 ˚C, on a different instrument (D22, ILL) and with a set-up that provided a higher resolution of the scattering peaks (Fig. 4.6). 10% T1107 shows no crystallinity peaks and the scattering curve can be fitted very well with the CSS+HS. The increase in concentration to 20% and 30% leads to a two-fold increase in the intensity and the appearance of sharp scattering peaks in the 0.07-0.09 $Å^{-1}$ range. The higher resolution of this region reveals a peak that was not detectable in the previous set-up (Fig. 4.6). The CSS+HS model is no longer suitable to describe the data from 20% and above in the higher *q* region (despite the fit being of higher quality in the lower *q* region), as it obviates the first peak at 0.07 $Å^{-1}$ (which is best seen in Fig. 4.7A). As stated above, the presence of these peaks evidence a higher degree of arrangement, probably an intermediate situation between a dense packing of micelles and a paracrystalline structure, which is favoured by the inherent polydispersity of the micelles. BCC fits were proposed for samples with concentrations of 20% T1107 and above, and the diffraction peaks at higher *q* are better described by this model, giving a sphere radius of 35.1 Å and 35.5 Å for 20% and 30% solutions and nearest neighbour distance (*dnn*) of 166.8 Å and 155.8 Å, respectively.

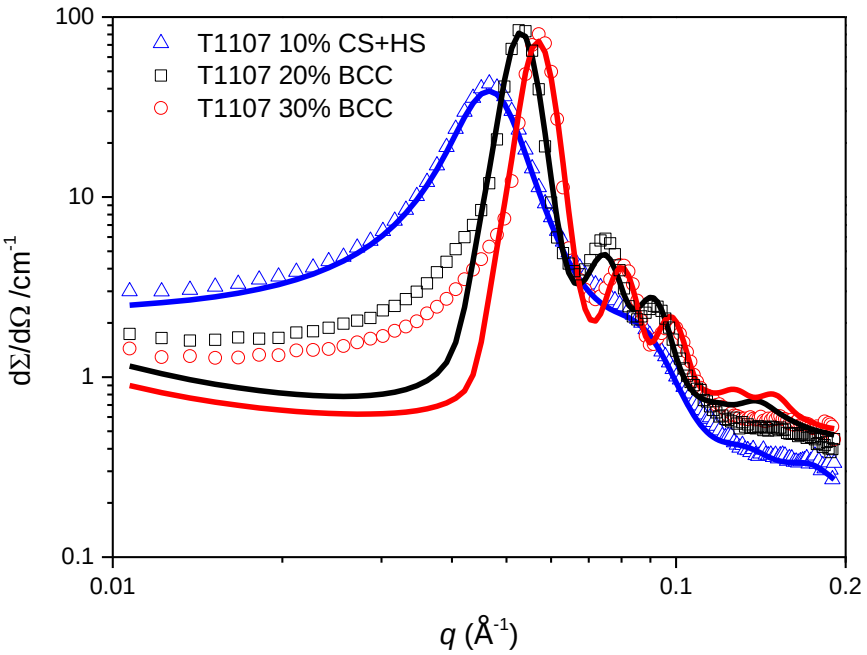

Fig. 4.6: SANS curves from T1107 10%, 20% and 30% solutions in D_2O at 40 ˚C and natural pH. Solid lines are fits to the models described in the text CSS+HS (10% sample) and BCC (20% and 30% sample). Data measured on D22 (ILL).

3.3. Hydrogel nanocomposites.

The structure of the nanocomposite gels was studied by SANS with 20% T1107 and a 5% load of $BaTiO_3$ nanoparticles (50 and 200 nm) to achieve a total dry load of 25 %. Figure 4.7A shows the scattering patterns of the different gel nanocomposites at 40˚C. In addition to the CSS-HS model used for low concentration Tetronic gels, a generic power law was added to account for the scattering of the large inorganic nanoparticles at low *q* (Campanella et al. 2015; Kanapathipillai et al. 2008). The fitted parameters (Table 4.4) show that the introduction of the nanoparticles in the gel does not seem to affect the size of the micelles, their volume fraction or their aggregation number. As observed for the pure Tetronic gels, the simple CSS+HS model however is not able to not fit the scattering peak adequately in the 0.07-0.09 $Å^{-1}$ *q*-region. These peaks are typical of crystalline or para-crystalline arrangements in the system due to structured nano-domains, as observed in Pluronic F127 gels (Dreiss et al. 2009) and in T1107 gels (Fig. 4.6). The presence of BT nanoparticles in an already concentrated solution may be able to promote this long-range order arrangement (Mortensen 1993).

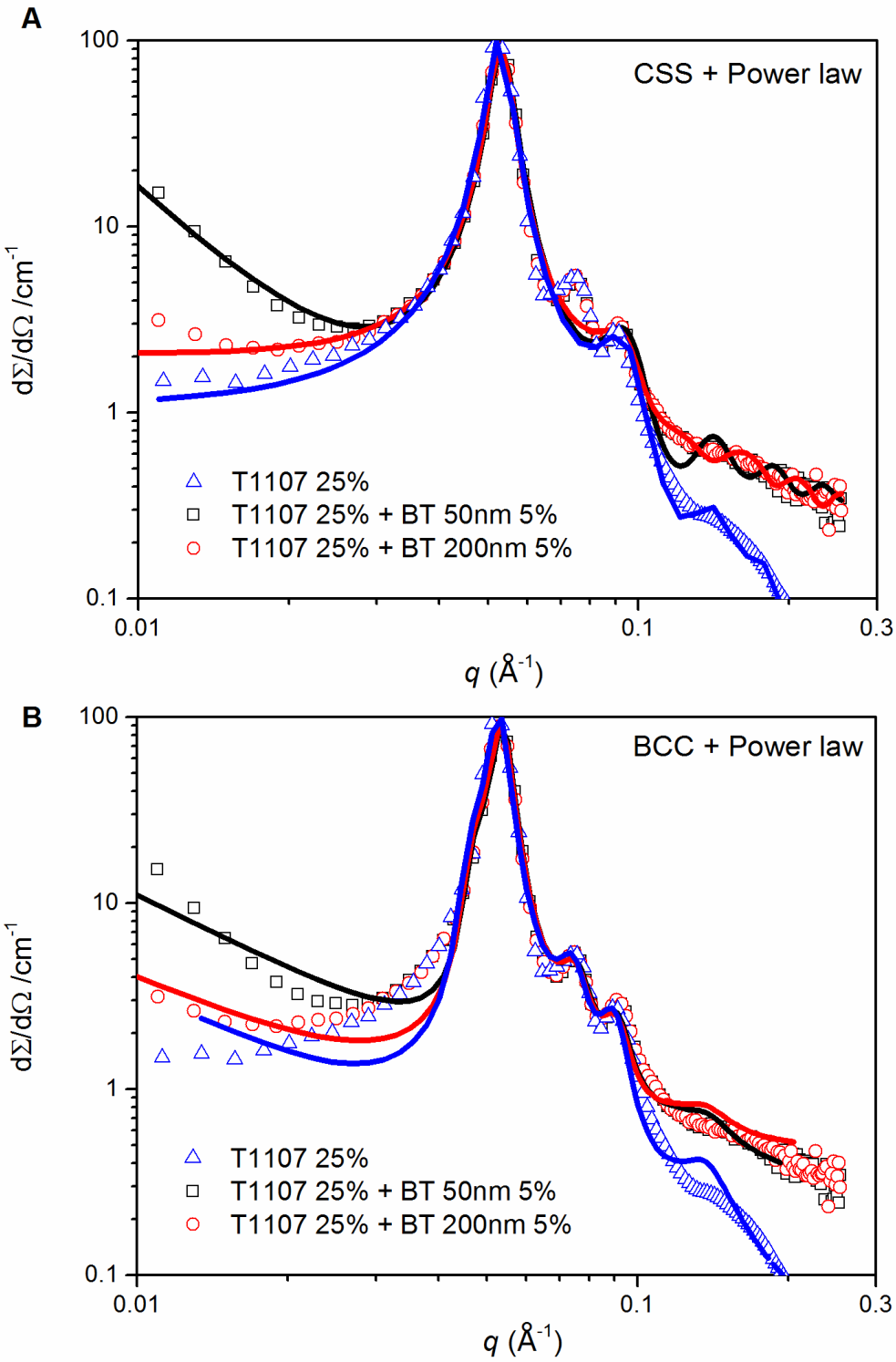

Fig. 4.7: SANS curves from T1107 25% solutions in D_2O and 20% solutions with 5 wt% of BT 50 nm (black) and BT200 nm (red) at 40 ˚C at natural pH. Solid lines are fits to the models described in the text: CSS+PL (A) and BCC+PL (B).

In order to precisely measure the structural parameters of the nanocomposite gels, the BCC approach was also tested, in combination with a power law model (Figure 4.7B and

Table 4.5). The introduction of the nanoparticles does not lead to major structural changes in the lattice, namely, a slight tightening of the network with a decrease in the nearest neighbour distance, dnn (Table 4.5), an effect similar to that obtained by increasing the concentration of T1107 (Fig. 4.6). The values obtained for the T1107+BT nanocomposites fall within the range between the T1107 samples at 20% and 30%. On the other hand, the addition of nanoparticles does not have any notable effect either on the band shift or the FWHM (Fig 4.8). At 25% and 20˚C, T1107 micelles are fully formed, and the compaction of the micelles that takes place when increasing the temperature and leads to the sol-gel transition does not involve changes in the local environment that are reflected in the characteristic vibrations of the EO or PO groups.

Table 4.4: Micellar parameters of 25% T1107 and 20% T1107 and 5% BT nanoparticles of 50 nm and 200 nm in D_2O extracted from SANS data analysis. R_c (core radius, Å), t (shell thickness, Å), ϕ (volume fraction from the hard-sphere potential), ρ (scattering length density), N_{agg} (aggregation number), n_{solv}/x (number of solvent molecules per EO units in the shell).

Sample	R_c / Å	t / Å	ϕ	$\rho_{shell} \times 10^6$ / Å^{-2}	N_{agg}	n_{sol}/ *EO*
25% T1107	32	36	0.552	6.13	10	16
20% T1107 + 5% BT50 nm	33	34	0.548	6.03	10	16
20% T1107 + 5% BT200 nm	32	36	0.554	5.96	10	16

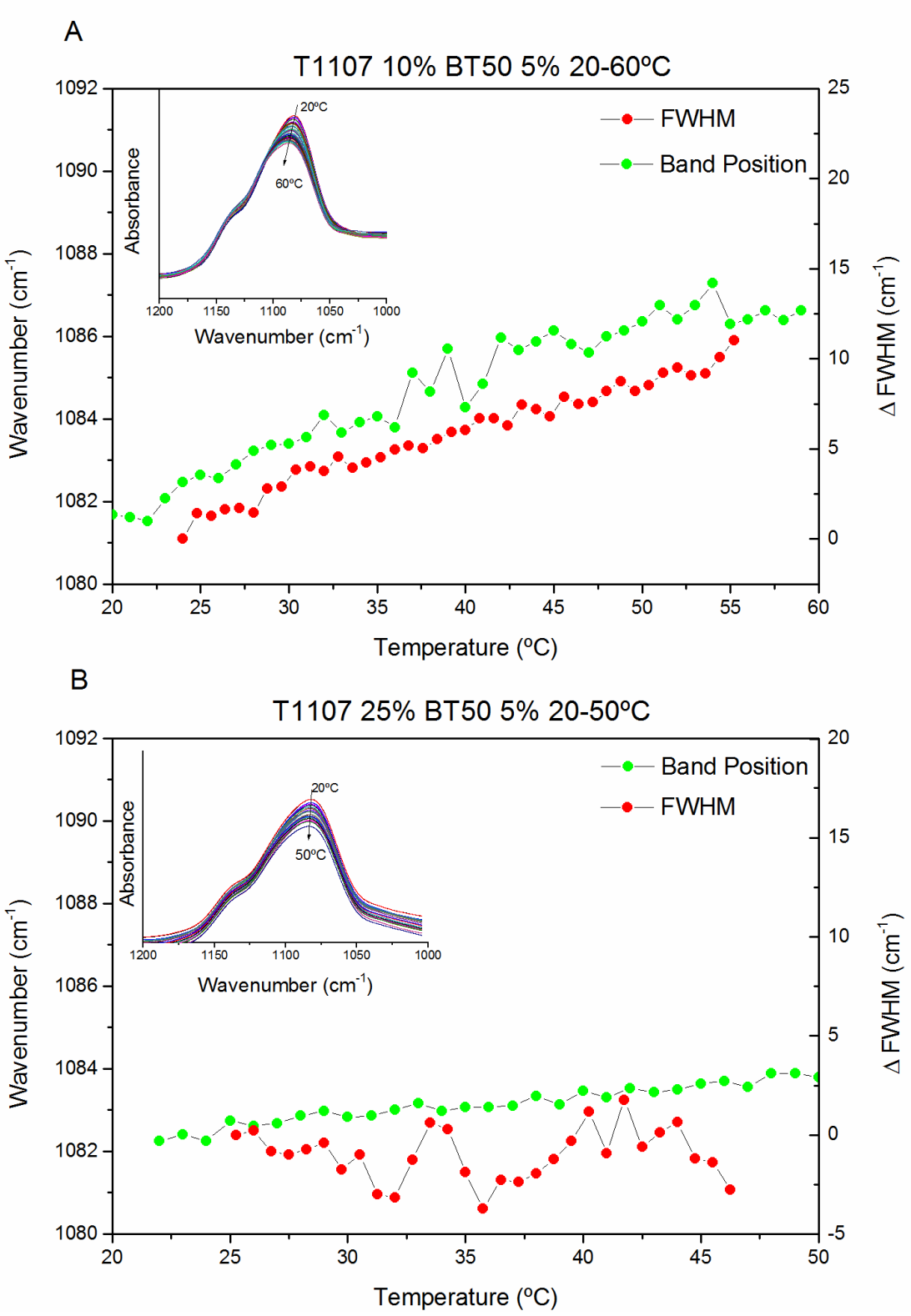

Fig. 4.8: Position and FWHM (Full Width at Half Maximum) of the 1085 cm^{-1} band of T1107+BT nanocomposites at 10% (A) and 25% (B) from 20 to 50 ˚C obtained by FTIR-ATR.

Table 4.5: Micellar parameters of 25% T1107 and BT nanoparticles of 50 nm and 200 nm in D_2O extracted from SANS data analysis using a BCC model. R_c (core radius, Å), *dnn* (nearest neighbor distance, Å), *D* factor (paracrystal distortion factor).

Sample	R_c / Å	*dnn* / Å	*D factor*
25% T1107	35	167	0.086
20% T1107 + 5% BT50 nm	35	165	0.086
20% T1107 + 5% BT200 nm	35	166	0.088

The presence of nanoparticles in a hydrogel is known to alter its mechanical properties, as well as the thermogelation behaviour of the system (Nambam & Philip 2012; Shen et al. 2015; Cha et al. 2014). We thus examine the rheological behaviour of the hydrogel nanocomposites, in particular the effect of nanoparticle size (50 nm and 200 nm), the relative proportion of poloxamine and NP (varied from 0 to 20% in $BaTiO_3$) and the effect of solvent (both water and phosphate buffered saline, PBS). The introduction of BT nanoparticles is expected to impact gel formation by either affecting the packing of the micelles or increasing connectivity in the network (da Silva & Dreiss 2016).

The temperature sweeps showing the elastic modulus between 10 and 80°C (Fig. 4.9) reveal a broadening of the gel phase region with increasing concentrations of BT from 0% to 20%. The onset of gelation shifts to lower temperatures by as much as 10 ˚C, while the gel-to-sol transition extends beyond 80 ˚C for the highest particle loadings. Replacing water with PBS induces a shift to both sol-gel and gel-sol transitions to lower temperatures (Table 4.6).

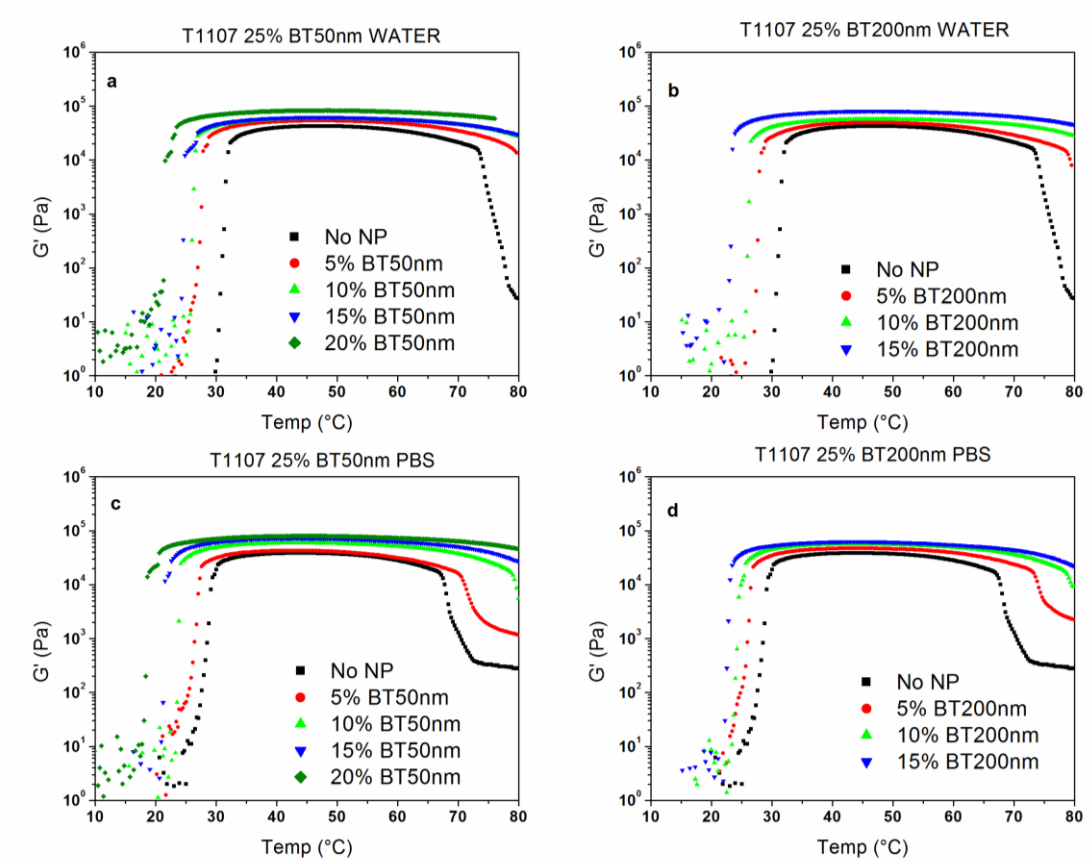

Fig. 4.9: Temperature sweeps of 25% T1107 with BT nanoparticles of 50 nm and 200 nm in water and PBS respectively: a) 50 nm BT in water b) 200 nm BT in water c) 50 nm BT in PBS d) 200 nm BT in PBS.

This may be attributed to the salting out effect caused by PO_4^{3-} anions present in the solvent (N Pandit, T Trygstad, S Croy, M Bohorquez et al. 2000) that reduce the solubility of the PPO blocks, thus lowering the cmc and promoting micellization. At the same time, these anions reduce the capability of the PEO chains to form hydrogen bonds with the surrounding water, also lowering the cloud point (Wang et al. 2010). This, overall, results in a slightly narrower gel phase, particularly at 0% and 5% BT, but at higher BT loading (above 10%), the effect of PBS is compensated by the effect of the filler, resulting in a gel phase extending beyond 80 ˚C.

An important effect of the addition of the nanoparticles, beyond extending the gel phase, is the increase in the elastic modulus (Table 4.7, Fig. 4.10). A direct relationship is observed between the amount of nanoparticles and the increase in G', with, however, no effect of particle size up to 10% concentration.

Table 4.7: Rheological Data for T1107 25% with 50 nm (BT50) and 200 nm (BT200) $BaTiO_3$ nanoparticles.

Sample	Solvent	Gel Formation Temperature (˚C)	Span of the gel phase (˚C)	G' Max (KPa)	Tan (δ)
25% T1107	Water	32	41	42.6	0.081
	PBS	29	38	38.3	0.057
5% BT50	Water	28	51	53.7	0.046
	PBS	27	43	42.6	0.048
10% BT50	Water	27	53	59.1	0.020
	PBS	24	55	59.3	0.021
15% BT50	Water	25	53	62.2	0.011
	PBS	22	57	72.4	0.020
20% BT50	Water	23	57	83.1	0.016
	PBS	18	60	80.2	0.021
5% BT200	Water	28	50	49.4	0.028
	PBS	27	46	47.0	0.049
10% BT200	Water	26	53	57.4	0.022
	PBS	24	52	56.6	0.031
15% BT200	Water	23	56	81.2	0.014
	PBS	23	57	63.1	0.017

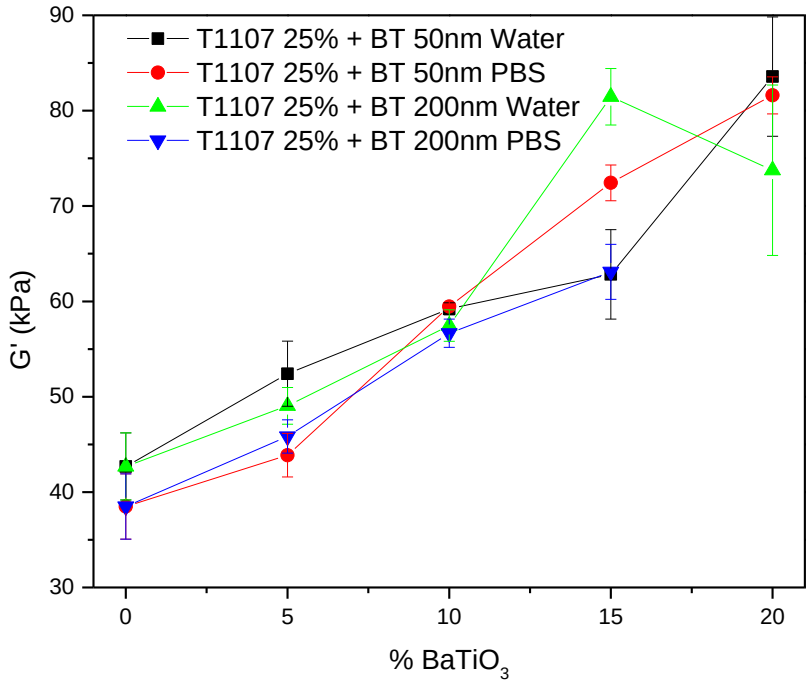

Fig. 4.10: Change in elastic modulus (G') as a function of BT concentration in T1107 25% samples.

There is, however, quite some variation between repeats at high particle loading (20%) and this erratic behaviour may be attributed to the difficulty in achieving sample homogeneity, an effect also seen by Tamborini et al in their work on micellar polycrystals (Tamborini et al. 2012). The overall increase in G' and sharp decrease in tan (δ) (Table 4.7) suggests that the introduction of the cyclodextrin-coated nanoparticles leads to a more rigid and connected network. Comparing tan (δ) values at the same compositions for the two different solvents shows again that the presence of charges from PBS leads to an increase in the liquid-like behaviour of the system and a looser packing of the network.

3.4. Cytotoxicity studies.

Previous investigations have reported good cytotoxicity results for BT alone (Ciofani, Danti, D'Alessandro, et al. 2010; Dempsey et al. 2013; FarrokhTakin et al. 2012). The surface modified BT with CDs, which helps to stabilize the nanoparticles in solution, display excellent viability of the cells, even up to concentrations of 200 µg/mL (Serra-Gómez et al. 2016). Figure 4.11 shows the MTT results for the T1107 hydrogels at different concentrations with and without BT200-βCD nanoparticles.

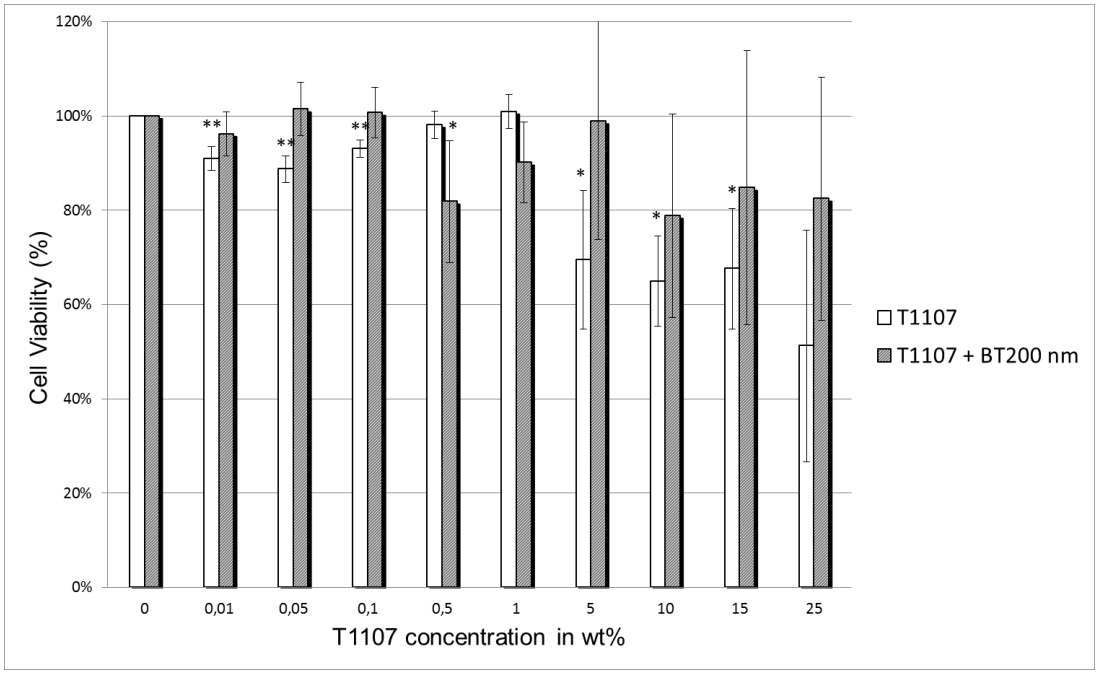

Fig. 4.11: MTT results for NIH3T3 cells and T1107 (White bars) and T1107 with BT 200 nm nanoparticles modified with β-CD (Black bars). * denotes p<0.05 and ** denotes p<0.01 by ANOVA variance and Student's T tests.

Tetronic T1107 shows cytotoxicity scores of 0 (<90%) and 1 (70-90%) after 72h at all the concentrations but the highest one (25 wt%), with and without BT nanoparticles. With poloxamine concentration above 1 wt%, it is difficult to achieve reproducible results in fibroblast cell lines (large standard deviations are shown as error bars), which is in accordance with some results reported in the literature (Rey-Rico et al. 2011). Fibroblasts are known to be particularly sensitive to nutritional requirements compared to other cell lines (Park et al. 2002). This may be combined with the fact that at higher concentrations (>1% T1107) and 37.5 ˚C, the high density of micelles or gel may prevent the nutrients to have continuous access to the cell layer in the 96-well plate, and thus contribute to the high deviations. The introduction of the CD-coated nanoparticles generally improves the viability of the cells, results that are in line with what has been reported for BT nanoparticles alone. Altogether, the introduction of BT in the hydrogel and the formation of the nanocomposites do not produce an increase in the toxic effect in the studied cells, thus showing promise for these nanocomposite gels as biomaterials.

Further research on this kind of nanocomposite hydrogels will surely lead to interesting applications in the biomedical field. One example could be as tissue adhesives to function as injectable surgical sealants in which the gelation and mechanical properties are tuned by the nanofiller content (Sanders et al. 2015). In addition to that, other appealing applications are being proposed, as those hydrogels could work not only as adhesives but also as

scaffolds to promote rapid tissue regeneration at dermal, tendon or cardiovascular levels, depending on the type of nanofiller used (Shin, Jung, et al. 2013; Tokunaga et al. 2015).

4. CONCLUSIONS

The phase behaviour of the hydrophilic, Tetronic T1107 has been fully characterised, using a combination of SANS, DLS and FTIR-ATR spectroscopy. At low concentrations and above 30˚C, the amphiphile forms spherical micelles with a dehydrated core and a highly hydrated shell, with aggregation numbers relatively small, mostly due to the hydrophilicity of the polymer, with dimensions that do not depend much on the temperature or concentration. Micellar size is notably affected by the degree of protonation of the central amine spacer, forming loose hydrated aggregates. In the high-concentration regime, T1107 forms gels. SANS data analysis shows that upon gelation the shell of the micelles becomes dehydrated, and long-range order is detected through the appearance of sharp scattering peaks, revealing a bcc order. The presence of BT nanoparticles modified with CDs produces substantial changes in the rheological behaviour of the system. By adjusting the concentration of the nanoparticles, the sol-gel transition temperature of 25% T1107 can be tailored, with a maximum reduction in the gelation temperature of 12 ˚C, as well as an increase of the same magnitude in the gel-sol transition, thus leading to a broadening of the gel phase region. At the same time, the elastic modulus G' of the nanocomposite increases up to 200% by incorporating the BT nanoparticles, and follows a linear trend with the concentration of the nanofiller. Thus, in addition to their inherent piezoelectric properties, the nanoparticles provide a handle to tune gelation point and elastic gel modulus, which is of interest for the preparation of injectable (thermoresponsive) hydrogels. From the structural point of view, the presence of the modified BT nanoparticles does not disturb the bcc arrangement of the micelles in the gels. Overall, the effect of filler size (50 nm vs 200 nm) is largely negligible, both on the macroscopic scale (rheology) and the nanostructure. Acidic conditions inhibit the formation of a gel phase, leaving a concentrated solution of small, extensively hydrated aggregates. The cytotoxicity of the nanocomposites was assessed both at high and low concentrations. Viability of fibroblasts at low concentration of poloxamine (up to 1 wt%), show excellent results (above 90% viability) for both the T1107 and the nanocomposite. At higher concentrations (1 wt% to 25 wt% T1107 with and without BT) the viability levels are between 70-90%, presenting higher variability for that specific cell line due to the presence of the micelles interfering with the nutrition demands of the cells. Overall, these results are promising for the further development of nanocomposite hydrogels based on BT for biomedical applications.

5. REFERENCES

Agrawal, S.K. et al., 2008. Nanoparticle-reinforced associative network hydrogels. *Langmuir : the ACS journal of surfaces and colloids*, 24(22), pp.13148–54.

Alakhova, D.Y. & Kabanov, A. V, 2014. Pluronics and MDR reversal: an update. *Molecular pharmaceutics*, 11(8), pp.2566–78.

Alvarez-Lorenzo, C. et al., 2010. Poloxamine-based nanomaterials for drug delivery. *Frontiers in bioscience*, 2, pp.424–440.

Alvarez-Lorenzo, C., Sosnik, A. & Concheiro, A., 2011. PEO-PPO Block Copolymers for Passive Micellar Targeting and Overcoming Multidrug Resistance in Cancer Therapy. *Current Drug Targets*, 12(8), pp.1112–1130.

Annaka, M. et al., 2011. Design of an injectable in situ gelation biomaterials for vitreous substitute. *Biomacromolecules*, 12(11), pp.4011–21.

Annaka, M. et al., 2012. Organic–inorganic nanocomposite gels as an in situ gelation biomaterial for injectable accommodative intraocular lens. *Soft Matter*, 8(27), p.7185.

Anon, http://www.sasview.org/, developed by the DANSE project under NSF award DMR-0520547.

Balazs, A.C., Emrick, T. & Russell, T.P., 2013. Nanoparticle Polymer Composites : Meet Two Small Worlds. *Science*, 314(5802), pp.1107–1110.

Barrère, F. et al., 2008. Advanced biomaterials for skeletal tissue regeneration: Instructive and smart functions. *Materials Science and Engineering: R: Reports*, 59(1–6), pp.38–71.

Baxter, F.R. et al., 2009. An in vitro study of electrically active hydroxyapatite-barium titanate ceramics using Saos-2 cells. *Journal of materials science. Materials in medicine*, 20(8), pp.1697–708.

Benoit, H., 1953. On the effect of branching and polydispersity on the angular distribution of the light scattered by gaussian coils. *Journal of Polymer Science*, 11(5), pp.507–510.

Blanco-Lopez, M.C., Rand, B. & Riley, F.L., 1997. The properties of aqueous phase suspensions of barium titanate. *Journal of the European Ceramic Society*, 17(2–3), pp.281–287.

Campanella, A. et al., 2015. Nanocomposites composed of HEUR polymer and magnetite iron oxide nanoparticles: Structure and magnetic response of the hydrogel and dried state. *Polymer*, 60, pp.176–185.

Cha, C. et al., 2014. Controlling mechanical properties of cell-laden hydrogels by covalent incorporation of graphene oxide. *Small (Weinheim an der Bergstrasse, Germany)*, 10(3), pp.514–23.

Chen, Q., Zhu, C. & Thouas, G.A., 2012. Progress and challenges in biomaterials used for bone tissue engineering: bioactive glasses and elastomeric composites. *Progress in Biomaterials*, 1(1), p.2.

Cho, E., Lee, J.S. & Webb, K., 2012. Formulation and characterization of poloxamine-based hydrogels as tissue sealants. *Acta Biomaterialia*, 8(6), pp.2223–2232.

Chu, Z., Dreiss, C. a & Feng, Y., 2013. Smart wormlike micelles. *Chemical Society reviews*, 42(17),

pp.7174–203.

Ciofani, G., Danti, S., D'Alessandro, D., et al., 2010. Barium Titanate Nanoparticles: Highly Cytocompatible Dispersions in Glycol-chitosan and Doxorubicin Complexes for Cancer Therapy. *Nanoscale research letters*, 5(7), pp.1093–101.

Ciofani, G., Danti, S., Moscato, S., et al., 2010. Preparation of stable dispersion of barium titanate nanoparticles: Potential applications in biomedicine. *Colloids and surfaces. B, Biointerfaces*, 76(2), pp.535–43.

Cuestas, M.L., Sosnik, A. & Mathet, V.L., 2011. Poloxamines display a multiple inhibitory activity of ATP-binding cassette (ABC) transporters in cancer cell lines. *Molecular pharmaceutics*, 8(4), pp.1152–64.

Dempsey, C. et al., 2013. Coating barium titanate nanoparticles with polyethylenimine improves cellular uptake and allows for coupled imaging and gene delivery. *Colloids and surfaces. B, Biointerfaces*, 112, pp.108–12.

Dreiss, C.A. et al., 2009. Assembling and de-assembling micelles : competitive interactions of cyclodextrins and drugs with Pluronics. *Soft Matter*, 5, pp.1888–1896.

Fan, Z. et al., 2014. A Novel Wound Dressing Based on Ag/Graphene Polymer Hydrogel: Effectively Kill Bacteria and Accelerate Wound Healing. *Advanced Functional Materials*, 24(25), pp.3933–3943.

FarrokhTakin, E. et al., 2012. Synthesis and characterization of new barium titanate core–gold shell nanoparticles. *Colloids and Surfaces A: Physicochemical and Engineering Aspects*, 415, pp.247–254.

Feng, J., Yuan, H. & Zhang, X., 1997. Promotion of osteogenesis by a piezoelectric biological ceramic. *Biomaterials*, 18(23), pp.1531–4.

Gaharwar, A.K. et al., 2013. Bioactive silicate nanoplatelets for osteogenic differentiation of human mesenchymal stem cells. *Advanced materials*, 25(24), pp.3329–36.

Gaharwar, A.K. et al., 2011. Highly extensible, tough, and elastomeric nanocomposite hydrogels from poly(ethylene glycol) and hydroxyapatite nanoparticles. *Biomacromolecules*, 12(5), pp.1641–50.

González-Gaitano, G., Müller, C., et al., 2015. Modulating the self-assembly of amphiphilic x-shaped block copolymers with cyclodextrins: structure and mechanisms. *Langmuir : the ACS journal of surfaces and colloids*, 31(14), pp.4096–105.

González-Gaitano, G., da Silva, M. a., et al., 2015. Selective Tuning of the Self-Assembly and Gelation of a Hydrophilic Poloxamine by Cyclodextrins. *Langmuir*, 31(20), pp.5645–5655.

Gonzalez-Lopez, J. et al., 2008. Self-associative behavior and drug-solubilizing ability of poloxamine (tetronic) block copolymers. *Langmuir*, 24(10), pp.10688–10697.

Hsieh, C.-L. et al., 2010. Bioconjugation of barium titanate nanocrystals with immunoglobulin G antibody for second harmonic radiation imaging probes. *Biomaterials*, 31(8), pp.2272–7.

Jeong, C.K. et al., 2013. Virus-Directed Design of a Flexible BaTiO3 Nanogenerator. *ACS Nano*, 7(12), pp.11016–11025.

Kabanov, A. V., Batrakova, E. V. & Alakhov, V.Y., 2002. Pluronic® block copolymers as novel polymer

therapeutics for drug and gene delivery. *Journal of Controlled Release*, 82(2–3), pp.189–212.

Kanapathipillai, M. et al., 2008. Synthesis and Characterization of Ionic Block Copolymer Templated Calcium Phosphate Nanocomposites. *Chemistry of Materials*, 20(18), pp.5922–5932.

Larrañeta, E. & Isasi, J.R., 2013. Phase behavior of reverse poloxamers and poloxamines in water. *Langmuir*.

Mortensen, K., 1993. Structural Study on the Micelle Formation of PEO-PPO-PEO triblock copolymer in aqueous solutions. *Macromolecules*, 26, pp.805–812.

Nambam, J.S. & Philip, J., 2012. Thermogelling properties of triblock copolymers in the presence of hydrophilic Fe3O4 nanoparticles and surfactants. *Langmuir : the ACS journal of surfaces and colloids*, 28(33), pp.12044–53.

N Pandit, T Trygstad, S Croy, M Bohorquez, C.K. et al., 2000. Effect of Salts on the Micellization, Clouding, and Solubilization Behavior of Pluronic F127 Solutions. *Journal of colloid and interface science*, 222(2), pp.213–220.

Nguyen, L.H. et al., 2012. Vascularized Bone Tissue Engineering: Approaches for Potential Improvement. *Tissue Engineering Part B: Reviews*, 18(5), pp.363–382.

Okabe, S. et al., 2003. Heat-induced self-assembling of thermosensitive block copolymer. Rheology and dynamic light scattering study. *Macromolecules*, 36(11), pp.4099–4106.

Paik, U. et al., 2002. Dissolution and reprecipitation of barium at the particulate BaTiO3–aqueous solution interface. *Materials Research Bulletin*, 37(9), pp.1623–1631.

Park, J.-C. et al., 2002. Evaluation of the cytotoxicity of polyetherurethane (PU) film containing zinc diethyldithiocarbamate (ZDEC) on various cell lines. *Yonsei medical journal*, 43(4), pp.518–26.

Pina, S., Oliveira, J.M. & Reis, R.L., 2015. Natural-Based Nanocomposites for Bone Tissue Engineering and Regenerative Medicine: A Review. *Advanced Materials*, (27), pp.1143–1169.

Rey-Rico, A. et al., 2011. Osteogenic efficiency of in situ gelling poloxamine systems with and without bone morphogenetic protein-2. *European Cells and Materials*, 21(14876), pp.317–340.

Sakai, T., Hoshiai, S. & Nakamachi, E., 2006. Biochemical compatibility of PZT piezoelectric ceramics covered with titanium thin film. *Journal of Optoelectronics and Advanced Materials*, 8(4), pp.1435–1437.

Sanders, L. et al., 2015. Mechanical characterization of a bifunctional Tetronic hydrogel adhesive for soft tissues. *Journal of Biomedical Materials Research Part A*, 103, pp.861–868.

Schexnailder, P. & Schmidt, G., 2008. Nanocomposite polymer hydrogels. *Colloid and Polymer Science*, 287(1), pp.1–11.

Schiraldi, C. et al., 2004. Development of hybrid materials based on hydroxyethylmethacrylate as supports for improving cell adhesion and proliferation. *Biomaterials*, 25(17), pp.3645–53.

Serra-Gómez, R. et al., 2016. Cyclodextrin-grafted barium titanate nanoparticles for improved dispersion and stabilization in water-based systems. *Journal of Nanoparticle Research*, 18(1), p.24.

Serra-Gómez, R. et al., 2012. Rhodamine solid complexes as fluorescence probes to monitor the

dispersion of cyclodextrins in polymeric nanocomposites. *Dyes and Pigments*, 94(3), pp.427–436.

Shen, J. et al., 2015. Supramolecular hydrogels of α-cyclodextrin/reverse poloxamines/carbon-based nanomaterials and its multi-functional application. *RSC Adv.*, 5(50), pp.40173–40182.

Shin, S.R., Aghaei-Ghareh-Bolagh, B., et al., 2013. Cell-laden microengineered and mechanically tunable hybrid hydrogels of gelatin and graphene oxide. *Advanced Materials*, 25(44), pp.6385–6391.

Shin, S.R., Jung, S.M., et al., 2013. Hydrogel Sheets for Engineering Cardiac Constructs and Bioactuators. , (3), pp.2369–2380.

Si, S. et al., 2013. A study of hybrid organic/inorganic hydrogel films based on in situ-generated TiO2 nanoparticles and methacrylated gelatin. *Fibers and Polymers*, 14(6), pp.982–989.

da Silva, M.A. & Dreiss, C.A., 2016. Soft nanocomposites: nanoparticles to tune gel properties. *Polymer International*, 65(3), pp.268–279.

Su, Y.L., Wang, J. & Liu, H.Z., 2002. FTIR spectroscopic investigation of effects of temperature and concentration on PEO-PPO-PEO block copolymer properties in aqueous solutions. *Macromolecules*, 35(16), pp.6426–6431.

Sun, K. & Raghavan, S.R., 2010. Thermogelling aqueous fluids containing low concentrations of pluronic F127 and laponite nanoparticles. *Langmuir*, 26(11), pp.8015–8020.

Tamborini, E. et al., 2012. Structure of nanoparticles embedded in micellar polycrystals. *Langmuir*, 28(22), pp.8562–8570.

Tokunaga, T. et al., 2015. Local Application of Gelatin Hydrogel Sheets Impregnated With Platelet-Derived Growth Factor BB Promotes Tendon-to-Bone Healing After Rotator Cuff Repair in Rats. *Arthroscopy: The Journal of Arthroscopic & Related Surgery*, 31(8), pp.1482–1491.

Tsuchiya, K. et al., 2011. Design of biocompatible high-piezoelectric BaTiO3 with additives. In S. Juodkazis & M. Gu, eds. *Smart Nano-Micro Materials and Devices*. International Society for Optics and Photonics, p. 82042A.

Wang, H. et al., 2013. Development of injectable organic/inorganic colloidal composite gels made of self-assembling gelatin nanospheres and calcium phosphate nanocrystals. *Acta biomaterialia*, 10(1), pp.508–519.

Wang, Y. et al., 2010. Poly(lactide-co-glycolide)/titania composite microsphere-sintered scaffolds for bone tissue engineering applications. *Journal of biomedical materials research. Part B, Applied biomaterials*, 93(1), pp.84–92.

Wu, C.-J. et al., 2011. Mechanically Tough Pluronic F127/Laponite Nanocomposite Hydrogels from Covalently and Physically Cross-Linked Networks. *Macromolecules*, 44(20), pp.8215–8224.

Zhang, J. et al., 2014. Poloxamine/fibrin hybrid hydrogels for non-viral gene delivery. *Journal of tissue engineering and regenerative medicine*.

GENERAL DISCUSSION

This thesis is written using the "article" format, where each of the chapters presented correspond to the papers that have been published in peer-reviewed publications, in chronological order. The aim of this general discussion is to walk through the results obtained as a whole, explaining the context and considerations that led to this particular research path and describing and highlighting the most valuable findings and achievements of the work.

As explained in the Introduction and developed in the previous chapters, there are two main characters in this work, barium titanate and cyclodextrins, which are modified and combined to prepare different kinds of polymeric nanocomposites based on different matrices. On a first stage, films are prepared with the thermoplastic polymer ethylene vinyl acetate (EVA) (Chapter 1), and cyclodextrin complexes with fluorescent probes are explored as a way to track the proper dispersion within a nanocomposite (Chapter 2). Later on, the modification of the surface of BT allows for the preparations of nanocomposites based in water-soluble polymers as PEO, PEG and block copolymers based on PEO-PPO blocks as poloxamers and poloxamines (Chapters 3 and 4), also known as Pluronics® and Tetronics®, to form hydrogels with prospect applications as injectable biomaterials for biomedical applications.

1. INITIAL CONSIDERATIONS

Nanocomposites of all kinds are nowadays in the front-line of research in many science fields, from engineering and construction to aerospace or biomedical, not mentioning the food, environmental, cosmetic or textile industries. The main reason is that the ability to work in the nanoscale has opened possibilities of combination and structural organization, providing new materials with improved properties compared to their antecessors, or what is more interesting, new properties derived from their tailored nanostructure, from their interface interactions, or both. Amongst all the kinds of nanocomposite materials, we are interested in those consisting of a polymeric matrix, known as polymeric nanocomposites, and within that category we have focused our work on those containing an inorganic filler, in particular barium titanate (BT, $BaTiO_3$).

In the case of $BaTiO_3$ and, in general, for the nanofillers in a composite, it is of outmost importance to achieve a good dispersion that ensures the homogeneity and uniformity of the material prepared. When working with nanoparticles, this can be a complicated part, as the elevated surface-area-to-volume ratio favors the agglomeration and aggregation of the nanofillers and, if not prevented, the result is a nanocomposite with faulty properties. To

overcome that challenge different solutions have been proposed, most of them based on the methods of preparation of the nanocomposites, or on the chemical modification of the filler to make it more compatible with the matrix. The nanocomposites of BT have been successfully employed in films that present high dielectric constant, thermal stability and high permittivity. In the recent years, some of the electronic applications of BT have been taken over by PZT's (lead zirconate titanates), and BT has emerged as a good piezoelectric material for biomaterial applications, as it presents as a competitive advantage over PZT's the lack of the toxicity from the lead component. For that reason, in the recent years, multiple applications in tissue engineering, bone regeneration, intracellular nanovectors and imaging probes present $BaTiO_3$ nanoparticles as the common ground.

Simultaneously, cyclodextrins (CDs) have been widely use over the last decades to improve the solubility in water of non-polar compounds through the formation of inclusion complexes, and their applications, albeit predominantly pharmaceutical, also include the food, textile and the cosmetic industry, as well as in environmental chemistry for the removal of pollutants. In the materials field, CDs uses are becoming more and more common, being present in fiber nanocomposites, smart food packaging and in biomedical devices, mainly though the combination of soluble polymers, CDs and drugs to form hydrogels that are able to deliver the molecule of interest upon request. The hydrogel form is very interesting for the biomedical industry, as their characteristics are very similar to those of biological tissues, and they have been successfully proposed for many biological applications over the years. To overcome one of their few disadvantages, the poor mechanical properties, the introduction of nanoparticles to form soft nanocomposites has been proposed, with the outcome of, not only improving that particular flaw, but also introducing new features derived from the type of filler introduced.

2. PREPARATION OF NANOCOMPOSITES: DISPERSION OF BARIUM TITANATE IN A POLYMERIC MATRIX.

The first goal that was set in the thesis was the preparation of piezoelectric nanocomposites in the form of films based on a thermoplastic polymer, ethylene vinyl acetate (EVA) and BT nanoparticles. As it has been explained, the uniformity and homogeneity of the nanocomposite is probably the most important characteristic to obtain a useful product. For that type of polymer composites, the usual preparation techniques include high temperatures to melt the polymer, or organic solvents to solubilize it and proceed to further casting, making it difficult to obtain uniform dispersions when the filler load is over 5 wt%. These techniques are not adequate to prepare the type of nanocomposite we intended to, as the BT

piezoelectric nanoparticles present a tetragonal structure that shifts to a cubic, non-piezoelectric crystalline structure, when the temperature surpass the BT Curie point, which for our particular ceramic was T_c = 128.5 °C, as determined by DSC. In addition to that, and after the initial characterization of the raw materials, it was noticed that the commercial nanoparticles were extensively aggregated, a point that needed to be addressed in order to prepare successful nanocomposites.

We proposed then that using High Energy Ball Milling (HEBM), a solid-state mixing technique commonly employed in alloy powder preparations, could be an advantageous technique for the preparation of the nanocomposite. By performing this technique in cryogenic conditions, the crystalline structure shift was prevented, as confirmed by XRD (Fig 1.4), and consequently the piezoelectric properties maintained. The aggregation of the particles was reduced considerably while a uniform mix of the nanofiller within the matrix was achieved at concentrations as high as 20 wt% (Fig 1.2, Fig 1.7 and Fig 1.8).

A thorough characterization of the nanocomposites was then performed, combining spectroscopic techniques and electron microscopy on samples prepared by HEBM in cryogenic and non-cryogenic conditions. The results show that HEBM is and efficient technique to achieve a proper dispersion of the nanofiller, provided that the conditions of the milling are cryogenic, showing also an important decrease of ca. 50% in the contamination of the samples due to the milling tools, commonly a major drawback in HEBM methods (Table 1.2). The morphology and structural features of the individual materials were maintained through the process, retaining their individual properties of easy processability and piezoelectricity.

Per contra, in non-cryogenic conditions the temperatures reached as a consequence of the high energy process are high enough to melt the polymer matrix, resulting in the subsequent trapping of the nanofiller (Fig 1.7 left). When the process finishes and the temperature goes back to normal, the mixture resulted macroscopically heterogenous and presented some domains richer in nanofiller than others (Fig 1.8 left), while the cryogenic HEBM yielded uniformly dispersed mixtures than could be easily processed into films (Fig 1.9 and Fig 3.4 left).

3. PROPOSAL OF A FLUORESCENT PROBE TO TRACK THE DISPERSION OF THE FILLER IN A NANOCOMPOSITE.

Through cryogenic HEBM and the hot pressing procedure to prepare the nanocomposites, a mere physical mixture of the filler in the matrix was obtained, with no chemical interaction between them. While that was good for the type of nanocomposite we pursued, we were aware that in some cases, chemical interaction between the filler and the matrix could be an

advantage. Our idea was then to use CDs to improve the interaction of the nanoparticles with the matrix, and at the same time add extra functionality to the system by means of the capability of the CDs to form inclusion complexes with other molecules or to generate functional groups on the nanoparticle surface. So far, CDs had been scarcely used in solid nanocomposites, so the concept of introducing them was appealing and an original approach, to our understanding. When starting to investigate on this topic, two different complications aroused, one of them was the difficulty to monitor the CDs within the nanocomposite, as the difference in sizes between them and the rest of components (nanoparticles and polymeric matrix) would make it almost impossible to evaluate their presence, state of aggregation or dispersion without the aid of techniques as AFM or TEM microscopy. The second one was how to modify the nanoparticle to attach the CDs to the surface and how to characterize the extent of the modification.

To tackle the first challenge, we considered using fluorescence spectroscopy, as it is a very sensitive technique and it can be used both in solids and in solution. CDs are known to form inclusion complexes with multitude of fluorophores that may be lodged in the cavity. If we were to find a fluorescent probe that could be included in the CD, so that its emission would experience a change upon inclusion, it could be possible to evaluate the presence of CDs through a simple fluorescence measurement. In our case the probe chosen was Rhodamine, as it has a high quantum yield of fluorescence and fits well the βCD. Tests with RhB and Rh6G types showed that RhB was a better candidate, as it produced more stable complexes with this macrocycle. ^{1}H RMN and ^{1}H ROESY spectra proved the successful inclusion of the probe within the cavity of βCD through one of the xantene rings of the RhB and the secondary hydroxyl rim of the CD with a 1:1 stoichiometry (Fig 2.2, Fig 2.3 and Fig 2.5). The complex experienced a blue-shift compared to the native RhB, along with the quenching of the fluorescence emission (Fig 2.6). The binding constants of the complex were relatively high, in the order of 10^{4} M^{-1} in the range from 15 °C to 45 °C, indicative of a stable association between the RhB and the CD (Table 2.2). The solution experiments were complemented with lifetime fluorescence analysis, which helped describe the self-aggregation effect of the RhB and how the CD acts as a disaggregating agent. At high concentrations of macrocycle, it prevented the self-quenching of the RhB improving the fluorescence response, but at lower RhB concentrations, where self-aggregation of RhB is not an issue, the complex reduced the emission, as expected (Fig 2.7).

As our goal was to achieve a complex to track the CDs in solid state form within the nanocomposite, the inclusion had to be sustained after solvent evaporation in a solid powder form and after the cryogenic HEBM (Cryo-HEBM) process. For that purpose, physical mixtures were prepared and analyzed side to side with the RhB:βCD complex by FTIR, XRD, TGA and

solid state fluorescence. The RhB:βCD complex showed a different thermal decomposition behavior, in one step, at a lower decomposition temperature, compared to RhB and the physical mixture, which presented multiple steps (Fig 2.8). The difference between the complex and the physical mixture was verified by X-ray diffraction results, which indicated a loss in the crystallinity upon complex formation (Fig 2.9). The fluorescence results were also encouraging, as while the RhB and the physical mixture presented exactly the same emission band, the complex displayed a blue-shift of 20nm that allowed for easy and quick differentiation (Fig 2.10).

Cryo-HEBM performed in βCD showed no damage to the macrocycle, and the same happened with the RhB:βCD complex. The complex and the physical mixtures were milled with EVA polymer to form the nanocomposite films, obtaining uniform films. In addition to the already visual difference, their fluorescence response presented a four-fold increase of the fluorescence signal of the RhB:βCD complex in comparison with the physical mixture, as well as a considerable blue-shift in the emission band (Fig 2.11).

The fact that the RhB:βCD complex was maintained in solid state and endured the aggressive conditions of cryo-HEBM (Fig 2.12) represents a novel application of an inclusion complex of CD and opens a number of possibilities for their use in nanocomposites.

4. SURFACE MODIFICATION OF THE BARIUM TITANATE NANOPARTICLES.

To improve the compatibility and interaction of the nanofiller with the matrix it is common to modify chemically the surface of the nanoparticles. Due to the high surface-area-to-volume ratio of the nanofiller, the interphase interactions of the nanoparticles with the polymeric matrix are one of the areas from where the nanocomposites obtain most of their benefits compared to traditional materials. As mentioned above, BT nanoparticles have recently been explored for other uses besides the microelectronic applications. Their piezoelectricity can be of great use in some biological processes as bone regeneration, biological imaging and tissue engineering, as described in the Introduction. However, the main challenge for those applications is that the nanoparticles need to be stable in aqueous systems, which can only be achieved through the modification of their surface. We proposed that a modification of the surface of the nanoparticles with CDs could help address the aggregation and stabilization behavior of the nanoparticles, in addition to benefitting from the host-guest chemistry of the macrocycles attached. In our case, after having prepared nanocomposites by solid state methods as cryo-HEBM, this type of modification would open

the possibility of the preparation of nanocomposites under mild conditions with water-soluble polymers used in the biomaterials field, like PEG, PEO, or biocompatible block copolymers.

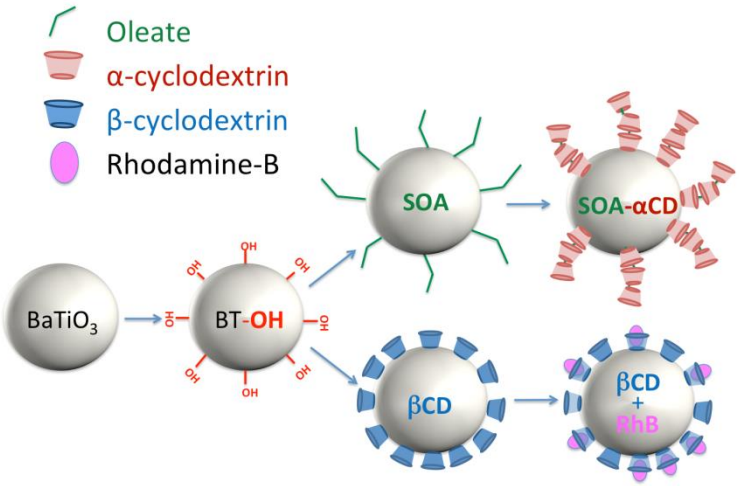

Fig 5.1: Scheme of the modifications carried out to the $BaTiO_3$ nanoparticles: common hydroxylation step and addition of SOA+αCD (top branch) or βCD +RhB (bottom branch).

Two different modifications were carried out in different BT nanoparticles (Fig 5.1), the tetragonal piezoelectric, with a diameter of 200nm, and the cubic one, with diameters of 100nm and 50nm. The first modification had the purpose of generating hydroxyl groups in the surface that would react with sodium oleate (SOA), to cover the surface with the long, hydrophobic chains to produce a "hairy" sphere. This surfactant helped improve the stability in organic dispersions, but still caused some aggregation in water. This aggregation in water can be prevented if the oleate chains are capped with αCD, which is able to include the oleate chains. Due to the length of the SOA tails, each molecule can accommodate an average of 3 αCD molecules.

The second modification, which was the one that presented better results, consisted in generating hydroxyl groups on the surface to directly incorporate αCD and βCD, obtaining a direct improvement in the stability of the suspension (Fig 3.6). Because of the difference in size of BT nanoparticles and the CDs, even though the effects could be instantly perceived, the characterization was extremely difficult, as the weight contribution of the coating is below 1 wt%, and the difference in diameter is of just a few nanometers. Consequently, the characterization process was addressed from different perspectives in a multi-technique approach, using spectrophotometry (FTIR-ATR, DLS, and Fluorescence), TEM microscopy, and zeta potential, each one contributing with a piece of information to accomplish the full characterization of the surface modification. By TEM microscopy a clear difference could be observed in the BT nanoparticles and the oleate modified ones (Fig 3.7). The whole

modification process could be tracked by FTIR-ATR, starting with the generation of –OH groups, continuing with the grafting of the oleate and the third step with the threading of αCD, as well as the βCD addition in the nanoparticles without SOA (Fig 3.1). The disaggregation capacity of βCD was verified by DLS, as the particle distributions showed a decrease from 300 nm and above in the commercial nanoparticles to around 60 nm in the βCD-modified BT (Fig 3.4 and Table 3.3). Z-potential confirmed the stability improvement at higher concentrations and, what is more important, at the physiological pH range (Fig 3.5). TGA exhibited values that, even though they were close to the detection limit of the technique, were well within the margins of the theoretical calculations of the SOA, αCD and βCD masses grafted to the surface (Fig 3.2). Finally, the inclusion complex between RhB and βCD that had been previously studied came in handy as it helped corroborate the surface modification, by displaying a decrease in the fluorescence of a solution of RhB when in contact with the nanoparticles. As the βCD in the surface is able to include RhB molecules, the solid state fluorescence response of the modified nanoparticles resulted considerably higher than the non-modified ones (Fig 3.3), as a confirmation of the extra functionality achieved via the complexing capacity of the cyclodextrin, which could be further explored with drugs or any other molecules of interest.

Once all the pieces of the puzzle fitted and the modification was confirmed, cytotoxicity studies were performed in different cell lines (NIH3T3 and MC3T3-E1) through MTT assays to explore the the viability of the cells in the presence of the modified nanoparticles. Confocal microscopy was used to track the tissue growth and both experiments yielded excellent results in terms of viability and cell growth, in concentrations up to 200 μg/ml of nanoparticles (Fig 3.8, Fig 3.9 and Fig 3.10).

One of the objectives of modifying the surface of the nanoparticles was to make them more compatible with a polymeric matrix. For this purpose, the commercial BT and the modified BT were put in a solution of hydrosoluble polymers, as PEG and Pluronic F127, to quantify the interaction through the different modifications. The coating of the nanoparticles with those polymers were measured and the results exhibited an enhancement in the coating with the polymer of up to 500% in the case of PEG and 165% for the poloxamer (Fig 3.11). Further on, nanocomposite films were casted and the dielectric properties tested, confirming that the modified BT retained its characteristic electrical properties upon modification (Fig 3.14 and Fig 3.16).

The modifications made on the surface of the BT nanoparticles allowed to maintain the suspension in aqueous solutions for a substantial amount of time, opening the possibility of preparing nanocomposites by casting with the most common polymers used as biomaterials.

5. PREPARATION OF A SOFT NANOCOMPOSITE.

In the first chapter of the Results we described the preparation of film nanocomposites by HEBM, focusing on achieving a proper uniformity and homogeneity of the nanoparticles, and it served us as a way to understand the aggregation behavior of the BT. Later on we developed the RhB:CD interaction both in solution and solid state to explore the inclusion complex ability of the cyclodextrins in conjunction with the nanocomposites, and in the third chapter we addressed the modification of the nanoparticles to improve their compatibility with biological matrixes. The logical next step was to unite it all together, and we chose the preparation of a hydrogel nanocomposite as an interesting approach, or proof or concept, to show the capabilities of our research, namely the preparation of a $BaTiO_3$ nanocomposite that could be used as a biomaterial. In this part of the work, described in Chapter 4, all the previous investigations carried out on BT and CDs link up.

Hydrogels are known to have limited mechanical properties, but at the same time they are the most used in the biomaterials field due to their similitudes with biological tissues. The combination of hydrogels and nanoparticles to form soft nanocomposites is a way of overcoming the mechanical deficiency and achieving new functionalities of interest. BT has been proposed in the literature as ceramic filler that due to its piezoelectric properties is able to promote bone regeneration. This can be achieved by the enhancement of the cellular and tissue stimulation through the BT piezoelectric interaction with the dipoles formed on the collagen fibers.

Tetronic 1107 (T1107) has been the polymer used to form the hydrogel. It is an X-shaped poloxamine with four PPO-PEO arms connected by and ethylene diamine central group. As a difference to Pluronics, their linear counterparts, the presence of the connector group makes Tetronics pH-sensitive, with key implications in the aggregation and gel formation that add up to their temperature and concentration responsiveness. T1107 has the ability to naturally form physical hydrogels, and it has been recently proposed for injectable formulations (Table 4.1). As a first step we fully characterized the phase behavior of this poloxamine in the low and high concentration regimes, up to 30% in a wide range of temperatures (20 °C – 80 °C) and at different pH's by the combined use of scattering techniques (DLS and SANS) and IR spectroscopy. This enabled us to describe, understand and predict the micellar behavior and aggregation into gels, as well as elucidating the structures it forms at different concentrations. In the dilute regime, the pH is critical, as acidic conditions prevent the formation of micelles, whereas neutral or alkaline pH contributes to the arrangement of the block copolymer in core-shell structured micelles with the PPO in the inner side and the PEO chains, highly hydrated, in

the hydrophilic corona (Fig 4.2 and Fig 4.3). At higher concentrations and upon gel formation, the micelles achieve a higher order of arrangement in between a dense packing of micelles and a paracrystalline arrangement in the form of BCC structures (Fig 4.4, Fig 4.5, Fig 4.6 and Fig 4.7).

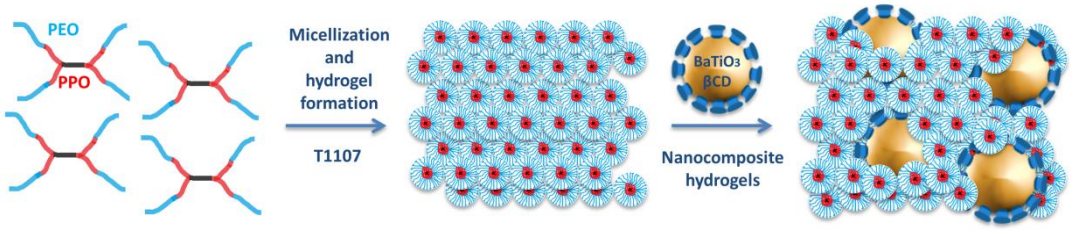

Fig 5.2: Scheme of the structure and formation of the nanocomposite hydrogel of Tetronic 1107 and βCD-modified $BaTiO_3$ nanoparticles.

By combination with CD-modified BT nanoparticles and formation of the soft nanocomposite (Fig 5.2), the gelation properties of the polymer changed. Being the nanoparticles bigger than the micelles, they did not affect their formation *per se*, but they arranged in a different way, contributing to the dense packing of the micelles with a paracystalline structure arrangement at lower concentrations than the hydrogel of the poloxamine alone. They did, however, modify drastically the rheological behavior of the hydrogel. The introduction of different quantities of CD-modified BT nanoparticles (5 -12 wt%) was able to lower the sol-gel point to a maximum of 12 °C, and at the same time expanded the gel phase as the gel-sol transition shifted to higher temperatures (Fig 4.9). In addition to that, the elastic modulus of the nanoparticles was also highly improved, achieving elastic modulus (G') increments of up to 200%, almost fitting a linear trend in the range of concentrations tested (Fig 4.10). Overall, the introduction of the BT did not only add the extra functionality of the piezoelectricity of the CD-modified nanoparticle, but also allowed for the production of a tailorable hydrogel, enabling us to adjust the sol-gel transition and the elastic module to our particular needs by fine-tuning the concentrations of the components.

Finally, and as it was studied with the modified nanoparticles, the cytotoxicity of the hydrogel nanocomposites was tested against a fibroblasts cell line. The results were satisfactory, of over 90% viability when the concentration is below 1 wt% in T1107 and between 70% - 90 % in the concentrations ranging from 1 wt% to 25 wt% (Fig 4.11).

With this last investigation concludes this thesis, initially started with the aim of preparing polymeric nanocomposites based on $BaTiO_3$ nanoparticles and CDs, and that due to the interesting findings that we found on the first two chapters presented, derived in the idea of shifting the focus from nanocomposites for the electronic industry to soft nanocomposites that

could be useful in the biomaterials field as injectable fillers or scaffold components. The final conclusions that have been extracted from this work are presented in the following section.

CONCLUSIONS

CONCLUSIONS

1. Cryogenic HEBM is a suitable technique for the preparation of polymeric nanocomposites based on $BaTiO_3$ piezoelectric nanoparticles and thermoplastic EVA as the matrix with lower contamination than HEBM at normal conditions. Moreover, it has been proven to be a successful technique to reduce $BaTiO_3$ inherent agglomeration and obtain a homogenous dispersion of the filler within the matrix without the need of external solvents or chemical modifications, while retaining the inherent properties of the components, method that can be extended to other systems of polymeric matrices.

2. 1D and 2D NMR spectroscopy methods combined with the fluorescence response of the RhB:βCD complex have permitted to elucidate the topology of the inclusion, with a 1:1 stoichiometry and high stability, as evidenced by the high binding constants, over a wide range of temperatures in solution, stability that is kept in the solid phase.

3. The solid RhB:βCD inclusion complex exhibits a blue shift in the fluorescence emission compared to the native RhB, as well as an enhancement compared to the physical mixture, which enables it to be used as a method to monitor the presence of βCD and its proper dispersion in nanocomposites prepared by cryo-HEBM with fluorescence spectroscopy.

4. The surface modification of the $BaTiO_3$ nanoparticles with sodium oleate plus αCD, or directly with βCD, improves the disaggregation of the nanoparticles and yields more stable suspensions of the nanoparticles in water based systems. Moreover, the presence of βCD on the surface adds extra functionality to the nanoparticles, derived from the ability of the macrocycle to form host-guest interactions with a molecule of interest

5. The βCD-modified BT nanoparticles are cytocompatible with the NIH3T3 fibroblast and MC3T3-E1 pre-osteoblasts cell lines, improving the viability of the cells compared to the unmodified BT nanoparticles.

6. The modified nanoparticles have been used to prepare nanocomposite films based on hydrosoluble polymers of PEG (Mw= $1 \cdot 10^5$), PEO (Mw = $4 \cdot 10^6$) and PPO/PEO poloxamer

Pluronic F127 by water casting methods, obtaining excellent results in terms of an homogeneous dispersion of the nanoparticles. The dielectric properties of the BT nanocomposites are sustained after the surface modification, the cryogenic-HEBM and water casting process.

7. The phase diagram, aggregation behavior and structure and the mechanical properties of the poloxamine Tetronic T1107 have been fully characterized. At low concentrations and above 30 °C, the poloxamine forms core-shell micelles with a dehydrated core and a highly hydrated corona. While the size is not largely affected by the temperature or the concentration, the changes in pH do change the degree of protonation of the central spacer, preventing the formation of compact micelles and favoring the formation of loose aggregates with direct influence in the micelle size and hindrance to the formation of a gel phase. At higher concentrations, micelles pack and form gels with a paracrystalline structure, as determined by SANS, conforming a BCC structure.

8. βCD-modified BT nanoparticles have been used in conjunction with the poloxamine to prepare a soft nanocomposite over a wide range of compositions. The gelation can be tailored for the preparation of injectable hydrogel and the mechanical properties of the nanocomposite are considerable enhanced by the addition of the BT nanoparticles. The structure, rheological properties and cytotoxicity of the prepared hydrogel nanocomposites as a function of temperature and nanoparticle composition, corroborate the excellent properties of the hydrogel for their use as a biomaterial.

ANNEXES

Composites Based on EVA and Barium Titanate Submicrometric Particles: Preparation by High-Energy Ball Milling and Characterization

R. Serra-Gómez,[1] G. González-Gaitano,[1] J. González-Benito[2]
[1]*Departamento de Química y Edafología, Universidad de Navarra, 31080 Pamplona, Spain*

[2]*Departamento de Ciencia e Ingeniería de Materiales e Ingeniería Química and IQMAAB, Universidad Carlos III de Madrid, 28911 Leganés, Spain*

Ethylene vinyl acetate copolymer, a thermoplastic semicrystalline polymer, has been blended with barium titanate submicrometric particles ($BaTiO_3$) by means of high-energy ball milling (HEBM) for obtaining composites in the form of films by hot pressing. Two different milling conditions have been considered: (i) milling at room temperature and (ii) milling under the temperature of the liquid nitrogen (cryomilling). The resulting composites have been fully characterized by spectroscopic and microscopic techniques to study the structure and morphology as a function of the processing conditions. A very good dispersion of the particles is attained under cryogenic conditions and, irrespective of the milling method, structural modifications were not observed in any of the materials used. Cross-contamination of iron from the milling tools is also reduced to acceptable values for HEBM standards, especially in the case of cryomilling, an important issue for the use of these composites in electrical applications. POLYM. COMPOS., 33:1549–1556, 2012. © 2012 Society of Plastics Engineers

INTRODUCTION

One of the most important prerequisites to reach best performance in polymeric composite materials is to ensure a uniform dispersion of the particles, because the formation of particles agglomerates may lead to the unwanted discontinuity or deterioration of their properties [1]. Up to now, several methods have been employed to achieve efficient dispersion of inorganic nanoparticles, either nano- or submicron-sized, in different matrices: (i) modification of the surface of the particles [2–4]; (ii) chemical modification of the filler with a monomer, to allow the subsequent polymerization when mixed with a co-monomer [5]; (iii) "in situ" polymerization by dispersion of the particles in a monomer for subsequent polymerization [6]; (iv) by conventional sol–gel methods to generate nanoparticles within the polymer matrix; and (v) addition of surfactants or other dispersant substances as phosphate esters [7]. In general, these methods are based on material processing in solution or melted state. Typically, when the particle diameter is small [3], a uniform mixture is really difficult to obtain if the amount of filler is higher than 5 wt%, or if the polymer melt presents a high viscosity.

High-energy ball milling (HEBM) is a good approach of processing thermoplastic matrix nanocomposite materials, not only due to the results in terms of dispersion, but also from an economical point of view. Initially intended for the synthesis and processing of inorganic materials [8–11], this method has been successfully used to obtain polymer blends with improved mechanical properties and polymer nanocomposites with real dispersion of nanoparticles, as poly(methyl methacrylate)-silica [12, 13], acrylonitrile-butadiene-styrene, polystyrene and polypropylene [14, 15], and high density polyethylene with TiO_2 nanoparticles [16]. However, due to the high energy involved in the process it may have adverse effects of wearing on the polymers by mechanisms of chain scission and sample oxidation, together with cross-contamination from the milling tools [17].

The aim of this work has been to prepare by means of HEBM a new thermoplastic composite formed by ethylene vinyl acetate (EVA) copolymer, blended with barium titanate submicrometric particles. $BaTiO_3$ has been chosen due to its ferroelectricity and high dielectric constant in its tetragonal structure [18], properties which make it use-

Correspondence to: J. González-Benito; e-mail: javid@ing.uc3m.es
Contract grant sponsor: Ministerio de Ciencia e Innovación; contract grant numbers: MAT2010-16815, AIB2010PT-00267; contract grant sponsor: Asociación de Amigos de la Universidad de Navarra and Fundació La Caixa.
DOI 10.1002/pc.22291
Published online in Wiley Online Library (wileyonlinelibrary.com).
© 2012 Society of Plastics Engineers

ful for applications in the field of electronics as printed circuits or in capacitors, for example. However, the high processing temperature it presents as a ceramic material makes it unsuited for many practical uses. This problem may be overcome by its preparation in the form of composites by making use of the low temperature processability of the polymer. EVA is a thermoplastic polymer with polar groups (vinyl acetate) and crystalline ethylene domains. When the amount of the ethylene comonomer is high enough, EVA copolymer can be easily processed in the form of films. The presence of polar vinyl acetate groups in the EVA copolymer may also favor its adhesion to $BaTiO_3$ particles, as observed in other fillers with polar surfaces [19]. In addition to that, the fact that the polymer is semicrystalline adds a potential interest because many of the final properties depend on the crystallinity of the composite matrix. The milling has been carried out under cryogenic and room temperature conditions, with the purpose of ascertaining the best way to achieve a uniform dispersion in the composite avoiding the degradation processes of the polymer and the phase change of the inorganic submicrometric particles. The characterization of the $BaTiO_3$/EVA composites and the study of their morphology and particle dispersion according to the processing conditions are also presented in this work.

EXPERIMENTAL PART

Materials

Poly(ethylene-*co*-vinyl acetate), EVA (12% wt/wt in vinyl acetate, density 0.933 g/cm^3 at 25°C, Vicat temperature ASTM D 1525 = 65°C and melting point = 95°C) was supplied by Sigma Aldrich. Inorganic submicrometric particles of barium titanate ($BaTiO_3$) were supplied by Nanostrucutred and Amorphous Materials. Their average diameter according to the manufacturer is 200 nm, with 99.9% purity, density of 6.02 g/cm^3, and tetragonal crystalline structure.

Sample Preparation

In order to make easier the subsequent blending process with the particles, EVA pellets were firstly ground in a MF 10 Basic IKA WERKE grinder at a rotation speed of 4500 rpm. The grinding time was short enough to avoid polymer melting due to the rise of temperature associated to the process. Two methods of processing were carried out to merge the $BaTiO_3$ with EVA:

1. *HEBM at room temperature*. $BaTiO_3$ was mixed with the ground EVA (20% wt/wt of $BaTiO_3$) and introduced in a vial of stainless steel together with 11 stainless steel balls of 20-mm diameter. The vial was then hermetically closed and placed in a Pulverisette 5 Fritsch apparatus where the powder was milled at 400 rpm for 2 h at room temperature. Each 10 min of active milling was followed by 3 min of resting. After the first hour of active milling the equipment was left to rest for 20 min.
2. *Cryo-HEBM*. A mixture of $BaTiO_3$ with EVA (20% wt/wt) was subjected to HEBM process under cryogenic conditions (cryomilling) in a MM400 RETSCH miller. A vessel of 50 mL and one ball of 20-mm diameter made of stainless steel were used. The procedure consisted in 1 h of active cryomilling divided into 12 cycles of 5 min of milling at 25 Hz (vessel oscillation) and 15 min of resting in liquid nitrogen.

Films of the composites were prepared by hot pressing. The milled powder was placed between two Teflon plates and pressed and heated in an oven at 150°C for 20 min. After that, the prefilms were cooled inside the oven down to 40°C. A small portion of the prefilm was placed between the two Teflon plates and sandwiched between two stainless steel plates fixed with clampers. A weight was placed on top of the sample, as described by Olmos et al. [17] and put into an oven to be heated at 150°C for 90 min. The film was slowly cooled down inside the oven to room temperature, avoiding any thermal stress in the sample. The thicknesses of the prepared films were of about 20 μm.

Techniques

The crystalline structure of the materials under study was characterized by X-ray diffraction, XRD, using a Philips X'PERT-MPD diffractometer with a copper anode emitting its typical $K\alpha_1$ radiation at a wavelength of 1.5405 Å applying a voltage of 40 kV. For randomly oriented powder preparations, the diffractograms were obtained scanning 2θ angles from 7° to 90° in steps of 0.02°. The analysis of the X-ray diffraction patterns was carried out using the Philips XPert Graphics software.

Elemental analysis was carried out by atomic absorption spectroscopy (AAS) using a Perkin Elmer Analyst 800. The milled samples were subjected to a digestion process in a closed vessel with microwaves in concentrated nitric acid and hydrogen peroxide medium. The content in iron was deduced from interpolation in the calibration curve prepared with Fe standards.

The topography of the samples was inspected by scanning electron microscopy (SEM) (Philips XL30), with the signal coming from secondary electrons (SE) while the morphology and distribution of domains with different compositions were imaged using backscattered electrons (BSE). Finally, microanalysis at specific sites of the samples was performed with a DX4i coupled energy-dispersive X-ray spectroscopy (EDAX) detector. To avoid charge accumulation on the surfaces under analysis, the samples were coated with Au by sputtering method.

Fourier transform infrared spectroscopy (FTIR) spectra were recorded in transmission mode with a FTIR Spectrum GX (Perkin-Elmer). Forty scans with a resolution of

 DOI 10.1002/pc

4 cm^{-1} were performed. The powders coming from the milling process were diluted in KBr (less than 1 wt%) and pressed in the form of discs. All samples had low enough amounts of EVA or EVA-$BaTiO_3$ as to satisfy the Lambert–Beer's law. On the other hand, the samples in the form of films were studied by attenuated total reflectance (FTIR-ATR) using an FTIR Nicolette Avatar 360 spectrometer coupled to a Golden Gate diamond ATR accessory. The resolution was of 4 cm^{-1} and 32 scans per spectrum.

Thermogravimetric analysis (TGA) was carried out in a Perkin Elmer STA 6000. The samples were subjected to a heating program from 30°C to 800°C at 30°C/min under a N_2 atmosphere.

The average size of the particles was determined by dynamic light scattering (DLS) using a DynaPro photon correlation spectrometer. The particles were dispersed in deionized water by sonication and diluted before the measurements without further filtration. The size distributions were calculated by the method of regularization with DynaLS 1.0 software, expressed in terms of the hydrodynamic diameter, D_h.

RESULTS AND DISCUSSION

Characterization of the Submicrometric Particles

$BaTiO_3$ shows piezoelectric response when its crystalline structure is tetragonal. XRD patterns of the commercial $BaTiO_3$ particles show the typical split of the tetragonal structure at 45° and 45.5° due to the planes (002) and (200), which come from the cubic cell distortion [20] according to the JCPDS chart no. 5-626. The differential scanning calorimetry (DSC) trace of the commercial $BaTiO_3$ shows also the Curie transition at 128.2°C, due to the $BaTiO_3$ allotropic transformation from the tetragonal structure to the cubic one, in agreement with literature values [21].

A SEM image of the commercial $BaTiO_3$ is shown in Fig. 1. Spherical shape agglomerates of submicrometric particles can be observed. The mean hydrodynamic diameter that can be measured is close to the mean average particle size (APS) provided by the supplier (≈200-nm diameter).

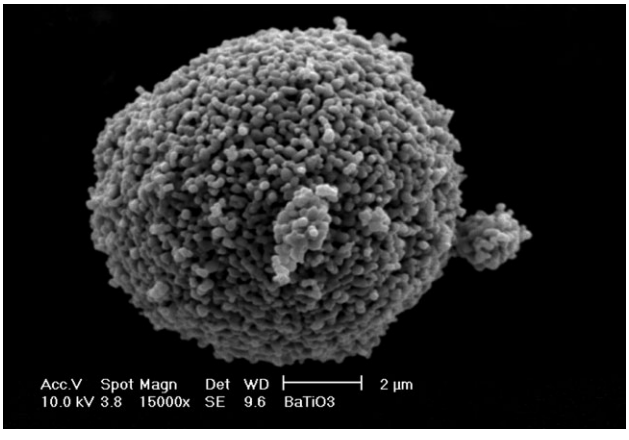

FIG. 1. SEM image of as received $BaTiO_3$ nanoparticles.

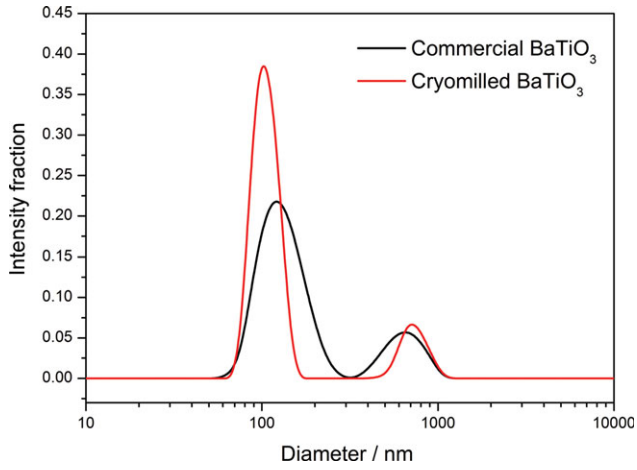

FIG. 2. Size distributions obtained by DLS of as received $BaTiO_3$ particles and after cryomilling. [Color figure can be viewed in the online issue, which is available at wileyonlinelibrary.com.]

DLS has been used to characterize more accurately the spectrum in size of the $BaTiO_3$. As seen in Fig. 2 the distribution is bimodal. The first peak corresponds to the submicrometric particles dispersed in water while the second one is ascribed to aggregates (Table 1). The size distribution can be converted from scattered intensity to mass by assuming that the particles have spherical shape. In terms of mass the distribution is quite monodisperse, with a negligible contribution of the aggregates (less than 1%). When cryomilling the $BaTiO_3$, the average particle diameter results to be slightly smaller but practically the same within the experimental uncertainty (Table 1), the width of the distribution is reduced (i.e., particles more monodisperse) and also is the percentage of aggregates. This implies that the milling procedure does not affect significantly the APS of $BaTiO_3$, contributing to break the scarce existing agglomerates.

Characterization of the Nanocomposites Prepared by HEBM

Figure 3 shows the XRD patterns of the commercial and cryomilled EVA. The characteristic peaks of EVA with high fraction of ethylene comonomer appear at 21.3°, 23.6°, and 36.1°, rising on the amorphous halo.

TABLE 1. DLS analysis for commercial and cryomilled $BaTiO_3$ particles.

	Peaks	Intensity (%)	D_h (nm)
Commercial	1	81	264 ± 80
	2	19	1524 ± 312
Cryomilled	1	85	212 ± 28
	2	15	1524 ± 226

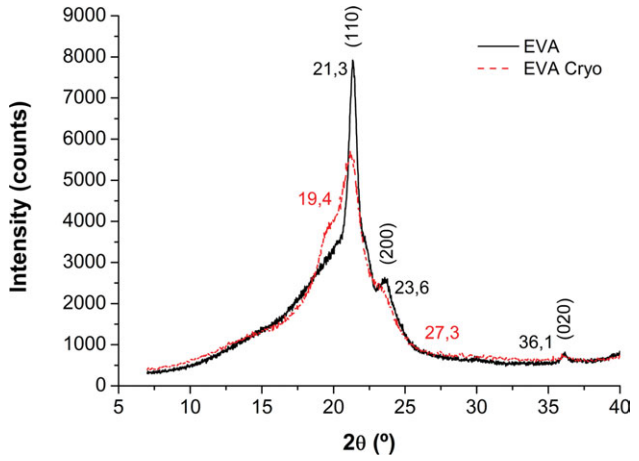

FIG. 3. XRD patterns of commercial and cryomilled EVA. [Color figure can be viewed in the online issue, which is available at wileyonlinelibrary.com.]

These correspond to the orthorhombic crystal planes (110), (200), and (020). The intensity of these reflections decreases after milling, which suggests a reduction in the crystalline fraction of the EVA matrix, associated to the main ethylene part of the copolymer. This decrease is usually assigned to the change from the orthorhombic to the monoclinic phase in the ethylene fraction, represented by three peaks at 19.4°, 21.3°, and 27.3°, respectively. Russell et al. [22] have pointed out that these changes in the crystal region cannot be obtained without a mechanical stress.

The X-ray diffraction patterns obtained for the samples EVA, commercial $BaTiO_3$, and cryomilled $BaTiO_3$+EVA are shown in Fig. 4. When comparing the diffractograms with those in Fig. 3 it can be observed how the reduction of the crystalline fraction of EVA after cryomilling is even higher in the presence of $BaTiO_3$. The higher reduction of crystallinity can be justified considering the additional mechanical stress imposed by the presence of

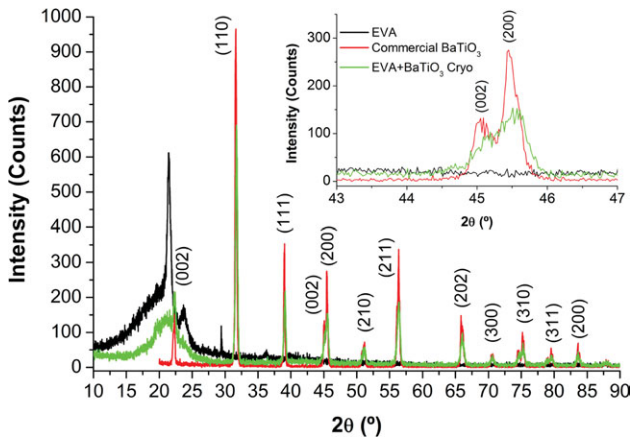

FIG. 4. X-ray diffractograms of EVA, commercial $BaTiO_3$, and cryomilled $BaTiO_3$ + EVA. [Color figure can be viewed in the online issue, which is available at wileyonlinelibrary.com.]

$BaTiO_3$ particles, which, in the meantime do not see altered their size. On the other hand, the typical peaks of $BaTiO_3$ remain after milling with EVA (Fig. 4), being slightly shifted to higher angles (0.5°) and presenting a somewhat larger half peak width, which is indicative of smaller crystals [23]. Finally, as seen in the inset of the Fig. 4, the splitting of the peak at 45.5° representative of the $BaTiO_3$ tetragonal phase is maintained when the particles are cryomilled with EVA. This result is really important in order to ensure the piezoelectric properties of the $BaTiO_3$ within the EVA matrix.

One of the main problems when HEBM is used is the cross-contamination from the milling tools, in this case made of stainless steel. The extent of such contamination largely depends on the milling time, the frequency, and the hardness difference between the powder and the milling tools [8,17]. In the case of a nanocomposite intended for electrical applications this undesired effect might be a drawback. Hence the milled powders have been analyzed for iron by AAS, more sensible than TGA and X-ray microanalysis. The Fe content of the milled samples is given in Table 2. In all cases, the contamination is rather small, lower than 0.03% wt/wt. Cryomilling (Cryo) produces also less contamination than that attained with the milling process at room temperature (RT).

To evaluate the dispersion in EVA-$BaTiO_3$ nanocomposites SEM images were obtained from BSE, which are sensible to the atomic mass of the elements imaged, ensuring that the domains observed are due to differences in elemental composition rather than topography contrast. Brighter domains should correspond to regions with higher concentration of heavier atoms, in our case Ba and Ti arising from the particles. Figures 5 and 7 show representative SEM images of the milled samples. As can be observed in the samples of neat EVA, only contrast coming from the topography can be visualized (Fig. 5). No contamination from the milling tools is observed, which has been confirmed by EDAX microanalysis shown in Fig. 6, with the results of the cryomilled EVA (left) and of the EVA + $BaTiO_3$ (right). The unassigned peak corresponds to the gold coating of the samples. No differences were observed between the samples milled at room temperature (Fig. 5, left) and that one milled under cryogenic conditions (Fig. 5, right).

In addition to the topography, Fig. 7 shows another contrast due to the presence of domains rich in Ba and Ti. This allows an easy evaluation of the dispersion of the

TABLE 2. Fe content of the milled samples as determined by AAS.

Sample	HEBM	Fe (mg/kg)	wt/wt %
EVA	RT	108.7	0.011
EVA	Cryo	30.08	0.003
EVA + $BaTiO_3$	RT	275.2	0.028
EVA + $BaTiO_3$	Cryo	128.4	0.013

DOI 10.1002/pc

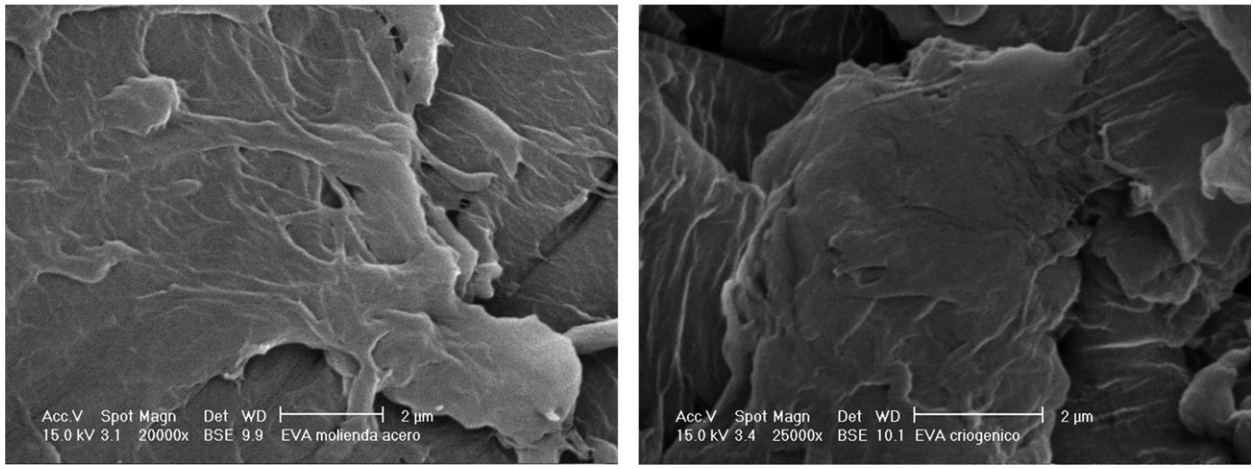

FIG. 5. SEM images obtained from BSE signal of EVA milled at room temperature (left) and cryogenically (right).

$BaTiO_3$ particles. From a careful analysis of the images (See the inset of Fig. 7 with the particle size distribution) it can be observed that the sizes of the domains (246 ± 59 nm) coincide with those of the commercial $BaTiO_3$ particles determined by SEM image analysis and DLS.

When HEBM is carried out at room temperature, low amounts of $BaTiO_3$ are observed near the surface of the milled powder (Fig. 7, left). This suggests a non-uniform dispersion of $BaTiO_3$ particles within the EVA matrix. This is confirmed by EDAX microanalysis upon different regions of the samples, showing different relative amounts of Ba and Ti. On the contrary, the cryomilled sample shows large amounts of $BaTiO_3$ particles uniformly dispersed in the EVA polymer (Fig. 7, right). Therefore, cryogenic conditions seem to be more effective to disaggregate the $BaTiO_3$ agglomerates and to adequately disperse the particles within the polymer matrix.

These materials will not be used typically in the form of powder but processed into films. Hence, SEM inspections have been also carried out on the film nanocomposites. Figure 8 shows SEM images from BSE of the films of EVA + $BaTiO_3$ milled at room temperature (left) and under cryogenic conditions (right). In both images, the presence of $BaTiO_3$ particles is evidenced by the clear contrast observed in the BSE image, where the presence of Ba and Ti elements produces brighter domains. When HEBM is carried out at room temperature the $BaTiO_3$ is not so well dispersed throughout the whole surface of observation, where a broad strip with lower concentration of $BaTiO_3$ can be seen from left to right (Fig. 8, left). This is in accordance with what has been already observed in the milled powder at room temperature. On the contrary, the film coming from the powder sample milled under cryogenic conditions shows large amounts of $BaTiO_3$ particles uniformly dispersed in the EVA matrix (Fig. 8, right). Thus, uniform particle dispersion is preserved after processing the cryomilled powders by hot pressure to obtain thin films. The size of the particles agrees with that provided by the supplier and those determined initially by SEM and DLS. Figure 9 presents an image at

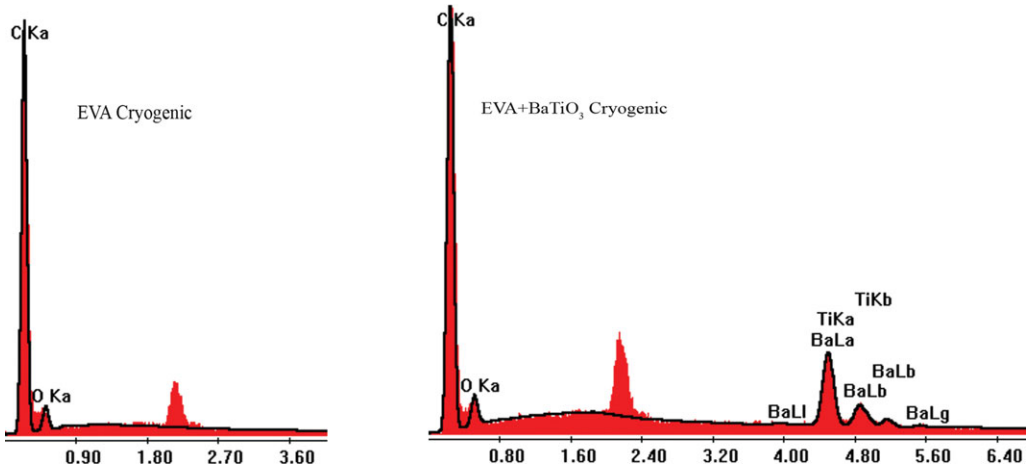

FIG. 6. EDAX analysis of cryomilled EVA (left) and cryomilled EVA + $BaTiO_3$ (right). [Color figure can be viewed in the online issue, which is available at wileyonlinelibrary.com.]

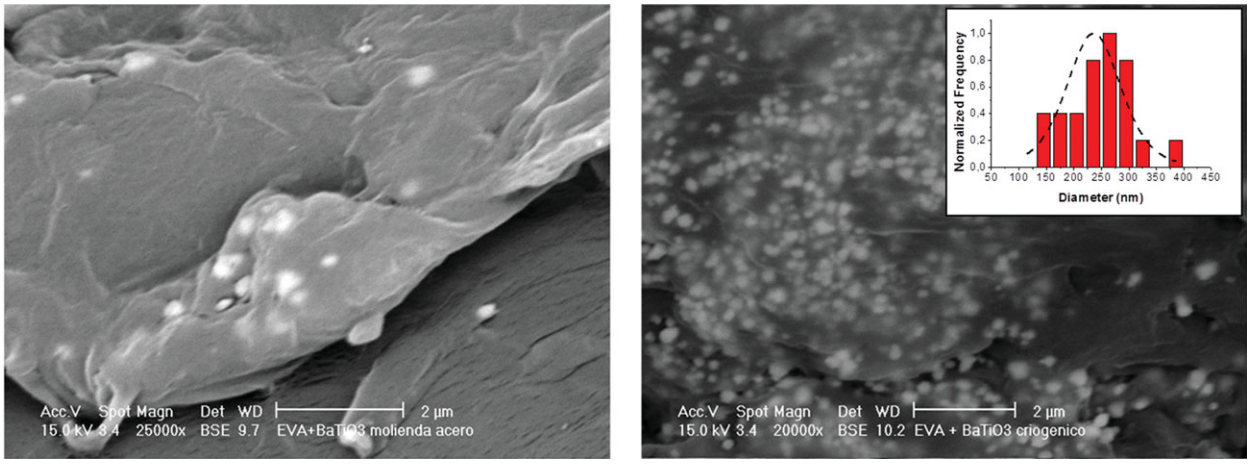

FIG. 7. SEM images obtained from BSE signal of EVA + $BaTiO_3$ milled at room temperature (left) and cryogenically (right). Inset (right) represents the particle size distribution. [Color figure can be viewed in the online issue, which is available at wileyonlinelibrary.com.]

higher magnification in the film obtained from the EVA + $BaTiO_3$ cryomilled powder, showing more clearly the proper dispersion of the filler.

The maximum amount of spherical particles that can be uniformly distributed within a polymer corresponds to a close-packing arrangement. For a certain amount of spherical particles uniformly dispersed within a matrix it seems reasonable to consider a similar arrangement in order to estimate the average distance between them. Taking into account this upper limit, for a certain volume of composite, overall composition and densities of filler and EVA, it is possible to estimate an average distance between $BaTiO_3$ particles of 600 nm. The analysis of the SEM image in Fig. 9 yields an average distance between $BaTiO_3$ particles of 600 nm, matching the estimated value and confirms the homogeneous dispersion of the submicrometric particles obtained using this method of processing.

Finally, in order to examine how the presence of $BaTiO_3$ affects the structure of the EVA polymer and the possible interactions between them, FTIR analysis of the powders and FTIR-ATR of the film samples has been carried out. The FTIR spectra of EVA as received, cryomilled, and milled at room temperature are shown in Fig. 10a. The most intense bands at 2915 cm^{-1} and 2854.8 cm^{-1} correspond respectively to the antisymmetric and symmetric stretching of the C—H bonds. The stretching of the carbonyl bond C=O from the EVA ester group can be seen at 1738 cm^{-1}, with a secondary band at 1238 cm^{-1}. The C—O stretching appears at 1020 cm^{-1}, also with a secondary band at 608 cm^{-1} that overlaps to the broad band of the Ti—O stretching at 559 cm^{-1}. Bending modes from the methyl and methylene groups can also be identified in the spectra at 1464 cm^{-1} and 1369 cm^{-1}. Other characteristic vibrations in the fingerprint region appear at 955 cm^{-1}, 720 cm^{-1}, and 730 cm^{-1}. There are no signifi-

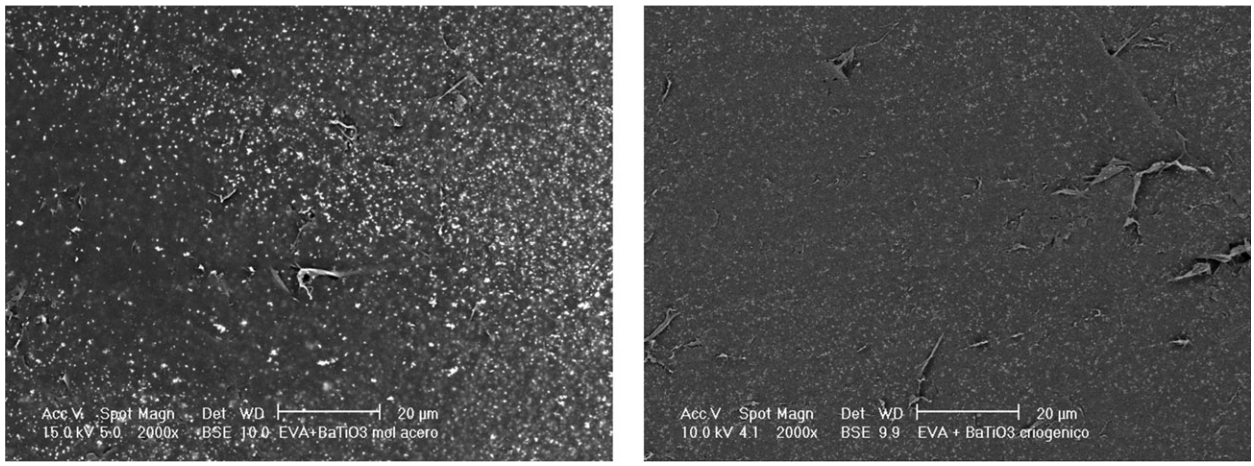

FIG. 8. SEM images obtained from the BSE signals of EVA + $BaTiO_3$ films milled at room temperature (left) and cryogenically (right).

 DOI 10.1002/pc

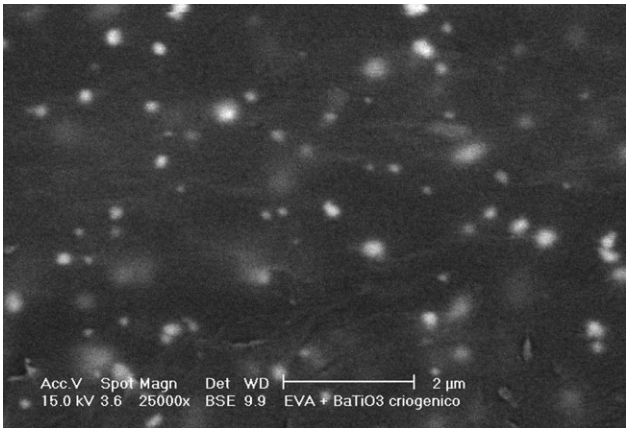

FIG. 9. SEM image obtained from the BSE signal of EVA + $BaTiO_3$ cryomilled films.

cant differences between the spectra of the milled or neat products, in contrast with the degradation effect stated by Smith et al. when milling other polymers such as poly (methyl methacrylate), polyisoprene, and poly(ethylene-alt-propylene) [24]. We must conclude then that the milling process does not affect the polymer EVA structure.

The FTIR-ATR spectra of films made from cryomilled EVA and EVA blended with $BaTiO_3$ are shown in Fig. 10b. The band associated to the carbonyl and to the ester group (1738 cm^{-1} and 1238 cm^{-1}, respectively) are the most probable candidates to interact specifically with the surface of $BaTiO_3$. However, no significant changes in the IR bands of EVA can be detected, which evidences a lack of strong interactions with the $BaTiO_3$ surface.

Finally the thermal behavior of the nanocomposites has also been studied. Figure 11 shows the thermogravimetric and differential thermogravimetric curves for all the samples prepared: EVA before the milling (EVA), EVA cryomilled (EVA Cryo), EVA milled at room temperature (EVA RT), EVA and $BaTiO_3$ blended by cryomilling (EVA+$BaTiO_3$ Cryo), and EVA and $BaTiO_3$ blended by milling at room temperature (EVA+$BaTiO_3$ RT). The degradation process for the EVA takes place in two stages. In the first one, deacylation with the loss of acetic acid and the formation of double bonds occurs between 300 and 400°C, with a maximum rate of degradation at around 370°C. Radical and anionic beta-elimination mechanisms have been proposed for this reaction [25–27].

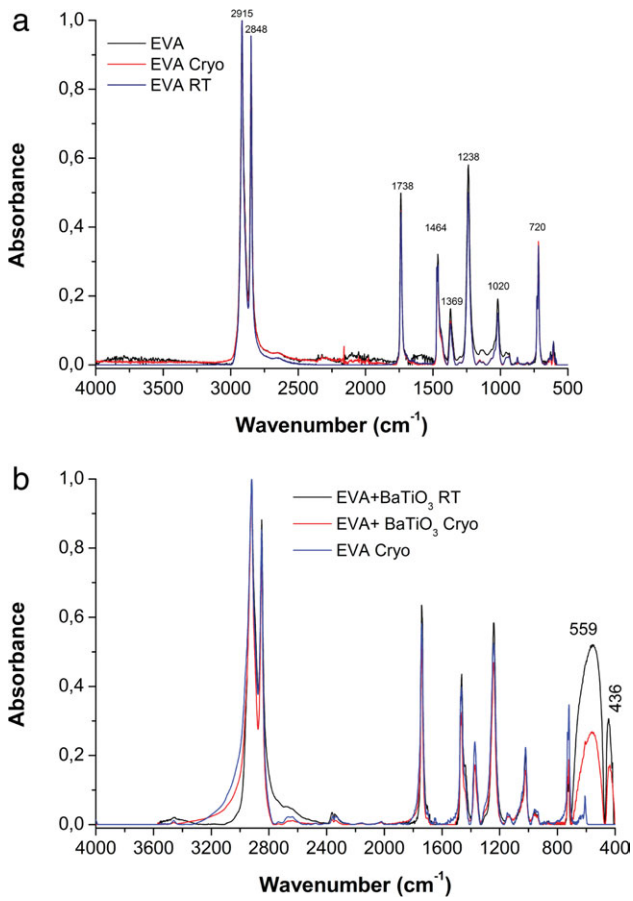

FIG. 10. (a) FTIR spectra of EVA: (i) as received (EVA); (ii) cryomilled (EVA Cryo); (iii) milled at room temperature (EVA RT). (b) FTIR-ATR spectra of cryomilled EVA and EVA blended with $BaTiO_3$ (under cryomilling conditions and at room temperature respectively). [Color figure can be viewed in the online issue, which is available at wileyonlinelibrary.com.]

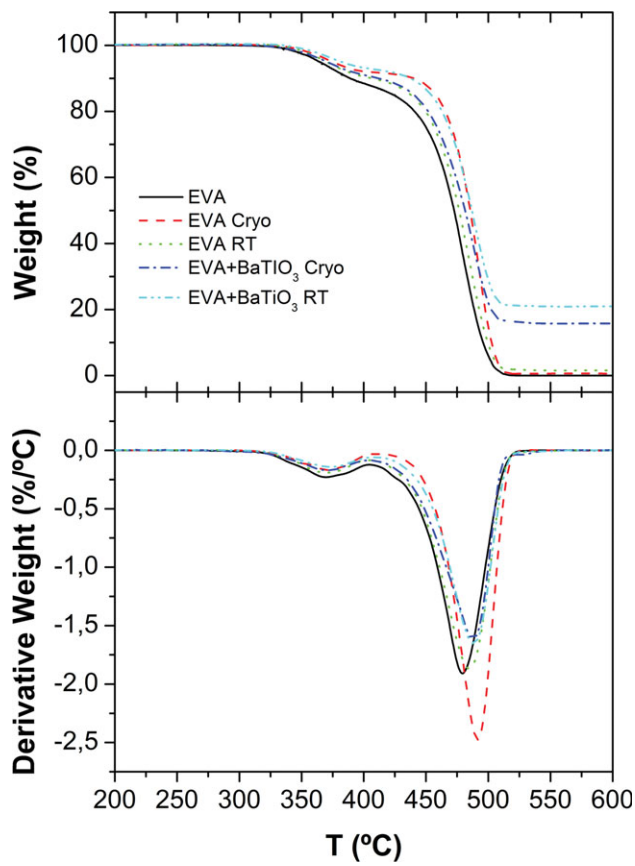

FIG. 11. Thermogravimetric and differential curves for powdered samples: EVA before milling (EVA), EVA cryomilled (EVA Cryo), EVA milled at room temperature (EVA RT), EVA and $BaTiO_3$ blended by cryomilling (EVA + $BaTiO_3$ Cryo), and EVA and $BaTiO_3$ blended by milling at room temperature (EVA + $BaTiO_3$ RT). [Color figure can be viewed in the online issue, which is available at wileyonlinelibrary.com.]

In the second step, the olefinic degradation between 450 and 520°C has been proposed [28]. In all cases the thermal profile is similar, which suggests that the mechanism of thermal decomposition is not significantly altered either by the HEBM process or the introduction of $BaTiO_3$ modifies the thermal degradation in an inert atmosphere.

CONCLUSIONS

HEBM has been used to prepare nanocomposites based on the mixture of EVA and $BaTiO_3$ particles. The characterization of the samples as powders and films shows the lack of strong interactions between the matrix and the $BaTiO_3$, and that the cryogenic conditions are the most suitable to achieve a uniform dispersion of the nanofiller without altering the structural and morphological properties of the base materials. In this way both the processability of EVA and the tetragonal structure of $BaTiO_3$ are kept. Cryogenic milling also yields lower contamination levels of iron coming from the milling tools, lessening one of the main problems of the HEBM when used for the manufacturing of composites.

REFERENCES

1. R. Pantaleón and J. González-Benito, *Polym. Compos.*, **31**, 9 (2010).
2. M.J. Yang and Y. Dan, *Colloid Polym. Sci.*, **284**, 243 (2005).
3. B.J. Ash, R.W. Siegel, and L.S. Schadler, *Macromolecules*, **37**, 1358 (2004).
4. P. Kim, S.C. Jones, P.J. Hotchkiss, J.N. Haddock, B. Kippelen, S.R. Marder, J.W. Perry, *Adv. Mater.*, **19**, 1001 (2007).
5. D.N. Bikiaris, A. Vassiliou, E. Pavlidou, and G.P. Karayannidis, *Eur. Polym. J.*, **41**, 1965 (2005).
6. E. Reynaud, T. Jouen, C. Gauthier, G. Vigier, and J. Varlet, *Polymer*, **42**, 8759 (2001).
7. J.P. He, H.M. Li, X.Y. Wang, and Y. Gao, *Eur. Polym. J.*, **42** (2006).
8. C. Suryanarayana, *Prog. Mater. Sci.*, **46** (2001).
9. J.S. Benjamin, *Metall. Trans. A*, **1** (1970).
10. F. Padella, E. Incocciati, C.A. Nannetti, C. Colella, S. Casadio, and M. Magini, *Mater. Sci. Forum*, **269–272**, 105 (1998).
11. S.A. Rowlands, A.K. Hall, P.G. McCormick, R. Street, R.J. Hart, G.F. Ebell, P. Donecker, *Nature*, **367**, 223 (1994).
12. P.D. Castrillo, D. Olmos, D.R. Amador, and J. Gonzalez-Benito, *J. Colloid Interface Sci.*, **308**, 318 (2007).
13. J. Gonzalez-Benito and G. Gonzalez-Gaitano, *Macromolecules*, **41**, 4777 (2008).
14. W.J.D. Shaw, *Mater. Sci. Forum*, **269–272**, 19 (1998).
15. F. Padella, M. Magnini, and E.U. Incocciati, Patent N1963825 B1, Bulletin 57/2003/3956.
16. D. Olmos, C. Dominguez, P.D. Castrillo, and J. Gonzalez-Benito, *Polymer*, **50**, 1732 (2009).
17. D. Olmos, F. Martínez, G. González-Gaitano, and J. González-Benito, *Eur. Polym. J.*, **47**, 1495 (2011).
18. M. Lombardi, A. Guerriero, G. Kortaberria, I. Mondragón, M. Sangermano, and L. Montanaro, *Polym. Compos.*, **34**, 8 (2011).
19. D.S. Chaudhary, R. Prasad, R.K. Gupta, and S.N. Bhattacharya, *Thermochim. Acta*, **433**, 187 (2005).
20. R. Asiaie, W.D. Zhu, S.A. Akbar, and P.K. Dutta, *Chem. Mater.*, **8**, 226 (1996).
21. F. Baeten, B. Derks, W. Coppens, and E. van Kleef, *J. Eur. Ceram. Soc.*, **26**, 589 (2006).
22. K.E. Russell, B.K. Hunter, and R.D. Heyding, *Polymer*, **38**, 1409 (1997).
23. S.W Kim, M.H. Lee, T.Y. Noh, and C. Lee, *J. Mater. Sci.*, **31**, 3643 (1996).
24. A.P. Smith, J.S. Shay, R.J. Spontak, C.M. Balik, H. Ade, S.D. Smith, and C.C Koch, *Polymer*, **41**, 6271 (2000).
25. M. Zanetti, G. Camino, R. Thomann, and R. Mülhaupt, *Polymer*, **42**, 4501 (2001).
26. Mc Neill, *Comprehensive Polymer Science*, Vol. **6**., Oxford, Pergamon Press (1989).
27. G. Camino, R. Sgobbi, A. Zaopo, S. Colombier, and C. Scelza, *Fire Mater.*, **24**, 85 (2000).
28. A.J. Zattera, O. Bianchi, R.V.B. Oliveira, L.B. Canto, C.A. Ferreira, and M. Zeni, *Cell. Polym.*, **24**, 139 (2005).

 DOI 10.1002/pc

Dyes and Pigments 94 (2012) 427–436

Contents lists available at SciVerse ScienceDirect

Dyes and Pigments

journal homepage: www.elsevier.com/locate/dyepig

Rhodamine solid complexes as fluorescence probes to monitor the dispersion of cyclodextrins in polymeric nanocomposites

R. Serra-Gómez [a], G. Tardajos [b], J. González-Benito [c], G. González-Gaitano [a,*]

[a] Dpto de Química y Edafología, Universidad de Navarra, Facultad de Ciencias, 31080 Pamplona, Navarra, Spain
[b] Dpto. Química-Física I, Universidad Complutense de Madrid, Spain
[c] Dpto. C. Ing. Materiales Ing. Química, Universidad Carlos III de Madrid, Spain

ARTICLE INFO

Article history:
Received 23 November 2011
Received in revised form
8 February 2012
Accepted 10 February 2012
Available online 22 February 2012

Keywords:
Cyclodextrins
Rhodamine
Polymeric nanocomposite
High energy ball milling
Fluorescence probe
NMR

ABSTRACT

Rhodamines B and 6G have been used to evaluate the dispersion of β-Cyclodextrin in a thermoplastic matrix, poly(ethylene-co-vinyl acetate), by high energy ball milling. In a first stage, a study of the binding properties of β-Cyclodextrin with both fluorophores has been carried out, to determine which of them forms the most stable complex with the macrocycle, its topology and to check whether their fluorescence is kept after the milling process. Both systems have been fully characterized in the solid state (FTIR and XRD, TGA and fluorescence spectroscopy), and in solution (^{1}H NMR ROESY, steady state and time-resolved fluorescence spectroscopy). Then, nanocomposites based on the thermoplastic matrix and the cyclodextrin complexes have been cryomilled and processed in the form of thin films. Only Rhodamine B forms a complex stable enough to track the nanofiller dispersion within the polymer. This labeled cyclodextrin is uniformly dispersed throughout the matrix after the milling and film forming, yielding a blue-shifted and remarkably enhanced fluorescent response when compared to the same material prepared with the mixture of Rhodamine B and β-Cyclodextrin.

© 2012 Elsevier Ltd. All rights reserved.

1. Introduction

Polymer nanocomposites are generally built by homogeneous dispersion of a nanoscopic filler (nanofiller) into the polymeric matrix [1]. Because of the large surface to volume ratio of nanoparticles, the interphase formed between the nanoparticles and the polymer constitutes a greater fraction of the whole material than in common composites, even with small amounts of the nanofiller (less than 5% by weight), a feature which has important consequences on the final properties of the material [2]. Obtaining a perfectly homogeneous dispersion is critical for a nanocomposite to have the properties that are expected. However, regardless of the method used for the mixing, this issue becomes more critical the smaller the nanofiller is. Recently, high energy ball milling (HEBM), a conventional method used for synthesis and processing of inorganic materials [3–5], has been revealed as a new way of processing thermoplastic matrix nanocomposite materials, not only due to its potential results in terms of nanoparticle dispersion, but also from an economical and clean point of view. Although the mechanical action may have adverse effects of wearing on solid polymers by mechanisms of chain scission and sample oxidation, HEBM has been successfully used to obtain polymer blends with improved mechanical properties and polymer nanocomposites with a real dispersion of nanoparticles [6–10].

Cyclodextrins (CDs) are cyclic oligosaccharides composed of 6, 7 or 8 D-glucopyranose rings termed α, β and γCD respectively. Their sizes (ca. 1 nm) fall within the lower limit of the nanometric scale so they can be considered as a limiting type of nanofiller. CDs are shaped like truncated cones, with a hydrophobic cavity and a hydrophilic exterior. The precise number of hydroxyl groups according to the number of glucose units makes it possible to establish strong interactions with certain polymeric matrices. CDs can also be easily modified with other functional groups which allow modulating such interactions according to the nature of the matrix, or can be grafted to common nanofillers (nanoparticles, layers,…) for improving the properties of the material. The ability to form inclusion complexes with organic molecules inside the cavity, e.g. a monomer for its further polymerization [11] also represents an added value to produce a material with features different from those of the single constituents of the nanocomposite. Yet, in spite of their exclusive properties the use of CDs in the field of nanocomposites is still very limited [12–14].

* Corresponding author. Tel.: +34 948 425 600x6315.
E-mail address: gaitano@unav.es (G. González-Gaitano).

0143-7208/$ – see front matter © 2012 Elsevier Ltd. All rights reserved.
doi:10.1016/j.dyepig.2012.02.009

A problem that arises when dispersing CDs in a polymer comes from the reduced size of these macrocycles, which makes it difficult to confirm that an adequate dispersion has taken place. AFM, SEM or TEM microscopy can be used to this purpose, but these are techniques which involve sample preparation processes that require a consistent amount of time and effort, more focused to a final product characterization and not convenient for regular checks. In addition to that, the electron beam can melt the matrix when thermoplastic polymers are being used.

A different approach may be to use fluorescence microscopy by previously tagging the CD by inclusion of a fluorophore in the cavity, provided it is stable enough. Rhodamine-based dyes present unique fluorescent properties and are therefore used in a wide variety of applications, ranging from applied chemistry and physics to biochemistry or microbiology [8]. Rhodamines are known to interact with βCD in different ways, depending on the state of aggregation of the fluorophore and its molecular form [15,16], increasing or decreasing the fluorescence quantum yield as a result of their interaction. In the solid state, however, the number of investigations is limited, most of them related to the development of solid state dye lasers [17,18] or to the use of CD-based resins to adsorb organic dyes [19].

In this work we propose the use of the fluorescent properties of Rhodamine B and Rhodamine 6G (hereafter RhB and Rh6G, Fig. 1a and b) and their ability to form complexes with βCD (Fig. 1c), to produce a solid complex that acts as a fluorescent probe to evaluate the dispersion of these oligosaccharides into a thin-film polymeric nanocomposite material prepared by HEBM. The polymeric matrix used here is ethylene vinyl acetate (EVA), a thermoplastic polymer with polar vinyl acetate groups and crystalline ethylene domains. EVA copolymers are a good choice to combine with these fluorophores, as they present optical homogeneity and organic dyes usually show good compatibility with polymeric matrices. In addition, their easy processability makes them excellent for miniaturization and to be included in other composite systems [20].

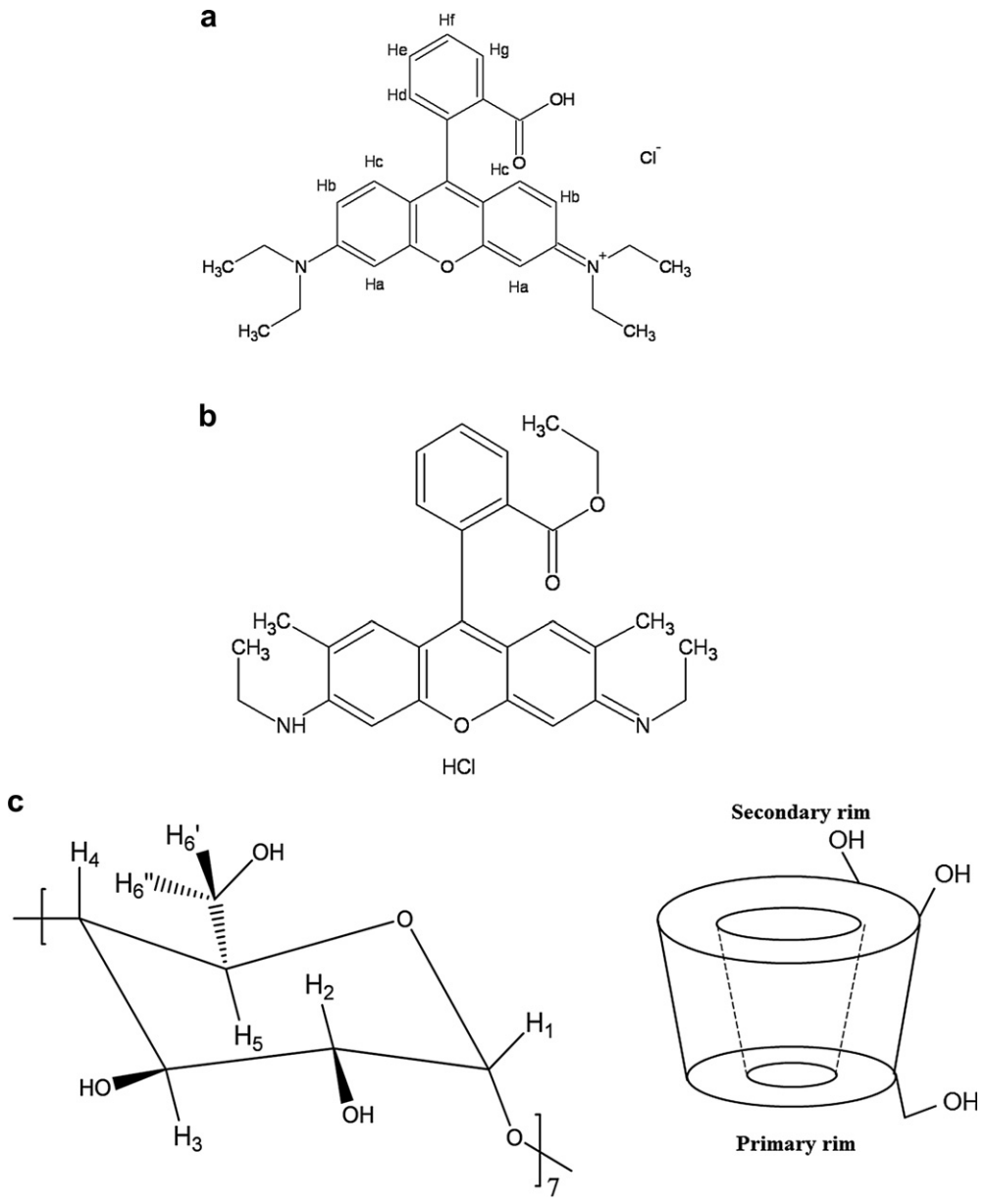

Fig. 1. (a) Rhodamine B; (b) Rhodamine 6G; (c) Scheme of β-Cyclodextrin.

In this research we have focused on the dispersion of the macrocycle as the nanofiller in the polymer, leaving the grafting of the βCD to nanoparticles and further nanocomposite synthesis for future projects. The first step is to evaluate that the complexes between the fluorophore and the CD form and are stable enough to endure the HEBM process, that they present a different fluorescent response when attached to the βCD than in free form and that they can be dispersed homogenously, so they can be used as dispersion fluorescence probes in nanomaterials. For this purpose the systems have been previously studied in solution to characterize their complex formation characteristics (stability, temperature dependence, stoichiometry and topology) and the fluorescent emission. Finally, the solid state products are tested and combined with the polymer using the HEBM method, to verify their adequate dispersion and whether their properties are retained along the nanocomposite processing.

2. Materials and methods

2.1. Materials

Rhodamine B 99% pure (Basic Violet 10; C.I. 45170; 9-(2-Carboxyphenyl)-3,6-bis(diethylamino)xanthylium chloride) and Rhodamine 6G 99% pure (Basic Red 1, C.I. 45160, ethyl 2-(6-(ethylamino)-3-(ethylimino)-2,7-dimethyl-3H-xanthen-9-yl)benzoate monohydrochloride) were purchased from Acros Organics. β-Cyclodextrin was bought from Wacker Chemicals (Cavamax Pharma, 99.5% pure). Polyethylene-co-vinyl acetate (composition 12% by weight in vinyl acetate, density 0.933 g/cm^3 at 25 °C, Vicat temperature ASTM D 1525 = 65 °C and melting point 95 °C), was supplied by Sigma Aldrich.

2.2. Sample preparation

RhB:βCD complex was prepared by mixing a RhB 2.5×10^{-3} M aqueous solution with βCD at an equimolar ratio followed by stirring for 10 min, poured into a crystallizer and placed in the stove at 70 °C until solvent evaporation. The resulting solid is a dark red flaked product. The physical mixture of RhB and βCD was prepared by weighing the same amounts used for the complex preparation and mixing them in a vortex shaker, resulting in a greenish powder mixture. The same procedure was carried out with Rh6G. In this case the solid mixture and the compound prepared by crystallization did not show any visual differences.

A mixture of 5% by weight of RhB:βCD and EVA was subjected to HEBM under cryogenic conditions (cryomilling) in a MM400 RETSCH miller. Stainless steel milling tools (a vessel of 50 mL of capacity and one ball of 20 mm diameter) were used. The process was carried according to the following protocol: 1 h of active cryomilling divided into 12 cycles of 5 min of milling at 25 Hz and 15 min of resting in liquid nitrogen. Another vessel endured the same procedure with the physical mixture of RhB and βCD and the EVA at the same proportions (95% by weight of EVA).

Thin films were prepared by hot pressing. The powder obtained from the milling processes was deposited between two Teflon plates and then pressed and heated in an oven at 150 °C for 20 min. After that, the prefilms obtained were cooled inside the oven down to 40 °C. A small portion of the prefilm (about 9 mm^2) was then sandwiched between the two Teflon plates and clamped within two stainless steel plates, introduced in a preheated oven at 150 °C and heated for 120 min. The film was slowly cooled down inside the oven to room temperature, thus avoiding any thermal stress in the sample.

2.3. Characterization techniques

The crystalline structure of materials under study was characterized by X-ray diffraction, XRD, on randomly oriented powder preparations using a Bruker D8 Advance diffractometer with a X Kristalloflex K760 X-Rays generator, with a copper anode emitting typical X radiation $K_{\alpha 1} = 1.5417$ Å at 40 kV and 30 mA. Diffraction angles were monitored from $2\theta = 2°–40°$ at a rate of 3 s/step (0.02° in 2θ). Analysis of the XRD patterns was carried out with XRD Wizard 2.4.11 software (Bruker GmbH). FTIR-ATR analyses of powder and films were performed with a FTIR-ATR Nicolette Avatar 360, using a resolution of 2 cm^{-1} and averaging 32 scans. Spectral analysis treatment was undertaken with the OMNIC E.S.P. v5.1 software (Nicolet). Thermogravimetric analysis, TGA, was carried out in a TGA-SDTA 851 Mettler Toledo. Samples were subjected to a heating program from 25 °C to 600 °C at a heating rate of 10 °C/min under a N_2 atmosphere.

Fluorescence studies were undertaken using an Edinburgh Instruments FLS920 spectrofluorimeter equipped with a 450 W Xenon arc lamp. Samples were excited at 553 nm and the emission recorded from 560 to 750 nm under constant stirring, averaging 5 scans with a 1 nm step and 0.1 s dwell time. Excitation and emission slits were 2 nm and 3 nm, respectively. Measurements in solution were carried out at 15 °C, 25 °C, 35 °C and 45 °C in a 10 mm path length quartz cuvettes controlled by a Lauda Ecoline RE104 thermostat. Each isotherm was repeated three times. For the solid samples the powder or a portion of the film was sandwiched between two quartz glasses in the instrument sample holder. Fluorescence lifetimes were measured with the same equipment using as the radiation source a PDL800-B Picoquant pulse diode driver and 455 nm and 500 nm diodes, with full width at half maximum (FWHM) of 1600 and 1700 ps, respectively. The instrument response was measured by using a Ludox 30% aqueous suspension, purchased from Aldrich. Data treatment was performed with FAST v3.0 software (Edinburgh Instruments). The films were observed with an Olympus CH40 fluorescence microscope equipped with a ColorView camera (Soft Imaging Systems).

NMR experiments were performed in a Bruker Avance 700 Ultrashield (700 MHz). The samples were prepared in D_2O (99.990% in deuterium purchased from Sigma Aldrich), with no buffers added, using the HDO signal as the reference. Monodimensional experiments were done by averaging 256 scans. ROESY experiments were carried out on 32 scans with presaturation of the solvent signal [21] by using the pulse sequence described in the literature [22], with an optimal mixing time of 600 ms. Temperature was set to 25 °C in all cases.

3. Results and discussion

3.1. Complexes in solution: stoichiometry, stability and structure

As a first stage, the complexes between rhodamines and βCD have been investigated. The analysis of the chemical shifts of the ^{1}H NMR signals of the complex in relation to the signals from the pure RhB and βCD (Table 1 and Figs. 2 and 3) are the main indication of the extent of the complex formation. For the βCD, the protons undergoing the most important changes are the H_6 and H_5, i.e., those located at the mid-bottom inner side of the cavity and at the narrower rim of the macrocycle, respectively. Less significant changes were noted for the inner H_3, at the mid-upper part of the CD. Finally, tiny shifts are detected in the outer protons H_1, H_2 and H_4. All these resonances except that for H_4 shift upfield. If we consider now the guest molecule, RhB, the protons of the substituents CH_3– and CH_2– (downfield) and the H_D (upfield) experience

Table 1
Changes in the chemical shifts of protons of βCD and RhB.

H	Free δ (ppm)	$\Delta\delta$ (ppm)
β-Cyclodextrin		
H_1	4.949	0.039
H_2	3.541	0.006
H_3	3.856	0.074
H_4	3.478	−0.015
H_5	3.748	0.155
H_6	3.769	0.101
Rhodamine B		
H_{CH3}	1.115	−0.059
H_{CH2}	3.455	−0.079
H_A	6.624	−0.028
H_{B1}	6.772	−0.019
H_{B2}	6.786	−0.018
H_C	7.100	−0.013
H_D	7.313	0.068
H_E	7.608	−0.013
H_F	7.608	−0.013
H_G	7.834	−0.008

the larger shifts. These results prove unambiguously the inclusion of the RhB in the CD, which involves the ethyl amino groups [23].

^{1}H ROESY experiments can provide more detailed information about the inclusion mode through the intensity of the cross peaks in the 2D spectrum, related to the closeness between protons of host and guest. Fig. 4 shows expanded views of the correlation between the methyl group and aromatic protons Ha and Hb of RhB with the CD.

Strong ROE cross peaks arise between the H_3 and H_5 of the CD (3.76 ppm and 3.55 ppm) with the CH_3 group of the RhB, that of H_5 being the most intense. In addition, a small peak arises between H_6 and CH_3 protons. These interactions imply unambiguously that RhB is entering the cavity by the secondary hydroxyl rim. At 6.62 ppm and 6.78 ppm two more interactions arise, corresponding to the Ha and Hb from the RhB xanthene rings with the H_5 of the βCD. The intramolecular interaction of Ha and Hb with the CH_2– can be ruled out, as no cross peaks arise in the ROESY spectrum for the RhB alone in water, confirming the intermolecular interaction with H_5.

The fact that the interaction is taking place not in the central carboxyphenyl ring, but in one of the diaminoethyl groups opens the possibility of 2:1 complex, i.e. two CDs per guest. Job's continuous variation analysis [24] has been used to determine the actual stoichiometry. For this purpose samples at different molar ratios prepared with βCD and RhB concentrations ranging from 0 to 5×10^{-4} M were prepared in D_2O and analyzed by ^{1}H NMR spectroscopy.

The Job plot for protons H_3, H_2 of βCD and CH_3, H_G and H_D of RhB is shown in Fig. 5, so a signal from inside the βCD cavity and one from outside can be seen. The maximum change in the chemical shift takes place when the molar ratio is 0.5, inferring that the stoichiometry of the complex is 1:1.

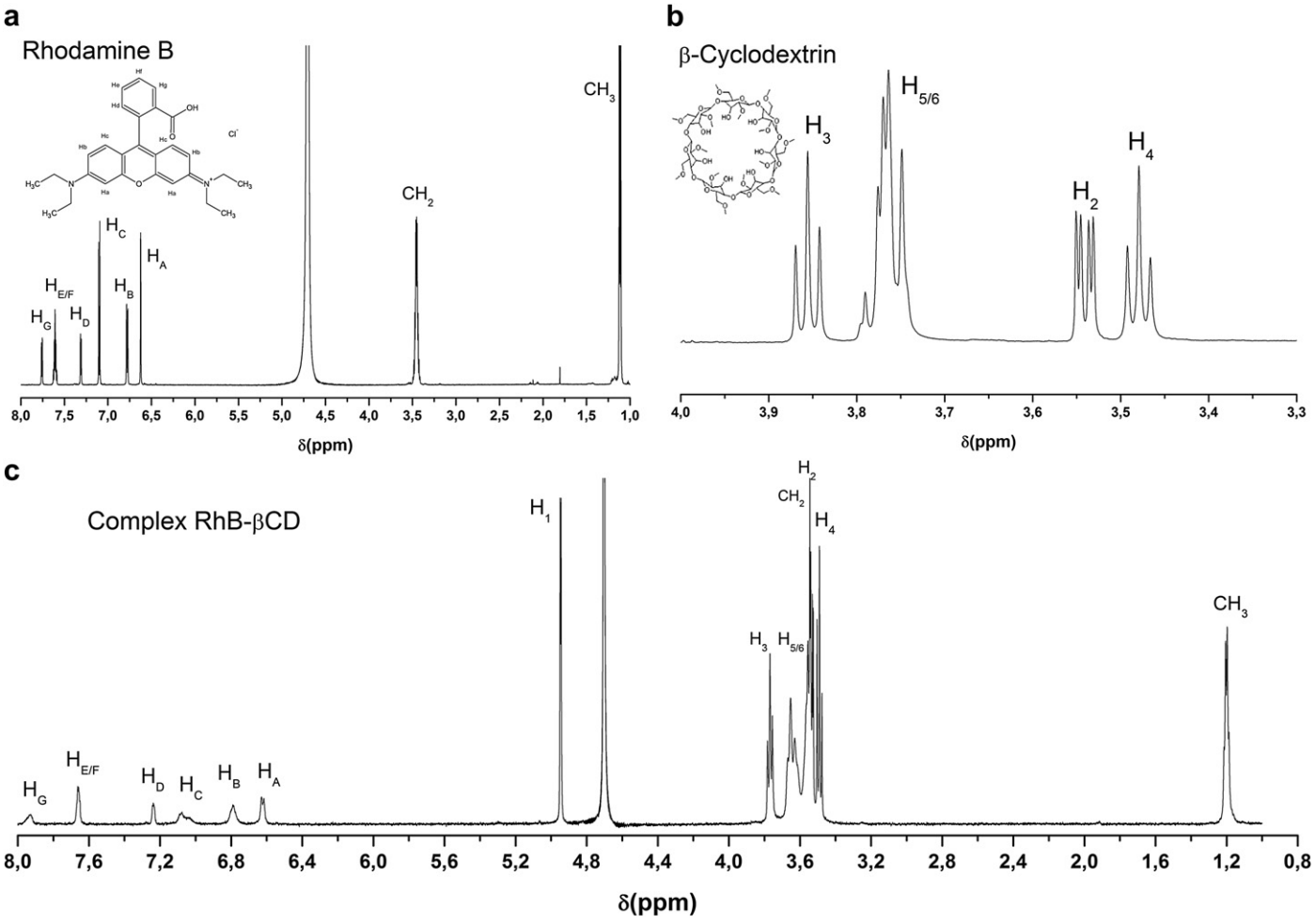

Fig. 2. ^{1}H NMR spectra in D_2O of: (a) RhB; (b) βCD; (c) molar ratio 1:1.

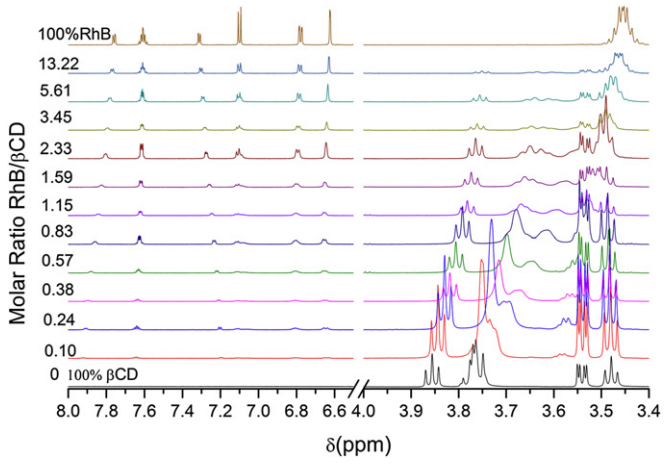

Fig. 3. ^{1}H NMR spectra of different molar ratios RhB:βCD. Concentrations of βCD and RhB range from 0 to 5 × 10^{-4} M.

As seen in Table 2, the protons of the carboxyphenyl ring also shift, although no NOE signals are detected. A possible explanation to the fact the stoichiometry sticks to 1:1 when having two diaminoethyl groups in the molecule, is that when the βCD approaches one of the diaminoethyl branches, it might induce the movement of the carboxyphenyl ring to the opposite side, as seen by the shift in

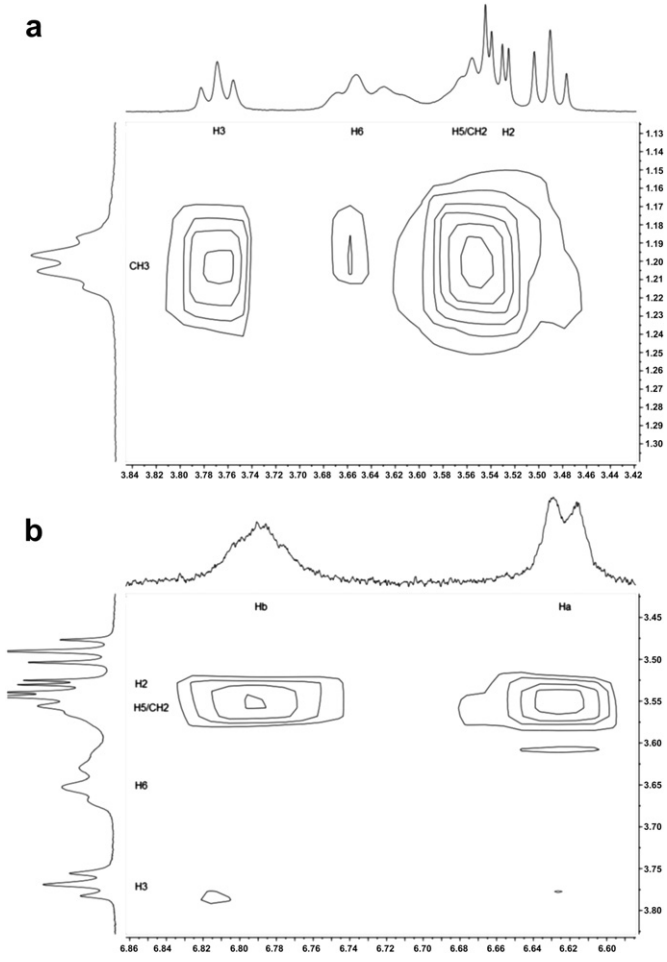

Fig. 4. (a and b). Zoomed view of the ROESY spectrum of RhB:βCD (1:1).

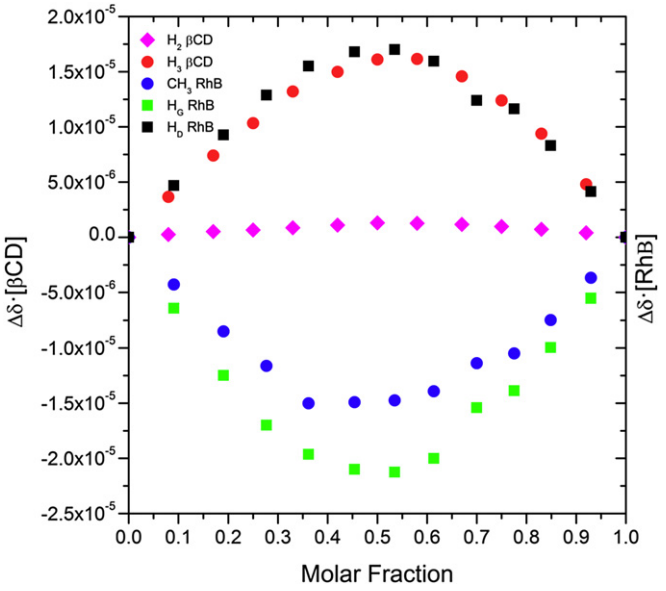

Fig. 5. Job plot for selected protons of βCD and RhB.

H_D, and thus the molecule is not receptive to dock with another βCD molecule in the other ring because of steric effects. Those same experiments were performed on the Rh6G–βCD system, but neither significant changes in the chemical shifts nor cross peaks in the ROESY spectrum were detected. These results confirm that only RhB forms a suitable stable inclusion complex with a 1:1 stoichiometry, where the βCD enters the RhB by one of its diethylamine sides.

Fluorescence emission can be used to gather precise information about the stability of the association. RhB presents a high fluorescence quantum yield, but it easily aggregates forming dimers and other species, especially in aqueous solution [25]. This process manifests as a quenching in the emission attributed to the long range dipole–dipole energy transfer from the monomer excited state to the aggregates [16] and also in bathochromic shifts from 587 nm to 650 nm in 10^{-3} M RhB solutions. Rhodamines and βCD may interact in different ways depending on the fluorophore concentration and its aggregation state. Thus, in dilute solutions of RhB, the βCD causes a decrease in emission due to the formation of the complex, less fluorescent than the free RhB. However, in conditions at which RhB is in the form of aggregates and its fluorescence quenched, the addition of βCD produces the opposite effect, yielding a fluorescent enhancement [26]. On the other hand, Rh6G does not aggregate as easily as the RhB [27] because of the bulkiness of the ester group in the phenyl ring and the methyl and ethyl substituents, which hinder the molecule stacking. Consequently, the presence of βCD enhances the emission in the case of Rh6G in aqueous solution.

The effect of successive additions of βCD to RhB 8 × 10^{-6} M is shown in Fig. 6. Free RhB has its maximum fluorescent emission at 582 nm, and experiences a slight blue shift of ca. 4 nm when βCD is added, along with a quenching in its fluorescence. Under our instrumental conditions, the linear response of the

Table 2
Binding constants for the complex βCD:RhB ([RhB] = 8 × 10^{-6} M).

	15 °C	25 °C	35 °C	45 °C	Δ*H* (kJ mol^{-1})	Δ*S* (J mol^{-1} K^{-1})
K·10^{-3} L mol^{-1}	5.1 ± 0.5	4.8 ± 0.2	4.1 ± 0.2	3.1 ± 0.2	−15 ± 3	21 ± 10

fluorescence for the RhB ranges up to 8×10^{-6} M, free of aggregation effects.

As the complex stoichiometry for the βCD is 1:1, its formation constant at a certain temperature can be expressed by the action mass law as:

$$K = \frac{[R:CD]}{[R][CD]} \tag{1}$$

being *R* the free fluorophore, *CD* the free βCD and *R:CD* the complex. In the experiments, the concentration of *R* is kept constant, varying that of *CD*. By combining the action mass law with the concentration mass balance for host and guest we get for [*R*] the following quadratic equation:

$$[R]^2 + \left(CD_0 - R_0 + \frac{1}{K}\right)[R] - \frac{R_0}{K} = 0 \tag{2}$$

The measured fluorescence at a certain wavelength, F_λ, is the result of the contributions of the two fluorescent species, *R* and *R:CD*, so thus

$$F_\lambda = F_\lambda^R + F_\lambda^{R:CD} = a_\lambda[R] + b_\lambda[R:CD] \tag{3}$$

where a_λ and b_λ are constants related to the fluorescence quantum yield and molar absorptivity of each fluorescent species at the excitation wavelength, λ, and to experimental conditions (source intensity, slit width and path length of the cell).

Dividing the above expression by $F_0 = a_\lambda R_0$, i.e., the fluorescence in the absence of cyclodextrin, eq. (3) can be written as

$$\left(\frac{F}{F_0}\right)_\lambda = [R] + \phi\frac{[R:CD]}{R_0} \tag{4}$$

where $\phi = b_\lambda/a_\lambda$. The experimental data at a certain emission wavelength can thus be fitted by a non-linear least-squares procedure to the above equation, in which ϕ and *K* are left as adjustable parameters. It is possible to improve the fitting using a wider set of data by taking into account the emission measured at each wavelength, and not only to a λ_{max}. A multivariable analysis can be performed by imposing the condition that the binding constants are the same for each wavelength. The error function to be minimized becomes

$$E = \sum_\lambda \sum_i \left(\left(F_i/F_{0,\lambda}\right)^{cal} - \left(F_i/F_{0,\lambda}\right)^{meas}\right)^2 \tag{5}$$

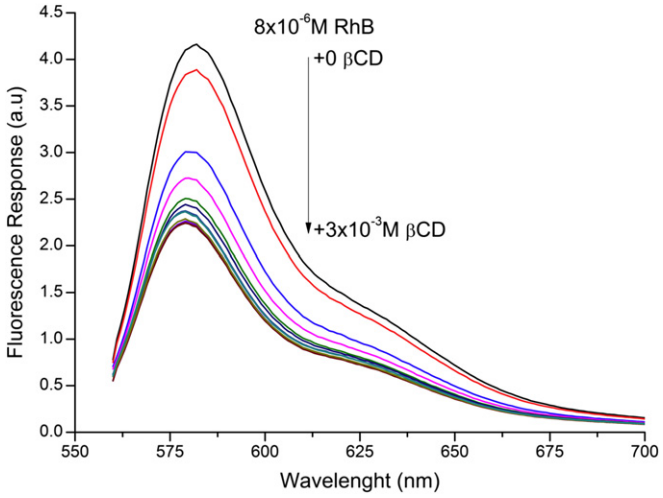

Fig. 6. Effect of the addition of βCD on the fluorescence of RhB 8×10^{-6} M in water.

where *i* sums over all the concentrations of CD and λ over all the wavelength range. The input parameter is a vector that contains the initial guess for the binding constants and ϕ_i, and the output is the estimation of the parameters with their error bounds, defined as the confidence intervals corresponding to a significance level, $\alpha = 0.16$. A weight factor, ω_λ, taken as the absolute value of the difference between $F_{0,\lambda}$, and the maximum value reached in the binding, is introduced at each wavelength in Eq (5), to give a higher statistical weight to that λ at which the changes in intensity are higher [28]. The enthalpy and the entropy have been obtained from the *K* dependence on the temperature through Van't Hoff equation and a weighted least-square method (Table 2).

The binding constants of RhB in water are relatively high, which indicates a stable association. The increasing temperature produces the diminution of *K*, as expected in an exothermic process. This same trend has been obtained by measuring at lower concentrations of RhB (data not shown). This stability with the temperature is important, considering that the formation of the nanocomposites requires conditions that, depending on the type of polymer, must be higher than 120 °C. As for the Rh6G:βCD system, it barely experiences changes in the emission by adding CD, resulting in the non-convergence of the fitting toward very low constants. This is a confirmation that there is no significant complex formation, in accordance with NMR data. It is worthy to mention that the enthalpy is not too high for these types of complexes, being the process controlled mainly by the entropy. According to ROESY data and considering the bulkiness of RhB and the size of the cavity, the

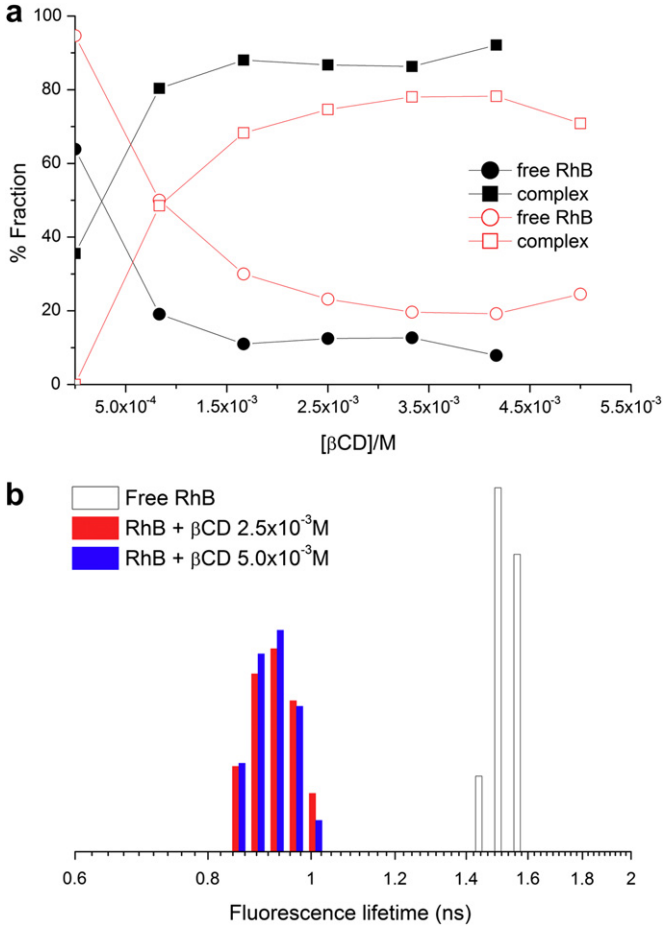

Fig. 7. Lifetime analysis: (a) fraction of the species found on 1×10^{-4} M (solid symbols) and 1×10^{-5} M (open symbols) of RhB upon addition of βCD; (b) Lifetime distributions.

inclusion is shallow and only part of the guest is included. Although the association constant is in good agreement with the one stated by Liu et al. [15], the enthalpy and entropy values are considerably different, as they obtain a non-expected positive $\Delta H = 40.8$ kJ mol^{-1} and $\Delta S = 0.21$ kJ mol^{-1} K^{-1} at 25 °C. These unusual values are reasoned in terms of the extra desolvation due to the lactonization of the hydrated benzoate moiety at the conditions of the experiment. It must be noticed that the constants obtained by this method are apparent constants, as the equilibrium between the cationic, lactone and zwitterionic form exists. However, as stated by Mchedlov-Petrossyan et al. [29] the fraction of the RhB molecules converting to the colorless lactone form in water at our concentration is less than 1%, so in our case we can rule out the lactonization effect mentioned before as being responsible for the different values. The use of a phosphate buffer 0.1 M to maintain the pH at 7.20 may be one of the reasons for this difference, as the ionic strength of the solution with this precise buffer is considerable and it is well known the quenching effect of some buffers on the fluorescence [30]. In our case, the pH has not been controlled by addition of buffers and the low concentration of RhB makes the ionic strength virtually zero.

In order to check the state of aggregation of the RhB at different concentrations and the effect the CD may have, fluorescence lifetime analyses were carried out upon these samples. In the experiments, RhB concentration was fixed at 1×10^{-4}, 1×10^{-5} and 1×10^{-6} M, and aliquots of a 5×10^{-3} M βCD stock solution were added to gradually increase the βCD concentration and induce the complex formation. The decay curves were processed by reconvolution distribution analysis at 200 intervals between 0 and 50 ns. Free RhB has a lifetime response of 1.7 ± 0.2 ns (Fig. 7), which correlates with the values found in the reference, 1.52 ns with emission at 400 nm and 1.68 ns at 560 nm [31]. Upon addition of βCD, a new mode appears with fluorescence lifetime of 0.75 ± 0.04 ns, which is retained upon successive additions (Fig. 7), its fraction increasing with the βCD concentration, accordingly to the shift of the equilibrium. When RhB 1×10^{-4} M is tested at 500 nm in the absence of βCD, a considerable fraction appears at approximately the same lifetime than the complex 0.97 ± 0.03 ns, which is attributable to the RhB aggregation effect at high concentrations. When RhB is at lower concentrations, from 1×10^{-5} to 1×10^{-7} M, and βCD is absent, this fraction does not appear and that corresponding to the free RhB is close to 100%. These results indicate the aggregation limit is between 10^{-4} M and 10^{-5} M for aqueous solutions, in good agreement with the literature values [32].

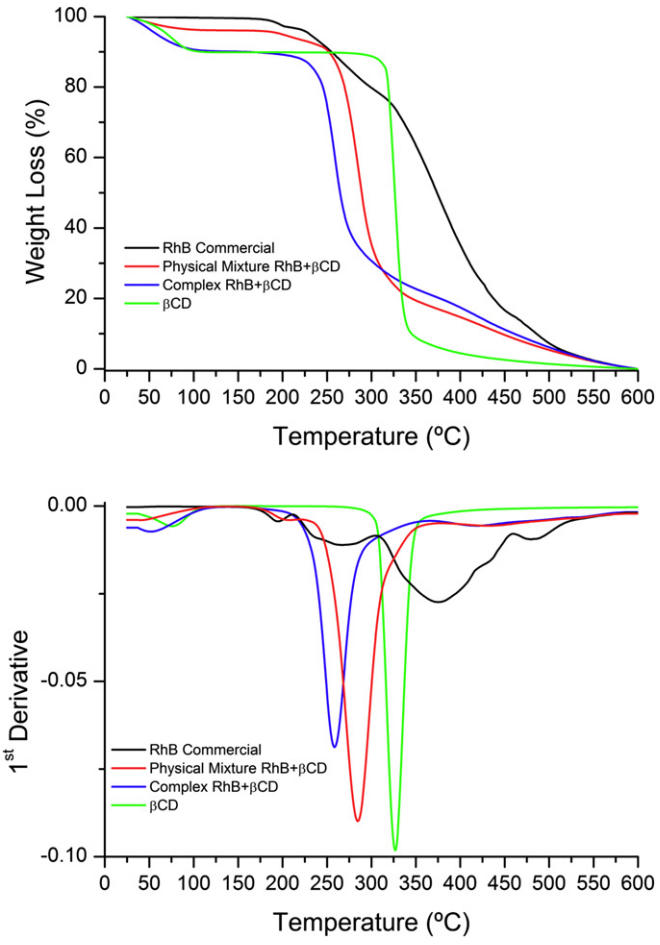

Fig. 8. TGA curves (top) and 1st derivative (bottom) of the RhB samples.

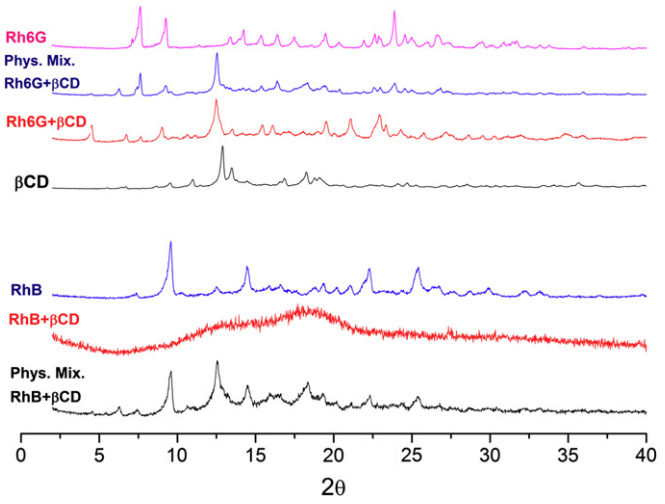

Fig. 9. X-ray diffractograms of the solid samples.

3.2. Solid complexes

The thermogravimetric analysis of the powder samples (Fig. 8) shows how the RhB presents at least a three-step decomposition

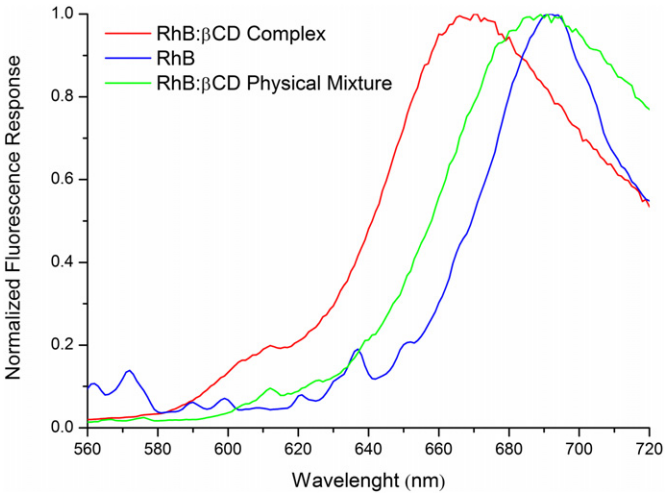

Fig. 10. Fluorescence response of the solid samples.

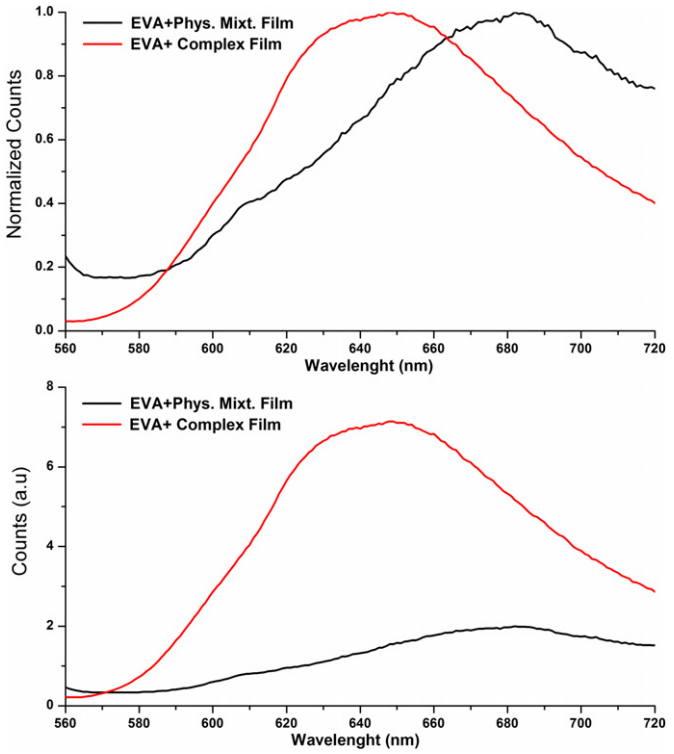

Fig. 11. Comparison of the fluorescence of films produced with RhB:βCD complex and the physical mixture. Top: normalized spectra; bottom: as measured.

process, starting around 180 °C and ending at 500 °C, and so does the physical mixture RhB-βCD. However, as confirmed by the first derivative trace, once the RhB:βCD complex is formed the decomposition process changes to a single step process, confirming that the inclusion yields a product with a different thermal behavior. This difference can be seen by the absence of the first minimum around 180 °C and the shift of the degradation temperature to 257 °C. When the same analysis is carried out with the Rh6G, only a slight shift in the temperature can be seen, but there is no evidence concerning the formation of a different product.

Confirming the results revealed above, FTIR-ATR analysis of the compounds shows that the RhB-βCD system presents important differences in the spectra compared to the physical mixture, whereas the Rh6B-βCD spectrum cannot be distinguished from the mixture. The strong band at 1587 cm^{-1} of RhB is assigned to the aromatic ring C–C vibrations and remains when forming the complex (data not shown). The rest of the RhB peaks in the aromatic region persist in the complex, while in the physical mixture they lose shape and are hidden in the baseline. Taking into account that the solid complex is formed from the aqueous solution, and with the previous data confirming that the Rh6G does not form complex with the βCD, we must conclude that the precipitate will be a bare physical mixture of both components.

X-Ray diffraction patterns (Fig. 9) corroborate the above results. The analysis shows a decrease in the crystallinity, as seen by the absence of peaks and the amorphous halo when the complex is formed in comparison to the commercial RhB and the physical mixture. The latter itself matches the sum of the RhB and the βCD diffractograms. As expected, Rh6G shows no evidence of complex formation.

Finally, solid state fluorescence measurements were also recorded on the commercial RhB, the physical mixture RhB-βCD and the RhB:βCD complex. The emission spectra show a 20 nm blue-shift upon complex formation. Commercial RhB has an emission peak at 690 nm, and the complex at 670 nm. The physical mixture behaves exactly like the commercial RhB (Fig. 10).

3.3. *Effect of milling*

The last step of the nanocomposite preparation is the milling of the fluorescent probe in its complex form with the polymeric matrix ensuring that the inclusion is kept after the HEBM and that the probe is homogeneously distributed throughout the matrix. It is known that the severe mechanical conditions occurring in these processes may break bonds or produce free radicals [9]. For this reason, the βCD has been milled alone under the same conditions as those of the films. According to ^1H NMR data, no changes are perceived in the spectrum after milling, which indicates that the process does not alter the chemical structure of the macrocycle. Regarding the nanocomposites, after the products were milled and processed into thin films, the fluorescence response of the film containing the RhB:βCD complex presented a four-fold fluorescence enhancement (Fig. 11, bottom) compared to the physical mixture and a blue shift of 40 nm (Fig. 11, top), which is in good agreement with the results of the solid samples before milling. It is worthy to mention that the trend is the same than in concentrated solution of RhB, where the fluorophore is extensively aggregated and the addition of βCD produces an enhancement on the fluorescent response, as explained above. All this confirms that the RhB:βCD complex can be used as a probe to monitor the dispersion of the oligosaccharide alone or attached to other nanostructure, as nanoparticles, as RhB behaves differently when bound to the βCD than when it is free in the matrix and that the complex is capable of enduring the extreme conditions of the HEBM process without losing its properties.

The films are shown in Fig. 12. The one containing the complex presents a uniform and homogeneous appearance in contrast to the

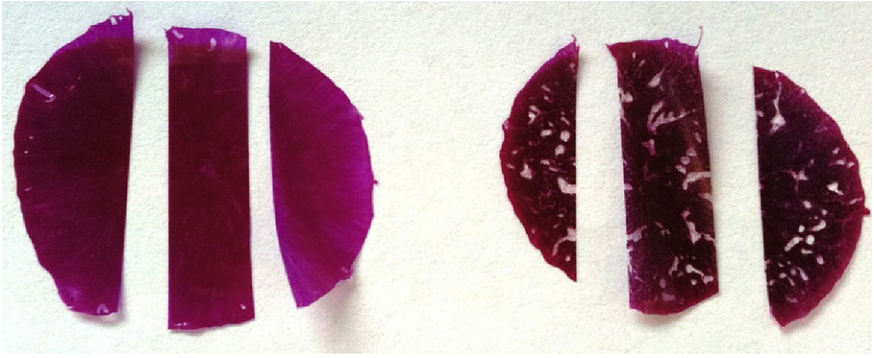

Fig. 12. Film formed with the complex (left) and with the physical mixture (right).

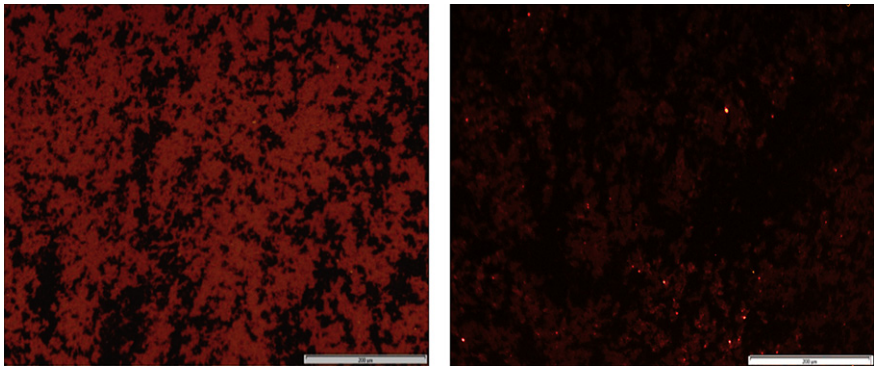

Fig. 13. 20× Fluorescent microscope image of the RhB:βCD complex film (left) and physical mixture (Right). Scale bar 200 μm. $\lambda_{ex} = 510$ nm.

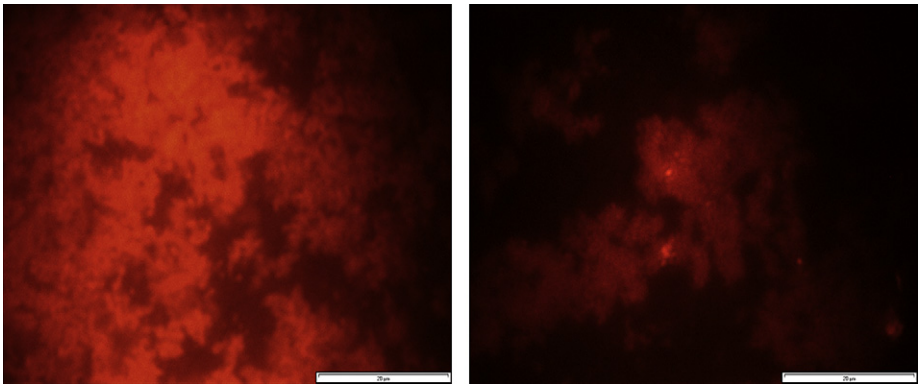

Fig. 14. 100× Microscope image of the RhB:βCD complex film (left) and physical mixture (Right). Scale bar 20 μm.

film with the simple physical mixture, also prepared by HEBM. The latter presents a darker color with white spots corresponding to macroscopic domains of aggregated βCD. As the complex lacks a crystalline structure, as XRD experiments have shown, it seems that in order to achieve a good dispersion of the βCD in the solid phase it is necessary to break its crystalline arrangement and convert it to an amorphous form.

Images at different scales of the films with the RhB:βCD complex and the physical mixture were taken with a fluorescence microscope. As it can be seen in Figs. 13 and 14, using the same diaphragm and magnification conditions (20× and 100×), the RhB:βCD film clearly shows an enhanced fluorescent response in relation to the other when excited at 510 nm. In addition to that, the complex produces an excellent dispersion throughout the matrix, whereas the mixture presents local domains of RhB at the bottom section and other sectors that are richer in βCD, where there is no fluorescence response at all resulting in a dark image.

4. Conclusions

The association between βCD and RhB and Rh6G has been studied both in solution and solid state by different techniques. ^{1}H NMR results combined with fluorescence spectroscopy confirm the formation of a stable complex of RhB of 1:1 stoichiometry, with a binding constant of the order of 10^4 M^{-1} on a wide range of temperatures. The mode of inclusion has been elucidated with the aid of ROESY spectra, proving that the RhB enters the βCD by any of the ethylammonium substituents toward the wider rim of the macrocycle, leaving exposed to the solvent the moiety of the RhB that bears the carboxylic group. Analysis of the solid products makes clear that the complex of RhB retains its stability in the solid phase, as stated by the disappearance of the endothermic peak at 200 °C in TGA, characteristic of the RhB, and to the blue shift and emission enhancement observed by fluorescence. On the other hand, Rh6G does not form complexes either in aqueous solution or in the solid phase.

The RhB complex mixed by cryo HEBM with the polymer, EVA, after the subsequent film production is homogeneously scattered through the matrix, undergoing a four-fold enhancement in its fluorescence, that is not observed with the physical mixture. The use of a fluorescent complex with βCD has thus the double effect of breaking the crystalline structure of the βCD by forming an amorphous phase that makes possible the proper dispersion of the macrocycle and to enhance the “visibility” of the macrocycle. These results, apart from eliminating the need of using more sophisticated techniques as SEM or AFM, are important for subsequent investigations of nanocomposites based in CDs, either as nanofillers by themselves or attached to other nanostructures.

Acknowledgments

Authors acknowledge the financial support of the projects MAT2010-16815 and CTQ2010-18564 from the Ministerio de Ciencia e Innovación, as well as the PhD grant for Rafael Serra provided by the “Asociación de Amigos de la Universidad de Navarra”.

References

[1] Hussain F, Hojjati M, Okamoto M, Russell E. Review article: polymer-matrix nanocomposites, processing, manufacturing and application: an overview. J Comp Mat 2006;40:1511–75.

[2] Zhao R, Torley P, Halley PJ. Emerging biodegradable materials: starch- and protein-based bio-nanocomposites. J Mater Sci 2008;43:3058–71.
[3] Suryanarayana C. Mechanical alloying and milling. Prog Mater Sci 2001; 46(1–2):1–184.
[4] Padella F, Incocciati E, Nannetti CA, Colella C, Casadio S, Magini M. Mechanically activated low temperature synthesis of Sr doped lanthanum manganite. Mechanically alloyed. J Metastable Nanocryst Mater Part 1 1998;269(2): 105–10.
[5] Rowlands SA, Hall AK, McCormick PG, Street R, Hart RJ, Ebell GF, et al. Destruction of toxic materials. Nature 1994;367(6460):223.
[6] Castrillo PD, Olmos D, Amador DR, González-Benito J. Real dispersion of isolated fumed silica nanoparticles in highly filled PMMA prepared by high energy ball milling. J Colloid Interface Sci 2007;308(2):318–24.
[7] Olmos D, Dominguez C, Castrillo PD, González-Benito J. Crystallization and final morphology of HDPE: effect of the high energy ball milling and the presence of TiO_2 nanoparticles. Polymer 2009;50(7):1732–42.
[8] González-Benito J, González-Gaitano G. Interfacial conformations and molecular structure of PMMA in PMMA/silica nanocomposites. Effect of high-energy ball milling. Macromolecules 2008;41(13):4777–85.
[9] Shaw WJD. Current understanding of mechanically alloyed polymers. Mater Sci Forum 1998;269(2):19–29.
[10] Padella F, Magini M, Incocciati EU. Patent N 0963825 B1, Bulletin; 2003/ 3956, 57.
[11] González-Gaitano G, González-Benito J. Pseudorotaxanes of cyclodextrin and diglycidyl ether of bisphenol A as precursors of new intramolecularly reinforced epoxy-based thermosets. Supramol Chem 2008;20:335–44.
[12] Xu M, Wu S, Zeng F, Yu C. Cyclodextrin supramolecular complex as a water-soluble ratiometric sensor for ferric ion sensing. Langmuir 2010;26(6): 4529–34.
[13] Patel K, Angelos S, Dichtel WR, Coscun A, Yang YW, Zink JI, et al. Enzyme-responsive snap-top covered silica nanocontainers. J Amer Chem Soc 2008; 130:2382–3.
[14] Wu J, Gao C. Click chemistry approach to rhodamine B-capped polyrotaxanes and their unique fluorescent properties. Macromol Chem Phys 2009;210: 1697–708.
[15] Liu Y, Chen Y, Li B, Wada T, Inoue Y. Cooperative multipoint recognition of organic dyes by bis(β-cyclodextrins) with 2,2′-bipyridine-4,4′-dicarboxy tethers. Chem Eur J 2001;7:2528–35.
[16] Saenger WR, Jacob J, Gessler K, Steiner T, Hoffmann D, Sanbe H, et al. Structures of the common cyclodextrins and their larger analogues – beyond the doughnut. Chem Rev 1998;98(5):1787–802.
[17] O'Conell RM, Saito TT. Plastics for high-power laser applications – a review. Opt Eng 1983;22(4):393–9.
[18] Peterson OG, Snavely BB. Stimulated emission from flashlamp-excited organic dyes in polmethyl methacrylate. Appl Phys Lett 1968;12(7):238–40.
[19] Crini G. Kinetic and equilibrium studies on the removal of cationic dyes from aqueous solution by adsorption onto a cyclodextrin polymer. Dyes Pigm 2008; 77:415–26.
[20] López Arbeloa F, López Arbeloa T, López Arbeloa I, Costela A, Garcia-Moreno I, Figuera JM, et al. Relations between photophysical and lasing properties of rhodamines in solid polymeric matrices. Appl Phys B 1997;64:651–7.
[21] Hwang TL, Shaka AJ. Water suppression that works. Excitation sculpting using arbitrary wave-forms and pulsed-field gradients. J Magn Reson Ser A 1995; 112(2):275–9.
[22] Bax A, Davis DG. Practical aspects of two-dimensional transverse NOE spectroscopy. J Magn Reson Ser A 1985;63(1):207–13.
[23] Bernini A, Spiga O, Ciutti A, Scarselli M, Bottoni G, Mascagni P, et al. Studies of the inclusion complex between β-cyclodextrin and paroxetine. Eur J Phar Sci 2004;22:445–50.
[24] Job P. Formation and stability of inorganic complexes in solution. Annali Chim Appl 1928;9:113–203.
[25] Mchedlov-Petrosyan NO, Kholin YV. Aggregation of rhodamine B in water. Russ J Appl Chem 2004;77(3):414–22.
[26] Degani Y, Willner I. Lasing of rhodamine B in aqueous solution containing β-cyclodextrin. Chem Phys Lett 1984;104(5):496–9.
[27] Politzer IR, Crago KT, Hampton T, Joseph J. Effect of β-cyclodextrin on the fluorescence, absorption and lasing of rhodamine 6g, rhodamine b and fluorescein disodium salt in aqueous solutions. Chem Phys Lett 1989;159(2–3):258–62.
[28] Sainz-Rozas PR, Isasi JR, González-Gaitano G. Spectral and photophysical properties of 2-dibenzofuranol and its inclusion complexes with cyclodextrins. J Photoch Photobio A Chem 2005;173:319–27.
[29] Mchedlov-Petrossyan NO, Kakhtik VI, Bezugliy VD. Dissociation, tautomerism and electroreduction of xanthene and sulfonephthalein dyes in N,N-dimethylformamide and other solvents. J Phys Org Chem 2003;16:380–97.
[30] Schulman SG. Acid–base chemistry of excited singlet states. In: Wehry EL, editor. Modern fluorescence spectroscopy, vol. 2. London: Heyden and Sons Ltd.; 1976. p. 239–74.
[31] Magde D, Rojas GE, Seybold P. Solvent dependence of the fluorescence lifetimes of xanthene dyes. Photochem Photobiol 1999;70:737–44.
[32] Ferreira JAB, Costa SMB. Non-radiative decay in rhodamines: role of 1:1 and 1:2 molecular complexation with β-ciclodextrin. J Photoch Photobio A Chem 2005;173:309–18.

J Nanopart Res (2016)18:24
DOI 10.1007/s11051-015-3321-x

RESEARCH PAPER

Cyclodextrin-grafted barium titanate nanoparticles for improved dispersion and stabilization in water-based systems

R. Serra-Gómez · J. M. Martinez-Tarifa · J. González-Benito · G. González-Gaitano

Received: 26 August 2015 / Accepted: 30 December 2015
© Springer Science+Business Media Dordrecht 2016

Abstract Ceramic nanoparticles with piezoelectric properties, such as $BaTiO_3$ (BT), constitute a promising approach in the fields of nanocomposite materials and biomaterials. In the latter case, to be successful in their preparation, the drawback of their fast aggregation and practically null stability in water has to be overcome. The objective of this investigation has been the surface functionalization of $BaTiO_3$ nanoparticles with cyclodextrins (CDs) as a way to break the aggregation and improve the stability of the nanoparticles in water solution, preventing and minimizing their fast precipitation. As a secondary goal, we have achieved extra-functionality of the nanoparticles, bestowed from the hydrophobic cavity of the macrocycle, which is able to lodge guest molecules that can form inclusion complexes with the oligosaccharide. The nanoparticle functionalization has been fully tracked and characterized, and the cytotoxicity of the modified nanoparticles with fibroblasts and pre-osteoblasts cell lines has been assessed with excellent results in a wide range of concentrations. The modified nanoparticles were found to be suitable for the easy preparation of nanocomposite hydrogels, via dispersion in hydrophilic polymers of typical use in biomedical applications (PEG, Pluronics, and PEO), and further processed in the form of films via water casting, showing very good results in terms of homogeneity in the dispersion of the filler. Likewise, as examples of application and with the aim of exploring a different range of nanocomposites, rhodamine B was included in the macrocycles as a model molecule, and films prepared from a thermoplastic matrix (EVA) via high-energy ball milling have been tested by impedance spectroscopy to discuss their dielectric properties, which indicated that even small modifications in the surface of the nanoparticles generate a different kind of interaction with the polymeric matrix. The CD-modified nanoparticles are thus suitable for easy preparation of the water-based nanocomposites either as hydrogels or as nanocomposites based on thermoplastic matrices.

Keywords Barium titanate · Cyclodextrins · Polymeric nanocomposites · Nanoparticle modification · Surface modification · Dispersion

Electronic supplementary material The online version of this article (doi:10.1007/s11051-015-3321-x) contains supplementary material, which is available to authorized users.

R. Serra-Gómez · G. González-Gaitano (✉)
Departamento de Química y Edafología, Universidad de Navarra, 31080 Pamplona, Spain
e-mail: gaitano@unav.es

J. M. Martinez-Tarifa
Departamento de Ingeniería Eléctrica, Universidad Carlos III de Madrid, Av. Universidad 30, 28911 Leganés, Spain

J. González-Benito
Departamento de Ciencia e Ingeniería de Materiales e Ingeniería Química, IQMAAB, Universidad Carlos III de Madrid, Av. Universidad 30, 28911 Leganés, Spain

Published online: 20 January 2016

Introduction

Nanocomposite materials, composed of polymers and nanostructures, form the basis on which most of the biomaterials are being developed at the moment, as a small amount of filler can dramatically modify the properties of the matrix, empowering tailored compositions for different uses (Gaharwar et al. 2011). Recently, a wide range of inorganic materials such as barium titanate ($BaTiO_3$, BT), hydroxyapatite, or synthetic silicates—such as laponites—have started to gain increasing consideration in view of their prospective use in the field of bioengineering due to their unique mechanical and chemical properties (Wang et al. 2013; Gaharwar et al. 2013; Mamana and Pellegri 2015). Specifically, biocompatible nanocomposites play a key role in important fields of medicinal, chemical, and biological researches, arousing important innovations for bone regeneration, tissue engineering, implants, or drug delivery systems (Shi et al. 2010).

BT is a perovskite-type ceramic, ferroelectric in all its crystalline phases except the cubic one. It possesses a high dielectric constant with piezoelectric properties on its tetragonal, orthorhombic, and rombohedral phases. These properties make BT to be useful for applications other than bioengineering, such as in electronics as printed circuits, and as piezoelectric sensors for ultrasonic transducers, capacitors, and random access memories as some notable examples (Ring and Kavanagh 2003; Yu et al. 2011). However, BT has been replaced in some of these applications by multiceramic materials as lead zirconate titanates, or PZTs (Park and Shrout 1997). On the other hand, the high processing temperatures of these ceramic materials makes them unsuitable for many practical uses where polymeric materials are involved, such as in printed circuit boards (PCBs). This problem may be overcome by its preparation in form of polymeric nanocomposites, which are easily processable and with tuneable properties, and in order to achieve this, the first and most important requisite is to ensure a uniform dispersion of the filler, since the formation of particles' agglomerates may lead to the unwanted discontinuity of or deterioration in their properties. In some previous works, we have described an easy, inexpensive, and solvent-free method of achieving a good dispersion of the filler in thermoplastic-matrix nanocomposites, based on high-energy ball milling (HEBM), a solid state method (Serra-Gómez et al. 2012a). Nonetheless, biocompatible nanocomposites mostly require that their components are soluble in water, or at least stable in suspension in order to achieve an adequate dispersion of the filler. As PZTs are not suitable materials for most biomedical applications, due to the high toxicity of the lead components (Sakai et al. 2006; Tsuchiya et al. 2011), BT has been recommended as a good alternative material provided that the stability issue is overcome; some examples of applications are as second-harmonic generators for imaging (Dempsey et al. 2013; Hsieh et al. 2010), as drug and gene delivery carriers (Ciofani et al. 2010; Jeong et al. 2013), or as ceramic fillers in bone defects to promote its regeneration (Feng et al. 1997; Baxter et al. 2009). All the more, these nanomaterials have often been used as fillers in polymers and hydrogels that do not present the desired mechanical properties for the use they were intended (Huang et al. 2007; Schexnailder and Schmidt 2008; Knauert et al. 2007). Yet, the main difficulty to use BT in biocomposites is to achieve a uniform and stable dispersion in aqueous media since the nanoparticles tend to aggregate as a result of their high surface area-to-volume ratio (Blanco-López et al. 1997; Paik et al. 2002). These aggregates can reach sizes of a few micrometers (Serra-Gómez et al. 2012b; Gao et al. 2015) which can be a drawback because of their high tendency to precipitate. The modification of the surface of the nanoparticles is a possible approach to improve the stability of the dispersions, either by adsorption onto the surfaces of different substances like polyethylene glycol, PEG (Čulić-Viskota et al. 2012), polyacrylic acid ammonium salts, PAA-ammonium (Jean and Wang 2005) and polyalcohols, or by covalent bonding by first generating either amine (FarrokhTakin et al. 2012), phosphonic (Kim et al. 2007), or hydroxyl (Chang et al. 2009) groups on the surface for further grafting of molecules of interest.

Cyclodextrins (CDs) are cyclic oligosaccharides composed of 6, 7, or 8 D-glucopyranose rings termed α-, β-, or γ-CDs respectively. CDs are shaped like truncated cones, with a relatively hydrophobic cavity and a hydrophilic exterior. The many hydroxyl groups, according to the number of glucose units, makes it possible to establish strong interactions with certain polymeric matrices. One of the few applications of CDs with ceramic nanoparticles, such as TiO_2 and BT,

has to do with the stabilization of nanocrystals and nanoparticles in their hydrothermal-synthesis steps to provide a shell for the nanocrystals to grow, allowing the sizes to be precisely controlled (2–10 nm) and therefore achieve a better stabilization as the aggregation is suppressed (Li et al. 2006; Sun et al. 2008; Shiraishi et al. 2015).

In this paper, we report on a novel method of disaggregation and water stabilization of commercially available BT nanoparticles of different sizes (50, 100, and 200 nm in diameter) by coating them with β-CD attached by hydrogen-bonding forces to the previously generated –OH groups via the hydroxylation of the surface through reaction with H_2O_2 (Choudhury 2012; Hiroki and Laverne 2005). As a consequence of this, the addition of the macrocycles on the surface opens the possibility of adding extra functionality to the nanoparticles, as they can include different types of molecules and drugs of interest in their cavity (Städe et al. 2015). Another type of covalent modification via conjugation with oleate (SOA), as proposed by Chang et al. to improve the dispersion in organic solvents, has been used, followed by the addition of α-cyclodextrin (α-CD), which is known to form supramolecular complexes via the inclusion of the hydrocarbon tail of the surfactant (Gonzalez-Gaitano et al. 2000), proving that, by this method, the stability in water is also enhanced when incorporating the CD to the surface of the nanoparticles.

With the modified nanoparticles, and as examples of possible applications, various types of nanocomposites have been prepared by changing the polymeric matrix and have been tested for their use in solid phase and in solution, confirming that the modified surface is able to endure both solid-state methods of dispersion (high-energy ball milling, HEBM) as well as water-casting. The cytotoxicity of the modified nanoparticles has been evaluated in different concentrations and cell lines, and films have been casted in different polymeric matrices as poly (ethylene-co-vinylacetate), EVA, polyethylene oxide (PEO), polyethylene glycol (PEG), and Pluronic® F127 (an amphiphilic PEO-PPO-PEO block copolymer) to show the ability of the nanoparticles to form stable suspensions and hydrogels for their use in biomedical applications. The samples have been fully characterized by means of FTIR-ATR spectroscopy, thermogravimetric analysis, dynamic light scattering, X-ray diffraction, and electron microscopy. The dielectric response of the films has also been evaluated to study the influence of the filler modification on the dielectric properties of the nanocomposites, showing that the individual properties of the components are maintained even after the solid-state treatments.

Materials and methods

Materials

Inorganic submicrometric particles of barium titanate (BT), with an average diameter size of 200 nm (99.9 % purity, $\rho = 6.02$ g cm^{-3}, and tetragonal crystalline structure) and nanoparticles of 100 nm (99.9 % purity, $\rho = 5.85$ g cm^{-3}, and cubic crystalline structure) were supplied by Nanostructured and Amorphous Materials Inc. BT of 50 nm in diameter was supplied by Sigma-Aldrich (99.9 % purity, $\rho = 6.08$ g cm^{-3}, and cubic crystalline structure). Sodium oleate , SOA (≥82 % fatty acids, as oleic acid) was provided by Aldrich, and αCD and βCD were supplied by Wacker as Cavamax®, W6, and W7, respectively. PEO with 4×10^6 g mol^{-1} from Aldrich. Polyethylene glycol (PEG), with Mw of 10.000 g mol^{-1} from Fluka; and Pluronic® F127 with an average Mw of 12,600 g mol^{-1} have been used for the preparation and casting of water-based composites. Poly (ethylene-co-vinyl acetate)—EVA (12 wt% in vinyl acetate, density 0.933 g cm^{-3} at 25 °C, Vicat temperature of 65 °C, and melting point of 95 °C) was supplied by Sigma Aldrich.

Sample preparation

(i) *Surface modification* The process used for the modification of the nanoparticles consisted of three steps: (a) Hydroxylation of BT by oxidation with H_2O_2 in a reflux setup for 4 h at 106 °C; (b) Covalent bonding of SOA to the hydroxyl groups generated in the previous step by stirring a suspension of nanoparticles (2 wt%) in a SOA aqueous solution (0.5 wt%) for 3 h at 90 °C. (c) Reaction with α-CD for 3 h at room temperature under vigorous stirring. Three washing and rinsing

cycles were done in each step. In the case of the modification only with CD, the second step was skipped, and the reaction with α-CD and β-CD was directly done on the hydroxylated surface. The resulting modified nanoparticles were freeze-dried and characterized.

(ii) *Cryo-HEBM* In order to make easier the subsequent blending process with the particles, EVA pellets were first ground in a MF 10 Basic IKA WERKE grinder at a rotation speed of 4500 rpm. A mixture of BT with EVA (20 wt%) was subjected to cryo-HEBM as described in our previous work (Serra-Gómez et al. 2012a), followed by the film preparation as described by Olmos et al. (2011).

The nomenclature used for the samples during the synthesis and characterization is as follows: BT plus a number depending on the diameter size of the nanoparticles (1 for 100 nm and 2 for 200 nm) plus the coating applied; –OH for the hydroxyl generation, -SOA for the oleate, -SOA-αCD for the oleate plus cyclodextrin, and –αCD and –βCD for the alpha and beta cyclodextrins, respectively.

Techniques

Attenuated total reflectance was used for the IR characterization using an FTIR-ATR Nicolette Avatar 360 spectrometer, with a resolution of 2 cm^{-1} and 32 scans per spectrum. Thermogravimetric analysis, TGA, was carried out in a TGA-SDTA 851 Mettler Toledo with a heating program from 25 to 600 °C at 10 °C/min under N_2 atmosphere.

Fluorescence studies on the modified nanoparticles tagged with rhodamine B (RhB) were done using an Edinburgh Instruments FLS920 spectrofluorimeter. Samples in a quartz cuvette of 10 mm of path length were excited at 553 nm, and the emission was recorded from 560 to 700 nm under constant stirring; average of five scans with a 1-nm step and 0.1-s dwell time were considered. Excitation and emission slits were set at 2 nm. 30 mg of CD-modified nanoparticles were made to come in contact with a 4×10^{-6} M RhB solution and stirred for 1 h. Then, they were centrifuged at 8000 rpm for 30 min, and the nanoparticles were separated from the supernatant and dried at 80 °C for 24 h.

The size distribution of the different particles was determined by dynamic light scattering (DLS) using a DynaPro photon correlation spectrometer. The particles were dispersed in deionized water by sonication and diluted before the measurements without further filtration. The intensity size distributions, expressed in terms of the hydrodynamic radius, R_h, were calculated by the method of regularization using DynaLS 1.0 software.

For the Zeta potential measurements, an electroacoustic-based zeta potential analyzer (ZetaProbe, Colloidal Dynamics), specifically intended for the study of concentrated suspensions, was used. Alkaline pH was achieved by addition of NaOH 0.1 M and the titration from pH = 12 to pH = 3 was conducted with HCl 0.1 M. For the transmission electron microscopy (TEM) images, the samples were treated with osmium tetroxide 1 % and were kept at 4 °C for 1 h. Then, a drop of the suspension was placed in a copper grid, and phosphotungstic acid 2 % as a negative contrast agent was applied. Samples were analyzed using a LIBRA 120 energy-filtering TEM (Zeiss) operated at 80 kV.

The cytotoxicity of the modified BT nanoparticles was tested on the fibroblast cell line of NIH3T3 and MC3T3-E1 pre-osteoblasts. The Tetrazolium assay (MTT) was used to assess the viability of the cells, and thus the cytotoxicity was established by the loss of viable cells upon treatment with the compounds of interest. The cells were incubated in Dulbecco's modified eagle medium supplied by Life's Technologies, supplemented with 10 % of fetal bovine serum and 0.1 % of penicillin/streptomycin at 37 °C and 5 % CO_2. Cells were seeded into 96-well plates at a concentration of $5x10^4$ cells/mL and 24 h later, the nanoparticles were added at different concentrations. MTT tests were conducted on day 3 and day 7 by addition of MTT 1 mg/mL and incubation of 3 h. The formazan absorbance at 540 nm was measured using a Thermo Scientific Multiscan EX microplate reader. DMSO was used as a positive control, and the appropriate negative controls were performed.

Impedance measurements in the frequency range of 1 Hz−1 MHz were carried out at room temperature using an impedance analyzer, SOLARTRON 1260A. A 3-V sinusoidal voltage signal was applied, measuring the current to finally obtain the complex impedance with its amplitude and phase over a range of frequencies (20 points per decade). Zview® software (Scribner Associates, Inc.) was used for the numerical fitting of the impedance data by considering a specific equivalent circuit. The measurements were

performed on capacitors in the form of a dielectric film contained on each sample between two plate electrodes with circular surfaces of 1.25 cm in diameter. The thicknesses of the dielectrics were measured using a thickness meter Easy-check FN of NEURTEK Instruments with an accuracy of ±1 μm.

Results and discussion

Characterization of the surface modification of the BT nanoparticles

The surface modification consists of a three-step process that can be easily tracked by FTIR-ATR spectroscopy. Figure 1a shows the spectra of the as-received nanoparticles (BT, black trace) where the Ti–O stretching band can be seen in the fingerprint region starting at 600 cm^{-1}; the C–O band at 1452 cm^{-1} corresponds to vibrations coming from residual $BaCO_3$ from the synthesis method, usually deposited on the surface (Chaudhary et al. 2011). After the H_2O_2 treatment (BT–OH, red trace), the particles start showing the typical broad band of hydroxyl groups around 3300 cm^{-1}. On the other hand, upon incorporating hydrophobic chains after the SOA reaction (BT-SOA, green trace), the characteristic bands at 2850–2910 cm^{-1} that correspond, respectively, to the antisymmetric and symmetric stretching, of the C–H bonds, together with their bending modes at 1510–1430 cm^{-1}, are clearly seen. The spectrum of BT-SOA-αCD (navy blue trace) shows the inclusion complex of the αCD, as seen by the growth of the –OH band due to the CD hydroxyl groups and the 1154 cm^{-1} bands of the C–O–C vibrations. From 1700 to 1300 cm^{-1}, the skeletal C–C vibrations appear, along with the stretching vibrations of C–H and C–O bonds at 1082 cm^{-1}. Lastly, the BT-βCD trace (light blue), shows how the –OH band and vibrations of the CD groups appear at the same wavenumbers as the previous one, but with considerable lower intensities, as expected due to the different proportions between the bulk of the nanoparticle and the CD on the surface.

Due to the proportions between the nanoparticle and amount of modifier bound to the surface, it can be challenging to fully characterize the three different steps of the modification process. In order to facilitate this, an estimation of the –OH groups that are generated on the surface can be calculated from the weight loss of the samples analyzed by thermogravimetry. As the stoichiometry of the reaction between SOA and the OH is 1:1, we can estimate the maximum number of bound SOA molecules per nanoparticle, and compare it to the experimental results to assess the extent of the functionalization. On the other hand, considering the size of the αCD (4.7–5.3 Å), its height (7.1 Å) (Saenger et al. 1998), and the length of the SOA chains (≈2 nm) (Lingley et al. 2013), it is expected that each SOA molecule can host a maximum of three αCD molecules, although steric effects as the bending of the oleate due to the insaturation and the proximity of neighbor chains already including CDs might reduce that number. The composition of the coating can be followed by TGA as SOA and the CD decompose around 300 °C, while the ceramic nanoparticles remain intact; therefore, the weight loss should indicate the weight percentage of the coating. Table 1 shows the results of the calculations as well as the experimental values obtained by TGA on the different nanoparticles for the SOA modification. As expected, the weight percentage decreases as the nanoparticle diameter increases, but always within the limits of the theoretical estimations.

The decomposition of the CD can be attributed to the weight loss occurring between 315 and 350 °C, the lower end of the range corresponding to the decomposition of CDs adsorbed in the surface and the higher value to that of the CDs with oleate chains included. The oleate loss takes place in the range of approximately 368–507 °C, which corresponds to the oleate chains that are covalently bonded to the surface. When free or weekly attached chains are considered, decomposition occurs at lower temperatures around 290 °C, as described by Ozel et al. (2013). As expected, the amount of SOA on the surface varies due to the different surface-volume ratios for the three sizes of nanoparticles. Figure 1b shows the TGA thermograms of the BT100 and BT200 samples, exhibiting a coating well within the limits of the estimation done before for the SOA treatment. The weight loss values of the CDs and oleate thermal degradation are shown in Table 2.

In the case of the modification only with CD, the values are considerably higher than the ones expected from the previous estimation, so it is clear that there is not a monolayer on the surface of the nanoparticle. It is known that CDs self-aggregate in water, both in native form or when forming complexes (González-Gaitano

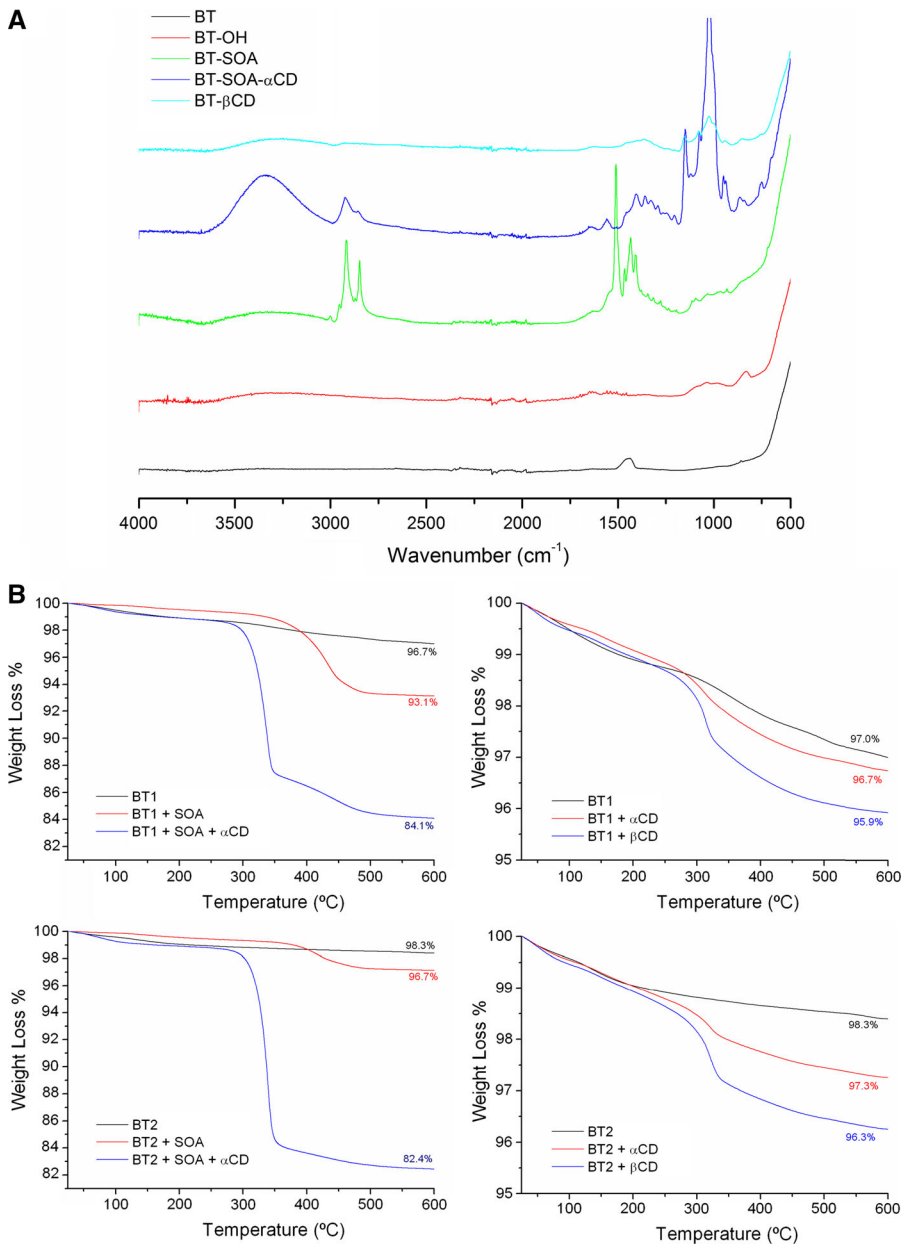

Fig. 1 **a** FTIR spectra of the BT nanoparticles along the different surface-modification steps. BT as-received (*black*), BT–OH (*red*), BT-SOA (*green*), BT-SOA-αCD (*navy blue*), and BT-βCD (*cyan*).1**b** TGA of the modified nanoparticles: 100 nm (*top*) and 200 nm (*bottom*), with SOA and αCD (*left*) and modified with αCD and βCD (*right*). (Color figure online)

Table 1 Theoretical and experimental values estimated by TGA of the wt% of –OH and oleate groups upon modification of BT 50-nm nanoparticles (BT50), BT-100 nm nanoparticles (BT100), and BT 200-nm nanoparticles (BT200)

Sample	–OH (TGA loss) (%)	Theoretical maximum SOA (1:1) (%)	Experimental SOA (%)
BT50	3.4	55	14
BT100	3.4	53	3.0
BT200	2.2	37	1.8

et al. 2002), so it is likely that a multilayer of CDs is formed on the surface of the nanoparticles, especially when the treatment involves the presence of the precursors in solution at relatively high concentration, and upon further drying. In both cases, BT100 and BT200, the binding of CDs to the surface of the nanoparticles is larger with βCD, which confirms the stated above since the βCD's self-aggregation tendency is notably higher than that of αCD (González-Gaitano et al. 2002).

However, the thermogravimetry results of the CD-modified samples fall within the sensitivity range of the technique (1 wt%), and in order to confirm the presence of the CD layer, given that the values from TGA are relatively low and that the amount of CD is scarce for a reliable FTIR quantification, an alternative procedure was used, taking advantage of the inclusion complex formation between RhB and βCD (Serra-Gómez et al. 2012b). The modified nanoparticles were dispersed in a RhB solution, and both the fluorescence signal emitted by the solid samples as well as the fluorescence loss in the solution measured.

After mixing the nanoparticles with the RhB solution, an extensive adsorption of the RhB in the surface takes place, indicated by the pinkish color acquired by the samples. Fluorescence measurements on the supernatant of the modified nanoparticles (Fig. 2) show a decrease in the emission of a 6 % in relation to the untreated BT as well as an increase in the fluorescence of the solid (not shown), evidencing the formation of the inclusion complex between the RhB and the adsorbed CDs. The decrease of the fluorescence yield of the BT-SOA modification is also remarkable being a 35 % loss over the native BT. In the case of the BT-SOA-αCD, the long oleate chains are capped with the CDs, and the fluorescence values show that, as the oleate chains are trapped in the CDs, the RhB molecules are pushed toward the long alkyl chains, leading to the subsequent reduction in the amount of RhB attached to the nanoparticle and the increase in its concentration in the supernatant. This result is important, not only because it provides evidence of the attachment of the CDs to the surface, but in fact it opens a wide array of possible molecules that can be successfully carried and released from the CDs, using the BT as a nanocarrier.

The aggregation behaviors of all the samples have been tested by DLS. Figure 3 shows the intensity size distributions for the 50-nm nanoparticles (the corresponding peak analyses are shown in SI Table 1). A strong aggregation of the native nanoparticles (black trace) can be perceived, with an important contribution of agglomerates of around 300 nm and >1000 nm in diameter. However, with the SOA–αCD complex (green trace in Fig. 3 left), as well as with βCD (blue trace in Fig. 3 left), the disaggregation is notably improved (50–80 nm). This corroborates that the first step to achieve a proper dispersion for an improved suspension in water is to break up the aggregates. The stability in suspension of these samples was invetigated by Z-potential measurements on a pH range from 3 to 12. Figure 3 (right) shows a significant change in the modified samples reaching potentials of −200 mV for the BT50-βCD (green trace upper graph) and −100 mV for the BT200-βCD (green trace bottom graph) when the pH is in the physiological range between 7 and 11.

These Z potential values, together with the above presented data, suggest that the modified nanoparticles with oleate and CDs as well as the ones with βCD present a stability improvement in this pH range, as the modifications involve enough change in the surface charge to prevent aggregation, in contrast to the untreated nanoparticles, as a result of the presence of

Table 2 Weight loss percentages calculated from TGA of the modified BT nanoparticles in the temperature region of the CDs and oleate degradation

Samples BT	αCD	SOA (%)	BT samples	αCD	βCD	CDs monolayer estimation (%)
BT0.5 + SOA		13.1	BT0.5 + αCD	0.56 %		0.23
BT0.5 + SOA + αCD	21.1 %	3.73	BT0.5 + βCD		0.59 %	0.21
BT1 + SOA		5.21	BT1 + αCD	0.75 %		0.12
BT1 + SOA + αCD	11.0 %	2.88	BT1 + βCD		1.31 %	0.11
BT2 + SOA		1.84	BT2 + αCD	0.58 %		0.06
BT2 + SOA + αCD	14.2 %	1.31	BT2 + βCD		1.20 %	0.05

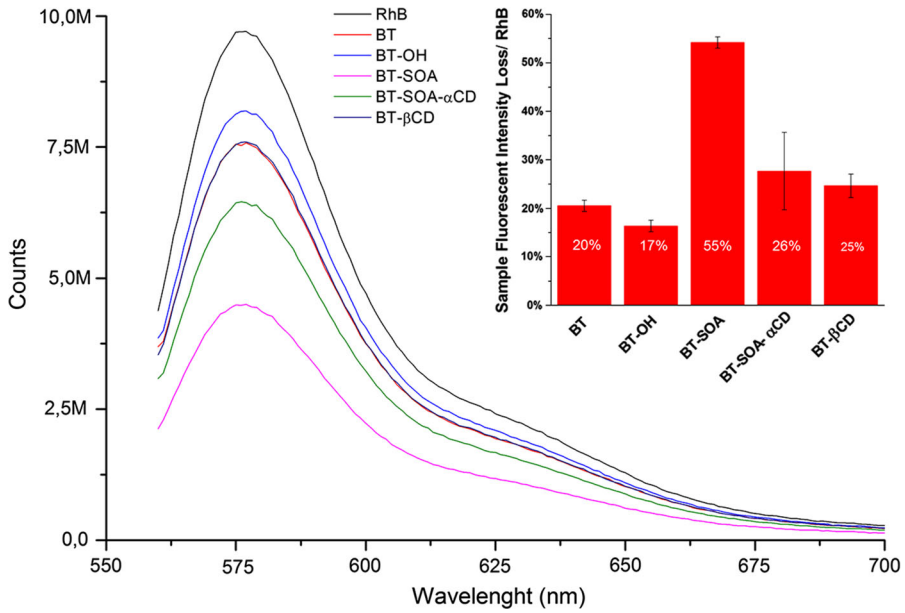

Fig. 2 Fluorescence emission of the supernatant of RhB 1.25×10^{-7} M aqueous solution containing modified nanoparticles. The *inset* shows the fluorescence signal loss of the samples in relation to RhB

the high density of hydroxyl groups on the βCD. The difference in Z-potential values is in accordance with Paik et al. (1998) where they state the direct dependence on the percentage of BT surface covered with the solution stability. As stated previously, the modification with CDs alone yields a multilayer due to the CD stacking and, therefore, a higher percentage of surface coverage than when the SOA treatment is applied. An example of the improved dispersion of the nanoparticles in water can be seen in the supplementary data photographs of samples after 4 h (SI, Fig. 1).

TEM microscopy was performed upon selected samples to show the difference in the nanostructures upon functionalization. The untreated nanoparticles (Fig. 4 left) present a homogeneous surface, while the SOA–αCD-modified BT ones (Fig. 4 right) display a surface with a variation of dark tonalities resulting from the osmium oxide reaction with the SOA unsaturation, which proves the presence of the functionalization all over the surface.

The cytotoxicity of the CD–modified BT has been assessed in a wide range of concentrations from 0 to 200 μg/mL. By reviewing the literature on BT cytotoxicity, mainly the studies of Dempsey et al. (2013) and Ciofani et al. (2010), it seems clear that the coating plays a crucial role as it can notably change the way the cells interact with the BT, and represent the main contribution to the cytotoxicity. In our case, the CD coating seems to allow for higher concentrations of nanoparticles without any negative effect in the cell viability. Figure 5 shows the MTT assay results for the different BT-CDs, showing excellent viability of the cells even up to concentrations of 200 μg/mL after a week of treatment with significant improvements in the cell proliferation at concentrations of 100 and 200 μg/mL according to the ANOVA and student's *T* test ($p < 0.01$; $n = 12$).

The same nanoparticles were tested against the MC3T3-E1 cell line and phase contrast (SI Fig. 2, 3) and confocal images were taken at days 3, 7, and 14 after treatment. The confocal image shows how, after 14 days of treatment, the nanoparticles (200 ug/mL, red) are internalized in the tissue formed by the cells that grew normally. Other images of the sequence are presented in the SI (Figs. 2 and 3). The βCD modification, as opposed to other coatings used to disperse BT, does not present cytotoxic effect in the concentrations studied.

Examples of application

As examples of the improvement achieved by the surface modifications, two cases will be shown in which the nanoparticles have been used to prepare

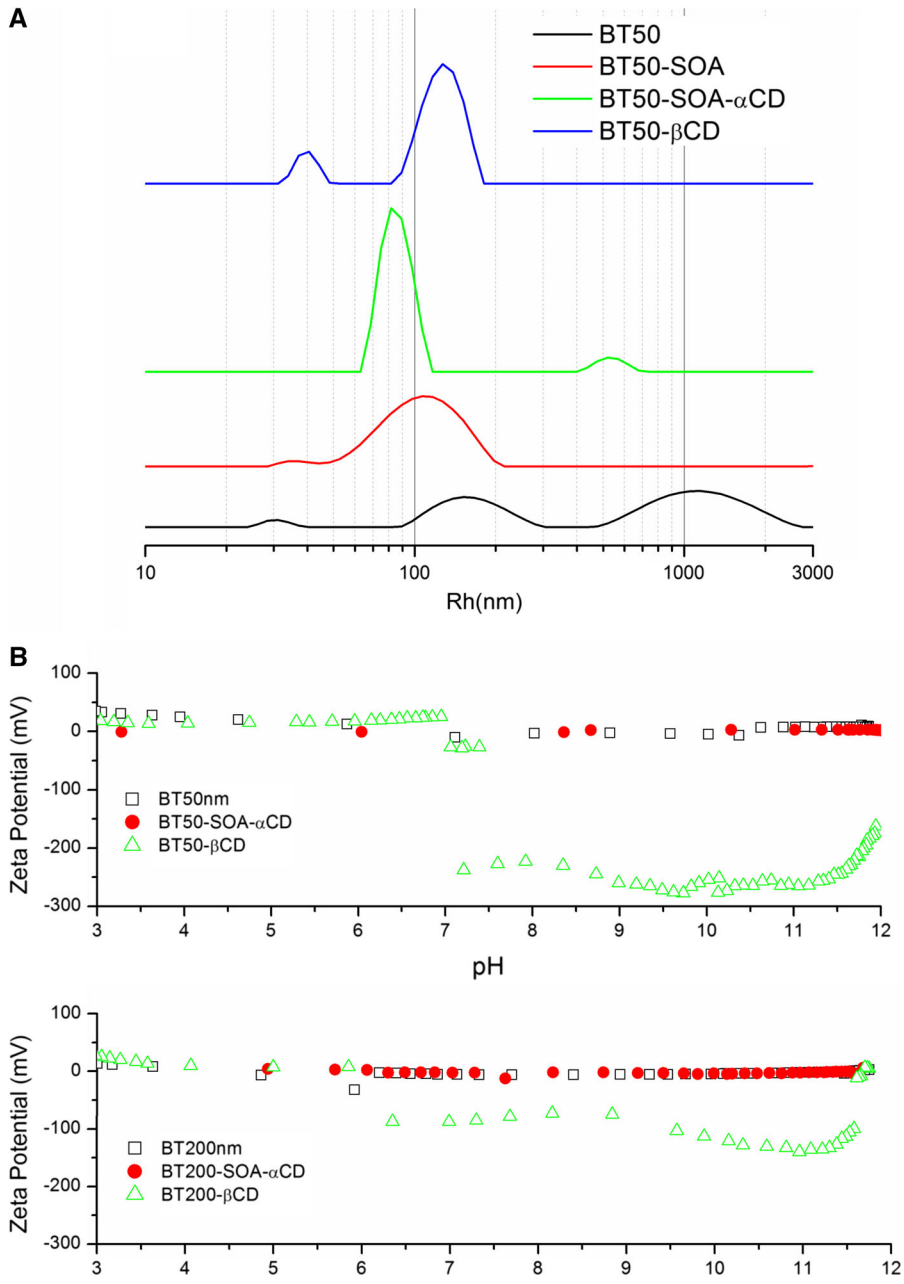

Fig. 3 **a** Intensity size distributions of the as-received and the modified BT 50-nm nanoparticles. 3**b** Z-potential measurements of 1 wt% suspension of the native and the modified BT samples

different types of nanocomposites: one by water casting with EO-based polymers to obtain nanocomposite hydrogels, and another one by cryo-HEBM as the processing method from a thermoplastic matrix. Lastly, the outcomes of these two examples of application will be tested by impedance spectroscopy to study the effect of the BT modification on some electrical properties of the composites. This is a common technique to study the capacitance and the relaxation behaviors of the nanocomposite films, particularly in those containing nanofillers with ferroelectric or piezoelectric properties, for their use as capacitors or as sensors and actuators (Beier et al., 2010).

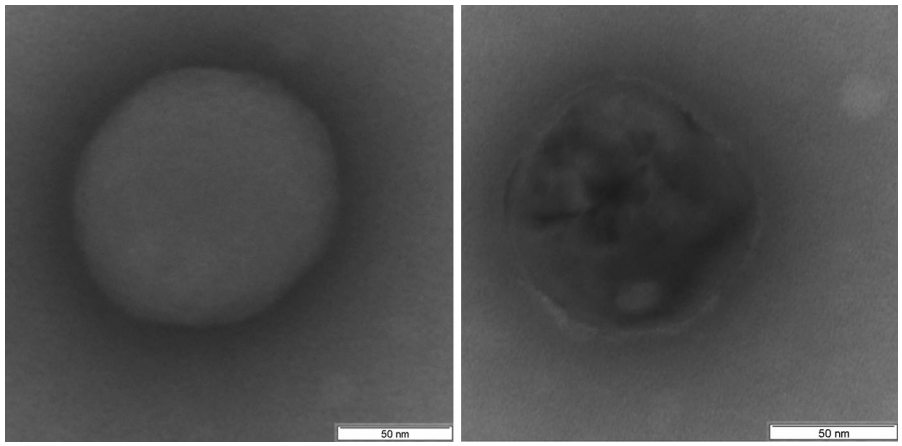

Fig. 4 TEM image of the commercial BT 100-nm (*left*) and the BT-SOA–αCD-modified nanoparticles (*right*)

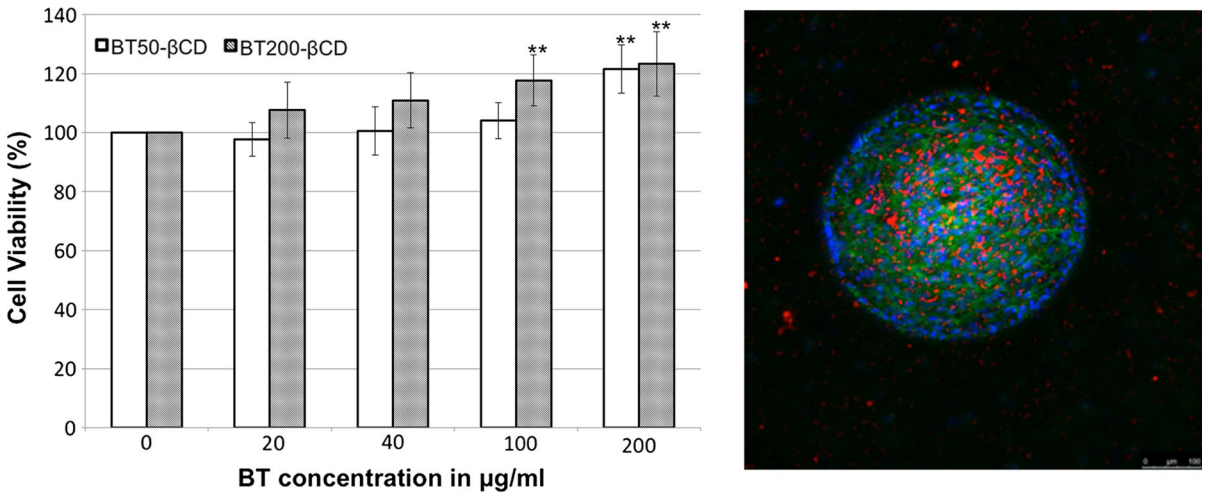

Fig. 5 MTT results for NIH3T3 cells and barium titanate nanoparticles modified with βCD. 50-nm nanoparticles are represented as *blank bars* and 200-nm nanoparticles as patterned *bars* (*left*). *Notes* ** denotes $p < 0.01$ by ANOVA variance test and student's *T* test. The confocal image (*right*) shows the MC3T3-E1 cells after 14 days of culture. Cell nuclei are stained *blue*, actin in *green* and the BT-βCD appears in *red*. (Color figure online)

(a) Interaction of the modified nanoparticles with water-soluble hydrogel matrices

Firstly, in order to test the preparations based on the modified NP with polymers, 15 wt%. solutions of PEG and Pluronic® F127 were prepared and mixed with 10 wt% of commercial and modified nanoparticles. These two polymers have been chosen as they are commonly used as hydrogel substrates and have similar average molecular weights. Therefore, the different interactions with the nanoparticle surface should be mainly derived from their structures and the modifications applied. Based on the coating of the nanoparticles (type of modification) by the polymers, it can be seen in Fig. 6 how the Pluronic® F127 presents a higher interaction than the PEG chains as seen by the weight loss in the 300–400 °C range. The effect is even more noticeable when αCD is attached on the surface, as this CD is known to form stable inclusion complexes with the PEO chains of the F127, in contrast to the βCD that due to its wider cavity is able to enter the chain and form the complex with the inner PPO chain (Larrañeta and Isasi 2012). As a result, the interaction of the particles with the hydrogel matrix

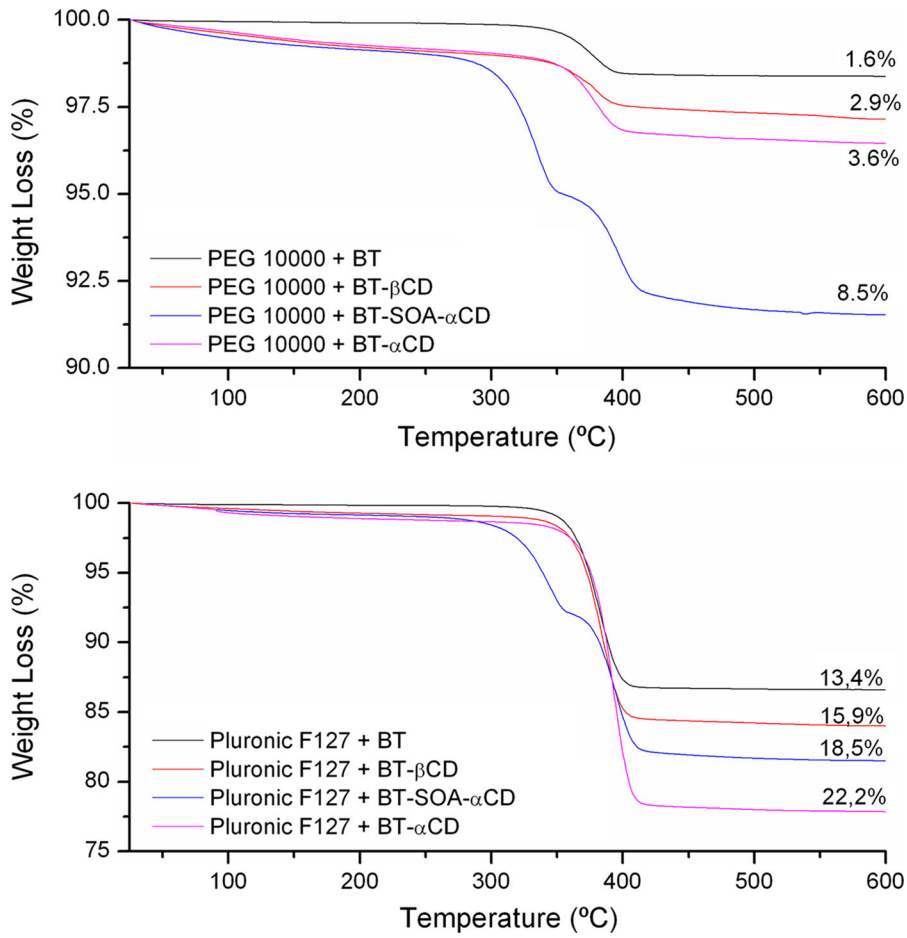

Fig. 6 Coatings of PEG and Pluronic® F127 on the BT nanoparticles before and after the different surface treatments

can be tailored to some extent by the type of CDs attached to the surface.

On a second step, we mixed by cryo-HEBM the modified BT at a 20 wt% with EVA to ensure that the surface modifications applied are kept and to contribute toward achieving a good dispersion in solid-state preparations. The powders were processed into films and characterized by FTIR-ATR and TGA to evaluate the effects the HEBM produces on the nanoparticles and its surface modifications. The main bands of the EVA polymer are in the same positions as the SOA ones (SI Fig. 4), as they mainly consist of -CH_2-groups. However, in the samples where αCD is added, absorbance increases of the –OH band over 3000 cm^{-1} as well as that of the characteristic bands of the CD at 1000, 1078, and 1150 cm^{-1} can be observed. In the samples where only the CDs are attached to the nanoparticles, their characteristics bands in FTIR cannot be clearly seen (SI Fig. 5), being hidden under the EVA ones due to the low amount of oligosaccharide (the CDs represent just 1 % of the filler in this case, which corresponds to the 20 wt% of the composite with EVA, accounting for the small contribution of the small band from the CDs OH groups above 3000 cm^{-1}).

Similar conclusions can be extracted from the TGA analysis (SI Fig. 6). The EVA thermodegradation occurs within the same temperature range as that for the SOA and CD. The degradation process for the thermoplastic takes place in two stages. In the first one, deacylation with the loss of acetic acid and the formation of double bonds occur between 300 and 400 °C, with a maximum rate of degradation at around 370 °C. In the second step, the olefin degradation between 450 and 520 °C takes place (Zattera et al. 2005). Both processes overlap the SOA and CD ones, so only the proportion between the total amount of filler and the polymeric matrix can be deduced from the thermal analysis.

Lastly, as another example of the dispersion from water casting, the nanoparticles were dispersed in a 1 % (w/v) polyethylene oxide aqueous solution. As a result, thin films were obtained as shown in Fig. 7 (right), where the uniform dispersion achieved is comparable to that obtained by solid-state methods (Fig. 7 left).

Impedance spectroscopy tests on films prepared from solid- and water-based precursors

In the frequency response analysis (FRA, impedance spectroscopy), the magnitude being measured is the complex impedance of the samples. The dielectric parameter as a function of frequency is described by the complex impedance in the following form (Tripathi et al. 2012):

$$Z = Z' + iZ'' \tag{1}$$

where Z′ and Z″ are real and imaginary parts of the complex impedance.

$$Z(\omega) = \frac{U(\omega)}{I(\omega)} = \frac{1}{i\omega C(\omega)} \tag{2}$$

$$C(\omega) = \frac{A}{d}\varepsilon(\omega) \tag{3}$$

The capacitance is defined by [3]. A is the area of the dielectric, and d is the thickness of the sample. The polarization phenomenon exerted by the oscillatory electric field applied during the FRA measurement can be modeled in many dielectric materials using a series RC circuit connected in parallel with another capacitor, which has been the model to fit the experimental results (SI Fig. 7). From this equivalent circuit and taking into account the Debye model (Scaife 1998), the following parameters can be deduced (Jonscher 1983):

$$\varepsilon_s = \frac{C_1 + C_2}{\frac{A}{d}} \tag{4}$$

$$\varepsilon_\infty = \frac{C_2}{\frac{A}{d}} \tag{5}$$

$$\tau = R_1 C_1 \tag{6}$$

where C_1 and C_2 are the capacities values associated to the bulk and the interphase, respectively, as C_1 relates to the atomic polarization and C_2 to the fastest dipoles, and from them, the real and imaginary parts of the permittivity as well as the loss factor can be obtained. The values thus calculated have been presented in Table 3.

The two sets of samples present significant differences. In the case of the samples prepared by HEBM, there is no difference in the capacities of the bulk (C_1) in the EVA alone or with the BT nanoparticles, as expected due to the low relative amount of filler. However, in the case of the capacity associated to the interphase, there are differences that can be attributed solely to the distinct modifications of the nanoparticles since they are higher than the reported errors. While EVA and EVA + BT100 (without modification) present the same values, there is a 20 % increase in the case of the nanoparticles that have been modified with oleate and CD. For the samples modified only with CDs, the difference appears for the samples of BT 100 nm with higher changes than those obtained for BT 200 nm samples, regardless the type of CD, probably because a higher polar surface area is facilitating the polarization. In the case of the water-casted PEO, the opposite trend is seen, with a dramatic decrease in the C_1 contribution when the nanoparticles are dispersed in the polymer and a twofold increment of the resistance, while the interphase contribution remains practically the same. In this case, the

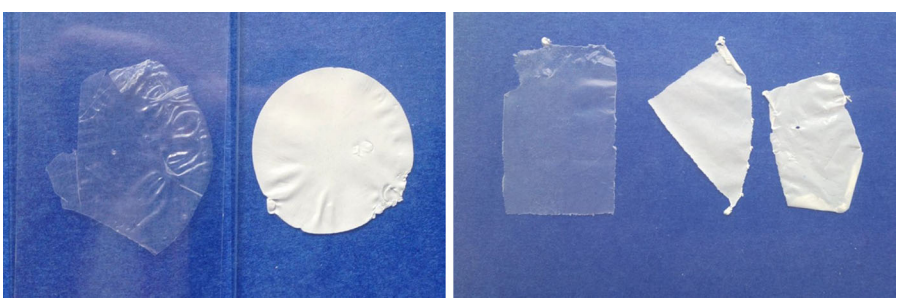

Fig. 7 Films casted from EVA samples prepared by HEBM (*left*) and PEO samples prepared by water suspension (*right*)

Table 3 Capacitance values calculated from impedance spectroscopy on selected samples

Sample	C_1 (nF)	R_1 ($M\Omega$)	τ ($\times 10^2$ s)	C_2 (pF)
EVA	9.3 ± 0.2	9.01 ± 0.09	8.4 ± 0.1	54.1 ± 0.4
EVA + BT100	9.3 ± 0.2	8.92 ± 0.08	8.3 ± 0.1	52.4 ± 0.4
EVA + BT1-SOA-αCD	9.3 ± 0.2	8.92 ± 0.08	8.3 ± 0.1	66.3 ± 0.5
EVA + BT2-SOA-αCD	9.3 ± 0.2	9.00 ± 0.09	8.3 ± 0.1	65.3 ± 0.5
EVA + BT1-αCD	9.3 ± 0.2	8.94 ± 0.08	8.3 ± 0.1	47.0 ± 0.4
EVA + BT2-αCD	9.3 ± 0.2	8.93 ± 0.08	8.3 ± 0.1	58.6 ± 0.5
EVA + BT1-βCD	9.3 ± 0.2	8.92 ± 0.08	8.3 ± 0.1	47.5 ± 0.4
EVA + BT2-βCD	9.3 ± 0.2	8.93 ± 0.08	8.3 ± 0.1	52.4 ± 0.4
PEO	26 ± 2	2.65 ± 0.07	6.8 ± 0.1	113 ± 3
PEO + BT-αCD	11.6 ± 0.4	6.40 ± 0.09	7.4 ± 0.1	119 ± 2

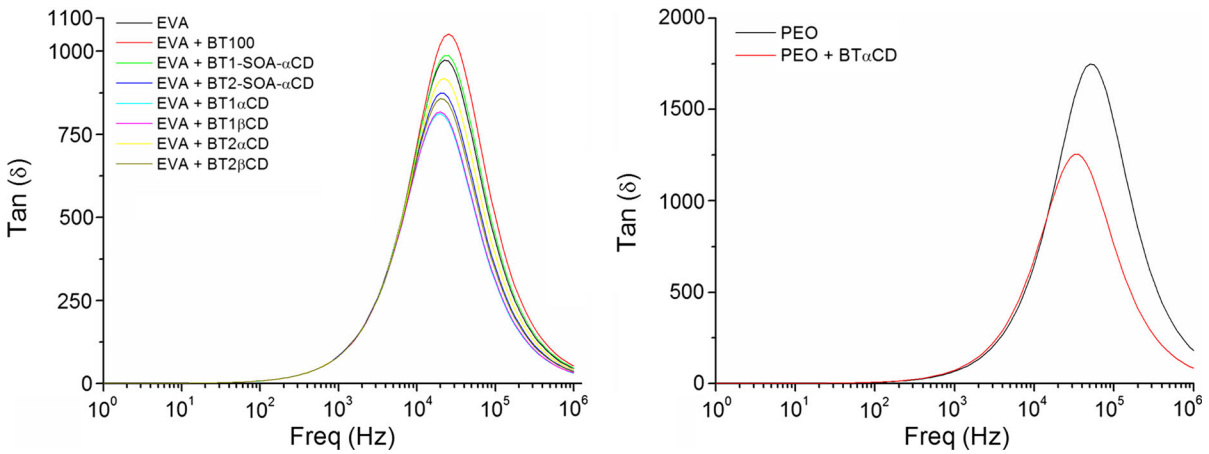

Fig. 8 Impedance spectroscopy loss factor measurements on selected samples with BT: EVA samples (*left*) and PEO samples (*right*)

contribution of the nanoparticles to the PEO system is by far more important than to the EVA one, as they intercalate in the PEO chains and therefore change their structure, crystallization, and rearrangement capacity in the system, similar to what Scrosati et al. mention in their study on PEO nanocomposites (Scrosati et al. 2000).

These different behaviors can be better visualized in the loss tangent plots (Fig. 8) showing a decrease in the height of the peaks as well as a shift to lower frequencies upon addition of the BT. As the relaxation behavior in polymeric nanocomposites depends on the interaction of the filler with the polymeric matrix, it can be concluded that the observed shifts are the result of the modifications made to the BT leading to slightly different interactions between the matrix and the nanoparticles surface. The differences also show that the modifications produced on the nanoparticles are kept despite the high-energy conditions of the solid state milling or the milder ones of the water-casting process.

Conclusions

A novel way of modification of barium titanate nanoparticles has been achieved by the incorporation of cyclodextrins to their surface, for their potential use as nanofillers in nanocomposites. While oleate-modified particles present a certain degree of aggregation in water, due to the hydrophobicity of the chains, once the hydrocarbon tails have been included in the cavity of the αCDs, the stability of the suspension over time is increased. However, when incorporating αCD and βCD directly on the surface, the disaggregation takes place much faster and is maintained through the same period of time, thereby becoming an easier, faster, and cleaner way of modification. Moreover, the addition of

CDs bestows the nanoparticles extra-functionality due to the wide array of host–guest interactions that can be established within the CD cavity, as tested by analyzing the fluorescence of RhB that is included in the macrocycles, attached to the nanospheres' surfaces. This opens a whole range of potential uses for these nanoparticles by their combination with and molecules that could be released in a controlled way, such as drugs, particularly in the case of biocomposites. The cytotoxicity of the modified nanoparticles with fibroblasts and pre-osteoblasts cell lines has been assessed with excellent results in a wide range of concentrations up to 200μg/ml. The surface modification with CDs allows the nanoparticles to be suspended in aqueous solutions of different polymers (PEO, PEG, and Pluronic F-127) and the further casting of films, with very good results in terms of homogeneity. The same conclusion is reached with the films obtained from the solid mixtures produced by HEBM using a thermoplastic polymer (EVA). In the latter case, the changes in the dielectric behavior as studied by impedance spectroscopy suggest that even little modifications in the surface of the nanoparticles involve a different kind of interaction with the polymeric matrix. The modified nanoparticles are thus suitable for easy preparation either of water-based nanocomposites as hydrogels or nanocomposites of thermoplastic matrices.

Acknowledgments Financial supports from Asociación de Amigos of the University of Navarra for the PhD scholarship of R. Serra-Gómez as well as the Ministerio de Economia y Competitividad in the form of funding under projects. MAT2010-16815 and MAT2014-59116, are greatfully acknowledged. The authors would also like to thank Prof. I. Navarro (U. de Navarra) for his assistance with Z-potential measurements, and S. Ehrig and J. Dunlop, PhD. from the MPI of Colloids and Interfaces (Potsdam, Germany) for their help with the confocal imaging experiments.

References

Baxter FR, Turner IG, Bowen CR et al (2009) An in vitro study of electrically active hydroxyapatite-barium titanate ceramics using Saos-2 cells. J Mater Sci Mater Med 20:1697–1708. doi:10.1007/s10856-009-3734-0

Beier CW, Cuevas MA, Brutchey RL (2010) Effect of surface modification on the dielectric properties of BaTiO3 nanocrystals. Langmuir 26:5067–5071. doi:10.1021/la9035419

Blanco-Lopez MC, Rand B, Riley FL (1997) The properties of aqueous phase suspensions of barium titanate. J Eur Ceram Soc 17:281–287. doi:10.1016/S0955-2219(96)00116-1

Chang S-J, Liao W-S, Ciou C-J et al (2009) An efficient approach to derive hydroxyl groups on the surface of barium titanate nanoparticles to improve its chemical modification ability. J Colloid Interface Sci 329:300–305. doi:10.1016/j.jcis.2008.10.011

Chaudhary YS, Bhatta UM, Khushalani D (2011) Octyl-β-D-glucopyranoside mediated synthesis of nanocrystalline BaTiO3 using a single-source precursor. J Mater Res 23:842–848. doi:10.1557/JMR.2008.0102

Choudhury A (2012) Preparation, characterization and dielectric properties of polyetherimide nanocomposites containing surface-functionalized BaTiO3 nanoparticles. Polym Int 61:696–702. doi:10.1002/pi.4181

Ciofani G, Danti S, Moscato S et al (2010) Preparation of stable dispersion of barium titanate nanoparticles: potential applications in biomedicine. Colloids Surf B Biointerfaces 76:535–543. doi:10.1016/j.colsurfb.2009.12.015

Čulić-Viskota J, Dempsey WP, Fraser SE, Pantazis P (2012) Surface functionalization of barium titanate SHG nanoprobes for in vivo imaging in zebrafish. Nat Protoc 7:1618–1633. doi:10.1038/nprot.2012.087

Dempsey C, Lee I, Cowan KR, Suh J (2013) Coating barium titanate nanoparticles with polyethylenimine improves cellular uptake and allows for coupled imaging and gene delivery. Colloids Surf B Biointerfaces 112:108–112. doi:10.1016/j.colsurfb.2013.07.045

FarrokhTakin E, Ciofani G, Gemmi M et al (2012) Synthesis and characterization of new barium titanate core–gold shell nanoparticles. Colloids Surfaces A Physicochem Eng Asp 415:247–254. doi:10.1016/j.colsurfa.2012.09.021

Feng J, Yuan H, Zhang X (1997) Promotion of osteogenesis by a piezoelectric biological ceramic. Biomaterials 18:1531–1534

Gaharwar AK, Schexnailder PJ, Schmidt G (2011) Nanocomposite polymer biomaterials for tissue repair of bone and cartilage: a material science perspective. Nanobiomaterials Handb. doi:10.1201/b10970

Gaharwar AK, Mihaila SM, Swami A et al (2013) Bioactive silicate nanoplatelets for osteogenic differentiation of human mesenchymal stem cells. Adv Mater 25:3329–3336. doi:10.1002/adma.201300584

Gao J, Shi H, Dong H et al (2015) Factors influencing formation of highly dispersed BaTiO3 nanospheres with uniform sizes in static hydrothermal synthesis. J Nanoparticle Res 17:286. doi:10.1007/s11051-015-3090-6

Gonzalez-Gaitano G, Crespo A, Tardajos G (2000) Thermodynamic investigation (volume and compressibility) of the systems -cyclodextrin + *n*-alkyltrimethylammonium bromides + water. J Phys Chem B 104:1869–1879

González-Gaitano G, Rodríguez P, Isasi JR et al (2002) The aggregation of cyclodextrins as studied by photon correlation spectroscopy. J Incl Phenom 44:101–105. doi:10.1023/A:1023065823358

Hiroki A, Laverne JA (2005) Decomposition of hydrogen peroxide at water-ceramic oxide interfaces. J Phys Chem B 109:3364–3370. doi:10.1021/jp046405d

Hsieh C-L, Grange R, Pu Y, Psaltis D (2010) Bioconjugation of barium titanate nanocrystals with immunoglobulin G antibody for second harmonic radiation imaging probes. Biomaterials 31:2272–2277. doi:10.1016/j.biomaterials.2009.11.096

Huang T, Xu HG, Jiao KX et al (2007) A novel hydrogel with high mechanical strength: a macromolecular microsphere composite hydrogel. Adv Mater 19:1622–1626. doi:10.1002/adma.200602533

Jean J-H, Wang H-R (2005) Dispersion of aqueous barium titanate suspensions with ammonium salt of poly(-methacrylic acid). J Am Ceram Soc 81:1589–1599. doi:10.1111/j.1151-2916.1998.tb02521.x

Jeong CK, Kim I, Park K-I et al (2013) Virus-directed design of a flexible BaTiO3 nanogenerator. ACS Nano 7:11016–11025

Jonscher AK (1983) Dielectric relaxation in solids. Chelsea Dielectric Press, London

Kim P, Jones SC, Hotchkiss PJ et al (2007) Phosphonic acid-modified barium titanate polymer nanocomposites with high permittivity and dielectric strength. Adv Mater 19:1001–1005. doi:10.1002/adma.200602422

Knauert ST, Douglas JF, Starr FWA (2007) The effect of nanoparticle shape on polymer-nanocomposite rheology and tensile strength. J Polym Sci, Part B 45:1882–1897. doi:10.1002/polb

Larrañeta E, Isasi J (2012) Self-assembled supramolecular gels of reverse poloxamers and cyclodextrins. Langmuir 28(34):12457–12462

Li L, Sun X, Yang Y et al (2006) Synthesis of anatase TiO2 nanoparticles with beta-cyclodextrin as a supramolecular shell. Chem Asian J 1:664–668. doi:10.1002/asia.200600103

Lingley Z, Mahalingam K, Lu S et al (2013) Nanocrystal-semiconductor interface: atomic-resolution cross-sectional transmission electron microscope study of lead sulfide nanocrystal quantum dots on crystalline silicon. Nano Res 7:219–227. doi:10.1007/s12274-013-0389-4

Mamana N, Pellegri N (2015) Functional BaTiO3 nanostructures immobilized onto si-based substrates using sol–gel and reverse micelle techniques. J Nanoparticle Res 17:115. doi:10.1007/s11051-015-2930-8

Olmos D, Martínez F, González-Gaitano G, González-Benito J (2011) Effect of the presence of silica nanoparticles in the coefficient of thermal expansion of LDPE. Eur Polym J 47:1495–1502. doi:10.1016/j.eurpolymj.2011.06.003

Ozel F, Kockar H, Beyaz S et al (2013) Superparamagnetic iron oxide nanoparticles: effect of iron oleate precursors obtained with a simple way. J Mater Sci 24:3073–3080. doi:10.1007/s10854-013-1213-3

Paik U, Hackley VA, Choi S-C, Jung Y-G (1998) The effect of electrostatic repulsive forces on the stability of BaTiO3 particles suspended in non-aqueous media. Colloids Surfaces A Physicochem Eng Asp 135:77–88. doi:10.1016/S0927-7757(97)00234-3

Paik U, Yeo J-G, Lee M-H et al (2002) Dissolution and reprecipitation of barium at the particulate BaTiO3–aqueous solution interface. Mater Res Bull 37:1623–1631. doi:10.1016/S0025-5408(02)00820-6

Park S-E, Shrout TR (1997) Ultrahigh strain and piezoelectric behavior in relaxor based ferroelectric single crystals. J Appl Phys 82:1804. doi:10.1063/1.365983

Ring KM, Kavanagh KL (2003) Substrate effects on the ferroelectric properties of fine-grained BaTiO[sub 3] films. J Appl Phys 94:5982. doi:10.1063/1.1615304

Saenger W, Jacob J, Gessler K et al (1998) Structures of the common cyclodextrins and their larger analogues-beyond the doughnut. Chem Rev 98:1787–1802

Sakai T, Hoshiai S, Nakamachi E (2006) Biochemical compatibility of PZT piezoelectric ceramics covered with titanium thin film. J Optoelectron Adv Mater 8:1435–1437

Scaife BKP (1998) Principles of dielectrics. Oxford University Press, New York

Schexnailder P, Schmidt G (2008) Nanocomposite polymer hydrogels. Colloid Polym Sci 287:1–11. doi:10.1007/s00396-008-1949-0

Scrosati B, Croce F, Persi L (2000) Impedance spectroscopy study of PEO-based nanocomposite polymer electrolytes. J Electrochem Soc 147:1718. doi:10.1149/1.1393423

Serra-Gómez R, Tardajos G, González-Benito J, González-Gaitano G (2012a) Rhodamine solid complexes as fluorescence probes to monitor the dispersion of cyclodextrins in polymeric nanocomposites. Dye Pigment 94:427–436. doi:10.1016/j.dyepig.2012.02.009

Serra-Gómez R, Gonzalez-Gaitano G, González-Benito J (2012b) Composites based on EVA and barium titanate submicrometric particles: preparation by high-energy ball milling and characterization. Polym Compos 33:1549–1556. doi:10.1002/pc

Shi J, Votruba AR, Farokhzad OC, Langer R (2010) Nanotechnology in drug delivery and tissue engineering: from discovery to applications. Nano Lett 10:3223–3230. doi:10.1021/nl102184c

Shiraishi Y, Tsujihata R, Sawai H et al (2015) Effect of particle size on electro-optic properties of liquid crystal devices doped with γ-cyclodextrin stabilized barium titanate nanoparticles. Mol Cryst Liq Cryst 611:100–108. doi:10.1080/15421406.2015.1028000

Städe LW, Nielsen TT, Duroux L et al (2015) Nonfouling tunable βCD dextran polymer films for protein applications. ACS Appl Mater Interfaces 7:4160–4168. doi:10.1021/am508350r

Sun X, Zheng C, Zhang F et al (2008) Synthesis of BaTiO3 nanocrystals with beta-cyclodextrin as a supramolecular shell. Wuji Huaxue Xuebao 24:93–97

Tripathi SK, Gupta A, Kumari M (2012) Dielectric and Modulus spectra studies on electrical conductivity and dielectric behaviour of PVdF–HFP–PMMA–NaI polymer blend electrolyte. Bull Mater Sci 35:969–975. doi:10.1007/s12034-012-0387-2

Tsuchiya K, Akagawa Y, Uetsuji Y, Nakamachi E (2011) Design of biocompatible high-piezoelectric BaTiO3 with additives. In: Juodkazis S, Gu M (eds) Smart nano-micro materials and devices. International society for optics and photonics, p 82042A

Wang H, Bongio M, Farbod K et al (2013) Development of injectable organic/inorganic colloidal composite gels made of self-assembling gelatin nanospheres and calcium

phosphate nanocrystals. Acta Biomater. doi:10.1016/j.actbio.2013.08.036

Yu C-R, Wu D-M, Liu Y et al (2011) Electrical and dielectric properties of polypropylene nanocomposites based on carbon nanotubes and barium titanate nanoparticles. Compos Sci Technol 71:1706–1712. doi:10.1016/j.compscitech.2011.07.022

Zattera AJ, Bianchi O, Oliveira RVB et al (2005) Characterization of EVA residues from the shoe industry and post-consumer urban-waste polyethylenes. Cell Polym 24:139–158

LANGMUIR

Article

pubs.acs.org/Langmuir

Structure and Rheology of Poloxamine T1107 and Its Nanocomposite Hydrogels with Cyclodextrin-Modified Barium Titanate Nanoparticles

Rafael Serra-Gómez,[†] Cécile A. Dreiss,[*,§] Javier González-Benito,[‡] and Gustavo González-Gaitano[*,†]

[†]Departamento de Química, Universidad de Navarra, 31080 Pamplona, Spain

[‡]Department of Materials Science and Engineering, IQMAAB, Universidad Carlos III de Madrid, 28911 Leganés, Spain

[§]Institute of Pharmaceutical Science, King's College London, Franklin-Wilkins Building, 150 Stamford Street, London SE1 9NH, United Kingdom

Supporting Information

ABSTRACT: We report the preparation of a nanocomposite hydrogel based on a poloxamine gel matrix (Tetronic T1107) and cyclodextrin (CD)-modified barium titanate (BT) nanoparticles. The micellization and sol−gel behavior of pH-responsive block copolymer T1107 were fully characterized by small-angle neutron scattering (SANS), dynamic light scattering (DLS), and Fourier transform infrared attenuated total reflectance (FTIR-ATR) spectroscopy as a function of concentration, pH and temperature. SANS results reveal that spherical micelles in the low concentration regime present a dehydrated core and highly hydrated shell, with a small aggregation number and size, highly dependent on the degree of protonation of the central amine spacer. At high concentration, T1107 undergoes a sol−gel transition, which is inhibited at acidic pH. Nanocomposites were prepared by incorporating CD-modified BT of two different sizes (50 and 200 nm) in concentrated polymer solutions. Rheological measurements show a broadening of the gel region, as well as an improvement of the mechanical properties, as assessed by the shear elastic modulus, G' (up to 200% increase). Initial cytocompatibility studies of the nanocomposites show that the materials are nontoxic with viabilities over 70% for NIH3T3 fibroblast cell lines. Overall, the combination of Tetronics and modified $BaTiO_3$ provides easily customizable systems with promising applications as soft piezoelectric materials.

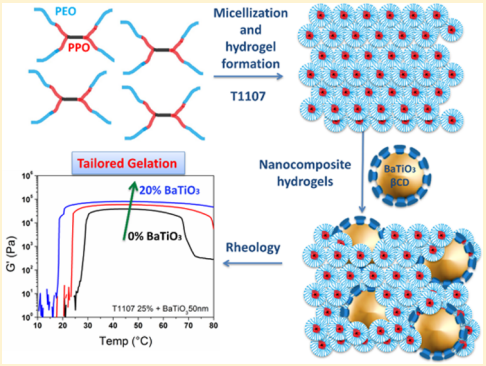

INTRODUCTION

Nanocomposite hydrogels are emerging as an attractive concept to craft materials with tailored properties, such as mechanical, optical, electronic, as well as promoting a specific biological response (self-healing materials, mechano-actuators, triggered delivery, etc.).[1] The combination of a polymer gel matrix (which affords mechanical support, phase modulation, and a hydrated environment) with nanoparticles (bringing specific functionalities, such as optical, magnetic, piezoelectric, antimicrobial, etc.) is the basis of fascinating properties, resulting from a synergistic interplay between matrix and filler.[1]

A promising type of matrix to produce nanocomposite hydrogels are poloxamines, also known by the commercial name of Tetronic (BASF). They are amphiphilic block copolymers, presenting an original X shape, where each of the four arms is made of a poly(propylene oxide) (PPO) and a poly(ethylene oxide) (PEO) block connected by a central ethylene diamine spacer. The number of PO and EO units that form the arms can be varied, offering a wide range of Mw and HLB values, and hence a rich phase behavior and custom-made properties, both in terms of thermal and pH response.[2−4] PEO−PPO-based polymeric micelles are now emerging as promising formulation candidates in the biomedical field, being available in large quantities in a large array of architectures, at low-cost, and also showing biological inhibitory activity of drug efflux pumps.[5,6] The more well-known linear counterparts of Tetronics, Pluronics, are currently undergoing clinical trials with the cancer drug doxorubicin,[7] and the recent demonstration of the ability of Tetronics to also inhibit ATP-binding cassette transporters in cancer cell lines, responsible for multidrug resistance,[5] in addition to their pH-responsiveness, has recently brought them into the spotlight as serious contenders in the biomedical field.[6] Indeed, they have been proposed as water-soluble copolymers for injectable formulations,[8] nanocarriers for drug and gene delivery,[9,10] and in tissue engineering for bone regeneration.[11]

The introduction of different types of nanoparticles into hydrogels is a successful way to not only improve existing characteristics (such as gel elasticity and toughness), but also add extra functionalities to the hydrogels,[12−14] resulting in new,

Received: April 22, 2016
Revised: May 30, 2016
Published: June 1, 2016

ACS Publications © 2016 American Chemical Society

DOI: 10.1021/acs.langmuir.6b01544
Langmuir 2016, 32, 6398−6408

functional materials. Extensive research is being carried out in this field covering a wide range of nanofillers, which, used in relatively low amounts, can yield remarkable changes in the final properties. Some examples are clays as natural and synthetic laponites,[15] ceramics as hydroxyapatite (HA) or beta-tricalcium phosphate (β-TCP) for bone regeneration[16,17] and delivery of growth factors.[18] Metallic nanoparticles such as silver and gold constitute other approaches, chosen for their antimicrobial properties,[19] as well as multiwall carbon nanotubes (MWCNT) and graphene oxide (GO), which are also exploited to create electrically active hydrogels mimicking cardiac tissue with mechano-actuation,[20] and polymer colloids to develop hydrogels for adhesives and surgical sealants.[21]

A substantial amount of work focuses on inorganic nanoparticles and ceramics as bioactive components in bioengineering,[22,23] such as bioactive silica nanoparticles for improved osteogenesis[24,25] or TiO_2 for antibacterial biodegradable hydrogels.[26] In this work, we focus on barium titanate ($BaTiO_3$, BT) nanoparticles, a perovskite-type ferroelectric ceramic that possesses a high dielectric constant with piezoelectric properties (in its tetragonal, orthorhombic and rhombohedral crystalline phases). BT has been replaced in some, mainly electric, applications by multiceramic materials, such as lead zirconate titanates, or PZTs. However, PZTs are not appropriate for biomedical applications due to the high toxicity of the lead component, and BT has been suggested as a good piezoelectric alternative due its better biocompatibility.[27−29] Some examples are as second harmonic generators for imaging applications[30,31] and in drug and gene delivery as nanocarriers and vectors.[27,32] In bone regeneration in particular, BT presents potential as a ceramic filler; its piezoelectricity and interaction with the dipoles formed on the collagen fibers of the inner bone have been shown to promote bone regeneration, as they are able to generate small electrical impulses under minimal mechanic stress, enhancing the cellular and tissue stimulation for the healing process.[33−35]

The main problem to overcome is that ceramic nanoparticles usually present poor processability and high aggregation due to their high area-to-volume ratio.[36,37] This problem may be overcome by surface modification of the nanoparticles. Based on our substantial work on cyclodextrins,[4,38] we explore here the effect of surface modification of BT with cyclodextrins (CDs)[39] prior to their introduction in the hydrogel matrix. Once the nanocomposite hydrogel has been prepared, the physical and chemical interaction between the matrix and the nanofiller is a determining factor for modulating the properties, which in our case are the changes in the sol−gel transition temperature and the improvement of the mechanical response of the hydrogels.

While it is clear that the introduction of nanoparticles inside a gel matrix may improve the mechanical properties and generally the functionality of the material, there are still few fundamental studies aiming at elucidating structural changes induced by the presence of the nanoparticles, in particular using techniques such as small-angle neutron scattering (SANS). A few exceptions are the studies by Namban and Philip's on the influence of Fe_3O_4 nanoparticles in a matrix of Pluronics,[40] the introduction of clays such as laponite nanoparticles into Pluronic gels,[41] and other ABA-type triblock copolymer hydrogels.[42] Annaka et al.[43] reported SANS studies where the introduction of hydrophilized silica nanoparticles (to match the refractive index of the natural lens) impacted the temperature and concentration regime of gel formation; SANS measurements showed that the silica particles did not affect micellar size but decreased their effective volume fraction. Tamborini et al.[44] also used SANS to study the nanocomposite structure of Pluronic crystals and silica nanoparticles as a function of the temperature rate used during preparation, where the volume fraction of the silica nanoparticles is kept low, and their size is similar to the micelles.

Within this framework, the objective of this work was to develop soft nanocomposites, using naturally gelling, low-cost poloxamines as a gel matrix, combined with piezoelectric $BaTiO_3$ nanoparticles, chemically modified with cyclodextrins[39] for improved compatibility. The $BatiO_3$ particles are relatively large compared to the micelles and introduced up to high volume fraction (20%). In the first part of this work, we perform a thorough characterization of the structural changes that lead to T1107 micellization and sol−gel transition, as a function of concentration, pH and temperature, using a combination of techniques (SANS, dynamic light scattering (DLS) and Fourier transform infrared attenuated total reflectance (FTIR-ATR)). Following this, cyclodextrin-modified BT nanoparticles of two different sizes are introduced in the polymer matrix to produce nanocomposite gels, which are characterized both rheologically and spectroscopically, with particular focus on the structural and mechanical changes induced by the addition of the nanofiller. Finally, cytotoxicity and cytocompatibility assays of the nanocomposites at different concentrations, in solution as well as in the gel phase, are performed, as an initial evaluation of their suitability as biomaterials.

MATERIALS AND METHODS

Materials. Tetronic 1107 (T1107) was a gift from BASF, with a reported composition per arm of 60 EO and 20 PO, HLB 18−23, and average molecular weight 15 000 g·mol^{-1}. Inorganic nanoparticles of barium titanate (BT, $BaTiO_3$), with an average diameter of 200 nm were supplied by Nanostructured and Amorphous Materials, Inc. (tetragonal crystalline structure, 99.9% purity, ρ = 6.02 g·cm^{-3}), while nanoparticles of 50 nm in diameter were supplied by Sigma-Aldrich (cubic crystalline structure, 99.9% purity, ρ = 6.08 g·cm^{-3}).

Preparation of $BaTiO_3$ Nanoparticles. BT nanoparticles present strong aggregation that leads to rapid precipitation in water. Surface modification of the NPs with β-cyclodextrin (CD) was performed to overcome this problem, according to the two-step procedure described in a previous work,[39] consisting in the generation of hydroxyl groups on the surface by reaction with H_2O_2, followed by mixing with a 10 mM β-CD solution under vigorous stirring. The resulting nanoparticles are centrifuged and washed three times to remove reagents in excess and freeze-dried for storage.

Small-Angle Neutron Scattering (SANS). Small-angle neutron scattering (SANS) experiments were carried out on LOQ instrument at ISIS spallation neutron source (ISIS, Rutherford-Appleton Laboratory, STFC, Didcot, Oxford). LOQ uses incident wavelengths from 2.2 to 10.0 Å, sorted by time-of-flight, with a fixed sample−detector distance of 4.1 m, which provides a range of scattering vectors (q) from 0.009 to 0.29 Å^{-1}. The samples were prepared in D_2O (Aldrich, > 99.9% in D) and placed in clean disc-shaped quartz cells (Hellma) of either 1 or 2 mm path length, controlling the temperature from 20 to 50 °C with an external thermostat. In the case of experiments in acidic solutions, the necessary volume of concentrated HCl was added to the samples to reach the desired pH. All scattering data were first normalized for sample transmission and then background-corrected using a quartz cell filled with D_2O to compensate for the inherent instrumental background, and finally corrected for the linearity and efficiency of the detector response using instrument-specific software package. The data were then converted to differential scattering cross sections expressed in absolute units of cm^{-1}

DOI: 10.1021/acs.langmuir.6b01544
Langmuir 2016, 32, 6398−6408

using the standard procedures at ISIS. Some additional samples (Figure 6) were measured on D22 at the Institut Laue-Langevin (ILL), The wavelength λ was set at 6 Å, the peak flux of the cold source. The sample-to-detector distance was 4 m with a collimation at 5.6 m and a detector offset of 400 mm to maximize the available q-range using rectangular cells of 1 mm of path length. All samples for SANS analysis were made in D_2O to ensure sufficient contrast between the polymer and the solvent.

SANS curves were fitted using the SasView 3.1.0 software and a brief explanation of the models can be found in the Supporting Information (SI).[45] Scattering curves from T1107 in its unimer form were fitted with a four-arm star-shape polymer model,[46] while micelles were fitted to a core−shell sphere (CSS) model combined with a hard-sphere structure factor. When letting the scattering length density (sld) of the micellar core float, this value converged consistently to values similar to that of pure PO ($\rho_{PO} = 3.44 \times 10^{-7}$ Å^{-2}), therefore this parameter was fixed in the fits, reflecting the fact that the micellar core is largely dehydrated, as observed with other poloxamines under dilute conditions.[4,47] Instead, the shell is extensively hydrated, and the level of hydration can be estimated from the fitted value of the sld of the PEO shell, ρ_{shell}. The volume fraction (occupied volume divided by the total volume) of solvent in the corona, x_{solv}, is related to the sld of the shell, PEO block, and D_2O by

$$x_{solv} = \frac{\rho_{shell} - \rho_{EO}}{\rho_{D_2O} - \rho_{EO}} \quad (1)$$

The number of water molecules, n_{solv}, in the shell is obtained from

$$n_{solv} = x_{solv}\frac{v_{shell}}{v_{D_2O}} \quad (2)$$

where v_{D_2O} is the volume of a molecule of solvent. The number of water molecules per EO group, n_{solv}/EO, can then be obtained from eq 2 and the value of the aggregation number, N_{agg}, is obtained from the hydration of the shell and the structural parameters of the core−shell model. Provided that the amount of water inside the core is negligible, the volume of the micelle is

$$v_m = N_{agg}v_s + x_{solv}v_{shell} \quad (3)$$

where v_s is the volume of a surfactant molecule. N_{agg} can be extracted by introducing into the equation the volume fraction of solvent in the shell, x_{solv}, deduced from eq 1.

SANS data for the nanocomposites were analyzed by a combination of the CSS and a generic power law model (CSS+PL), as well as the combination of different types of paracrystals (SC, BCC, and FCC) and the PL model. In all the calculations, the polydispersity of the micelles was taken into account by assuming a Gaussian size distribution either of core radii (dilute regime) or overall micellar radii (gel region).

Dynamic Light Scattering (DLS). Size distributions of the poloxamine in water were obtained with a photon correlation spectrometer Malvern Zetasizer Nano, with a laser wavelength of 633 nm. The samples were filtered prior to the measurements by 0.22 μm Millex syringe PVDF filters onto semimicro glass cells, and the temperature of the samples was controlled with 0.1 °C accuracy by the built-in Peltier in the cell compartment. The viscosity and refractive index of the solvent at different temperatures were taken into account to obtain the particle size distribution from the analysis of the autocorrelation function, which was performed with the Zetasizer software in the high resolution mode to better distinguish overlapping distributions.

Infrared Spectroscopy. The gelation processes were studied by attenuated total reflectance infrared spectroscopy (FTIR-ATR), using a Nicolette Avatar 360 spectrometer, equipped with a Golden-Gate temperature controlled ATR. The spectra were collected on 0.1 mL samples placed directly on the diamond, at 2 cm^{-1} resolution and 32 scans per spectrum, in the temperature range from 20 to 60 °C.

Rheology. Small-amplitude shear oscillatory experiments were performed on a dynamic strain-controlled rheometer ARES (TA Instruments) using plate−plate geometry (25 mm), with a temperature-controlling Peltier unit and a solvent trap. All solutions were left to rest at least 1 day at room temperature after preparation before conducting the rheological measurements. After loading, a thin layer of low viscosity paraffin oil was added to the geometry edge in order to prevent evaporation. Samples were allowed to rest for a few minutes before the start of the experiments to ensure dissipation of any preshearing due to manipulation and loading. Temperature sweeps at constant angular frequency of 6.28 rad·s^{-1} and 1% strain amplitude, within the limit of the linear viscoelastic range as measured by strain amplitude experiments, were conducted at a heating rate of 2 °C/min covering the temperature range from 20 to 80 °C. The gel points are calculated by monitoring the elastic modulus, G', along the temperature sweeps and identifying the gel point as the onset of the region in which G' reaches values corresponding to a solid-like behavior.

Preparation of the Nanocomposite Gels. Concentrated solutions of T1107 and NPs were prepared by weighing the required amounts of Tetronic, modified $BaTiO_3$ nanoparticles (50 and 200 nm in diameter) and water, D_2O or PBS, followed by mixing. To ensure appropriate dispersion of the NPs in the gel matrix, cycles alternating magnetic stirring, vortex mixing and cooling to 4 °C were performed, to facilitate the dissolution of the polymer, while keeping the viscosity low.

Cytotoxicity Studies. The cytocompatibility of the nanocomposite gels of T1107 and BT was tested on the fibroblast cell line NIH3T3 by means of the tetrazolium assay (MTT), in which the viability of the cells is assessed by the loss of viable cells upon treatment with the compounds of interest. The cells were incubated at 37 °C and 5% CO_2 in Dulbecco's modified eagle medium from Life's Technologies, supplemented with 10% fetal bovine serum and 0.1% of penicillin/streptomycin. T1107 solutions were prepared in PBS and filtered through 0.22 μm for sterilization. Cells were seeded into 96-well plates at a concentration of 5×10^4 cells·mL^{-1} and 24 h later the nanocomposite was introduced into the wells. MTT tests were conducted on day 3 by the addition of MTT 5 mg/mL and incubation for 4 h. The formazan absorbance at 540 nm was measured with a Thermo Scientific Multiscan EX microplate reader. DMSO was used as a positive control, and the appropriate negative controls performed by incubating the cells in the absence of the nanocomposite.

RESULTS AND DISCUSSION

Self-Aggregation of T1107 and Phase Behavior: The Dilute Regime. The phase diagram of T1107 in water at its natural pH (ca. 7.8) is shown in Figure 1. At 20% and 40 °C,

	T (°C)												
T1107	20	25	30	35	40	45	50	55	60	65	70	75	80
5%	○	○	○	○	○	○	○	○	○	○	○	○	○
10%	○	○	○	○	○	○	○	○	○	○	○	○	○
15%	○	○	○	○	○	○	○	○	○	○	○	○	○
20%	□	□	□	□	●	●	●	□	□	□	○	○	○
25%	□	□	□	●	●	●	●	●	●	●	●	●	●
30%	□	●	●	●	●	●	●	●	●	●	●	●	●

Figure 1. Phase behavior of T1107 in water. ○ Solution; □ viscous solution; ● gel.

the solution becomes gel-like up to 50 °C, with a wider gel region at higher concentrations (spanning 30 to 80 °C at 30%). Gel formation is impeded at acidic pH, due to the protonation of the diamino middle block. For example, at pH 6, no gel is detected from 25 to 80 °C for a 20% mixture. A similar behavior has been observed with poloxamine T1307, which has a larger molecular weight (18 000 g·mol^{-1}) and higher HLB (>24); however, with this larger poloxamine, at 20% and pH =

DOI: 10.1021/acs.langmuir.6b01544
Langmuir 2016, 32, 6398−6408

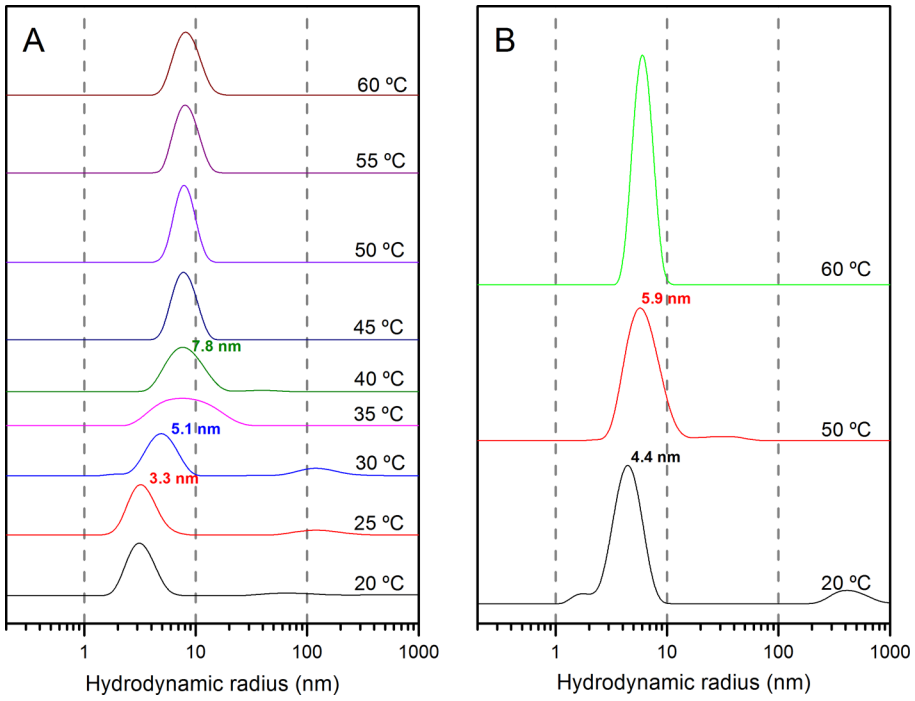

Figure 2. Intensity size distributions as a function of temperature obtained by DLS for a 1% aqueous solution of T1107 at (A) pH 7.8 and (B) pH 2.8 in H_2O.

6, a gel phase still exists between 40 and 50 °C.[4] More acidic pH totally hinders gel formation. Replacement of H_2O by D_2O slightly shifts the gel phase boundary to higher concentration and temperature (SI Table 1).

Figure 2A shows the intensity size distribution of 1% T1107 at different temperatures obtained from DLS measurements. Unimers are detected at 20 °C, with a hydrodynamic radius, R_h, of 3.2 nm. Between 30 and 35 °C, the distribution broadens and shifts toward higher sizes, reflecting the micellization process. Micelles are fully formed at 40 °C, with a R_h nearly constant above that point (7.8 nm). The relative size of the micelles compared to that of the unimers, R_{mic}/R_{unim}, is 2.4, which is intermediate between the larger T1307 (1.6, with N_{EO} = 72, N_{PO} = 23)[2] and the more hydrophobic T904 (2.8, N_{EO} = 15, N_{PO} = 17),[3] suggesting that the micelles of T1107 must contain a relatively low number of unimers, as found for T1307[4] and also reported with Pluronic of high HLB, such as P85.[48] At pH 2.8 (Figure 2B), the formation of micelles is hindered, resulting in a smaller micellar size of 6.9 nm at 50 °C.

More detailed structural information on the unimers and micelles can be obtained from SANS; combining these data with DLS enables one to unambiguously identify concentration regimes where unimers, micelles, or both, are present, thus directing the choice of a suitable fitting model. Figure 3A shows the scattering curves for a 2% T1107 solution in D_2O. Below 30 °C, the poloxamine is in the form of unimers (as established by DLS), whereas at 40 and 50 °C micelles are the dominant species, and the overall scattering increases accordingly. A four-arm star-shape polymer model was shown to successfully describe the unimers.[46] With this model, the radius of gyration, R_g, at 20 °C decreases with concentration, from 3.6 nm at 0.5%, to 2.9 nm at 2% and 1.9 nm at 5%; the first value is close to 3.2 nm obtained by DLS for R_h at 1%.

At 40 and 50 °C, micelles dominate the scattering, and hence a core−shell sphere model (CSS) combined with a structure factor for hard spheres (HS) were used. The fitted and calculated parameters in the dilute regime (2%) are collected in Table 1 for two values of the pH (data at 0.5% and 5% are provided in SI Table 2).

Micellar size is fairly insensitive to temperature or concentration up to 5% (Table 1), with a total radius around 8 nm (in agreement with DLS, Figure 2A). The sld of the shell, ρ_{shell}, takes values close to that of D_2O (6.36×10^{-6} Å^{-2}), indicating an extensive solvation of the hydrophilic corona, reflected in the high number of solvent molecules per EO. The aggregation number, N_{agg}, does not vary much with temperature or concentration, while the hydration of the shell (n_{solv}/EO) decreases slightly with concentration, suggesting a more compact micellar structure.

In contrast to temperature and concentration, pH has a strong impact on micellar structure (Figure 3B, Table 1). At pH 2.2, the low scattering at 20 and 30 °C reflects the presence of unimers with R_g = 2.7 nm (similar to 2.8 nm, at natural pH). At 40 °C, both aggregates and micelles coexist (as shown by DLS). At 50 °C, the micelles are substantially smaller than at neutral pH (Table 1), in agreement with DLS results (Figure 2B). N_{agg} is of only 9 molecules per aggregate, comparable to the value of 4 reported in water by static light scattering at pH 2 (37 °C).[2] Thus, a drop in pH can be envisaged as a trigger for the release of a cargo from the interior of the micelles, which do not break fully, thus enabling delivery in a stepwise fashion.

IR spectroscopy can provide information on changes in the chemical surroundings of specific functional groups, such as those occurring in micellization processes or temperature induced sol−gel transitions. There is a precedent of this type of study in the literature,[49] where the aggregation of Pluronic F127 and reverse Tetronic 10R5[3] was followed by monitoring the band at 1085 cm^{-1} (corresponding to the combination of stretching and vibration of the C−O−C from PEO and PPO blocks). The same approach applied to 10% T1107 is shown in Figure 4. When increasing the temperature from 20 to 60 °C, a shift of the 1085 cm^{-1} band toward higher wavenumbers (blue

DOI: 10.1021/acs.langmuir.6b01544
Langmuir 2016, 32, 6398−6408

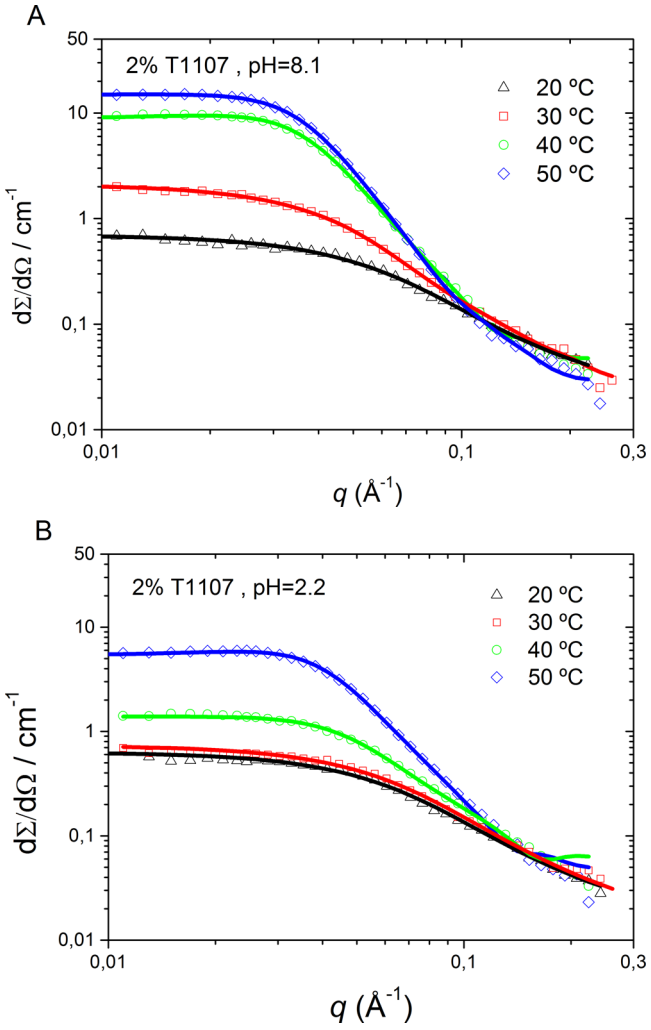

Figure 3. SANS curves for 2% T1107 solutions in D_2O as a function of temperature at pH 8.1 (A) and pH 2.2 (B). Solid lines are fits to the different models described in the text.

Table 1. Micellar Parameters of 2% T1107 in D_2O Deduced from Fits to the SANS Data (Core-Shell Model with a Hard-Sphere Structure Factor)[a]

pH	T/°C	R_c/Å	t/Å	ϕ	$\rho_{shell} \times 10^6$/Å^{-2}	N_{agg}	n_{solv}/EO
8.1	40	34	47	0.08	5.95	14	20
	50	34	46	0.08	6.06	12	23
2.2	50	30	43	0.08	5.99	9	22

[a] R_c (core radius), t (shell thickness), ϕ (volume fraction from the hard-sphere potential), ρ_{shell} (scattering length density of the hydrophilic corona), N_{agg} (aggregation number), n_{solv}/EO (number of solvent molecules per EO in the shell).

shift) is observed, as well as a broadening in the bandwidth (fwhm). There is no clear breakpoint in any of the plots, but a smooth change of slope at around 32 °C (shown with the linear fits) in the maximum of the band, suggesting a small degree of dehydration once micelles form (above the cmc). The broadening of the IR band also points to the coexistence of different environments or states of dehydration. FTIR-ATR analysis of the T1107 25% is shown in SI Figure 1B. This pattern is qualitatively similar to that obtained for Pluronic F127,[49] although in that previous study the breakpoint was sharper. The more open structure of the T1107 compared to

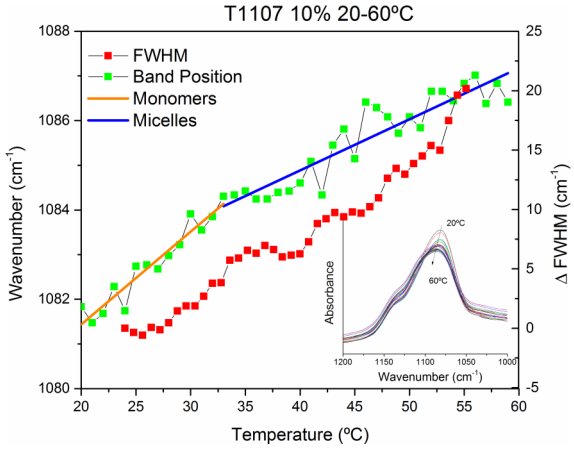

Figure 4. FTIR-ATR analysis of the position and fwhm of the 1085 cm^{-1} band of T1107 samples at 10%. The linear fits of the monomer region (orange) and micelles region (blue) are shown.

that of the Pluronics may explain that changes in hydration occur in a continuous manner, with less of a sharp change, as the micelles are comparatively less compact, with looser unimers.

The Concentrated Regime: T1107 Gels. Raising the temperature and increasing the concentration of T1107 induces the formation of physical gels (Table 1). Figure 5A shows the SANS data obtained at 25% T1107 when gradually increasing the temperature from 20 to 50 °C; samples turn to gels at 40 and 50 °C (see SI Table 1 for the phase diagram in D_2O). Up to 30 °C the solution is viscous, and the system consists of a concentrated solution of micelles, whose interactions are reflected by a strong peak in the mid-q range. At 20 °C, a fit to the CSS model reveals micelles of 26 Å core and 33 Å shell (Table 2). Despite the considerably higher concentration, N_{agg} is lower than for 2% micelles at 40 or 50 °C, and the shell contains more solvent molecules per EO unit (Table 1), showing that temperature more readily enhances aggregation than concentration. At 30 °C, the solution becomes very viscous, producing a high intensity peak around 0.06 $Å^{-1}$ (Figure 5A), as seen in physical gels consisting of packed micelles.[50] In the gel phase (40 and 50 °C), good fits were obtained by using the CSS model with a structure factor for hard spheres, with the sld of the core fixed to that of PO (as for dilute micelles), rather than the paracrystal model used elsewhere for Pluronic gels.[50,51]

FTIR-ATR data of T1107 gel (Figure 1B, SI), unlike what had been observed at 10%, show very little change either in the position of the C−O−C band or its width, suggesting that the chemical environment (i.e., hydration state) of the EO and PO groups remains very similar over the sol-to-gel transition, while it increases more noticeably as a result of micellization (Figure 4).

As acidic pH hinders the formation of the micelles, or results in smaller micelles (as observed in the dilute regime), this must have direct consequences on the structure of the gels (Figure 5B). Clearly, the overall scattering is much lower than at natural pH (Figure 5A). At 20 °C, the lower intensity suggests a transition state, corresponding to a mixture of unimers and micelles, while at higher temperatures (30 °C, 40 °C, 50 °C) the scattering reflects the presence of strongly interacting aggregates, whose structural parameters have been calculated according to a model of CSS with a HS structure factor. The

DOI: 10.1021/acs.langmuir.6b01544
Langmuir 2016, 32, 6398−6408

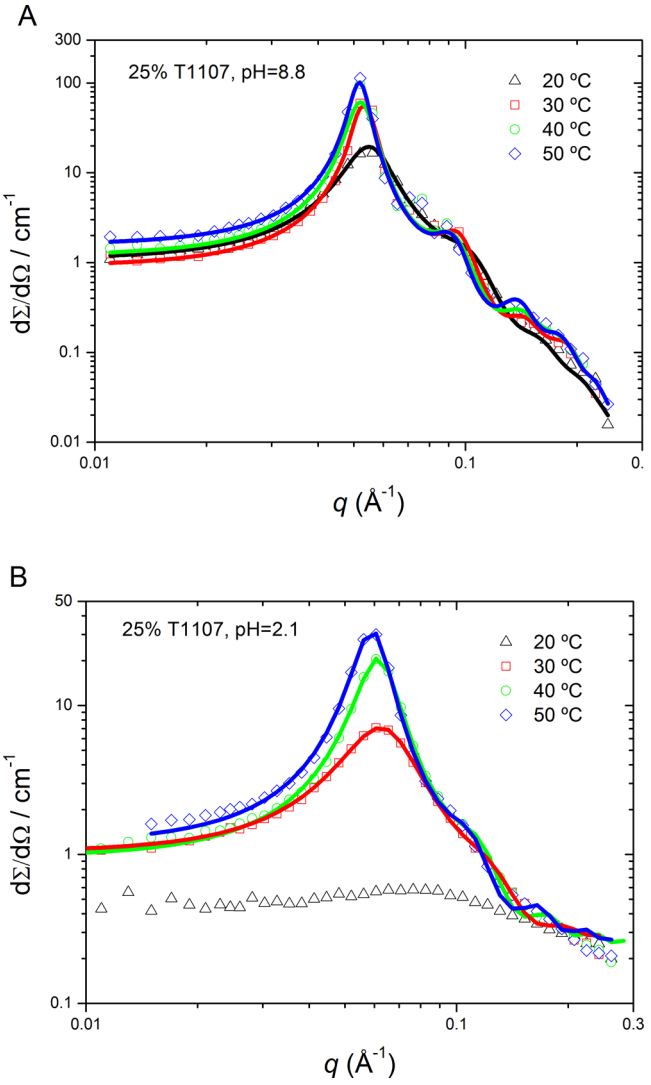

Figure 5. SANS curves from 25% T1107 solutions in D_2O as a function of temperature at pH 8.8 (A) and at pH 2.1 (B). Solid lines are fits to the models described in the text.

Table 2. Micellar Parameters of 25% T1107 in D_2O Deduced from SANS Data Analysis[a]

pH	T/°C	phase	R_c/Å	t/Å	ϕ	$\rho_{shell} \times 10^6$/ Å^{-2}	N_{agg}	n_{sol}/ EO
8.8	20	sol	26	33	0.39	6.29	4	31
	30	sol−gel	30	36	0.52	5.98	8	18
	40	gel	32	36	0.53	5.92	10	16
	50	gel	33	36	0.53	5.94	10	15
2.1	30	sol	23	25	0.29	6.05	3	18
	40	sol	26	27	0.41	5.90	5	14
	50	sol	28	28	0.44	5.80	7	12

[a] R_c (core radius), t (shell thickness), ϕ (volume fraction from the hard-sphere potential), ρ_{shell} (scattering length density of the hydrophilic corona), N_{agg} (aggregation number), n_{sol}/EO (number of solvent molecules per EO in the shell).

resulting aggregation numbers are low compared to the gels at natural pH, but the trend with temperature is the same: a dehydration of the shell and increase of N_{agg}, along with an increase in the dimensions of the aggregates. Finally, the volume fractions and sizes are smaller than at natural pH, in agreement with the reduced N_{agg} under acidic conditions.

The volume fraction returned from the fits gives some valuable insights into the structural changes occurring with temperature. At 20 °C and natural pH, where the solution is still viscous but no gelation has occurred, a value of 0.39 reflects the concentration of strongly interacting particles. This value increases with temperature and becomes practically constant within the gel region at 0.53. The theoretical volume fraction for a compact packing of spheres fcc is 0.74, 0.68 for a bcc, and 0.52 for a scc arrangement, hence the value obtained would correspond to a simple cubic paracrystal arrangement, as for Pluronic F127.[51] The estimated fraction volume of 0.53 suggests that the arrangement, although displaying some long-range order responsible for the intense diffraction peaks, might rather be a dense mixture of micelles, in close contact, which do not form a completely ordered structure.

In order to test this hypothesis further, a wider range of concentrations of T1107 (10%, 20%, and up to 30%) were measured at 40 °C, on a different instrument (D22, ILL) and with a setup that provided a higher resolution of the scattering peaks (Figure 6). 10% T1107 shows no crystallinity peaks, and

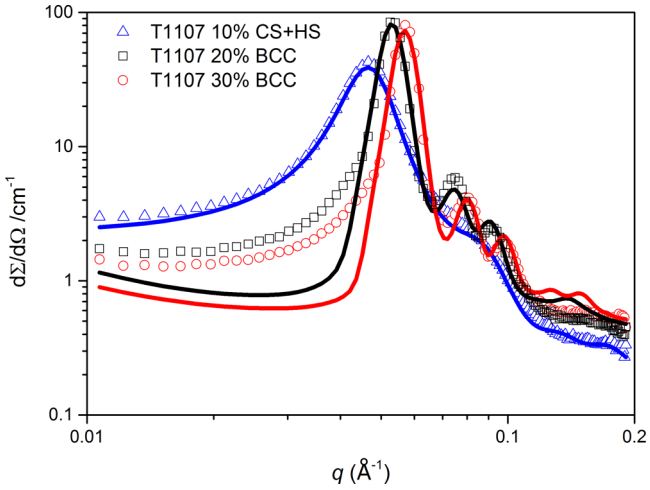

Figure 6. SANS curves from T1107 10%, 20%, and 30% solutions in D_2O at 40 °C and natural pH. Solid lines are fits to the models described in the text CSS+HS (10% sample) and BCC (20% and 30% sample). Data measured on D22 (ILL).

the scattering curve can be fitted very well with the CSS+HS. The increase in concentration to 20% and 30% leads to a 2-fold increase in the intensity and the appearance of sharp scattering peaks in the 0.07−0.09 Å^{-1} range. The higher resolution of this region reveals a peak that was not detectable in the previous setup (Figure 5). The CSS+HS model is no longer suitable to describe the data from 20% and above in the higher q region (despite the fit being of higher quality in the lower q region), as it obviates the first peak at 0.07 Å^{-1} (which is best seen in Figure 7A). As stated above, the presence of these peaks evidence a higher degree of arrangement, probably an intermediate situation between a dense packing of micelles and a paracrystalline structure, which is favored by the inherent polydispersity of the micelles. bcc fits were proposed for samples with concentrations of 20% T1107 and above, and the diffraction peaks at higher q are better described by this model, giving a sphere radius of 35 and 36 Å for 20% and 30%

DOI: 10.1021/acs.langmuir.6b01544
Langmuir 2016, 32, 6398−6408

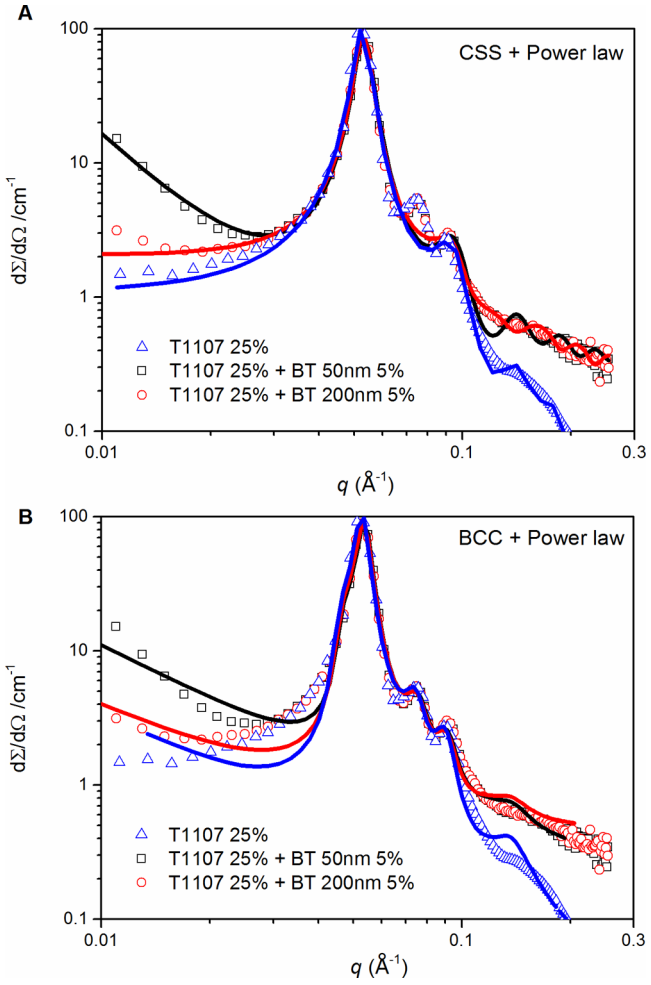

Figure 7. SANS curves from T1107 25% solutions in D_2O and 20% solutions with 5 wt % of BT 50 nm (black) and BT200 nm (red) at 40 °C at natural pH. Solid lines are fits to the models described in the text: CSS+PL (A) and BCC+PL (B).

solutions and nearest neighbor distance (d_{nn}) of 167 and 156 Å, respectively.

Hydrogel Nanocomposites. The structure of the nanocomposite gels was studied by SANS with 20% T1107 and a 5% load of $BaTiO_3$ nanoparticles (50 and 200 nm) to achieve a total dry load of 25%. Figure 7A shows the scattering patterns of the different gel nanocomposites at 40 °C. In addition to the CSS-HS model used for low concentration Tetronic gels, a generic power law was added to account for the scattering of the large inorganic nanoparticles at low q.[52,53] The fitted parameters (Table 3) show that the introduction of the nanoparticles in the gel does not seem to affect the size of the micelles, their volume fraction, or their aggregation number. As observed for the pure Tetronic gels, the simple CSS+HS model, however, is not able to fit the scattering peak adequately in the 0.07−0.09 $Å^{-1}$ q-region. These peaks are typical of crystalline or para-crystalline arrangements in the system due to structured nanodomains, as observed in Pluronic F127 gels[51] and in T1107 gels (Figure 6). The presence of BT nanoparticles in an already concentrated solution may be able to promote this long-range order arrangement.[54] In order to precisely measure the structural parameters of the nanocomposite gels, the bcc approach was also tested, in combination with a power law model (Figure 7B and Table 4). The introduction of the

Table 3. Micellar Parameters of 25% T1107 and 20% T1107 and 5% BT Nanoparticles of 50 and 200 nm in D_2O Extracted from SANS Data Analysis[a]

sample	R_c/Å	t/Å	ϕ	$\rho_{shell} \times 10^6$/ $Å^{-2}$	N_{agg}	n_{sol}/ EO
T1107 25%	32	36	0.552	6.13	10	16
T1107 20% BT50 nm	33	34	0.548	6.03	10	16
T1107 20% BT200 nm	32	36	0.554	5.96	10	16

[a] R_c (core radius, Å), t (shell thickness, Å), ϕ (volume fraction from the hard-sphere potential), ρ (scattering length density), N_{agg} (aggregation number), n_{solv}/x (number of solvent molecules per EO or PO units in the shell).

nanoparticles does not lead to major structural changes in the lattice, namely, a slight tightening of the network with a decrease in the nearest neighbor distance, d_{nn} (Table 4), an effect similar to that obtained by increasing the concentration of T1107 (Figure 6). The values obtained for the T1107+BT nanocomposites fall within the range between the T1107 samples at 20% and 30%. On the other hand, the addition of nanoparticles does not have any notable effect on either the band shift or the fwhm (SI Figure 2). At 25%, T1107 micelles are fully formed at 20 °C, and the compaction of the micelles that takes place when increasing the temperature and leads to the sol−gel transition does not involve changes in the local environment that are reflected in the characteristic vibrations of the EO or PO groups.

Table 4. Micellar Parameters of 25% T1107 and BT Nanoparticles of 50 and 200 nm in D_2O Extracted from SANS Data Analysis Using a BCC Model[a]

sample	R_c/Å	d_{nn}/Å	D factor
T1107 25%	35	167	0.086
T1107 25% BT50 nm	35	165	0.086
T1107 25% BT200 nm	35	166	0.088

[a] R_c (core radius, Å), d_{nn} (nearest neighbor distance, Å), D factor (paracrystal distortion factor).

The introduction of nanoparticles in a hydrogel is known to alter its mechanical properties, as well as the thermogelation behavior of the system.[40,55,56] We thus examine the rheological behavior of the hydrogel nanocomposites, in particular, the effect of nanoparticle size (50 and 200 nm), the relative proportion of poloxamine and NP (varied from 0 to 20% in $BaTiO_3$) and the effect of solvent (both water and phosphate buffered saline, PBS). The presence of BT nanoparticles is expected to impact gel formation by either affecting the packing of the micelles or increasing connectivity in the network.

The temperature sweeps showing the elastic modulus between 10 and 80 °C (Figure 8) reveal a broadening of the gel phase region with increasing concentrations of BT from 0% to 20%. The onset of gelation shifts to lower temperatures by as much as 10 °C, while the gel-to-sol transition extends beyond 80 °C for the highest particle loadings. Replacing water with PBS induces a shift to both sol−gel and gel−sol transitions to lower temperatures (Table 5). This may be attributed to the salting out effect caused by PO_4^{3-} anions present in the solvent[57] that reduce the solubility of the PPO blocks, thus lowering the cmc and promoting micellation. At the same time, these anions reduce the capability of the PEO chains to form

DOI: 10.1021/acs.langmuir.6b01544
Langmuir 2016, 32, 6398−6408

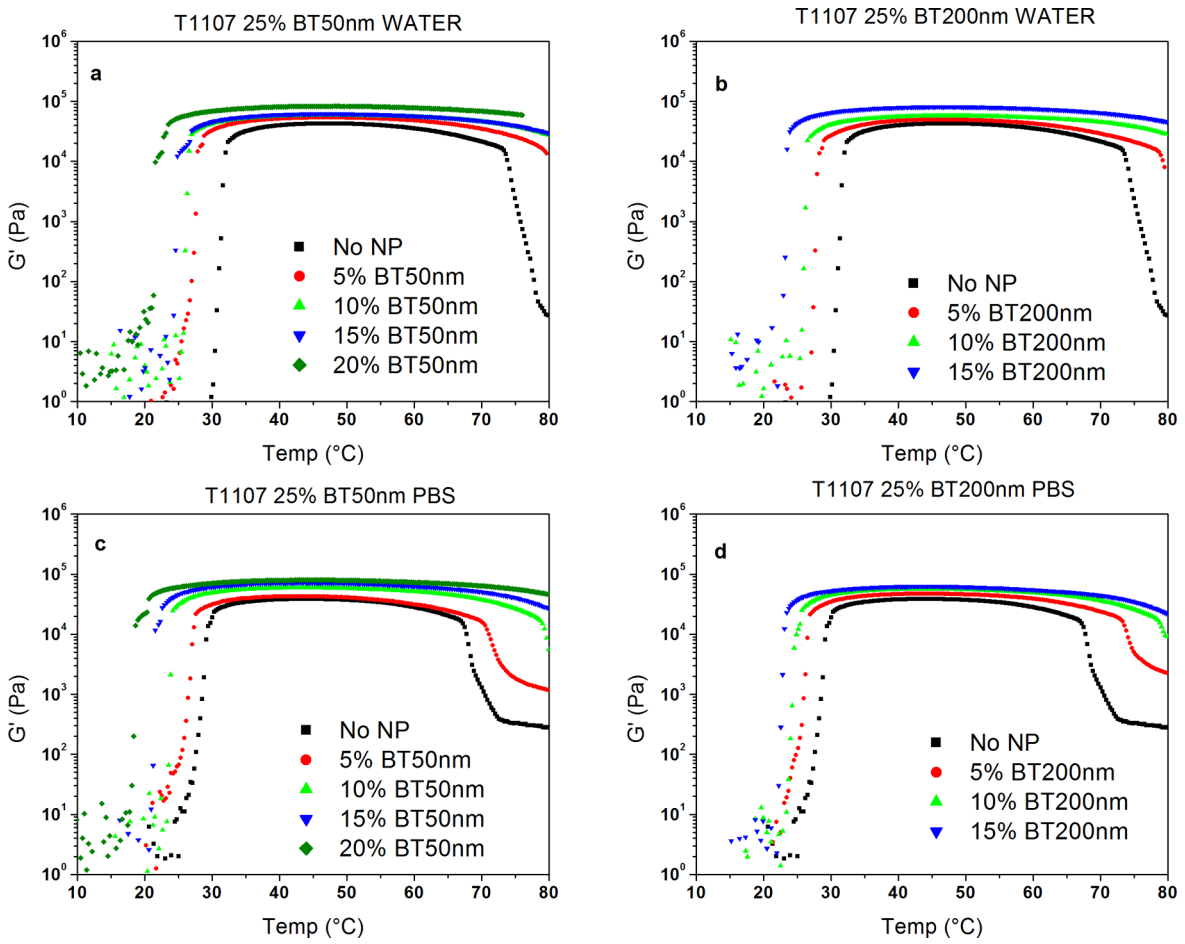

Figure 8. Temperature sweeps of 25% T1107 with BT nanoparticles of 50 and 200 nm in water and PBS, respectively: (a) 50 nm BT in water, (b) 200 nm BT in water, (c) 50 nm BT in PBS, (d) 200 nm BT in PBS.

Table 5. Rheological Data for T1107 25% with 50 nm (BT50) and 200 nm (BT200) $BaTiO_3$ Nanoparticles

sample	solvent	gel temperature (°C)	span of the gel phase (°C)	G′ max (KPa)	tan (δ)
T1107 25%	water	32	41	42.6	0.081
	PBS	29	38	38.3	0.057
5% BT50	water	28	51	53.7	0.046
	PBS	27	43	42.6	0.048
10% BT50	water	27	53	59.1	0.020
	PBS	24	55	59.3	0.021
15% BT50	water	25	53	62.2	0.011
	PBS	22	57	72.4	0.020
20% BT50	water	23	57	83.1	0.016
	PBS	18	60	80.2	0.021
5% BT200	water	28	50	49.4	0.028
	PBS	27	46	47.0	0.049
10% BT200	water	26	53	57.4	0.022
	PBS	24	52	56.6	0.031
15% BT200	water	23	56	81.2	0.014
	PBS	23	57	63.1	0.017

hydrogen bonds with the surrounding water, also lowering the cloud point.[58] This, overall, results in a slightly narrower gel phase, particularly at 0% and 5% BT, but at higher BT loading (above 10%), the effect of PBS is compensated by the effect of the filler, resulting in a gel phase extending beyond 80 °C.

An important effect of the addition of the nanoparticles, beyond extending the gel phase, is the increase in the elastic modulus (Table 5, Figure 9). A direct relationship is observed between the amount of nanoparticles and the increase in G', with, however, no effect of particle sizes up to 10% concentration.

There is, however, quite some variation between repeats at high particle loading (20%) and this erratic behavior may be attributed to the difficulty in achieving sample homogeneity, an effect also seen by Tamborini et al. in their work on micellar polycrystals.[44] The overall increase in G' and sharp decrease in tan (δ) (Table 5) suggests that the introduction of the cyclodextrin-coated nanoparticles leads to a more rigid and connected network. Comparing tan (δ) values at the same compositions for the two different solvents shows again that the presence of charges from PBS leads to an increase in the liquid-like behavior of the system and a looser packing of the network.

Cytotoxicity Studies. Previous investigations have reported good cytotoxicity results for BT alone.[30,59,60] The surface modified BT with CDs, which helps to stabilize the nanoparticles in solution, display excellent viability of the cells, even up to concentrations of 200 μg/mL.[39] Figure 10 shows the MTT results for the T1107 hydrogels at different concentrations with and without BT200-βCD nanoparticles.

Tetronic T1107 shows cytotoxicity scores of 0 (<90%) and 1 (70−90%) after 72 h at all the concentrations but the highest one (25 wt %), with and without BT nanoparticles. With

DOI: 10.1021/acs.langmuir.6b01544
Langmuir 2016, 32, 6398−6408

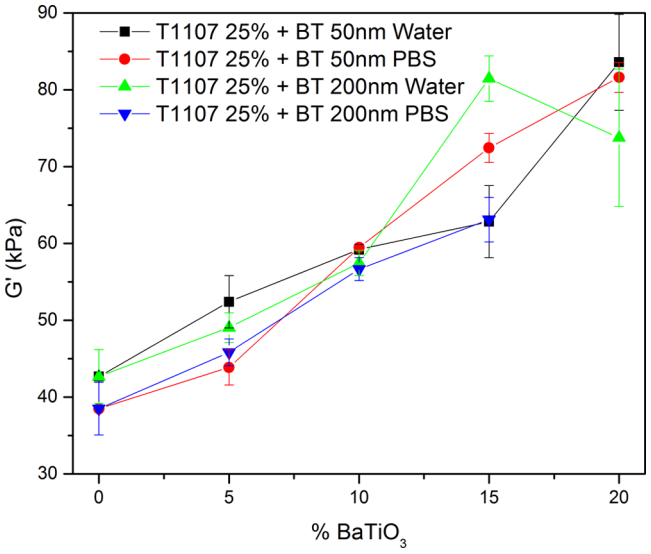

Figure 9. Change in elastic modulus (G') as a function of BT concentration in T1107 25% samples.

poloxamine concentration above 1 wt %, it is difficult to achieve reproducible results in fibroblast cell lines (large standard deviations are shown as error bars), which is in accordance with some results reported in the literature.[11] Fibroblasts are known to be particularly sensitive to nutritional requirements compared to other cell lines.[61] This may be combined with the fact that at higher concentrations (>1% T1107) and 37.5 °C, the high density of micelles or gel may prevent the nutrients to have continuous access to the cell layer in the 96-well plate, and thus contribute to the high deviations. The introduction of the CD-coated nanoparticles generally improves the viability of the cells, results that are in line with what has been reported for BT nanoparticles alone. Altogether, the introduction of BT in the hydrogel and the formation of the nanocomposites do not produce an increase in the toxic effect in the studied cells, thus showing promise for these nanocomposite gels as biomaterials.

CONCLUSIONS

The phase behavior of the hydrophilic, Tetronic T1107 has been fully characterized, using a combination SANS, DLS and FTIR-ATR spectroscopy. At low concentrations and above 30 °C, the amphiphile forms spherical micelles with a dehydrated core and a highly hydrated shell, with relatively small aggregation numbers, mostly due to the hydrophilicity of the polymer, with dimensions that do not depend much on the temperature or concentration. Micellar size is notably affected by the degree of protonation of the central amine spacer, forming loose hydrated aggregates. In the high-concentration regime, T1107 forms gels. SANS data analysis shows that upon gelation the shell of the micelles becomes dehydrated, and long-range order is detected through the appearance of sharp scattering peaks, revealing a bcc order. The presence of BT nanoparticles modified with CDs produces substantial changes in the rheological behavior of the system. By adjusting the concentration of the nanoparticles, the sol−gel transition temperature of 25% T1107 can be tailored, with a maximum reduction in the gelation temperature of 12 °C, as well as an increase of the same magnitude in the gel−sol transition, thus leading to a broadening of the gel phase region. At the same time, the elastic modulus G' of the nanocomposite increases up to 200% by incorporating the BT nanoparticles, and follows a linear trend with the concentration of the nanofiller. Thus, in addition to their inherent piezoelectric properties, the nanoparticles provide a handle to tune gelation point and elastic gel modulus, which is of interest for the preparation of injectable

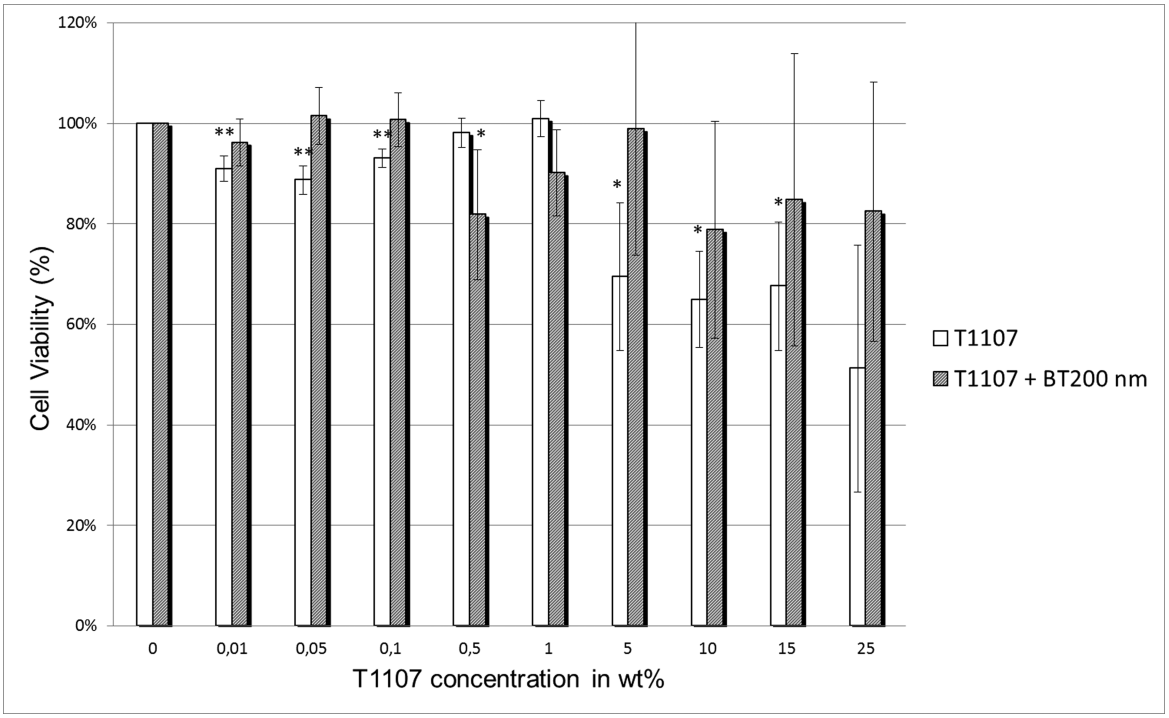

Figure 10. MTT results for NIH3T3 cells and T1107 (white bars) and T1107 with BT 200 nm nanoparticles modified with β-CD (black bars). * denotes $p < 0.05$ and ** denotes $p < 0.01$ by ANOVA variance and Student's t tests.

DOI: 10.1021/acs.langmuir.6b01544
Langmuir 2016, 32, 6398−6408

(thermoresponsive) hydrogels. From the structural point of view, the presence of the modified BT nanoparticles do not disturb the bcc arrangement of the micelles in the gels. Overall, the effect of filler size (50 nm vs 200 nm) is largely negligible, both on the macroscopic scale (rheology) and the nanostructure. Acidic conditions inhibit the formation of a gel phase, leaving a concentrated solution of small, extensively hydrated aggregates. The cytotoxicity of the nanocomposites was assessed both at high and low concentrations. Viability of fibroblasts at low concentration of poloxamine (up to 1 wt %), show excellent results (above 90% viability) for both the T1107 and the nanocomposite. At higher concentrations (1 wt % to 25 wt % T1107 with and without BT), the viability levels are between 70 and 90%, presenting higher variability for that specific cell line due to the presence of the micelles interfering with the nutrition demands of the cells. Overall, these results are promising for the further development nanocomposite hydrogels based on BT for biomedical applications.

■ ASSOCIATED CONTENT

Supporting Information

The Supporting Information is available free of charge on the ACS Publications website at DOI: 10.1021/acs.langmuir.6b01544.

General description on the different models for fitting the SANS data; phase diagram of T1107 in D_2O; fitting results for T1107 0.5 and 5% (CSS-HS); FTIR analysis of T1107 and nanocomposites with $BaTiO_3$ (PDF)

■ AUTHOR INFORMATION

Corresponding Authors

*E-mail: gaitano@unav.es.

*E-mail: cecile.dreiss@kcl.ac.uk.

Notes

The authors declare no competing financial interest.

■ ACKNOWLEDGMENTS

The authors thank ISIS and ILL for the provision of beam time and R. Heenan (Rutherford Appleton Laboratory), Isabelle Grillo, and E. Larrañeta (Queen's University Belfast) for their assistance with the SANS experiments. Prof. G. Martínez de Tejada is acknowledged for his invaluable assistance with the cell viability studies. Financial support from projects MAT2014-59116-C2-2-R of the Spanish MINECO is acknowledged. G.G.-G. is grateful to the Vicerrectorado de Relaciones Internacionales of the UN for the mobility grant for his sabbatical leave at KCL and Asociación de Amigos of the University of Navarra for the Ph.D. grant of R. Serra-Gómez.

■ REFERENCES

(1) da Silva, M. A.; Dreiss, C. A. Soft Nanocomposites: Nanoparticles to Tune Gel Properties. *Polym. Int.* **2016**, *65*, 268−279.

(2) Gonzalez-Lopez, J.; Alvarez-Lorenzo, C.; Taboada, P.; Sosnik, A.; Sandez-Macho, I.; Concheiro, A. Self-Associative Behavior and Drug-Solubilizing Ability of Poloxamine (Tetronic) Block Copolymers. *Langmuir* **2008**, *24*, 10688−10697.

(3) Larrañeta, E.; Isasi, J. R. Phase Behavior of Reverse Poloxamers and Poloxamines in Water. *Langmuir* **2013**, *29*, 1045.

(4) González-Gaitano, G.; da Silva, M. a.; Radulescu, A.; Dreiss, C. a. Selective Tuning of the Self-Assembly and Gelation of a Hydrophilic Poloxamine by Cyclodextrins. *Langmuir* **2015**, *31*, 5645−5655.

(5) Cuestas, M. L.; Sosnik, A.; Mathet, V. L. Poloxamines Display a Multiple Inhibitory Activity of ATP-Binding Cassette (ABC) Transporters in Cancer Cell Lines. *Mol. Pharmaceutics* **2011**, *8*, 1152−1164.

(6) Alvarez-Lorenzo, C.; Sosnik, A.; Concheiro, A. PEO-PPO Block Copolymers for Passive Micellar Targeting and Overcoming Multidrug Resistance in Cancer Therapy. *Curr. Drug Targets* **2011**, *12*, 1112−1130.

(7) Alakhova, D. Y.; Kabanov, A. V. Pluronics and MDR Reversal: An Update. *Mol. Pharmaceutics* **2014**, *11*, 2566−2578.

(8) Annaka, M.; Mortensen, K.; Vigild, M. E.; Matsuura, T.; Tsuji, S.; Ueda, T.; Tsujinaka, H. Design of an Injectable in Situ Gelation Biomaterials for Vitreous Substitute. *Biomacromolecules* **2011**, *12*, 4011−4021.

(9) Alvarez-Lorenzo, C.; Rey-Rico, A.; Sosnik, A.; Taboada, P.; Concheiro, A. Poloxamine-Based Nanomaterials for Drug Delivery. *Front. Biosci., Elite Ed.* **2010**, *2*, 424−440.

(10) Zhang, J.; Sen, A.; Cho, E.; Lee, J. S.; Webb, K. Poloxamine/fibrin Hybrid Hydrogels for Non-Viral Gene Delivery. *J. Tissue Eng. Regener. Med.* **2014**, DOI: 10.1002/term.1906.

(11) Rey-Rico, A.; Silva, M.; Couceiro, J.; Concheiro, A.; Alvarez-Lorenzo, C. Osteogenic Efficiency of in Situ Gelling Poloxamine Systems with and without Bone Morphogenetic Protein-2. *Eur. Cells Mater.* **2011**, *21*, 317−340.

(12) Balazs, A. C.; Emrick, T.; Russell, T. P. Nanoparticle Polymer Composites: Where Two Small Worlds Meet. *Science (Washington, DC, U. S.)* **2006**, *314*, 1107−1110.

(13) Schexnailder, P.; Schmidt, G. Nanocomposite Polymer Hydrogels. *Colloid Polym. Sci.* **2009**, *287*, 1−11.

(14) Chu, Z.; Dreiss, C. a; Feng, Y. Smart Wormlike Micelles. *Chem. Soc. Rev.* **2013**, *42*, 7174−7203.

(15) Wu, C.-J.; Gaharwar, A. K.; Chan, B. K.; Schmidt, G. Mechanically Tough Pluronic F127/Laponite Nanocomposite Hydrogels from Covalently and Physically Cross-Linked Networks. *Macromolecules* **2011**, *44*, 8215−8224.

(16) Gaharwar, A. K.; Dammu, S. a; Canter, J. M.; Wu, C.-J.; Schmidt, G. Highly Extensible, Tough, and Elastomeric Nanocomposite Hydrogels from Poly(ethylene Glycol) and Hydroxyapatite Nanoparticles. *Biomacromolecules* **2011**, *12*, 1641−1650.

(17) Chen, Q.; Zhu, C.; Thouas, G. A. Progress and Challenges in Biomaterials Used for Bone Tissue Engineering: Bioactive Glasses and Elastomeric Composites. *Prog. Biomater.* **2012**, *1*, 2.

(18) Nguyen, L. H.; Annabi, N.; Nikkhah, M.; Bae, H.; Binan, L.; Park, S.; Kang, Y.; Yang, Y.; Khademhosseini, A. Vascularized Bone Tissue Engineering: Approaches for Potential Improvement. *Tissue Eng., Part B* **2012**, *18*, 363−382.

(19) Fan, Z.; Liu, B.; Wang, J.; Zhang, S.; Lin, Q.; Gong, P.; Ma, L.; Yang, S. A Novel Wound Dressing Based on Ag/Graphene Polymer Hydrogel: Effectively Kill Bacteria and Accelerate Wound Healing. *Adv. Funct. Mater.* **2014**, *24*, 3933−3943.

(20) Shin, S. R.; Aghaei-Ghareh-Bolagh, B.; Dang, T. T.; Topkaya, S. N.; Gao, X.; Yang, S. Y.; Jung, S. M.; Oh, J. H.; Dokmeci, M. R.; Tang, X.; et al. Cell-Laden Microengineered and Mechanically Tunable Hybrid Hydrogels of Gelatin and Graphene Oxide. *Adv. Mater.* **2013**, *25*, 6385−6391.

(21) Cho, E.; Lee, J. S.; Webb, K. Formulation and Characterization of Poloxamine-Based Hydrogels as Tissue Sealants. *Acta Biomater.* **2012**, *8*, 2223−2232.

(22) Wang, H.; Bongio, M.; Farbod, K.; Nijhuis, A. W. G.; Van Den Beucken, J.; Boerman, O. C.; Van Hest, J. C. M.; Li, Y.; Jansen, J. A.; Leeuwenburgh, S. C. G. Development of Injectable Organic/inorganic Colloidal Composite Gels Made of Self-Assembling Gelatin Nanospheres and Calcium Phosphate Nanocrystals. *Acta Biomater.* **2014**, *10*, 508−519.

(23) Pina, S.; Oliveira, J. M.; Reis, R. L. Natural-Based Nanocomposites for Bone Tissue Engineering and Regenerative Medicine: A Review. *Adv. Mater.* **2015**, *27*, 1143−1169.

(24) Schiraldi, C.; D'Agostino, A.; Oliva, A.; Flamma, F.; De Rosa, A.; Apicella, A.; Aversa, R.; De Rosa, M. Development of Hybrid Materials

DOI: 10.1021/acs.langmuir.6b01544
Langmuir 2016, 32, 6398−6408

Based on Hydroxyethylmethacrylate as Supports for Improving Cell Adhesion and Proliferation. *Biomaterials* **2004**, *25*, 3645−3653.
(25) Gaharwar, A. K.; Mihaila, S. M.; Swami, A.; Patel, A.; Sant, S.; Reis, R. L.; Marques, A. P.; Gomes, M. E.; Khademhosseini, A. Bioactive Silicate Nanoplatelets for Osteogenic Differentiation of Human Mesenchymal Stem Cells. *Adv. Mater.* **2013**, *25*, 3329−3336.
(26) Si, S.; Zhou, R.; Xing, Z.; Xu, H.; Cai, Y.; Zhang, Q. A Study of Hybrid Organic/inorganic Hydrogel Films Based on in Situ-Generated TiO2 Nanoparticles and Methacrylated Gelatin. *Fibers Polym.* **2013**, *14*, 982−989.
(27) Jeong, C. K.; Kim, I.; Park, K.-I.; Oh, M. H.; Paik, H.; Hwang, G.-T.; No, K.; Nam, Y. S.; Lee, K. J. Virus-Directed Design of a Flexible BaTiO3 Nanogenerator. *ACS Nano* **2013**, *7*, 11016−11025.
(28) Sakai, T.; Hoshiai, S.; Nakamachi, E. Biochemical Compatibility of PZT Piezoelectric Ceramics Covered with Titanium Thin Film. *J. Optoelectron. Adv. Mater.* **2006**, *8*, 1435−1437.
(29) Tsuchiya, K.; Akagawa, Y.; Uetsuji, Y.; Nakamachi, E. Design of Biocompatible High-Piezoelectric BaTiO3 with Additives. In *Proceedings of the SPIE*; Juodkazis, S., Gu, M., Eds.; International Society for Optics and Photonics: Bellingham, WA, 2011; p 82042A.10.1117/12.903230
(30) Dempsey, C.; Lee, I.; Cowan, K. R.; Suh, J. Coating Barium Titanate Nanoparticles with Polyethylenimine Improves Cellular Uptake and Allows for Coupled Imaging and Gene Delivery. *Colloids Surf., B* **2013**, *112*, 108−112.
(31) Hsieh, C.-L.; Grange, R.; Pu, Y.; Psaltis, D. Bioconjugation of Barium Titanate Nanocrystals with Immunoglobulin G Antibody for Second Harmonic Radiation Imaging Probes. *Biomaterials* **2010**, *31*, 2272−2277.
(32) Ciofani, G.; Danti, S.; Moscato, S.; Albertazzi, L.; D'Alessandro, D.; Dinucci, D.; Chiellini, F.; Petrini, M.; Menciassi, a. Preparation of Stable Dispersion of Barium Titanate Nanoparticles: Potential Applications in Biomedicine. *Colloids Surf., B* **2010**, *76*, 535−543.
(33) Barrère, F.; Mahmood, T. a.; de Groot, K.; van Blitterswijk, C. a. Advanced Biomaterials for Skeletal Tissue Regeneration: Instructive and Smart Functions. *Mater. Sci. Eng., R* **2008**, *59*, 38−71.
(34) Feng, J.; Yuan, H.; Zhang, X. Promotion of Osteogenesis by a Piezoelectric Biological Ceramic. *Biomaterials* **1997**, *18*, 1531−1534.
(35) Baxter, F. R.; Turner, I. G.; Bowen, C. R.; Gittings, J. P.; Chaudhuri, J. B. An in Vitro Study of Electrically Active Hydroxyapatite-Barium Titanate Ceramics Using Saos-2 Cells. *J. Mater. Sci.: Mater. Med.* **2009**, *20*, 1697−1708.
(36) Blanco-Lopez, M. C.; Rand, B.; Riley, F. L. The Properties of Aqueous Phase Suspensions of Barium Titanate. *J. Eur. Ceram. Soc.* **1997**, *17*, 281−287.
(37) Paik, U.; Yeo, J.-G.; Lee, M.-H.; Hackley, V. A.; Jung, Y.-G. Dissolution and Reprecipitation of Barium at the Particulate BaTiO3−aqueous Solution Interface. *Mater. Res. Bull.* **2002**, *37*, 1623−1631.
(38) Serra-Gómez, R.; Tardajos, G.; González-Benito, J.; González-Gaitano, G. Rhodamine Solid Complexes as Fluorescence Probes to Monitor the Dispersion of Cyclodextrins in Polymeric Nanocomposites. *Dyes Pigm.* **2012**, *94*, 427−436.
(39) Serra-Gómez, R.; Martinez-Tarifa, J. M.; González-Benito, J.; González-Gaitano, G. Cyclodextrin-Grafted Barium Titanate Nanoparticles for Improved Dispersion and Stabilization in Water-Based Systems. *J. Nanopart. Res.* **2016**, *18*, 24.
(40) Nambam, J. S.; Philip, J. Thermogelling Properties of Triblock Copolymers in the Presence of Hydrophilic Fe3O4 Nanoparticles and Surfactants. *Langmuir* **2012**, *28*, 12044−12053.
(41) Sun, K.; Raghavan, S. R. Thermogelling Aqueous Fluids Containing Low Concentrations of Pluronic F127 and Laponite Nanoparticles. *Langmuir* **2010**, *26*, 8015−8020.
(42) Agrawal, S. K.; Sanabria-Delong, N.; Tew, G. N.; Bhatia, S. R. Nanoparticle-Reinforced Associative Network Hydrogels. *Langmuir* **2008**, *24*, 13148−13154.
(43) Annaka, M.; Mortensen, K.; Matsuura, T.; Ito, M.; Nochioka, K.; Ogata, N. Organic−inorganic Nanocomposite Gels as an in Situ Gelation Biomaterial for Injectable Accommodative Intraocular Lens. *Soft Matter* **2012**, *8*, 7185.
(44) Tamborini, E.; Ghofraniha, N.; Oberdisse, J.; Cipelletti, L.; Ramos, L. Structure of Nanoparticles Embedded in Micellar Polycrystals. *Langmuir* **2012**, *28*, 8562−8570.
(45) Http://www.sasview.org/, Developed by the DANSE Project under NSF Award DMR-0520547.
(46) Benoit, H. On the Effect of Branching and Polydispersity on the Angular Distribution of the Light Scattered by Gaussian Coils. *J. Polym. Sci.* **1953**, *11*, 507−510.
(47) González-Gaitano, G.; Müller, C.; Radulescu, A.; Dreiss, C. A. Modulating the Self-Assembly of Amphiphilic X-Shaped Block Copolymers with Cyclodextrins: Structure and Mechanisms. *Langmuir* **2015**, *31*, 4096−4105.
(48) Kabanov, A. V.; Batrakova, E. V.; Alakhov, V. Y. Pluronic® Block Copolymers as Novel Polymer Therapeutics for Drug and Gene Delivery. *J. Controlled Release* **2002**, *82*, 189−212.
(49) Su, Y. L.; Wang, J.; Liu, H. Z. FTIR Spectroscopic Investigation of Effects of Temperature and Concentration on PEO-PPO-PEO Block Copolymer Properties in Aqueous Solutions. *Macromolecules* **2002**, *35*, 6426−6431.
(50) Okabe, S.; Sugihara, S.; Aoshima, S.; Shibayama, M. Heat-Induced Self-Assembling of Thermosensitive Block Copolymer. Rheology and Dynamic Light Scattering Study. *Macromolecules* **2003**, *36*, 4099−4106.
(51) Dreiss, C. A.; Nwabunwanne, E.; Liu, R.; Brooks, N. J. Assembling and de-Assembling Micelles: Competitive Interactions of Cyclodextrins and Drugs with Pluronics. *Soft Matter* **2009**, *5*, 1888.
(52) Campanella, A.; Di, Z.; Luchini, A.; Paduano, L.; Klapper, A.; Herlitschke, M.; Petracic, O.; Appavou, M. S.; Müller-Buschbaum, P.; Frielinghaus, H.; et al. Nanocomposites Composed of HEUR Polymer and Magnetite Iron Oxide Nanoparticles: Structure and Magnetic Response of the Hydrogel and Dried State. *Polymer* **2015**, *60*, 176−185.
(53) Kanapathipillai, M.; Yusufoglu, Y.; Rawal, a.; Hu, Y.-Y.; Lo, C.-T.; Thiyagarajan, P.; Kalay, Y. E.; Akinc, M.; Mallapragada, S.; Schmidt-Rohr, K. Synthesis and Characterization of Ionic Block Copolymer Templated Calcium Phosphate Nanocomposites. *Chem. Mater.* **2008**, *20*, 5922−5932.
(54) Mortensen, K.; Pedersen, J. S. Structural Study on the Micelle Formation of PEO-PPO-PEO Triblock Copolymer in Aqueous Solutions. *Macromolecules* **1993**, *26*, 805−812.
(55) Shen, J.; Xu, G.; Xin, X.; Wang, L.; Song, Z.; Zhang, H.; Tong, L.; Yang, Z. Supramolecular Hydrogels of α-Cyclodextrin/reverse Poloxamines/carbon-Based Nanomaterials and Its Multi-Functional Application. *RSC Adv.* **2015**, *5*, 40173−40182.
(56) Cha, C.; Shin, S. R.; Gao, X.; Annabi, N.; Dokmeci, M. R.; Tang, X. S.; Khademhosseini, A. Controlling Mechanical Properties of Cell-Laden Hydrogels by Covalent Incorporation of Graphene Oxide. *Small* **2014**, *10*, 514−523.
(57) Pandit, N.; Trygstad, T.; Croy, S.; Bohorquez, M.; Koch, C. Effect of Salts on the Micellization, Clouding, and Solubilization Behavior of Pluronic F127 Solutions. *J. Colloid Interface Sci.* **2000**, *222*, 213−220.
(58) Wang, Y.; Shi, X.; Ren, L.; Yao, Y.; Zhang, F.; Wang, D.-A. Poly(lactide-Co-Glycolide)/titania Composite Microsphere-Sintered Scaffolds for Bone Tissue Engineering Applications. *J. Biomed. Mater. Res., Part B* **2010**, *93*, 84−92.
(59) Ciofani, G.; Danti, S.; D'Alessandro, D.; Moscato, S.; Petrini, M.; Menciassi, A. Barium Titanate Nanoparticles: Highly Cytocompatible Dispersions in Glycol-Chitosan and Doxorubicin Complexes for Cancer Therapy. *Nanoscale Res. Lett.* **2010**, *5*, 1093−1101.
(60) FarrokhTakin, E.; Ciofani, G.; Gemmi, M.; Piazza, V.; Mazzolai, B.; Mattoli, V. Synthesis and Characterization of New Barium Titanate Core−gold Shell Nanoparticles. *Colloids Surf., A* **2012**, *415*, 247−254.
(61) Park, J.-C.; Park, B. J.; Lee, D. H.; Suh, H.; Kim, D.-G.; Kwon, O.-H. Evaluation of the Cytotoxicity of Polyetherurethane (PU) Film Containing Zinc Diethyldithiocarbamate (ZDEC) on Various Cell Lines. *Yonsei Med. J.* **2002**, *43*, 518−526.

DOI: 10.1021/acs.langmuir.6b01544
Langmuir 2016, 32, 6398−6408